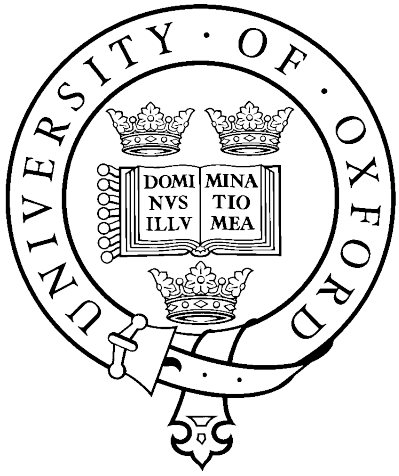
TARGETING THE VLA-4/VCAM-1 INTERACTION FOR THE DIAGNOSIS AND PREVENTION OF BRAIN METASTASES



Vinton Wai Tung Cheng

Wolfson College

Department of Oncology

A thesis submitted to the Medical Sciences Division of the University of Oxford in partial fulfilment of the requirements for the degree of Doctor of Philosophy in Oncology

Hilary Term 2019

ABSTRACT

Background: Brain metastasis is a major cause of cancer patient morbidity and mortality. The late stage of diagnosis and the difficulty in defining the tumour boundary both contribute to the lethality of brain metastases. Cell adhesion molecules (CAMs), such as very late antigen-4 (VLA-4) and its ligand vascular cell adhesion molecule-1 (VCAM-1), have been implicated in the metastatic process. By targeting the VLA-4/VCAM-1 interaction, I applied different methods to improve the diagnosis of brain metastases and to prevent their formation.

Aims: (i) To determine if VCAM-1 targeted MRI is able to detect brain micrometastases from different tumour types in mouse models; (ii) to determine if VCAM-1 targeted MRI is able to detect the brain metastasis invasive margin in rat models; and (iii) to determine if tumour cell VLA-4 knockdown inhibits metastatic spread of cancer to the brain in mouse models.

Findings: VCAM-MPIO MRI could detect brain metastases of different tumour types before gadolinium enhanced T_1-weighted MRI. Furthermore, the imaging contrast improved delineation of the invasive margin of brain macrometastases on T_2^*-weighted MRI, when used in conjunction with conventional techniques. Whilst knockdown of VLA-4 does not entirely prevent brain metastasis formation, the trend to benefit suggests testing in combination with knockdown of other CAMs may yield a significant reduction in metastatic potential.

Discussion: I present a multi-faceted approach, exploiting the roles of VLA-4 and VCAM-1 in brain metastatic formation and progression, for improved diagnosis of brain micro/macrometastases and possible inhibition of metastatic seeding in the brain. Future studies will focus on improving the preventative capacity of anti-CAM therapy and the clinical translation of VCAM-MPIO MRI to human applications.

ACKNOWLEDGEMENTS

A DPhil is not just a research degree, but also a long and winding journey of scientific endeavour and self-discovery. I wish to express my deepest gratitude to my two supervisors, Professors Nicola Sibson and Mark Middleton for their tireless patience in guiding me along this three (and a bit) years' journey. Without them, this thesis would almost certainly never have come to fruition.

I have been very fortunate to work alongside some outstanding individuals in the Experimental Neuroimaging Group and I count them all as friends. Most important has been Dr Manuel Sarmiento Soto, my Spanish post-doctoral supervisor, who was instrumental in teaching me the 'tricks-of-the-trade'. I hope my demonstration of these skills here will do him proud. This thesis has also been reliant on input from Dr Nick de Pennington, Dr Rasheed Zakaria, Dr Sasha Khrapitchev, Christina Simoglou Karali and Dr Francisco Perez-Balderas. A special mention to Dr Maria Pannell, Dr Joanna Gould and Professor Georgios Xenis for their friendship and motivation throughout the writing up phase.

I wish to thank you, the reader, for taking the time to scrutinise and critique this work. One of the important lessons I have learnt is to graciously accept feedback and to listen, as only by doing so can one expand their way of thinking.

Finally, I wish to dedicate this work to my family and, in particular, my parents for their unwavering support throughout my life, but especially during the tough times of this DPhil.

GLOSSARY

°	Degree (angular unit)
α	Alpha
α-error	False positive error
β	Beta
β-error	False negative error
Ɛ	Extinction coefficient
C	siRNA concentration
%	Percentage
°C	Degrees centigrade (thermal unit)
μg/mL	Micrograms per millilitre (unit of concentration)
μL	Microlitre (unit of volume)
μm	Micrometre (microns; unit of length)
μM	Micromolar (unit of concentration)
2D	2-dimensional
3D	3-dimensional
5-ALA	5-aminolevulinic acid
A_{260}	Absorbance at 260 nanometres
ABC	Avidin-biotin complex
ABP	Adjacent brain parenchyma
ADC	Apparent diffusion coefficient
ALCAM	Activated leucocyte cell adhesion molecule
ANOVA	Analysis of variance
AP	Anterior-posterior
ATCC	American Type Culture Collection
B0	Main magnetic field
BBB	Blood-brain barrier
BCA	Bicinchoninic acid
BM-BP	Brain metastasis-brain parenchyma

BMS	Biomedical sciences
BRCA1	Breast cancer 1, early onset
BSA	Bovine serum albumin
ca.	Approximately
CAM	Cell adhesion molecule
Cas9	CRISPR-associated 9 protein
CD	Cluster of differentiation
CNS	Central nervous system
CO_2	Carbon dioxide
CS-1	Connecting segment-1
CRISPR	Clustered regularly interspaced palindromic repeats
CT	Computed tomography
CTA	Computed tomography angiography
CTC	Circulating tumour cell
CTV	Clinical target volume
DAB	3,3'-Diaminobenzidine
DAPI	4',6-diamidino-2-phenylindole
dH_2O	Deionised water
DNA	Deoxyribonucleic acid
DMEM	Dulbecco's Modified Eagle Medium
DMSO	Dimethylsulfoxide
DTPA	Diethylenetriaminepentaacetic acid
DTT	Dithiothreitol
DWI	Diffusion-weighted image
ECL	Enhanced chemiluminescence
EDC	1-Ethyl-3-(3-dimethylaminopropyl)carbodiimide
EDTA	Ethylenediaminetetraacetic acid
EMT	Epithelial to mesenchymal transition
ER	Oestrogen receptor
ESC	Embryonic stem cell
FACS	Fluorescence-activated cell sorting

FBS	Foetal bovine serum
Fe/kg	Iron per kilogram
FFPE	Formalin-fixed paraffin-embedded
FMISO	Fluoromisonidazole
fMRI	Functional magnetic resonance imaging
FOV	Field of view
FSRT	Fractionated stereotactic radiotherapy
G	Gauge (unit of aperture size of hypodermic needles)
g/L	Grams per litre (unit of concentration)
GAPDH	Glyceraldehyde 3-phosphate dehydrogenase
Gd	Gadolinium
GE3D	Gradient echo 3D sequence
GEMM	Genetically engineered mouse model
GTR	Gross total resection
GTV	Gross tumour volume
Gy	Gray (unit of ionising radiation dose)
H1_DL2	Human-derived brain metastasis melanoma cell line
HCl	Hydrochloric acid
hCMEC/D3	Immortalised human brain microvascular endothelial cells
HEPES	4-(2-hydroxyethyl)-1-piperazineethanesulfonic acid
HER2	Human epidermal receptor-2
HIER	Heat induced epitope retrieval
HIF-1	Hypoxia inducible factor-1
HRP	Horseradish peroxidase
hr	Hour (unit of time)
ICAM-1	Intercellular cell adhesion molecule-1
ICB	Intracerebral
ICD	Intracardiac
Ig	Immunoglobulin
IgG1	Immunoglobulin G subclass 1
IgG-MPIO	Immunoglobulin G conjugated to microparticles of iron oxide

IHC	Immunohistochemistry
IL-1β	Interleukin-1β
ITGA4	Integrin α_4 subunit
i.v.	Intravenous
KCl	Potassium chloride
kd	Knockdown
kDa	Kilo Dalton (unit of mass)
kHz	Kilohertz (unit of frequency)
L	Litre (unit of volume)
L	Path length of cuvette
LFA-1	Leucocyte function-associated antigen-1
LPAM-1	Lymphocyte Peyer's patch adhesion molecule-1
LSAB	Labelled streptavidin-biotin
m	Metre (unit of length)
mA	Milliampere (unit of electric current)
MAdCAM-1	Mucosal addressin cell adhesion molecule-1
MDA231Br-GFP	Subclone of MDA231Br human metastatic breast carcinoma cell line labelled with green fluorescence protein
MES	4-Morpholineethanesulfonic acid
$MgCl_2$	Magnesium chloride
MGE3D	Multi gradient-echo 3D sequence
MHz	Megahertz (unit of frequency)
min	Minute (unit of time)
mL	Millilitre (unit of volume)
ML	Medio-lateral
mM	Millimolar (unit of concentration)
mmol/L	Millimoles per litre (unit of concentration)
MMTV	Murine mammary tumour virus
MPIO	Microparticles of iron oxide
MR	Magnetic resonance
MRA	Magnetic resonance angiography

MRI	Magnetic resonance imaging
mRNA	Messenger ribonucleic acid
ms	Milliseconds (unit of time)
MTT	3-(4,5-dimethylthiazol-2-yl)-2,5-diphenyltetrazolium bromide
n	Number
N	Normal (unit of solution concentration)
NADH	Nicotinamide adenine dinucleotide (reduced form)
NADPH	Nicotinamide adenine dinucleotide phosphate (reduced form)
NaOH	Sodium hydroxide
NE	Number of echoes
nGEMM	Non-germline genetically engineered mouse model
ng/µL	Nanogram per microlitre (unit of concentration)
ng/mL	Nanogram per millilitre (unit of concentration)
NK	Natural killer
nm	Nanometre (unit of length)
NO	Nitric oxide
NS	Number of slices
NSCLC	Non-small cell lung cancer
NT	Number of averages
OCT	Optimal cutting temperature
P	Passage (unit of cell subculture)
PAGE	Polyacrylamide gel electrophoresis
PBS	Phosphate buffered saline
PBS-T	Phosphate buffered saline with 0.05% v/v Tween 20
PDX	Patient derived xenograft
PET	Positron emission tomography
PFA	Paraformaldehyde
PIER	Proteolytic induced epitope retrieval
PIL	Procedure Individual Licence
PLP	Periodate-lysine-paraformaldehyde
pmol	Picomole (unit of quantity)

PpIX	Protoporphyrin IX
PPIB	Cyclophilin B
PPL	Procedure Project Licence
PR	Progesterone receptor
PTV	Planning target volume
PVDF	Polyvinylidene fluoride
R_2^*	Transverse relaxation rate
R3-IGF-1	R3-insulin-like growth factor-1
rCBV	Relative cerebral blood volume
RF	Radiofrequency
rhEGF	Recombinant human endothelial growth factor
rhFGF-b	Recombinant human fibroblast growth factor-beta
RISC	Ribonucleic acid-induced silencing complex
RNA	Ribonucleic acid
RNAi	Ribonucleic acid interference
RNase	Ribonuclease
ROI	Region of interest
ROS	Reactive oxygen species
rpm	Revolutions per minute (unit of rotational speed)
SCID	Severe combined immunodeficiency
SCR	Scrambled negative transfection control
SD	Standard deviation
SEBTA-001	Human-derived brain metastasis lung adenocarcinoma cell line
Sec	Second (unit of time)
sEnd-1	Murine skin endothelial cell line
siRNA	Small interfering ribonucleic acid
SNR	Signal-to-noise ratio
SRS	Stereotactic radiosurgery
STR	Short tandem repeat
SW	Spectral width
T	Tesla (unit of magnetic flux density or magnetic field strength)

T_1	Longitudinal relaxation time
T_2	Transverse relaxation time
TALEN	Transcription activator-like effector nuclease
TCPE	Tumour cell-platelet emboli
TE	Echo time
TE2	Second echo time
TR	Repetition time
TME	Tumour microenvironment
TNB	Tris·NaCl blocking buffer
TSA-BIO	Tyramide signal amplification–biotin
TTF-1	Thyroid transcription factor-1
UNT	Untransfected negative control
V	Volt (unit of electric potential)
v/v	Volume by volume (unit of concentration)
VCAM-1	Vascular cell adhesion molecule-1
VCAM-MPIO	VCAM-1 targeted microparticles of iron oxide
VEGF	Vascular endothelial growth factor
VLA	Very late antigen
vs.	Versus
w/v	Weight by volume (unit of concentration)
WBRT	Whole brain radiotherapy

LIST OF TABLES AND FIGURES

Fig 1.1. Invasion-metastasis cascade. 4

Table 1. Comparison of tumour-specific brain metastasis prevalence to corresponding prevalence of primary cancer. 8

Fig 1.2. Cellular constituents of the blood-brain barrier. 15

Fig 1.3. Classes of cell adhesion molecules. 20

Fig 1.4. Leucocyte adhesion cascade. 22

Fig 2.1. Avidin-biotin complex method. 46

Table 2. Antibody and optimum conditions for immunohistochemistry. 49

Fig 2.2. Experimental set-up for intrastriatal injection. 53

Fig 2.3. Experimental set-up for intracardiac injection. 55

Fig 2.4. Protein quantitation assay. 62

Fig 2.5. Protein transfer from gel to member for western blot. 64

Fig 2.6. Post-processing mask of hypointensities from T_2^*-weighted MRI. 72

Fig 3.1. Experimental schedule for intrastriatal xenograft induction. 79

Fig 3.2. Experimental schedule for intracardiac brain metastasis induction. 81

Fig 3.3. Method of analysing gadolinium enhancement on MRI. 84

Fig 3.4. Intrastriatally injected interleukin-1β induces local inflammation in SCID mice. 86

Fig 3.5. Volume of intrastriatal xenografts from different cancer types. 88

Fig 3.6. Gadolinium contrast enhancement of intrastriatal xenografts on T_1-weighted MRI. 90

Fig 3.7. Volume of brain metastases in mice at different timepoints. 92

Fig 3.8. Endothelial VCAM-1 expression in relation to mouse brain metastases over time. 94

Fig 3.9. Co-localisation of VCAM-1 to vasculature in proximity to tumour. 94

Fig 3.10. Example T_2^*-weighted images in tumour-bearing mouse brains following VCAM-MPIO administration. ... 96

Fig 3.11. Hypointensity analysis on T_2^*-weighted MRI and histology following VCAM-MPIO administration. ... 97

Fig 3.12. VCAM-MPIO imaging in control cohorts. ... 99

Fig 3.13. Example MRI sequences for a MDA231Br-GFP metastasis bearing mouse brain. ... 100

Fig 3.14. Example MRI sequences for a H1_DL2 metastasis bearing mouse brain. ... 101

Fig 3.15. Example MRI sequences for a SEBTA-001 metastasis bearing mouse brain. ... 102

Fig 3.16. VCAM-1 and MRI positivity in relation to tumour volume. ... 104

Fig 3.17. VCAM-1 positive vessels around a SEBTA-001 tumour. ... 105

Fig 3.18. Expression of endothelial VCAM-1 in human brain metastasis biopsies. ... 107

Fig 4.1. Method for analysing post-gadolinium T_1-weighted human MR images. ... 122

Fig 4.2. Method for analysing diffusion-weighted human MR images. ... 123

Fig 4.3. Method for quantification of peri-tumoural VCAM-1 positive vessel ... 125

Fig 4.4. Experimental schedule for rat brain imaging of intrastriatal tumours. ... 126

Fig 4.5. Annotation of specific regions of interest in rat brain slices with intrastriatal tumours. ... 128

Fig 4.6. Contrast enhancement across the brain metastasis-brain parenchyma interface in human MRI. ... 131

Fig 4.7. ADC values across the brain metastasis-brain parenchyma interface in human MRI. ... 132

Fig 4.8. Peri-tumoural microvessel density in human brain metastases. ... 134

Fig 4.9. Assessment of vessel distribution in relation to human brain metastasis tumour. ... 135

Fig 4.10. Peri-tumoural VCAM-1 positive vessel distribution in human brain metastases. ... 137

Fig 4.11. Histological examination of intrastriatal MDA231Br-GFP tumours. ... 139

Fig 4.12. Histological examination of intrastriatal U87 tumours. ... 141

Fig 4.13. Tumour marker expression corrected by tumour cell density. ... 143

Fig 4.14. Hypointensity analysis for VCAM-MPIO imaging with MDA231Br-GFP tumours. ... 145

Fig 4.15. Hypointensity analysis for VCAM-MPIO imaging with U87 tumours. 147

Fig 4.16. Comparison of VCAM-MPIO imaging vs. standard MRI sequences. 150

Fig 4.17. Hypointensities beyond gadolinium enhancement in MDA231Br-GFP rat brain xenografts. 151

Fig 4.18. Hypointensities beyond gadolinium enhancement in U87 rat brain xenografts. 152

Fig 5.1. Method for analysing static binding assay confocal images. 167

Fig 5.2. Experimental schedule for brain metastasis induction by intracardiac injection. 167

Fig 5.3. Selection of siRNA for maximum ITGA4 knockdown. 169

Fig 5.4. Tumour cell ITGA4 protein quantitation following siRNA transfection. 171

Fig 5.5. Cellular ITGA4 expression following siRNA transfection. 172

Fig 5.6. MTT assay of ITGA4 siRNA transfected cells. 173

Fig 5.7. Static binding assay of ITGA4 knockdown tumour cells. 174

Fig 5.8. Transwell assay of ITGA4 knockdown tumour cells. 175

Fig 5.9. *In vivo* brain metastases from ITGA4 knockdown tumour cells. 178

Fig 6.1. Diagnostic and therapeutic strategy against brain metastases using anti-CAM therapy and VCAM-MPIO imaging. 198

TABLE OF CONTENTS

ABSTRACT ..... **I**

ACKNOWLEDGEMENTS ..... **II**

GLOSSARY ..... **III**

LIST OF TABLES AND FIGURES ..... **X**

TABLE OF CONTENTS ..... **XIII**

CHAPTER 1: INTRODUCTION **1**

1.1 CANCER 1
1.1.1 Cancer as a genetic and epigenetic disease *1*
1.1.2 Cancer invasion and metastasis *2*
1.1.3 Theories of metastatic seeding *5*
1.2 BRAIN METASTASIS 6
1.2.1 Epidemiology of brain metastasis *6*
1.2.2 Diagnostic imaging for brain metastases *8*
1.2.3 Imaging the brain tumour microenvironment *11*
1.2.4 Role of the blood-brain barrier *14*
1.2.5 Therapeutic options for brain metastases *16*
1.3 CELL ADHESION MOLECULES 19
1.3.1 An introduction to cell adhesion molecules *19*
1.3.2 Vascular cell adhesion molecule-1/Very late antigen-4 interaction *20*
1.3.3 The role of VCAM-1 and VLA-4 in cancer invasion and metastasis *23*
1.4 PRE-CLINICAL MODELS OF BRAIN METASTASIS 25
1.4.1 In vivo animal models for studying cancer metastasis *25*
1.4.2 Methods of tumour engraftment for brain metastasis modelling *29*
1.5 AIMS 31

CHAPTER 2: MATERIALS AND METHODS **32**

2.1 MATERIALS 32
2.1.1 Chemicals and reagents *32*
2.1.2 Injectable agents *32*
2.1.3 Antibodies *33*
2.1.4 Cells *34*
2.1.5 Cell culture tools and reagents *34*
2.1.6 Animal work *35*
2.1.7 Immunohistochemistry *35*
2.1.8 Gene expression studies *36*
2.1.9 Instrumentation *37*
2.1.10 Software *37*
2.2 METHODS 38
2.2.1 Preparation of standard reagents *38*
2.2.1.1 Reagents for animal work 38
2.2.1.2 Buffer solutions for immunohistochemistry 39
2.2.1.3 Buffer solutions for Western blotting 39
2.2.2 Cell culture *39*
2.2.3 Preparation of injectable agents *42*
2.2.3.1 Antibody-MPIO synthesis for mouse imaging 42
2.2.3.2 Antibody-MPIO synthesis for rat imaging 43
2.2.4 Immunohistochemistry (IHC) *43*
2.2.4.1 Tissue preparation 43

2.2.4.2 Antigen retrieval 44
2.2.4.3 3,3'-Diaminobenzidine (DAB) staining 45
2.2.4.4 Immunofluorescence 49
2.2.5 Animal work *50*
2.2.5.1 Animal husbandry 51
2.2.5.2 Preparation of tumour cells for injection 51
2.2.5.3 Intrastriatal injection into mouse brain 52
2.2.5.4 Intrastriatal injection in rat brain 54
2.2.5.5 Intracardiac injection of tumour cells 54
2.2.5.6 Intravenous injections 56
2.2.5.7 Perfusion-fixation and cryostorage of tissue 57
2.2.6 Gene knockdown *58*
2.2.6.1 Ribonucleic acid interference (RNAi) 58
2.2.6.2 Liposomal siRNA delivery 59
2.2.7 Western blotting *60*
2.2.7.1 Protein quantitation 61
2.2.7.2 SDS-PAGE 62
2.2.8 Cell-based phenotypic assays *65*
2.2.8.1 Cell viability assays 65
2.2.8.2 Static binding assay 66
2.2.8.3 Cell transmigration assay 68
2.2.9 Pre-clinical MRI *69*
2.2.9.1 Mouse brain imaging 69
2.2.9.2 Rat brain imaging 70
2.2.9.3 MR Image processing 71
2.2.9.4 Comparison of hypointense signal on T_2^*-weighted MRI with gadolinium enhancement on T_1-weighted MRI 73
2.2.10 Human data collection *73*
2.2.10.1 Stereotactic brain biopsy 73
2.2.10.2 MRI data acquisition 74

CHAPTER 3: VCAM-1 TARGETED MAGNETIC RESONANCE IMAGING FOR THE DETECTION OF BRAIN MICROMETASTASES 75

3.1 INTRODUCTION 75
3.2 METHODS 78
3.2.1 Intracerebral injection brain metastasis models *78*
3.2.2 Intracardiac injection brain metastasis models *80*
3.2.3 In vivo imaging *80*
3.2.4 Immunohistochemistry for VCAM-1 expression *82*
3.2.5 Quantitation of tumour volume and VCAM-1 expression *82*
3.2.6 MR image analysis *83*
3.2.7 Statistical analysis *84*
3.3 RESULTS 85
3.3.1 Development of in vivo pre-clinical models of brain metastasis *85*
3.3.2 Time course of tumour growth following intracerebral induction *87*
3.3.3 Time course of metastatic growth in the brain following intracardial induction *91*
3.3.4 In vivo detection of VCAM-1 upregulation by MRI *95*
3.3.5 Assessment of VCAM-1 expression and VCAM-MPIO MRI positivity *103*
3.3.6 VCAM-1 expression in human brain metastasis *106*
3.4 DISCUSSION 107
3.4.1 Pre-clinical models of brain metastases from different primary tumour types *107*
3.4.2 Endothelial VCAM-1 upregulation in association with micrometastases *110*
3.4.3 Pre-clinical application of VCAM-1 targeted MRI to detect brain micrometastases *111*
3.4.4 Clinical potential of VCAM-1 targeted MRI for the detection of brain micrometastases *113*

CHAPTER 4: VCAM-1 TARGETED MAGNETIC RESONANCE IMAGING TO CHARACTERISE THE INVASIVE BORDER OF BRAIN METASTASIS 116

4.1 INTRODUCTION 116
4.2 METHODS 121

4.2.1 Human brain MRI image analysis *121*
4.2.2 Immunohistochemistry: Human tissue *124*
4.2.3 Intrastriatal tumour models *125*
4.2.4 In vivo MRI *127*
4.2.5 Immunohistochemistry: Rat tissue *127*
4.2.6 Statistical analysis *129*
4.3 RESULTS 130
4.3.1 Defining the brain metastasis-brain interface on human MRI *130*
4.3.2 Endothelial VCAM-1 distribution in the peri-tumoural region of human brain metastasis *133*
4.3.3 Tumour biology at the invasion front in pre-clinical models *138*
4.3.4 VCAM-MPIO MRI in intrastriatal tumour rat brain models *143*
4.4 DISCUSSION 153
4.4.1 Limitations of human MRI in accurately delineating brain metastasis *153*
4.4.2 Pre-clinical xenograft models of brain tumours for VCAM-MPIO imaging *156*
4.4.3 Clinical potential of VCAM-MPIO MRI for detection of the brain metastasis border *159*

CHAPTER 5: DISRUPTING VLA-4 FUNCTION TO PREVENT BRAIN METASTASES 163

5.1 INTRODUCTION 163
5.2 METHODS 165
5.2.1 Knockdown of ITGA4 expression *165*
5.2.2 Quantitation of static binding assay *165*
5.2.3 Animal studies *167*
5.2.4 Immunohistochemistry *168*
5.2.5 Statistical analysis *168*
5.3 RESULTS 168
5.3.1 Selection of siRNA for optimum VLA-4 expression knockdown *168*
5.3.2 Quantitation of VLA-4 expression knockdown *170*
5.3.3 Phenotypic profiling of reduced cellular ITGA4 expression *172*
5.3.4 Effect on in vivo brain metastasis development *176*
5.4 DISCUSSION 178
5.4.1 Disruption of VLA-4 expression interferes with tumour cell adhesion and migration *178*
5.4.2 Brain metastasis seeding is attenuated by VLA-4 disruption *179*
5.4.3 RNAi to achieve VLA-4 knockdown *180*
5.4.4 Beyond the VLA-4/VCAM-1 interaction *183*
5.4.5 Choice of ITGA4 knockdown *185*
5.4.6 Translational potential of disrupting the VLA-4/VCAM-1 interaction in cancer *186*
5.4.7 Future work *187*

CHAPTER 6: DISCUSSION 189

6.1 THE TRANSLATIONAL GAP IN BRAIN METASTASIS RESEARCH 189
6.2 VCAM-1 TARGETED MRI ENABLES DETECTION OF BRAIN MICROMETASTASES FROM DIFFERENT PRIMARY TUMOURS 191
6.3 VCAM-1 TARGETED MRI ENHANCES DETECTION OF THE INVASIVE MARGIN IN BRAIN METASTASES 193
6.4 DISRUPTING TUMOUR-EXPRESSED VLA-4 TO PREVENT METASTATIC SEEDING IN THE BRAIN 195
6.5 A NEW PARADIGM FOR MANAGING BRAIN METASTASES 197

REFERENCES 199

CHAPTER 1: INTRODUCTION

1.1 Cancer

1.1.1 Cancer as a genetic and epigenetic disease

Cancer is the uncontrolled, malignant proliferation of cells that have escaped the normal regulatory processes of cell cycle arrest (senescence) and programmed cell death (apoptosis). Carcinogenesis describes the evolution of normal cells towards malignancy, which is thought to arise from the acquisition of random genetic mutations. In the majority of cases, the alteration of DNA in cells occurs following differentiation from the germ cells (sperm and egg), also known as somatic mutations. Certain genetic changes in the DNA in the germ cells, or germ-line mutations, can also contribute to cancer development with subsequent transmission to progeny. A prime example is the mutation of the *BRCA1* tumour suppressor gene where the association with an increase in the risk of familial breast (1) and ovarian cancers is well established (2).

It is largely accepted that many cancers arise due to a combination of somatic and germ-line mutations; with an underlying genetic predisposition caused by a germ-line heterozygous mutation followed by a somatic mutation in the unaffected gene later in life, a phenomenon coined the two-hit hypothesis as early as 1971 (3). Specific changes relating to activation of proto-oncogenes or inactivation of tumour suppressor genes are particularly important in malignant transformation, as these genes have an important function in maintaining the homeostasis of cell division and cell death, respectively. More recently, with a greater understanding of DNA repair pathways, a class of mutator genes have been proposed to

contribute to genomic instability, such as the accumulation of microsatellite defects through mutated mismatch repair genes (4).

Environmental factors also play a significant role in the development of cancer, through the exposure of an individual to substances that have cancer-causing properties. These carcinogens have the potential to cause mutations following direct exposure to susceptible tissue, such as ultraviolet radiation to skin cells. Moreover, greater interest is being placed on the impact of the environment in modifying the gene expression without direct interference of the DNA code. These so-called epigenetic factors, including DNA methylation, histone modification and microRNA silencing, have been shown to affect cancer initiation and progression, and accounts for the individual variation seen in spite of inherited genetic risk (5). Thus, cancer is shown to be a complex disease requiring a deep understanding of the interplay between the body and the environment.

1.1.2 Cancer invasion and metastasis

Malignant tissue may be differentiated from its normal counterpart by a number of phenotypic traits that are shared across cancers. In an original landmark article, Hanahan and Weinberg (6) elegantly described six hallmarks of cancer, originally comprising the potential for limitless replication, sustained angiogenesis, evading apoptosis, insensitivity to anti-growth signals, self-sufficiency in growth signals, and tissue invasion and metastasis. More recently this list has been updated to include deregulation of cellular energetics, avoidance of immune destruction, genome instability and mutation, and tumour-promoting inflammation (7). Of these, the ability to invade beyond the natural confines of the tissue compartment and spread to a distant secondary site, a process called metastasis, is perhaps considered to be

cancer's most sinister quality. Metastatic disease is thought to contribute to approximately 9 out of 10 of all cancer deaths worldwide (8).

Cancer metastasis is a multistep process thought to be governed by genetic alterations that cause phenotypic changes in the cancer cell. Specifically this includes the promotion of stem cell-like features that permit disruption of homotypic cell interactions, survival in a hostile environment, including the bloodstream, and clonal expansion (9). A process similar to the epithelial to mesenchymal transition (EMT), seen in normal embryonic development, is thought to contribute to the altered phenotype that permits cells to escape from a tumour and spread; importantly this phenotypic crossover is felt to be a two-way process and the ability of cells to dedifferentiate and vice versa indicates cellular plasticity (10). The complex genetic evolution of cancer and its metastases, contributing to intra- and inter-tumoral heterogeneity, are areas of continued exploration in research.

The mechanism of cancer metastasis may be interpreted as a cascading pathway, as illustrated in Fig 1.1. This begins with the separation of a single tumour cell or a cluster of cells from a malignant tumour and invasion of the stroma adjacent to the primary site. Intravasation into the blood or lymphatic circulation provides a route for systemic dissemination. Haematogenous spread, that is metastasis occurring through the blood circulation, is particularly significant due to the readily available access to the rest of the body. Once the tumour cells reach a site for deposition they must extravasate and subsequently colonise the secondary organ. Rare, but alternative routes for metastasis include through the cerebrospinal fluid and iatrogenic means, for example needle track seeding has been reported following surgical biopsy of malignant pleural mesothelioma (11).

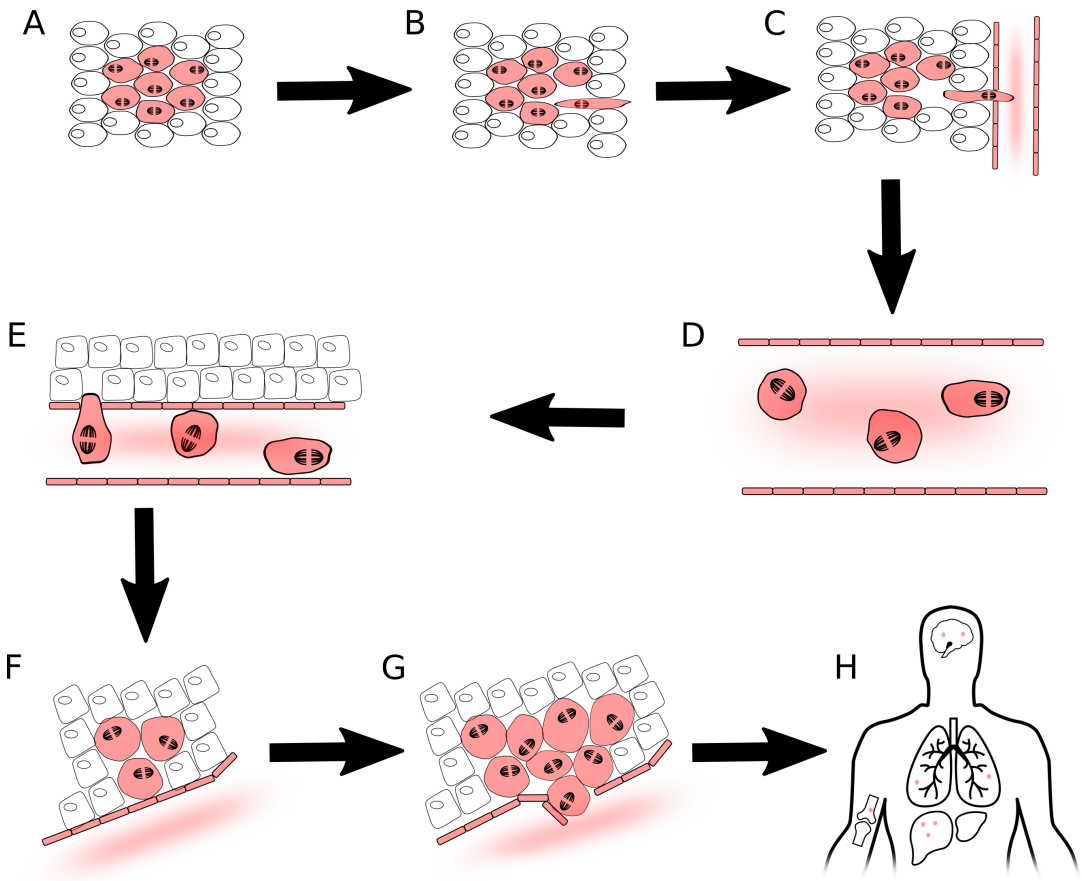


Fig 1.1. Invasion-metastasis cascade. Illustration of the sequence of events leading to haematogenous spread as proposed in the invasion-metastasis cascade, as follows: (A) malignant cells (red colour) develop in the tissue of the primary organ, (B) phenotypic changes lead to tumour cells invading into the local parenchyma and (C) intravasating into nearby blood vessels. (D) The tumour cells must survive in the circulating blood, (E) before arresting in the microvasculature of the secondary organ and extravasating from the blood vessel. (F) The malignant cells establish a micrometastatic focus and, after a latent phase, (G) proliferate into a macrometastasis, with (H) colonisation at sites distant from the primary tumour. Adapted from Valastyan and Weinberg (12).

Mutations in the molecular pathways of the malignant cells chiefly initiate the complex cell-biological events that eventually progress to metastasis. However, there are additional factors

in the tumour microenvironment that contribute, such as the immune response, stroma, vascular density and chemical composition. The tumour microenvironment can stimulate the process of metastasis, through activation of survival pathways that promote tumour cell invasion, like HIF-1 in tissue hypoxia, or the presence of stromal factors that facilitate cell motility, for example linear collagen fibres (13). Understanding the complex interactions between the malignant cell, the tumour colony and its microenvironment will be key towards discovering an effective means to manage cancer metastasis.

1.1.3 Theories of metastatic seeding

As previously mentioned, the potential of mutated cells to invade and disseminate from a primary source to a distant region of the body is a hallmark of cancer. However, the governing principles that determine the site of metastasis are not well understood. It is known that certain cancers have a propensity to preferentially metastasise to the brain and the rest of the central nervous system (CNS). Ewing accounted for this according to the circulatory mechanics of the lymphatic and blood circulation (14). This “mechanical” hypothesis postulates that tumour cells arrest in the draining capillary beds and, therefore, metastasis occurs according to the patterns of blood flow for a specific organ (15, 16). However, the inclination to spread to the brain cannot be solely explained by anatomical location, as close proximity to the CNS structures or even the cerebral circulation does not necessarily predispose to subsequent brain metastasis development. Such tendency to metastasise to specific parts of the body – also known as organotropism – remains poorly understood, for example our understanding of the molecular mechanisms causing breast cancer to commonly spread to the liver, lungs, bone and the brain is still limited (17).

The logical conclusion is that the determinants must be multifactorial in nature and may be influenced by certain characteristics of both the cancer cells and the host. One theory to explain this conundrum was postulated over 100 years ago, by an English surgeon called Stephen Paget. This Victorian era surgeon noted the ability and inclination of cancers to home in on susceptible organs. In what has become known as the "seed and soil" theory of metastasis, Paget proposed that the properties of the recipient organ – or the soil – is as important to study as the nature of the transformed malignant cells – also known as the seed (18). This theory has become a driving proponent towards the exploration of the host microenvironment and the role it plays in permitting tumour deposition, survival in a hostile alien environment and subsequent growth within the metastatic niche.

The process of cancer genetic evolution that contributes to intra- and intertumoral heterogeneity is an exciting recent development in our understanding of this disease (19, 20). Host factors that permit the creation, survival and subsequent growth of a metastatic niche relate to the microenvironment, such as upregulated endothelial expression of adhesion molecules and presence of a susceptible stroma that is conducive to metastatic seeding. Additional host factors that further contribute to the susceptibility include the presence of systemic inflammation and a dysfunctional immune response (21, 22).

1.2 Brain metastasis

1.2.1 Epidemiology of brain metastasis

Brain metastases are the most common intracranial malignancy in adults, far outstripping the incidence of primary central nervous system (CNS) cancers such as high grade gliomas and medulloblastoma. Theoretically, a cancer of any histological type has the potential to spread

to the brain. However, as previously discussed, certain cancers demonstrate a particular inclination, with the top 5 typically comprising of cancers arising from the lung, breast, kidney, colon and melanoma. Lung cancer is the biggest contributor of cases, particularly those of non-small cell lung cancer (NSCLC) origin, with an estimated 39 to 56% of people with lung cancer expected to suffer from brain metastasis over the course of their disease (23).

By far the greatest risk arises from lung cancer, breast cancer and melanoma, which according to some studies make up nearly 1 in 5 of all cases (23). Within these groups of cancer there is marked heterogeneity with respect to risk of brain metastasis development according to histological, and even molecular, subtypes. This lack of uniformity is also seen between individual patients. The data in Table 1 highlights that certain cancers, specifically lung cancer, breast cancer and melanoma, account for a higher proportion of brain metastasis cases in excess of the expected numbers based on prevalence of the primary cancer; thus reiterating the susceptibility of some cancers to successfully colonise the brain. For example, small cell lung cancer (SCLC) is relatively rare, with a worldwide prevalence of around 180,000 cases per year, however it forms around 10% of all brain metastasis cases (24). Similarly, melanoma presents another anomaly in the statistics between primary prevalence against secondary presence in the brain.

Both the incidence and prevalence of people with brain metastases are predicted to rise as the management of patients with cancer means that there is better control over extracranial disease and improved patient survival leading to a larger number of late intracranial relapse.

Primary cancer	Prevalence of brain metastases worldwide (%)	Prevalence of primary cancer in the UK (%)
Lung **(NSCLC)** **(SCLC)**	39-56 (24-42) (6-15)	13 (11-12) (1-2)
Breast	13-30	15
Melanoma	6-10	4
Gastrointestinal **(Colorectal)**	6-9 (3-8)	18 (11)
Renal	2-6	3

Table 1. Comparison of tumour-specific brain metastasis prevalence to corresponding prevalence of primary cancer. Statistics outlining the 5 major groups of primary cancer with the highest prevalence of brain metastasis worldwide and the corresponding prevalence of the primary cancer in the UK. Data compiled from Nayak *et al*. (23) and Cancer Research UK (25).

1.2.2 Diagnostic imaging for brain metastases

To date, the detection of brain metastases has predominantly relied on non-invasive diagnostic imaging. It is not unusual for cancer patients to undergo multiple imaging modalities as part of their diagnostic work-up. The choice of modality in cancer imaging is guided by a number of factors, which can be divided into logistical (access to hardware, availability of relevant clinical expertise for image interpretation, suitable contrast agents/tracers), patient-related (tolerability of test, comorbid disease), treatment-related (accuracy for radiotherapy planning, diagnostic accuracy) and tumour-related (parameter of interest, structural vs. functional testing). Of the most commonly used diagnostic imaging

techniques, X-ray computed tomography (CT), magnetic resonance imaging (MRI) and positron emission tomography (PET) form the bulk of scans used in the clinical radiology department.

X-ray CT involves the capture of many X-ray measurements from an external source directed at a body part. These measurements are then digitally processed to construct cross-sectional – or tomographic – images of the scanned region. Furthermore, it is possible to digitally reconstruct a 3-dimensional (3D) volume from these tomographic images to visualise the scanned body part through multiple planes. Since its introduction several decades ago, X-ray CT has been heavily used in the field of medical imaging, including for the diagnosis of brain metastasis. The ready availability of this imaging modality, high patient tolerability and rapid scan acquisition times means that it continues to be a widely used tool for imaging the brain. With the use of intravenously administered iodinated radiocontrast media, X-ray CT is enhanced for the detection of space occupying lesions in the brain, including cancer. Radiocontrast agents function through absorption of external X-rays, resulting in decreased exposure on the X-ray detector. The major limitation of X-ray CT for brain metastasis imaging is the exposure of patients to ionising radiation, which poses a safety risk if there are repeated scans; in addition, the restrictions on the use of contrast media, in patients with renal impairment and hypersensitivity reactions, means that this imaging technique may not be appropriate in a subsection of patients (26).

MRI remains the mainstay of diagnostic tests for detecting intracranial abnormalities. The biophysical properties of the molecules that make up the human body composition, which is predominantly water, particularly lends itself to this technology. MRI exploits the magnetic

moment inherent in the protons found in water. In the presence of an external strong magnetic field, each particle's magnetic vector becomes aligned as a group and when this alignment is disrupted by a radiofrequency (RF) pulse, the return to a steady state releases energy in the form of signal that can be measured using a magnetic resonance (MR) detector. In the context of neuroimaging, the abundant water content of brain matter proves advantageous in generating superior soft tissue contrast compared to either X-ray CT or PET. An additional advantage is the avoidance of patient or operator exposure to ionising radiation. Standard MRI for detecting intracranial malignancy makes use of contrast media, which alter the magnetic properties of surrounding tissues. In the case of the most commonly used MRI contrast agents, which are gadolinium-based, these have a long relaxation half-life that serve to enhance the signal in T_1-weighted imaging.

PET imaging allows the assessment of certain functional characteristics of malignant tumours depending on the radiopharmaceutical tracer used. The most commonly used tracer, fluorodeoxyglucose (FDG), permits assessment of the uptake of radiolabelled glucose into a lesion and provides a surrogate marker for cellular metabolic activity. Although it also relies on electromagnetic radiation, unlike externally delivered X-rays, PET imaging involves the emission of gamma radiation generated by the radioactive decay of the tracer within the body, which is then measured by an external detector. Other PET tracers currently available include radiolabelled amino acids, such as glutamine, and choline. When co-registered with structural imaging such as MRI or CT, PET imaging becomes a powerful tool that infers functional activity localised to specific regions of the body. Its main limitation is the exposure to radioactive substances; therefore, careful consideration needs to be made with regard to the PET tracer to balance the need for signal intensity against a favourable pharmacokinetic profile that

maximises safety, such as the radioactive decay half-life. In addition, as the tracer uptake is dependent on metabolic activity, lower grade tumours tend to be less responsive to this imaging modality. The utility of FDG-PET is generally sub-optimal in the diagnosis of brain tumours due to the high glucose uptake in normal brain parenchyma, which creates a significant degree of signal noise (27).

1.2.3 Imaging the brain tumour microenvironment

Anatomical imaging provides relevant information about the structural characteristics of the tumour, particularly relating to volume of tumour, maximum diameter, anatomical location and presence of invasion into critical structures. These provide important determinants as to suitability of a patient for therapy, particularly localised treatments such as stereotactic radiosurgery (SRS), targeted radiotherapy or surgical resection. However, the limitations of this approach are that it provides only a static snapshot of the tumour characteristics, which necessitates the need for interval imaging to accurately assess the tumour development over time, especially in response to treatment or clinical symptoms. Moreover, it provides only limited biological information about a lesion, which may complicate the differentiation of malignant disease from benign lesions.

More recently, attempts have been made to interrogate the tumour microenviroment (TME) as a way of understanding the complex tumour physiology. The TME is composed of the tumour, stroma, immune cells and extracellular space. Non-invasive imaging of the TME can provide important dynamic information on the aggressiveness of the cancer, its metastatic potential, and can also help to determine early response to treatment. Given the abundance of the TME compared to the cancerous lesion, which in some tumour types such as pancreatic

cancer may compose up to 90% of the tumour bulk (28), targeting it for imaging would yield a far greater volume of information. Probing the TME through non-invasive means has required a diverse range of imaging techniques as each provides specific detail about individual parameters. One method has been to use molecular probes targeted against particular biomarkers, for example fluoromisonidazole (FMISO) when labelled with fluorine-18 is currently under investigation as a tracer for determining tissue hypoxia in primary brain tumours using PET and is suggested to provide details about treatment response and tumour grading (29, 30).

It is widely accepted that tissue hypoxia plays an important role in shielding cancer against the therapeutic effects of radiotherapy, as oxygen depletion activates transcriptional upregulation of protective factors, such as hypoxia inducible factor-1 (HIF-1). In this situation, radioresistance of the tumour is conferred by induction of gene expression regulating angiogenesis, cellular metabolism and invasive potential (31). A hypoxic environment also leads to reduced radiation-induced reactive species, through absence of free oxidative radicals, thereby contributing to lower radiation efficacy. Armed with more information about the tumour biology, the clinician is able to tailor treatments in a more personalised fashion, such as by targeting radiotherapy to well oxygenated regions of the tumour and applying treatment in dose fractionations.

Interrogating the cerebrovascular blood flow may be performed in a number of ways. Traditionally, X-ray subtraction angiography was the gold standard for visualising the vasculature, which is a fluoroscopic technique involving the injection of radiopaque contrast usually direct into the arterial circulation followed by exposure to time-lapsed X-rays. However,

more recently this technique has been largely superseded by CT or MR angiography. CT angiography (CTA) requires the injection of radiopaque contrast agent into the venous circulation. Following a delay, to permit vascular transport of the contrast to the site of interest, many X-ray images are acquired and subsequently digitally reconstructed to map the 3D vascular network. MR angiography (MRA) is performed in a similar fashion following the underlying principles of MRI physics.

With the advent of immune-modulating therapies – or immunotherapy – in the treatment of cancer, there has been more recent interest in understanding the interaction between the tumour and the immune system, particularly the role of tumour associated macrophages. Cell tracking techniques with labelled immune cells, such as injected host macrophages loaded with iron oxide nanoparticles are capable of demonstrating the systemic distribution of these cells within the body, including the brain, when examined with MRI (32).

Despite the availability of a multitude of imaging modalities and with novel ways of interrogating brain metastases and the surrounding TME on the horizon, as outlined above, there remain a number of key issues limiting the utility of non-invasive imaging. Specifically, for brain metastases, even with improving spatial resolution there is a window of disease that is currently undetectable by conventional imaging methods. This subclinical disease contributes to the late diagnosis of brain metastases and incomplete detection of tumour margins.

1.2.4 Role of the blood-brain barrier

Tumours that develop in the brain, whether as a secondary or primary growth, reside within a unique environmental niche of the body. The brain poses a particular conundrum, as it has long been known as a site of immune privilege, with a protective immune system independent of the systemic immune system. The cerebral vasculature is surrounded by a highly selective semi-permeable membrane barrier, also known as the blood-brain barrier (BBB), which serves to separate the vascular circulation between the CNS and the rest of the body. The BBB is predominantly formed by adherent tight junctions between the brain endothelial cells, but also includes a thickened basement membrane and astrocytic cell projections, as illustrated in Fig 1.2.

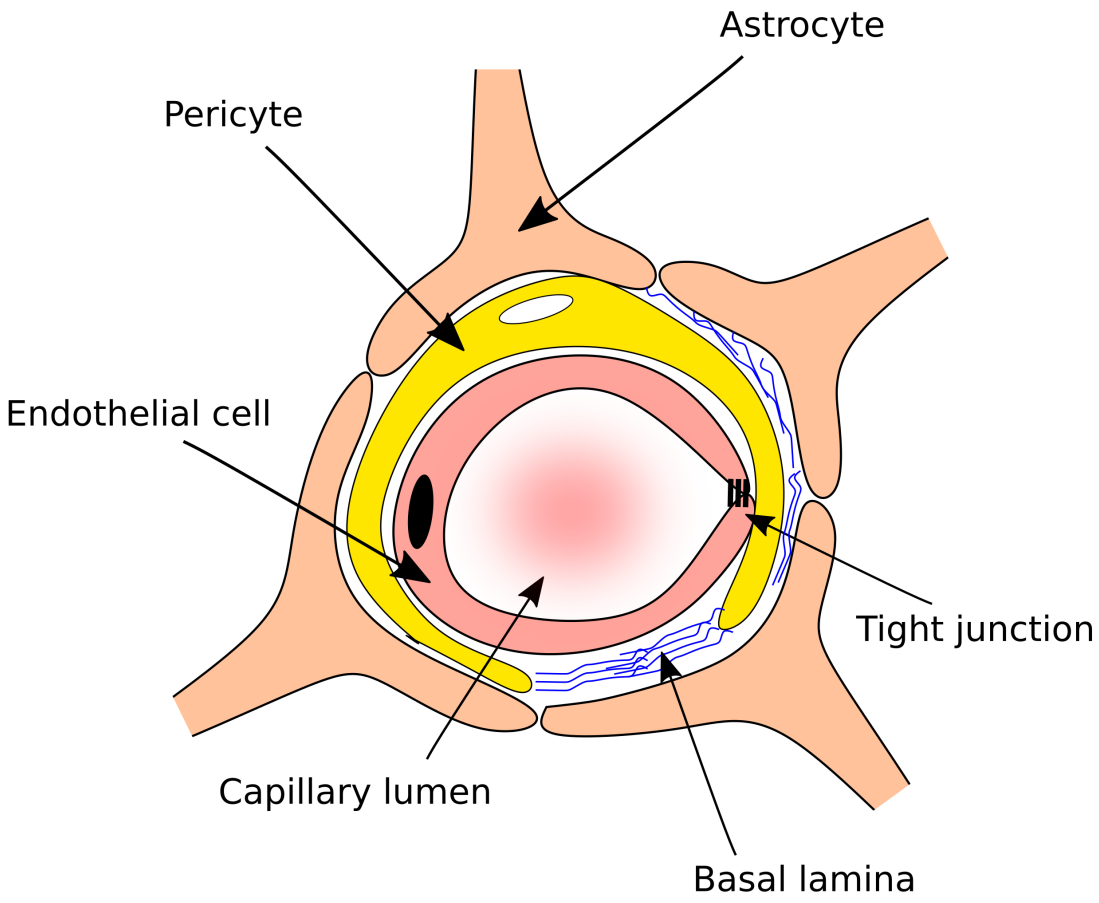


Fig 1.2. Cellular constituents of the blood-brain barrier. Diagrammatic representation of a typical brain capillary, involving specialised endothelial cells bound by adherent tight junctions. The capillaries are surrounded by astrocytic projections, pericytes and the basal lamina and together these prevent the free flow of substances from the circulating blood into the brain parenchyma, through what is known as the blood-brain barrier (BBB). Adapted from Abbott *et al*. (33).

The BBB functions as a physicochemical barrier for the brain by creating a distinct blood circulation that restricts the passive diffusion of lipophilic substances that may be neurotoxic, as well as preventing entry of potentially harmful agents including pathogens and malignant cells. The BBB also serves to permit a stricter regulation of the CNS homeostasis, facilitated by active transport of certain substances, for example generating a higher glucose consumption capacity compared to the rest of the body through the abundancy of glucose transporters on brain endothelium (34).

Despite the inherent benefits of the BBB properties, in certain situations these may become maladaptive and harmful towards the survival of the person. For example, when infectious organisms gain access to the CNS the treatment using drugs intravenously administered through the systemic circulation may be sub-optimal owing to the impermeability of the BBB to most pharmacotherapeutic agents. This has been a historic problem in the context of cancer treatment for CNS malignancies; even to this day, systemic chemotherapy on its own is not generally considered as effective treatment for brain metastases and are typically employed when there are limited options available for local control and to relieve symptoms in the presence of additional extracranial disease burden. With larger tumours, it is known that the BBB becomes disrupted as the invading tumour cells interfere with the endothelial

tight junctions and the underlying stroma. This permeability can permit drugs to reach the tumour, although the distribution in which this occurs is uneven; consequently, the penetration of systemically administered agents remains poor.

The BBB also contributes to diagnostic challenges, particularly for non-invasive imaging that relies on contrast media enhancement. At present, contrast enhanced imaging exploits the passive extravasation of the contrast agent at the site of BBB disruption. Coupled with the clinical suspicion of cancer, clinicians can infer the presence of malignancy through interpretation of an enhancing space occupying lesion, seen on an imaging sequence of the brain. It has been previously shown that xenografted tumours in nude mice of approximately 500μm in diameter will eventually cause a breakdown of the BBB (35); however, in the case of smaller metastases, despite the requirement of traversing the BBB it is thought that this does not result in irreversible damage to the BBB. The utility of imaging contrast agents is negated where there is no BBB breakdown, which then leads to the inability to detect micrometastases at standard imaging resolutions. Consequently, brain metastases are usually detected at a later stage and this limitation highlights that paramount importance of developing a suitable imaging tool that allows earlier detection of brain metastases, preferably when they are subclinical and are more likely to respond to treatment.

1.2.5 Therapeutic options for brain metastases

Historically, the treatments for brain metastases were limited to surgery and/or whole brain therapy (WBRT). Although systemically administered cytotoxic chemotherapy has been used to manage metastatic cancer, including in the brain, as discussed previously its impact is largely attenuated by inadequate penetration into the brain parenchyma. The best option

available is surgical resection as studies have shown that this produces the greatest chance of long-term survival, particularly in oligometastatic disease (36, 37). However, effective surgery requires the tumour bulk to be localised and not demonstrably abutting or invading into adjacent critical structures in the brain.

Used alone, WBRT is known to have limited efficacy in the management of brain metastases, with the significant risk of causing harm through adverse effects of treatment. External beam radiotherapy causes damage to the DNA code in living cells using X-rays to induce cell death, which exploits the ability of normal cells to successfully repair the DNA damage using intact repair mechanisms, in contrast to malignant cells. Whilst effective for cancer, unfortunately it also has the potential to injure healthy cells, thereby causing harmful side effects. The Medical Research Council-funded QUARTZ trial was a large clinical study that demonstrated no overall improvement in the survival or quality of life of patients with inoperable NSCLC brain metastases treated with WBRT over optimal supportive care, including steroids (38). Nevertheless, WBRT may still have a role in the management of brain metastases as an adjunctive treatment following curative localised therapy to treat subclinical distant disease in the brain.

Over the past few decades, technological advancements with imaging and radiotherapy planning have revolutionised the management of brain metastases, especially with respect to improving local therapeutic options, such as conformal radiotherapy, SRS and image-guided surgical techniques. SRS, in particular, has allowed the non-invasive ablation of brain metastases using focal, high intensity radiotherapy beams, which can be targeted to the location of the tumour; thereby limiting the off-target side effects on normal tissue. It has

been shown to provide favourable local control rates for brain metastases and therefore, in the absence of extracranial disease, can significantly prolong survival with an overall survival ranging from 5.5 to 11.3 months and 1-year progression free survival recorded between 71 to 90% (39). However, distant brain relapse remains a primary cause of SRS failure and this is more likely to indicate the presence of occult disease below the detectability of current imaging systems at the time of initial SRS treatment.

The application of SRS for brain tumour treatment is still constrained by the volume and location of the tumour, with a common stipulation that the entire treated tumour bulk volume should be less than 20cm^3, although the criterion limiting the number of treatable tumours has been relaxed (40, 41). As SRS becomes more widely used in clinical practice and its long-term risk is revealed, then it is anticipated that a larger population of patients may benefit from this therapeutic modality in the future. Similarly, surgical resection is mostly indicated in oligometastatic disease, a specific disease state where metastases are few in number, which is a relatively rare situation owing to the challenges of detecting tumours early enough. Therefore, there is a clear clinical rationale for targeting the ability of the cancer to metastasise to the brain and to detect the tumours earlier to improve the prognosis of patients suffering from brain metastases. Moreover, current methods such as gadolinium contrast enhanced MRI fail to detect the full extent of the tumour, particularly at the invasive edge. Therefore, it is also important to develop methods that better identify the extent of tumour infiltration, which will also enhance the efficacy of local therapies, including surgery and radiotherapy.

1.3 Cell adhesion molecules

1.3.1 An introduction to cell adhesion molecules

Cell adhesion molecules (CAMs) are specialised transmembrane proteins, present on the cell surface membrane, that specifically function to permit the adherence and attachment of cells to neighbouring cells or the extracellular matrix. Cell adhesion performs an important role in regulating a diverse range of cell functions, including cell migration, proliferation, apoptosis and signal transduction. On a macroscopic level, cell adhesion serves to maintain tissue structural integrity, thus playing a vital role in organ function and locomotion.

Within the class of CAMs, it is possible to cluster the proteins into families of either cadherins, integrins, immunoglobulin (Ig) superfamily, mucins or selectins, as illustrated in Fig 1.3. With the exception of integrins, which mediate cell-matrix interactions, the remaining CAMs are involved in regulating cell-cell adhesion. Cadherins and the Ig-superfamily predominantly depend on homophilic adhesion, which is the binding of overlapping domains of the same structure on an opposing cell surface, however they are also capable of binding to non-homologous structures (heterophilic adhesion) (42, 43). By contrast the mucin-like CAMs and selectins rely on heterophilic interactions as the lectin component of the selectin binds to a carbohydrate chain on the corresponding mucin-like glycoprotein, for example P-(platelet) selectin binds to P-selectin glycoprotein ligand-1 (44). Meanwhile, the integrins bind to matrix molecules, such as fibronectin and laminin.

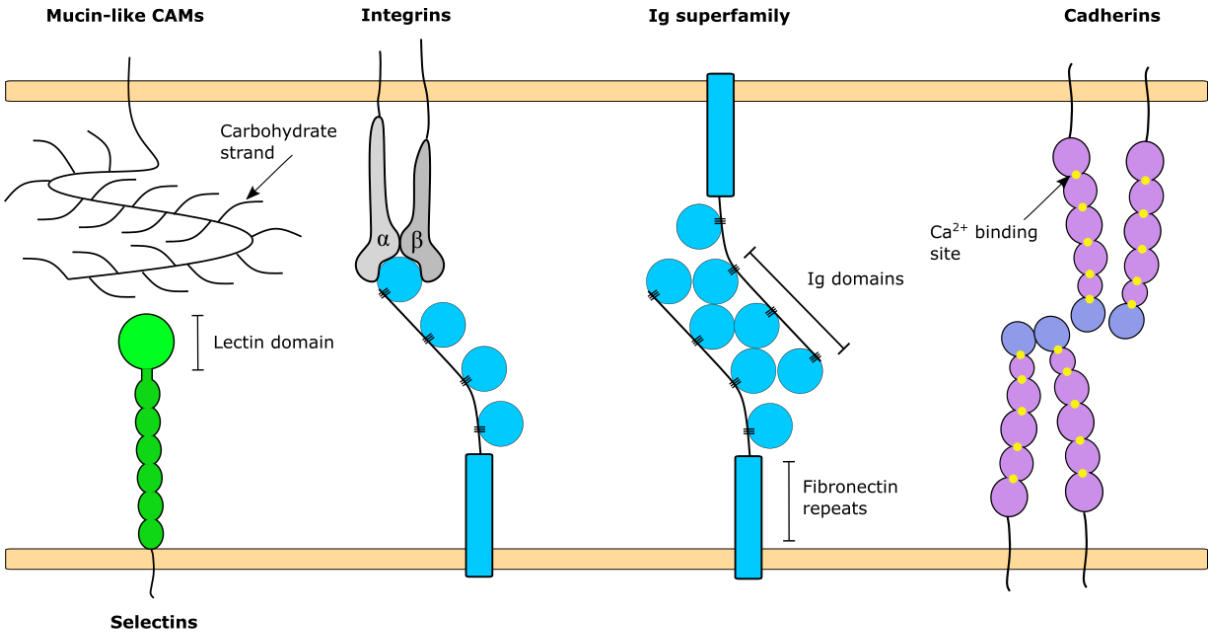


Fig 1.3. Classes of cell adhesion molecules. Diagrammatic representation of the classes of cell adhesion molecules (CAMs) – mucin-like CAMs, integrins, immunoglobulin (Ig) superfamily, cadherins and selectins – and the typical binding interactions. Adapted from Lodish *et al*. (45).

1.3.2 Vascular cell adhesion molecule-1/Very late antigen-4 interaction

Very late antigens (VLA) belongs to a subfamily of integrins, which share a characteristic of a beta-1 (β_1) subunit – also known as cluster of differentiation 29 (CD29). Typical of other integrins, VLAs exist as heterodimers and the β_1 subunit may be non-covalently linked with a number of alpha (α) subunits. The large α subunit ranges in molecular weight from 120-170kDa, whereas the smaller β subunit is between 90-100kDa. Of these, the most important is VLA-4, which is a heterodimer comprising the alpha-4 (α_4) – also known as CD49d – and the β_1 subunits.

Besides functioning as a CAM, VLA-4 is also thought to modulate T-cell signalling by enhancing proliferation, causing effector multifunctionality and *in vivo* memory formation (46). It is expressed on most leucocytes, although on neutrophils it is only expressed in certain circumstances. Two major natural ligands of VLA-4 are specific domains on fibronectin and vascular cell adhesion molecule-1 (VCAM-1; CD106) (47). In an activated form, VLA-4 may bind with other sequences on fibronectin as well as thrombospondin. It also interacts with invasin, a bacterial coat protein, in an activation-independent manner (48). VCAM-1 binding has between 6 to 20 times greater affinity with VLA-4 than binding to fibronectin, based on an *in vitro* model of leucocyte migration on endothelial cells (49).

VCAM-1 belongs to the Ig superfamily and is present on the cell surface membranes of endothelial cells, epithelial cells, fibroblasts and smooth muscle cells (50). It is known to be inducible by cytokines and, therefore, is closely associated with tissue inflammation in a variety of diseases, such as atherosclerosis, multiple sclerosis and infection (51-53). Its primary function is to promote leucocyte trafficking from the vasculature to the site of disease, through facilitation of leucocyte adhesion and transmigration across the endothelium. The expression of VCAM-1 on activated endothelial cells permits the tethering of circulating leucocytes as they come into contact with the luminal surface of the blood vessels.

Leucocyte trafficking from the circulating blood to the site of inflammation follows a well-described sequence of events. After initial attachment, the cell gradually rolls along the surface of the vessel and, in doing so, gradually arrests its movement as the binding of the VLA-4 ligand to the endothelial VCAM-1 overcomes the shear stress generated by flowing blood. As the leucocyte firmly adheres to the endothelial wall, it comes into proximity of

chemoattractant signals such as chemokines. This, in turn, promotes the transmigration of the leucocyte across the endothelial layer, leading to extravasation into the tissue parenchyma, as shown in Fig 1.4.

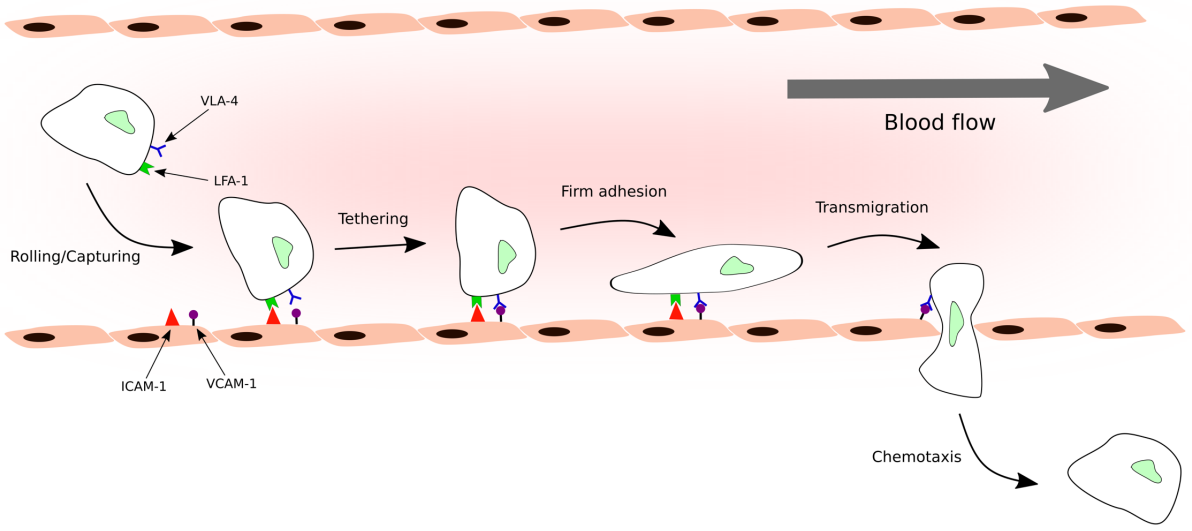


Fig 1.4. Leucocyte adhesion cascade. A simplified diagram illustrating the sequence of events during leucocyte trafficking from the circulating blood to the tissue and the role of two specific CAMs, intercellular cell adhesion molecule-1 (ICAM-1) and vascular cell adhesion molecule-1 (VCAM-1). This initially involves the integrins, alongside selectins (not shown here), on a leucocyte cell randomly making contact with their corresponding ligands on the luminal surface of activated endothelial cells, leucocyte function-associated antigen-1 (LFA-1) and very late antigen-4 (VLA-4), respectively. After forming loose attachments, the cell undergoes rolling on the endothelial surface, creating more opportunities for the receptors to come into contact with the CAMs. As they begin to tether, the circulating cells finally arrests as they become firmly adherent to the vascular wall. The VCAM-1/VLA-4 interaction also assists the cell in transmigrating across the endothelial cell layer and chemotactic signals induce cell motility towards the site of inflammation. Adapted from Ley *et al*. (54) and Greenwood *et al*. (55).

Notably, the process of cell trafficking is not governed solely by the VCAM-1/VLA-4 interaction; it occurs in combination with a number of CAMs, including intercellular cell adhesion molecule-1 (ICAM-1) and E-selectin. *In vitro* studies have shown that the expression of CAMs is time-dependent and cell-specific (56, 57).

1.3.3 The role of VCAM-1 and VLA-4 in cancer invasion and metastasis

As previously mentioned, cancer invasion/metastasis is a multi-step process that culminates in the haematogenous spread of tumour cells, extravasation and colonisation of a secondary site. These final steps, similar to immune trafficking, require the attachment of tumour cells to the endothelial cells mediated by CAMs. Tumour cells have also been shown to aberrantly express certain CAMs, including VCAM-1 and VLA-4 (58, 59), although the distribution is not uniform across all tumour cells. Moreover, endothelial expression of VCAM-1 has been shown to be increased within 5 days after tumour cells have been introduced into the circulating blood of a mouse via intracardiac injection (58).

Endothelial activation of VCAM-1 by circulating tumour cells (CTCs) is thought to occur through a number of mechanisms. When tumour cells enter the circulation, they interact with the blood components including the circulating host cells and signalling factors. A particularly important component encompasses the platelets, which are cytoplasmic fragments derived from megakaryocytes. The primary function of platelets is to induce thrombosis – a natural host defence mechanism against bleeding. Platelets attach to the circulating tumour cells and have been shown to promote survival in the circulation by enabling evasion of host immune attack, protection from intravascular shear stress and release of a myriad of substances, including growth factors, pro-inflammatory cytokines and matrix metalloproteinases (60, 61).

The CTCs form aggregates with platelets, usually in the form of platelet clusters surrounded by tumour cells attached at the periphery. These heterotypic aggregates – or tumour cell-platelet emboli (TCPE) – increase the likelihood of arrest in the microvasculature, thus enabling the seeding of tumour cells prior to extravasation. Furthermore, TCPE lodged in microvessels disrupts the laminar flow of the circulating blood. This turbulent blood flow generates fluctuating shear forces on the endothelial cells, which respond by release of reactive oxygen species (ROS) and nitric oxide (NO) (62). The direct effect of altered haemodynamic forces and the maladaptive release of ROS have been implicated in activation of endothelial VCAM-1 (63, 64).

Endothelial VCAM-1 stimulation is also inducible through direct cell-to-cell interaction between tumour cells and the endothelium. It has previously been demonstrated that tumour cells secrete soluble factors that can stimulate VCAM-1 upregulation on vascular endothelial cells (65). Moreover, the attachment of monocytes/macrophages to tumour cells, through aberrantly expressed VCAM-1, has been shown to be vital to the establishment of the pre-metastatic niche in extracranial tissue beds such as the lung and liver; by secretion of pro-survival factors, exclusion of natural killer cells and enhanced tumour cell extravasation through activation of endothelial-associated CAMs (66, 67). Based on a subcutaneous model of murine lung TC-1 cell line tumours, ectopic VCAM-1 expression has also been shown to facilitate immune evasion directly, through modulating the motility of cytotoxic CD8+ T cells so that they do not remain within the tumour space (68).

In an *in vivo* study of the integrin VLA-4, when ectopically expressed on human HT1080 fibrosarcoma tumour cells, have been shown to enhance tumour cell adhesion to the murine lung endothelial cell surface through the VLA-4/VCAM-1 interaction (69). Furthermore, it has been demonstrated that the binding is specific to VCAM-1 and heterogeneous across tumour cells, dependent on the quantity of VLA-4 expression (70). Conversely, *in vitro* low expression of VLA-4 has also been postulated to enhance the invasive potential of tumours. Qian *et al*. have previously shown that tumour-expressed VLA-4 promotes homotypic intercellular adhesion and by inhibiting its function increased melanoma cell invasion in a 3D matrix was induced (71).

Thus, it is clear that the VLA-4/VCAM-1 interaction regulates several key components of the tumour invasion-metastasis cascade pathway; from tumour cell invasion to modulating immune evasion, tumour cell adhesion and transmigration, and the establishment of the premetastatic niche. As mentioned, this extends beyond the direct tumour cell-to-endothelium interaction and includes the homotypic tumour cell and tumour cell-to-immune cell interactions, as well as indirectly through platelet activation. Therefore, the VLA-4/VCAM-1 interaction has potential for therapeutic targeting to manage metastases (72). Nevertheless, owing to the scarcity of evidence for the role of VLA-4/VCAM-1 in the brain, the potential for combating brain metastases is unknown.

1.4 Pre-clinical models of brain metastasis

1.4.1 *In vivo* animal models for studying cancer metastasis

Despite increasing sophistication of *in vitro* and *ex vivo* models, *in vivo* animal experiments remain a vital tool in the armamentarium for investigating novel management strategies in

cancer. Ethical scientific conduct requires the careful selection of the most appropriate animal model, to maximise the advancement of human medicine, whilst ensuring that the harm to other living organisms in this process is minimised and remains proportionate to the gain. Since Russell and Burch introduced the concept of the 3Rs – replacement, reduction and refinement – in 1959, this has become the guiding principle in the conduct of animal research (73).

One argument for continued *in vivo* experimentation is that a complete organism more accurately portrays the complex biology found in humans, compared to the reductionist approach taken with *in vitro* experiments (74). However, it is also well-known that many promising targets and compounds discovered in the pre-clinical phase using rodents models fail to demonstrate a similar level of efficacy when translated into humans (75). A number of reasons may explain why the translation gap between bench and bedside continues to exist. Firstly, the pre-clinical models may not successfully replicate the environment in which a human tumour develops. Secondly, the obvious physiological differences between a human and a small rodent means that extrapolating the pharmacokinetics, from the model organism to a human, is challenging. Finally, the established tumours usually fail to account for the cellular heterogeneity seen in human tumours (76, 77). Nevertheless, many past animal experiments have also led to major advances in the understanding of tumour biology, with opportunities for future development of novel therapeutic strategies.

Rodent models of brain metastasis can be developed in several different forms: syngeneic, xenogeneic, or genetically engineered mouse models (GEMMs), which may be traditional germline models or newer, non-germline GEMMs (nGEMMs). Syngeneic rodent models

involve the engraftment of tumour cells that have been derived from the same species as the host organism. In contrast, xenogeneic models involve engrafting tumour cells derived from a different species, therefore necessitating the use of an immunocompromised host to prevent immune rejection of the foreign tumour.

Usually, the inoculated tumour cells have been obtained from immortalised cell lines, which permits *in vitro* culture and, therefore, provides a potentially limitless supply. Examples of tumour cells used in this manner include the murine 4T1 mammary pad carcinoma cell line – a subclone derived from a spontaneously arising mammary tumour in a murine mammary tumour virus (MMTV) positive female BALB/c mouse – which has been shown to be highly invasive and is capable of producing spontaneous metastases at multiple sites including lymph nodes, liver, lung, brain and bone (78). For human-rodent xenograft models, a commonly used cell line to investigate brain metastasis tumorigenesis is the MDA231Br cell line – a subclone derived from a human breast cancer cell line MDA-MB-231 that is negative for the oestrogen receptor (ER), progesterone receptor (PR) and human epidermal receptor-2 (HER2) – which, following repeated passages in nude mice and isolation of brain metastasis cells, preferentially metastasises to the brain (79, 80).

Syngeneic models benefit from the availability of an immunocompetent host, meaning that the stroma more accurately mimics the TME and its impact on tumour progression. However, as the tumours are rodent-derived, they may lack the analogous targets present in human tumours and are also known to have a lower mutational load (81), with implications on assessing the efficacy of new therapeutic agents. Human-rodent xenograft models, by contrast, result in tumours that are biologically similar in terms of tumorigenesis and antigen

presentation as found in humans. However, the absence of an adaptive immune system may confound a true response to anti-cancer therapeutics. Humanised mouse models, whereby the immune system of an immunocompromised mouse is reconstituted by implantation of human haematopoietic stem and progenitor cells, has overcome some of the forementioned issues in traditional syngeneic and human-rodent xenograft models; although this approach is limited by the financial cost and the technical complexity of developing such a model (82).

Owing to the altered characteristics of tumour cells associated with long-term *in vitro* monolayer culture (83), there has been greater interest in engrafting tumours taken directly from the patient, whether from the primary site or a metastatic lesion. These patient derived xenografts (PDX) involve direct implantation, either subcutaneously or orthotopically, of complete tumour tissue into an immunocompromised animal. The main benefit of this method is the retention of tumour-specific stroma, including the immune cells and extracellular matrix, which better replicates the TME. Furthermore, direct implantation of a patient's tumour sample into a model organism opens the opportunity for testing tailored therapeutics, thus enhancing the strategy of personalised medicine (84). The limitations of PDX models lie in the inherent variability of engraftment, replacement of human stroma by mouse stromal components post-engraftment and the immunocompromised background of the host organism (74).

Germline GEMMs have allowed an investigation of the impact of target genes on tumourigenesis through selective knockout, whether constitutive or conditional, of tumour suppressor genes. However, in many cases these models do not successfully generate a similar

phenotypic response as the human condition. This discrepancy may be accounted for by the lack of a complex interaction with sporadic somatic mutations, absence of environmental triggers for carcinogenesis and inherent species-specific differences. On the other hand, nGEMMs have been developed through *in vitro* implantation of genetically engineered embryonic stem cells (ESCs) into embryos to generate animals with a chimeric genome. Alternatively, cells from a transgenic animal or that had been genetically manipulated *ex vivo* may be transplanted into the respective adult tissue of a mouse with an unmodified genome (85-87).

1.4.2 Methods of tumour engraftment for brain metastasis modelling

Various methods of tumour engraftment have been used to study brain metastasis *in vivo*, each with their relative strengths and weakness in modelling this disease. Simulating the entire invasion-metastatic cascade leading up to the colonisation of the brain is technically very challenging. It is possible through orthotopic models, whereby tumour tissue or tumour cells are engrafted into the equivalent organ from which the cancer originated (88). However, as brain metastases are typically a late event, animals tend to succumb to complications from the primary tumour or other visceral disease before the opportunity to form brain metastasis presents. Therefore, other methods have been used to investigate the later stages of the metastatic cascade, namely tumour cell extravasation and brain colonisation.

As the most direct route of inoculation, intracerebral (ICB) injection of tumour cells bypasses the circulation and ensures their successful delivery into the brain parenchyma. Consequently, the ICB model cannot be used to examine the tumour seeding process via haematogenous spread. However, it holds the advantage of providing a consistent and highly reproducible ICB

tumour with known starting characteristics, such as quantity of cells injected and location. The ICB model provides important information about how the tumour interacts with the various components of the brain microenvironment and its impact on tumour growth and survival.

Examination of tumour seeding in the brain requires the cells to be disseminated in the circulating blood, which can be achieved through the introduction of tumour cells directly into the vasculature. This provides a better approximation of the sequence of events leading to brain colonisation, as phenotypic changes that promote tumour survival may be activated by interaction with various components of the host circulation, as discussed in Section 1.3.3. Commonly used routes of inoculation of tumour cells to induce brain metastases include via the tail vein, the left ventricle of the heart or the carotid artery.

The intravenous route has the advantage of being easily accessible through the tail vein and requires relatively minimal operator training. However, it is also the route least likely to produce brain colonisation as the bulk of the tumour cells are trapped in the pulmonary vasculature before circulatory distribution to the brain and the rest of the body. In contrast, delivering tumour cells into the carotid artery leads to immediate dissemination to the brain and, thus, minimises the loss of volume to the systemic circulation (89, 90). However, the procedure to ligate the carotid artery is highly skilled and there is a significant risk of post-procedural mortality. Added to which is the complication of a significantly invasive surgical procedure on normal animal physiology and immune system. The alteration of the cerebral circulation may also impact on tumour cell implantation and tumour growth (91).

Introducing tumour cells intracardially is relatively simple to perform and also bypasses the pulmonary circulation, although the potential for concomitant dissemination into the cerebral and systemic circulations produces some degree of variability in brain colonisation. Furthermore, the intracardial (ICD) method can suffer from procedural mortality, for example due to cerebral ischaemia caused by large tumour emboli, and intracardiac tumours due to blind inoculation. The application of ultrasound guidance of the needle injection has been shown to improve the reproducibility and reduced mortality of the ICD method substantially (92, 93).

Thus, the selection of *in vivo* model must be carefully considered from the outset to ensure the maximum information to test the experimental hypothesis.

1.5 Aims

On the basis of previous work, this thesis will achieve the following aims:

1. To determine whether a molecularly targeted MR contrast agent against VCAM-1 can detect brain micrometastases in murine xenograft models of brain metastasis from different tumour types, before there is BBB disruption (Chapter 3).
2. To determine whether a molecularly targeted MR contrast agent against VCAM-1 enables the detection of the tumour invasive edge in rat xenograft models of human breast cancer brain metastasis and human glioblastoma (Chapter 4).
3. To examine the impact of VLA-4 integrin knockdown on metastatic seeding of tumour cells in the brain using murine xenograft models of brain metastasis (Chapter 5).

CHAPTER 2: MATERIALS AND METHODS

2.1 Materials

2.1.1 Chemicals and reagents

Dulbecco's Phosphate Buffered Saline (PBS) tablets (10030290), glacial acetic acid (10171460), xylene (10784001), industrial methylated spirits (11412884), sodium chloride (10316943), Coomassie Brilliant Blue G-250 dye (11886744), 5M hydrochloric acid (10605882), Triton X-100 (BP151), isopentane (10030290), boric acid (B/3800/53) and di-sodium hydrogen orthophosphate (Sorenson's salt; S/4440/60) were all sourced from Fisher Scientific (Loughborough, UK). Sodium dodecyl sulfate (SDS; 74255), methanol (32213), 30% v/v hydrogen peroxide solution (H1009), Tween 20 (P9416), TrisBase (T1503), glutaraldehyde solution (G5882), 4-Morpholineethanesulfonic acid (MES; M5287), glycine (G8898), 1-Ethyl-3-(3-dimethylaminopropyl)carbodiimide (EDC; E1769), bovine serum albumin (BSA; A3059), sodium citrate (S4641), paraformaldehyde (PFA; 158127), lysine hydrochloride (L5626) and sucrose (S9378) were obtained from Sigma-Aldrich (Gillingham, UK). Sodium metaperiodate (27986.235) was obtained from VWR (Lutterworth, UK). Aqueous 2% w/v cresyl violet acetate (RT 26089-20) was obtained from Electron Microscopy Services.

2.1.2 Injectable agents

Dynabeads™ MyOne™ Carboxylic Acid (65011) and Dynabeads™ MyOne™ Tosylactivated (65502) were sourced from Fisher Scientific (Loughborough, UK). Micro Fine+ 0.5mL insulin syringes and needles 30G x 8mm (324869) were obtained from BD (Wokingham, UK).

Omniscan 0.5mmol/mL (1035 074) was obtained from GE Healthcare (Hatfield, UK). Recombinant murine IL-1β (211-11B) was obtained from Peprotech (London, UK).

2.1.3 Antibodies

Anti-human Melan A antibody (ab5106), anti-human Nestin antibody (ab105389), anti-human Vimentin antibody (ab92547), anti-human Thyroid Transcription Factor-1 antibody (TTF1; ab72876) and anti-human Ki67 antibody (ab16667) were obtained from Abcam (Cambridge, UK). Anti-human cytokeratin CAM5.2 (345779) was obtained from BD Biosciences (Wokingham, UK). Anti-Human ITGA4 (119-13960), anti-mouse VCAM-1 (1510-01), Rat IgG1 Isotype Control (1510-01), anti-mouse VCAM-1 low endotoxin/azide-free (1510-14) and Rat IgG1 Isotype Control low endotoxin/azide-free (0116-14) were sourced from Cambridge Bioscience (Cambridge, UK). Anti-rat VCAM-1 purified clone: eBioMR106 (14-1060-85) and mouse IgG K Iso Control Functional Grade Purified Clone: P3.6.2.8.1 (E06660-1641) were obtained from eBioscience (Lutterworth, UK). Streptavidin Dylight 405 conjugated antibody (21831) was obtained from Life Technologies (Lutterworth, UK). Anti-rabbit IgG antibody with horseradish peroxidase (HRP) conjugate (AP307P) was obtained from Millipore (Watford, UK). Anti-mouse/rat CD31 antibody (AF3628) was obtained from R&D Systems (Abingdon, UK). Anti-human VCAM-1 antibody (sc8304) was obtained from Santa Cruz Biotechnology (Heidelberg, Germany). Anti-chicken IgY 488 antibody (SAB4600031) and anti-SOX2 antibody (SAB5500176) were obtained from Sigma-Aldrich (Gillingham, UK). Biotinylated goat anti-rat IgG antibody (BA-9401), biotinylated horse anti-mouse IgG antibody (BA-2001), biotinylated goat anti-rabbit IgG antibody (BA-1000), DyLight 488 streptavidin antibody (SA-5488-1) and Texas Red goat anti-rabbit IgG antibody (TI-1000) were obtained from Vector Laboratories (Orton Southgate, UK).

2.1.4 Cells

MDA231Br-GFP cells (subclone of metastatic breast carcinoma that preferentially metastasises to the brain; kind gift from Prof. P. Steeg, USA); passage (P) number 10. H1_DL2 cells (brain metastasis-derived melanoma; kind gift from Prof. F. Thorsen, Norway); P38. SEBTA-001 cells (brain metastasis-derived lung adenocarcinoma; kind gift from Prof. G. Pilkington, UK); P6. Murine endothelial-derived sEND-1 cells; P30. Human glioblastoma U87 cells (kind gift from Prof. A. Harris, UK); P28. Human brain microvascular endothelial hCMEC/D3 immortalised cells (kind gift from Prof. I. Romero, UK); P25. Human cell lines were authenticated annually using short tandem repeat (STR) profiling via the LGC standards (London, UK) cell line authentication service. STR markers were matched to the known American Type Culture Collection (ATCC) profiles or DNA fingerprints supplied by our collaborators.

2.1.5 Cell culture tools and reagents

Cell scrapers (11597692), cryo 1°C freezing container (Mr Frosty freezing container) (5100-0001) and glass coverslips (circular diameter 12mm) (SDA67761333) were obtained from Fisher Scientific (Loughborough, UK). Tissue culture treated flasks with filter caps (658175) and sterile 2mL cryovials (126263) were obtained from Greiner Bio-One (Stonehouse, UK). Foetal bovine serum (FBS) tetracycline free (FB-1001T/500) was obtained from Labtech International (Heathfield, UK). Trypan blue 0.4% solution (T10282) was obtained from Life Technologies (Lutterworth, UK). MycoAlert™ Mycoplasma Detection Kit (LT07-218) was obtained from Lonza (Blackley, UK). Dulbecco's Modified Eagle's Medium - high glucose (D5796), sterile-filtered human serum (H4522), non-essential amino acid solution 100x

(M7145), sterile-filtered cell freezing medium 1x (C6164), trypsin- Ethylenediaminetetraacetic acid (EDTA) solution 1x (T3924), collagen type I powder from rat tail (C8897) and L-Glutamine solution 200 mM (G7513) were obtained from Sigma-Aldrich (Gillingham, UK). EBM-2 Basal Medium Endothelial Cell Growth Medium-2 BulletKit (CC-3162) was obtained from Lonza (Cambridge, UK).

2.1.6 Animal work

OCT Embedding Matrix (R40020-E) was obtained from Pyramid Innovation (Polegate, UK). Ethicon Mersilk sutures (W582), sterile surgical gloves (AJ5795204EU) and sterile scalpel blades (ILS894) were obtained from NHS supply chain). Feather S35 Microtome blades (JDA-0100-00A) were obtained from CellPath (Newtown, Wales). Scalpel handles (91003-12), Dumont forceps - Dumoxel Standard Tip (11251-35), Olsen-Hegar Needle Holder (12002-12), Graefe forceps (11052-10) and Metzenbaum scissors (14017-14) were sourced from FST GmbH (Essen, Germany). Stainless steel burrs 0.9mm (19008-09) were obtained from Interfocus (Cambridge, UK). Aquasonic 100 ultrasound transmission gel (PMC4679) was obtained from Medisupplies (Bournemouth, UK). Calibrated microcapillary tubes (P0549) were obtained from Sigma-Aldrich (Gillingham, UK).

2.1.7 Immunohistochemistry

3,3'-Diaminobenzidine tetrahydrochloride (DAB; 11209-0050) and microscope slide Superfrost Plus (10149870) were obtained from Fisher Scientific (Loughborough, UK). Image-iT FX Signal Enhancer (I36933) was obtained from Life Technologies (Lutterworth, UK). Tyramide signal amplification-biotin (TSA-BIO) system (NEL700001KT) was obtained from PerkinElmer (London, UK). DPX mounting medium (06522) was obtained from Sigma-Aldrich

(Gillingham, UK). Shandon™ Sequenza™ Immunostaining slide racks (10098889), Pierce™ High Sensitivity Streptavidin-HRP (21134) and Shandon™ Glass Coverplates (11927774) were obtained from Thermo Scientific (Lutterworth, UK). ImmEdge hydrophobic barrier PAP pen (H-4000), normal goat serum (S-1000), normal horse serum (S-2000), normal rabbit serum (S-5000), Vectastain Elite ABC kit (PK-6100), Vectashield mounting medium (H-1000), Vectashield Mounting Medium with 4',6-diamidino-2-phenylindole (DAPI) (H-1200), streptavidin/biotin blocking kit (SP-2002) and Mouse on Mouse (M.O.M.™) basic kit (BMK-2202) were sourced from Vector Laboratories (Orton Southgate, UK).

2.1.8 Gene expression studies

Precision plus dual colour protein standards (161-0374), 10% Mini-PROTEAN-TGX precast protein gels 15-well (4561036) and 4x Laemmli sample buffer (161-0747) were obtained from Bio-Rad (Watford, UK). ON-TARGETplus Human ITGA4 siRNA (L-005189-00-0005), ON-TARGETplus Human Cyclophilin B Control Pool (D-001820-10-05), ON-TARGETplus Non-targeting Pool (D-001810-10-05) and 5x siRNA buffer (B-002000-UB-100) were obtained from Dharmacon (Cambridge, UK). Protein assay kit (23225) was obtained from Fisher Scientific (Loughborough, UK). Opti-MEM® I Reduced Serum Medium (11058-021) was obtained from Life Technologies (Lutterworth, UK). Immobilon-P Polyvinylidene fluoride membranes (32524095) were obtained from Millipore (Watford, UK). CellTiter-Glo® luminescent cell viability (G7571) was obtained from Promega (Southampton, UK). Corning® Transwell® polyester membrane cell culture inserts (GLS3870) were obtained from Sigma-Aldrich (Gillingham, UK). Halt™ Protease and Phosphatase inhibitor cocktail 100x (78442), Lipofectamine® RNAiMAX transfection reagent (13778030), RIPA lysis and extraction buffer

(89900) and SuperSignal West Pico chemiluminescent substrate (34079) were sourced from Thermo Scientific (Loughborough, UK).

2.1.9 Instrumentation

Preclinical ultrasound imaging Vevo 3100 platform and ultrasound probe 707B were obtained from VisualSonics (Toronto, Canada). Microcentrifuge 6000rpm (N2631-0007) was obtained from Starlab (Milton Keynes, UK). Ultrasonic bath (FB15047) was obtained from Fisher Scientific (Loughborough, UK). Vibra-Cell VCX 130 ultrasonic liquid processor was obtained from Sonics (Newtown, USA). Leica CM1950 cryostat platform, Leica TCS SP8 confocal laser microscopy scanning platform and Aperio CS2 digital pathology slide scanner were obtained from Leica Biosystems (Wetzlar, Germany). Odyssey® Fc imaging system was obtained from LI-COR (Lincoln, USA). Countess II Automated Cell Counter (AMQAX1000) was obtained from Invitrogen (Loughborough, UK). Homeothermic monitoring system (55-7020) was obtained from Harvard Apparatus (Cambridge, UK). Quadrature dual tuned birdcage coil with 28mm diameter aperture was obtained from Pulse Teq (Chobham, UK). Mains powered drill 240V (503599) and WPI Stereotaxic Frame with 45° Ear Bars (502650) were obtained from World Precision Instruments (Hitchin, UK). Nuvo Lite Mark 5 Liter Oxygen Concentrator was obtained from Nidek Medical (Birmingham, USA).

2.1.10 Software

The following software were utilised in this body of work: FlowJo v10 (FlowJo LLC), ImageJ v1.51 (NIH), Leica Application Suite X v3.3.0 (Leica), Aperio ImageScope v12.3.3 (Leica), VnmrJ v4.2 (Varian), Horos v3.0 (The Horos Project), ITK-SNAP v3.6.0 (UPenn and UNC), MATLAB

vR2018a (MathWorks), Prism v5 (GraphPad Software) and DtiStudio v2.0 (John Hopkins University).

2.2 Methods

2.2.1 Preparation of standard reagents

2.2.1.1 Reagents for animal work

Heparinised saline was prepared by dissolving 50mL of 1000 i.u./mL heparin sodium solution in 4950mL of 0.9% w/v sodium chloride in dH_2O.

Periodate-lysine-paraformaldehyde (PLP) fixative was prepared by dissolving 13.7g of lysine hydrochloride and 1.8g of Sorenson's salt in 475mL dH_2O. To this, 200mL of 10% w/v paraformaldehyde in dH_2O was added and mixed, before dissolving 2.14g of sodium metaperiodate. The solution was buffered with 0.1M phosphate buffer solution to a total volume of 1L and pH adjusted to 7.2 with 10M sodium hydroxide (NaOH) solution. Prior to perfusion-fixation, 0.025% v/v glutaraldehyde was added to create PLP light.

A 0.1M sodium borate buffer solution was prepared by dissolving 0.6183g of boric acid in 100mL dH_2O. The pH was adjusted to 9.5 with 5M NaOH solution. The 3M ammonium sulphate solution was prepared by dissolving 19.8g ammonium sulphate in 50mL 0.1M sodium borate buffer, before pH correction to 9.5.

2.2.1.2 Buffer solutions for immunohistochemistry

A concentrated 10x sodium citrate buffer stock solution was prepared as follows: dissolve 2.94g trisodium citrate dihydrate in 1L dH_2O. Adjust pH to 6.0 with 1N hydrochloric acid (HCl) and add 0.5mL of Tween-20.

A concentrated 10x phosphate buffer stock solution was prepared as follows: dissolve 31.2g of sodium dihydrogen phosphate with 136g of Sorrenson's salt in 1L dH_2O and pH adjusted to 7.4.

To prepare phosphate buffered saline-Tween 20 (PBS-T), 50 tablets of standard Dulbecco's PBS was dissolved in 5L dH_2O. To this, 2.5mL of Tween 20 solution was dissolved to achieve a final concentration of 0.05% v/v.

2.2.1.3 Buffer solutions for Western blotting

A concentrated 10x running buffer stock solution was prepared as follows: dissolve 15.15g TrisBase, 72g glycine and 5g SDS in 500mL of 20% v/v methanol in dH_2O.

A concentrated 10x transfer buffer stock solution was prepared as follows: dissolve 15.15g TrisBase and 72g glycine in 500mL of dH_2O.

2.2.2 Cell culture

All aspects of cell handling, including preparation of cell culture reagents, were performed under sterile conditions within a laminar flow tissue culture hood that had been cleaned and sterilised with 70% v/v denatured ethanol in deionised water (dH_2O) purified by reverse

osmosis. Where appropriate, cell culture reagents were aliquoted into sterile 15mL falcon tubes and stored at -20°C. Prior to use in cell culture, the reagents were thawed in a temperature-controlled water bath and allowed to equilibrate at 37°C.

Cryopreserved MDA231Br-GFP cells were resuscitated by thawing in a water bath for 10 mins. A cell pellet was separated from the cell freezing medium under centrifugation (1000rpm, 5 mins, 21°C) in a falcon tube. Following aspiration of the freezing medium, the cells were resuspended in growth medium. Growth medium was DMEM containing 4.5g/L (25mmol/L) glucose supplemented with 10% v/v FBS and 2% v/v L-glutamine. The cell suspension was transferred to a sterile uncoated polystyrene flask and allowed to culture in a 37°C incubator with a controlled atmosphere of 5% CO_2 and 95% humidified air. Waste material was removed every 2 to 3 days through aspiration of the waste culture fluid, gently washing the cells with PBS and exchange with new culture medium. Cultured cells were regularly inspected for morphology, confluence, adherence and absence of infection using an inverted light microscope. At 70-80% confluence, the adherent cells were passaged by removing the culture medium, gently washing with PBS and enzymatically disassociated from the culture flask base by incubation at 37°C with 1mL trypsin-EDTA for 5 mins. The trypsin-EDTA was inactivated by addition of 5mL of growth medium and one sixth of the cell suspension was subcultured into a new sterile culture flask containing growth medium.

Similar culture conditions were applied to the H1_DL2 cells and the SEBTA-001 cells, with the exception of different growth media and passage conditions. Specifically, the H1_DL2 cells were cultured in growth medium comprising DMEM containing 4.5g/L (25mmol/L) glucose supplemented with 10% v/v FBS, 2% v/v L-glutamine and 3.2% v/v NEAA. Similar to the

MDA231Br-GFP cells, the H1_DL2 cells were also passaged at one sixth of the original cell suspension. For the SEBTA-001 cells, the growth medium comprised DMEM containing 4.5g/L (25mmol/L) glucose supplemented with 2% v/v human serum only. The SEBTA-001 cells were passaged at one quarter of the original cell suspension and required an additional centrifugation step after enzymatic dissociation to separate the cell pellet from the trypsin-EDTA, before resuspension in growth medium. All cell lines in active culture underwent routine *Mycoplasma* testing every eight weeks, according to the MycoAlert (Lonza) standardised protocol.

Culture of the human U87 glioblastoma cell line was undertaken by Dr Nicholas de Pennington and required growth medium comprising DMEM containing 4.5g/L (25mmol/L) glucose supplemented with 10% v/v FBS and 1% v/v L-glutamine. The endothelial cell lines were cultured under similar conditions, with the exception of different growth media. Murine sEND-1 cells were cultured in growth medium comprising DMEM containing 4.5g/L (25mmol/L) glucose supplemented with 10% v/v FBS and 2% v/v L-glutamine. Meanwhile, the human hCMEC/D3 brain endothelial cells were grown in a specially formulated growth medium for the culture of human microvascular endothelial cells (EBM-2 Basal Medium), which was supplemented with 0.025% v/v recombinant human endothelial growth factor (rhEGF), 0.025% vascular endothelial growth factor (VEGF), 0.025 % v/v R3-insulin-like growth factor-1 (R3-IGF-1), 0.1 % v/v recombinant human fibroblast growth factor-beta (rhFGF-b), 0.1 % v/v gentamicin and amphotericin-B cocktail, 0.1 % v/v ascorbic acid, 0.04 % (v/v) hydrocortisone and 2.5% v/v FBS. The hCMEC/D3 cells were cultured in tissue culture flasks pre-coated with collagen type I as a basement membrane substrate.

Preparation of new seed stocks of cells for future use involved enzymatic dissociation of the adherent cells as described above. The number of viable cells was measured, before the total cells were pelleted under centrifugation and, following removal of the supernatant, were resuspended in PBS to wash off any remaining traces of trypsin-EDTA. A final centrifugation step was performed to allow removal of the supernatant and the cells were resuspended in cell freezing medium containing the cryoprotective agent DMSO to achieve a concentration of $1x10^6$ viable cells per 1.5mL supernatant. The cell suspension was aliquoted into sterile cryovials and allowed to freeze at a controlled rate using an isopropanol chamber stored in a -80°C freezer. For long-term storage, the cryopreserved cell suspension was maintained at -135°C in a liquid nitrogen storage tank.

2.2.3 Preparation of injectable agents

2.2.3.1 Antibody-MPIO synthesis for mouse imaging

Conjugation of antibodies to the outer coating of MPIOs was performed as follows: 1μm diameter MPIO (Dynabeads MyOne Carboxylic Acid) were washed in 1mL of 15mM 4-Morpholineethanesulfonic acid (MES) buffer pH 6, then chemically treated with 1-Ethyl-3-(3-dimethylaminopropyl)carbodiimide (EDC) to yield amide bonds as antibody binding sites. Activated carboxy-MPIO were incubated overnight with 80μg of rat anti-mouse VCAM-1 antibody under continuous agitation 1000rpm at room temperature. On the final day, the MPIO beads were pelleted and sequentially washed in 0.1% w/v BSA in PBS-T three times, before storage in 200μL of 0.1% w/v BSA in PBS. Rat IgG1 isotype control antibody was used for control IgG-MPIO. Successful antibody loading (~20,000 antibodies per MPIO) was confirmed via fluorescence-activated cell sorting, compared against standardised calibration beads.

2.2.3.2 Antibody-MPIO synthesis for rat imaging

Conjugation of antibodies to the outer coating of MPIOs was performed by Dr Nicholas de Pennington, as previously described (94). Briefly, 5mg of 1μm diameter MPIO (Dynabeads MyOne Tosylactivated) were suspended in equal measures of 0.1M sodium borate buffer, 3M ammonium sulphate buffer and 0.5mg/mL antibody, either VCAM-1 or mouse IgG isotype control. The MPIO suspension was incubated for 24hrs at 37°C under continuous agitation at 1000rpm. The following day, the beads were pelleted in a magnet, the supernatant removed and replaced with 0.5% w/v BSA in PBS-T, before another incubation period as per previous step. On the final day, the MPIO beads were pelleted and sequentially washed in 0.1% w/v BSA in PBS-T three times, before storage in 200μL of 0.1% w/v BSA in PBS. Successful antibody loading (~20,000 antibodies per MPIO) was confirmed via fluorescence-activated cell sorting, compared against standardised calibration beads.

2.2.4 Immunohistochemistry (IHC)

2.2.4.1 Tissue preparation

The techniques for performing IHC differed according to the method of sample preservation. As mentioned previously, the animal brains were perfused with a formalin-based fixative before cryopreservation. The animal brains were cut with a cryostat into slices of 10μm thickness, which were serially collected on a labelled positively charged glass slide. Slides holding the fresh frozen sections were dried overnight in a 37°C oven, before long-term storage in a -20°C freezer.

Conversely, the human biopsy samples were processed and archived remotely under the care of Mr Khaja Syed at The Walton Centre NHS Foundation Trust brain tissue biobank, Liverpool. Briefly, the samples were stored in a neutral-buffered formalin-based fixative for 4 to 6 hours to allow adequate tissue penetration. The samples were then processed under a standardised protocol, as previously described, to sequentially dehydrate and clear the tissue in ascending concentrations of ethanol, before infiltration by paraffin wax and then embedding into a paraffin wax block. The paraffin wax embedding process maintains the sample integrity and permits tissue sectioning using a microtome. The human biopsy samples were finely sectioned to 6μm thickness and serially collected on a labelled microscope glass slide. After drying overnight by incubation in a 37°C oven, the slides were stored at room temperature.

Prior to immunostaining, fresh frozen sections were allowed to equilibrate to room temperature before undergoing 3 sequential washes in PBS for 5 mins each time to rehydrate the tissue. Formalin-fixed paraffin-embedded (FFPE) samples underwent dewaxing by 3 sequential baths in xylene for 5 mins each time, before undergoing 3 sequential washes in absolute ethanol to remove excess xylene for 2 mins each time. The FFPE samples were rehydrated in 3 PBS washes, as described for the fresh frozen sections.

2.2.4.2 Antigen retrieval

Formaldehyde is known to cause crosslinking of amino acids (95) and therefore formalin fixation of tissue also results in protein denaturation. Whilst this has been exploited for tissue preservation, the modification of native proteins may present a problem with the recognition of antigens by antibodies used for immunostaining. A number of techniques have been developed to unmask the antigen expression, which may be categorised into either heat

induced epitope retrieval (HIER) or proteolytic induced epitope retrieval (PIER), and a combination have been used in this body of work. Due to the lighter fixation process used for the frozen tissue, antigen retrieval was only required for the FFPE samples.

For antigen retrieval the slides were placed in a microwave-safe container, which was then filled with citrate buffer pH 6.0 solution until all the slides were fully immersed. The container was then placed in a larger microwave-safe container that was partly filled with dH_2O. Both containers were placed in the centre of the microwave oven and allowed to run on the medium heat setting for 5mins. Upon completion of the first run, the containers were removed and the citrate buffer solution and dH_2O in the containers were exchanged for new liquids accordingly. Following the second run, with the same settings as previous, the slides were allowed to cool to room temperature whilst remaining fully immersed. Once cool, the slides were washed 3 times in PBS to remove any trace of the citrate buffer solution.

2.2.4.3 3,3'-Diaminobenzidine (DAB) staining

3,3'-Diaminobenzidine (DAB) is a commonly used chromogen for immunostaining of cells and tissues and is favoured due to its relative resistance to photobleaching. As a derivative of benzene, DAB is potentially carcinogenic (96), although this property has not been proved with confidence in previous animal studies. In its unoxidised form DAB is water-soluble and colourless, however when oxidised it is converted into an insoluble polymer that precipitates as a dark brown pigment (97). IHC exploits this property by using peroxidase, which has become conjugated to an antibody targeting an antigen of interest, to oxidise the DAB chromogen and reveal sites of antigen expression localised to areas of pigment deposition.

In this thesis, I used the avidin-biotin complex (ABC) method, which has been extensively described in the literature (98). The ABC method is an indirect approach to protein detection, as it relies on a labelled secondary antibody; in contrast to direct detection, where the primary antibody is labelled with a fluorescent or chromogenic signal. One of the main benefits of this indirect approach is that it permits signal amplification, due to the multiple biotin-binding sites in each tetravalent avidin molecule, which results in a large complex bound to each targeting antibody; thus, leading to a higher ratio of reporter enzyme to antibody. An illustration of the ABC method is shown in Fig 2.1. Alternative indirect methods for chromogenic detection include labelled streptavidin-biotin (LSAB) and polymer-based techniques.

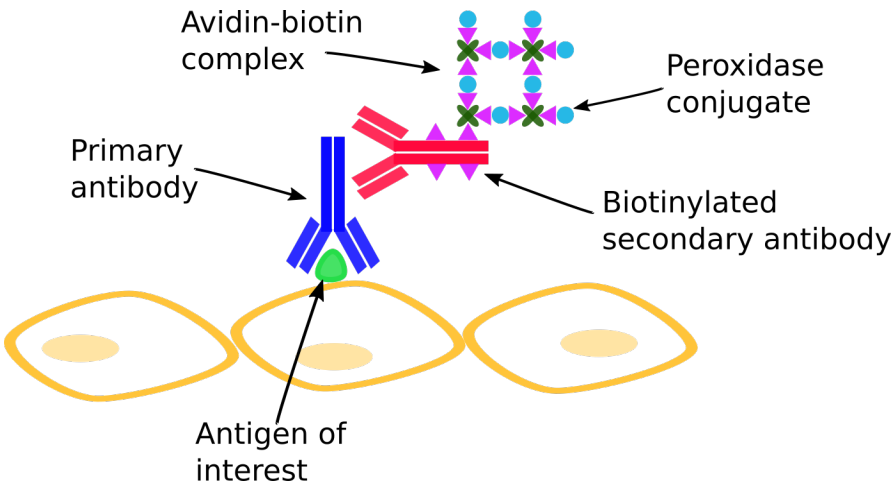


Fig 2.1. Avidin-biotin complex method. Illustration showing the avidin-biotin complex (ABC) method of immunohistochemistry (IHC). Due to the high enzyme-to-primary antibody ratio, induced by the bound biotinylated secondary antibody and the ABC, this indirect method amplifies the signal and, therefore is more sensitive than the direct method of IHC.

Endogenous tissue peroxidase was blocked as previously described (99). Slides were quenched in 0.3% v/v hydrogen peroxide in methanol for 20mins at room temperature. Afterwards, the slides were sequentially washed in PBS, followed by a PBS-T wash for 5mins each. The slides

were then assembled onto the Shandon Coverplate™, ensuring a tight seal between the slide and coverplate, before transferring to the Shandon Sequenza immunostaining rack. To prevent non-specific binding of the secondary antibody to off-target antigens, the sections were blocked by incubation with diluted serum (10% v/v serum in PBS), corresponding to the animal in which the secondary antibody was raised, for 1hr at room temperature. The primary antibody diluent was prepared using 1% v/v serum in PBS-T and the primary antibody was then prepared at the desired concentration that yields the greatest signal-to-noise ratio. The slides were incubated with 150μL antibody mixture overnight at 4°C in the cold room.

The following day, the slides were allowed to equilibrate to room temperature, before undergoing 3 PBS rinses to remove unbound primary antibody. The secondary antibody was diluted in PBS to the desired concentration and the slides were incubated with 150μL antibody mixture for 1hr at room temperature. Following on, the slides underwent 3 PBS rinses to remove unbound secondary antibody and then was incubated with 150μL ABC mixture for 45mins at room temperature, which was prepared at least 30mins prior to administration according to the instructions as laid out by VectorStain Elite ABC Kit™.

After the ABC step, the slides were rinsed in 2 changes of PBS before being developed in a DAB mixture (5mL DAB aliquot mixed with 125μL 30% v/v hydrogen peroxide, prepared in 125mL phosphate buffer solution) for between 15secs to 5mins. The length of time required for the chromogenic development varied and was optimised for each antibody. The DAB precipitation was halted by quenching in phosphate buffer solution. The tissue sections were counterstained with 0.5% v/v cresyl violet in dH_2O until the cell nuclei were clearly visible. Following dehydration in sequential rinses of ascending concentrations of ethanol, the tissue

was cleared by three 10mins washes in a xylene bath and then mounted with glass coverslips using DPX mountant medium. Once dry, the stained tissue sections were digitally scanned using the Leica Aperio machine and the images were saved for future analysis.

For each experiment, a negative control slide was used to examine background staining due to experimental variation, by omission of the primary antibody step. This required a slide containing tissue sections of the same type as that undergoing experimental testing. The positive control to determine signal strength required one of 2 types of slides – for VCAM-1, tissue sections of mouse brain intrastriatally injected with IL-1β were used; for tumour specific markers, tissue sections of mouse brain intrastriatally injected with the appropriate tumour type were used. Table 2 outlines the different antibodies used for IHC, including information about the secondary antibody used and the corresponding blocking agent.

Primary antibody	Concentration	Biotinylated secondary antibody	Blocking serum
Rat anti-mouse VCAM-1	10μg/mL	Goat anti-rat	Goat
Goat anti-mouse/rat CD31	2μg/mL		
Mouse anti-rat VCAM-1	5μg/mL	Horse anti-mouse	Horse
Mouse anti-human CAM5.2	12.5μg/mL		
Rabbit anti-human Melan-A	1:100	Goat anti-rabbit	Goat
Rabbit anti-human ITGA4	10μg/mL		
Rabbit anti-human Nestin	1:100		
Rabbit anti-human SOX2	1:100		

Rabbit anti-human Vimentin	2.5µg/mL		
Rabbit anti-human Ki67	1:100		

Table 2. Antibody and optimum conditions for immunohistochemistry. Table outlining the antibodies and the various conditions required for optimal DAB staining.

2.2.4.4 Immunofluorescence

For immunofluorescent co-localisation of tumour-associated blood vessels and VCAM-1, tissue sections were quenched with 0.3% v/v hydrogen peroxide in methanol and then sequentially streptavidin- and biotin-blocked for 15mins, followed by 1hr incubation in Tris·NaCl blocking buffer (TNB). Sections were incubated overnight at 4°C with the primary rat anti–mouse VCAM-1 antibody (10µg/mL) and primary goat anti-mouse CD31 antibody (2µg/mL) in TNB. In addition, the sections were incubated with antibodies targeting tumour specific markers as follows: primary chicken anti-GFP antibody (20µg/mL) for MDA231Br-GFP, primary rabbit anti-human (1:100) for H1_DL2 and primary mouse anti-human TTF-1 (1:50) for SEBTA-001. After rinsing with PBS, slides were incubated with a corresponding biotinylated IgG secondary antibody against the tumour specific marker antibody (1:100) in TNB for 30min, washed with PBS, incubated with streptavidin-HRP (1:200) in TNB for 30mins, washed, and incubated for 8mins in the dark with tyramide signal amplification–biotin (TSA-BIO; 1:100) in dilution buffer. Slides were washed and incubated with a streptavidin-488 fluorophore (10µg/mL), a secondary donkey anti-rat Dylight 405 fluorophore (1:100) and a secondary rabbit anti-goat 555 fluorophore (20µg/mL) for 1hr. MDA231Br-GFP sections were incubated with a secondary donkey anti-chicken CF 488A (10µg/mL) fluorophore. Slides were cover-slipped using Vectashield mounting medium.

For immunofluorescent detection of ITGA4 on tumour cell monolayers, cells were cultured on sterile glass coverslips, retained in a 24 well plate, to 70-80% confluence. After 2 brief rinses in PBS to remove traces of growth media, the cells were fixed in 4% w/v PFA in PBS for 20mins. The cell membranes were then permeabilised by incubation in 0.1% v/v Triton-X-100 in PBS for 5mins, before 3 further brief rinses in PBS, then 5mins incubation in TNB blocking buffer. The primary rabbit anti-human ITGA4 antibody (10µg/mL) was diluted in TNB and the cells were incubated at room temperature for 1hr in the mixture, followed by 3 brief PBS rinses. The cells were incubated with the secondary goat anti-rabbit Texas Red (15µg/mL) fluorophore diluted in TNB for 1hr at room temperature shielded from light. Cell nuclei were counterstained with DAPI and the coverslips were mounted onto glass microscope slides before imaging.

Images were acquired using a confocal microscope (Leica TCS SP8 Confocal platform; Leica Microsystems) and analysed using ImageJ (rsbweb.nih.gov) and Leica Application Suite X (Leica Microsystems) software. Detection ranges were set to eliminate cross-talk between fluorophores: 409–485 nm for DAPI, 494–553 nm for Alexa Fluor 488, and 564–712 nm for Alexa Fluor 555.

2.2.5 Animal work

All animal procedures were undertaken in strict accordance to UK Home Office Regulations and performed under Procedure Project Licence (PPL) 30/3187 and Procedure Individual Licence (PIL) I71C49B7D (mice). Animal procedures on rats were performed by Dr Nicholas de Pennington under PIL IBF69387S.

2.2.5.1 Animal husbandry

Female BALB/c variant SCID mice, aged between 6 to 10 weeks, were purchased from Charles River (UK) and housed in isolated negative-pressure cages (Tecniplast, Buguggiate, Italy) in the animal facility at the Radiobiology Research Institute, Oxford. A controlled environment was maintained at 19-21°C, 50 ± 15% humidity and a 12hr light-dark cycle. Food and water were supplied *ad libitum*. To minimise potential stress, animals were acclimatised to their new environment for a minimum of 5 days prior to any experimental procedures.

Male RNU nude rats were purchased from Charles River (UK). Animals were housed as described above.

2.2.5.2 Preparation of tumour cells for injection

Tumour cells lines were grown until 70-80% confluent in the culture flask. On the day of the experiment, the tumour cells were washed and trypsinised, as previously described in section 2.2.1. The trypsin was removed by aspiration of the supernatant after the cells were centrifuged into a pellet. The cells were resuspended in 1mL ice-cold sterile PBS and checked for cell viability using the trypan blue method. The cell suspension was diluted to form a final viable cell concentration of 1×10^7 cells in 1mL PBS, for intrastriatal injections, or 1×10^6 cells in 1mL PBS, for intracardiac injections. The cell suspension was maintained on ice and not stored for longer than 2hrs, to maximise cell viability at the time of injection. Prior to injection the cells were resuspended using a 23G needle to minimise the risk of clumping.

2.2.5.3 Intrastriatal injection into mouse brain

On the day of experiment, the procedure room was prepared and set-up with the sterilised equipment, as illustrated in Fig 2.2. The procedure was performed under strict aseptic technique and the operator was required to wear a sterile surgical gown, sterile gloves, a micro nylon hair net and face mask to maintain adequate sterility. Surgical apparatus was autoclaved 24hrs prior to the procedure.

Intrastriatal injections were performed as previously described (100). Firstly, animals were anaesthetised by delivering a vaporised mixture of 2-3% v/v isofluorane with oxygen, for inhalation in an induction chamber. Successful induction was confirmed by loss of pedal reflex, i.e. no limb withdrawal following a firm paw pinch. The anaesthetised mouse was shaved over the apex of the skull using hair clippers and then transferred to the stereotactic frame, where the skull was fixed in the neutral position with the aid of ear bars and a nose piece. Vaporised anaesthetic gases continued to be administered throughout the procedure via the nose piece on the frame and surgical plane was maintained with 1-2% v/v isofluorane with oxygen. Lubricating ophthalmic ointment was applied to both eyes to prevent desiccation. Internal body temperature was monitored using a probe connected to a homeothermic monitoring system that was inserted into the animal's rectum. External thermoregulation was administered by an electric heating pad, which was automatically adjusted via a feedback loop, to maintain a stable rectal temperature of 37-38°C. Cardiovascular and respiratory function were qualitatively measured throughout the procedure to assess the depth of anaesthesia.

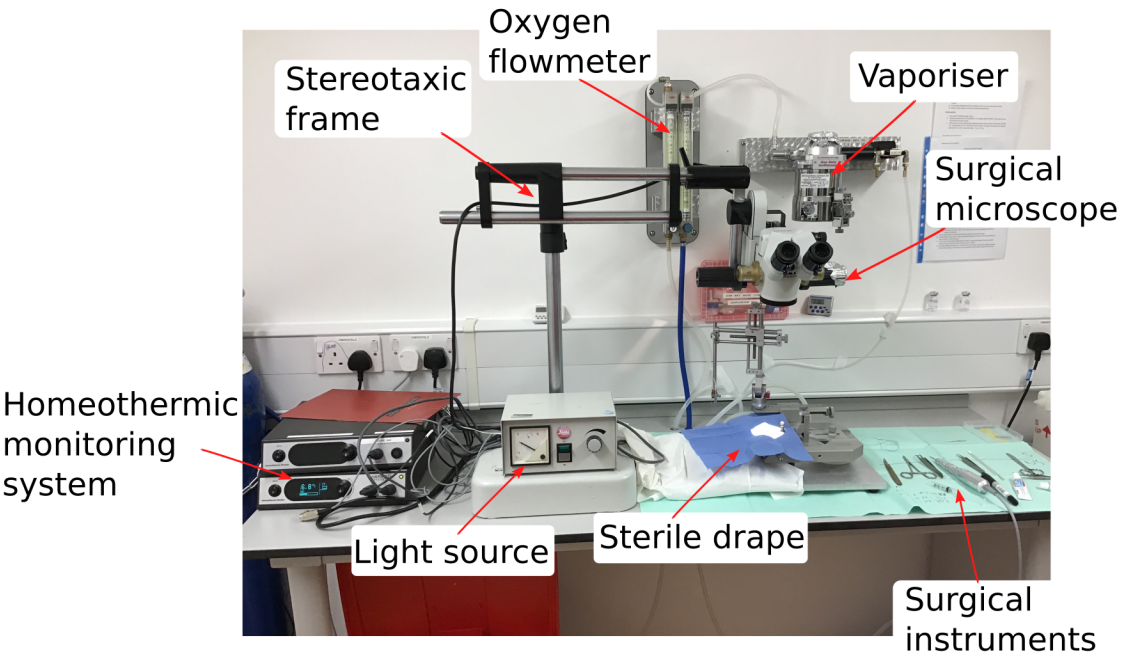


Fig 2.2. Experimental set-up for intrastriatal injection. Photograph demonstrating typical set-up of equipment for performing sterile animal surgery to inject substances in the striatum.

The animal was covered with a sterile drape and the shaved skin overlying the skull was cleaned with 4% w/v chlorhexidine gluconate. A midline anterior-posterior (AP) incision, of *ca.* 1-1.5cm, was made to the skin overlying the skull and the incised skin was gently teased apart using forceps to expose the skull bones. The bregma – the intersection between the coronal suture and the sagittal suture – was identified as an anatomical reference point using the surgical microscope. A hole was drilled through the skull at the following coordinates from bregma: AP +0.5mm and medio-lateral (ML) +1.8mm. A pulled microcapillary tube with a tapered end was filled with 0.5µl of either cell suspension or sterile PBS. The microcapillary tube was sited over the drilled hole and introduced into the brain parenchyma to a depth of 3mm, with the aid of the stereotactic frame. Over a 2mins duration the total volume of fluid was slowly injected into the striatum, before the microcapillary tube was removed. Primary

closure of the skin was achieved with 1 or 2 simple interrupted sutures, which were surgically tied.

Upon completion of the surgical procedure, the animal was released from the stereotactic frame and allowed to recover in a warm, clean and dry environment. Each animal was monitored throughout the recovery phase and returned to its cage once maintaining an upright posture and was walking normally. Experimental animals were regularly inspected for post-procedural complications and weighed every 48hrs to assess animal health following tumour engraftment.

2.2.5.4 Intrastriatal injection in rat brain

For intrastriatal injections into rat brains, the same process was followed as described in subsection 2.2.4.3, barring a couple of alterations. Firstly, topical local anaesthetic was applied to the ears at the time the rat's head was fixed in the stereotactic frame. Secondly, the injection coordinates from bregma differed as follows: AP +0.5mm, ML +2.2mm and depth 2.8mm.

2.2.5.5 Intracardiac injection of tumour cells

On the day of experiment, the procedure room was prepared and set-up with the equipment, as illustrated in Fig 2.3.

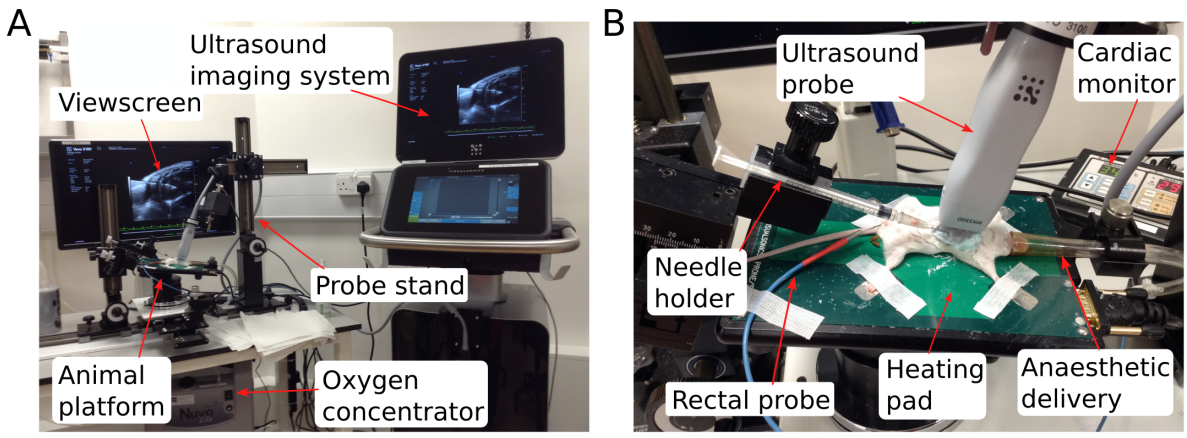


Fig 2.3. Experimental set-up for intracardiac injection. (A) Photograph demonstrating typical set-up of equipment for performing ultrasound-guided tumour cell injections into the left ventricle. (B) Closer view showing correct animal position on the heated platform, with cardiac and thermal monitoring.

Intracardiac injection was performed under ultrasound guidance as previously described (92, 94). General anaesthetic was administered as reported in subsection 2.2.4.3, with appropriate checks to ensure adequate induction. The animal was transferred to the adjustable imaging platform and laid supine to allow access to the thoracic cavity. Each limb was securely held in position, so that the animal laid spread-eagled on the platform, over electrodes that enabled quantitative monitoring of heart rate and respiratory rate. Hair overlying the thorax was removed using depilatory cream and a generous layer of ultrasound gel was applied over the chest wall, to allow effective transmission of ultrasound waves from the imaging probe to the chest and vice versa.

A stand-mounted 707B ultrasonographic probe was used with B-mode imaging settings at 60MHz frequency to locate the left ventricle. A 1mL syringe was loaded with 100μL of tumour cell suspension and attached to a 27G needle, which was then mounted on an adjustable

needle holder. The position of the needle was confirmed under ultrasonographic inspection and, when the trajectory was deemed suitable, the needle was advanced through the intercostal space into the left ventricle. Confirmation of correct siting of the needle in the left ventricle was available by a pulsating flashback of bright red blood into the syringe, visualisation of the needle in the ventricular cavity and visible bright specks on injection, indicating signal caused by tumour cells reflecting the ultrasound as they flow out of the syringe. Tumour cells were injected slowly at increments of 20μL over 1min. Following injection, the needle was withdrawn from the chest cavity and the animal was allowed to recover.

Throughout the procedure, each animal was monitored for heart rate and respiratory rate to assess the depth of anaesthesia. Temperature monitoring was undertaken using a rectal probe and external thermoregulation was performed by the in-built heating system on the imaging platform, to maintain a stable rectal temperature between 37-38°C. Post-procedural monitoring, during the initial recovery phase and beyond, followed the pattern outlined in subsection 2.2.4.3.

2.2.5.6 Intravenous injections

All intravenous (i.v.) injections were performed on anaesthetised animals. Animals were induced as described above and laid on a heating pad, where their body temperature was maintained at 37°C. Injection of substances occurred via a modified cannula, comprising a 30G needle attached to calibrated tubing of approximately 1m in length; this permitted remote administration of substances, for example imaging contrast agents for MRI.

Prior to cannulation, the tail was swabbed with 70% v/v ethanol in dH_2O and warmed using a heat lamp for *ca.* 10-15secs to induce peripheral vasodilatation of the tail veins. Care was taken to not overheat or burn the tails during this process. The needle was inserted under direct inspection at a 20-30° angle into the lateral tail vein. Correct siting of the needle was confirmed by successful aspiration of a small volume of blood and absence of resistance when flushing the cannula with sterile 0.9% saline solution. Injections were aborted if the procedure failed on two attempts on each side of the tail, to prevent venous thrombosis causing tissue necrosis.

2.2.5.7 Perfusion-fixation and cryostorage of tissue

Tissue preservation is important for histological analysis and chemical fixation using formalin is a common technique used for this purpose. Immersion in fixative is suitable for small specimens, however for larger tissues such as the intact brain this method does not allow adequate diffusion of the solution throughout the tissue, leading to uneven fixation. As a result, tissue changes such as hypoxia-related cell death may occur unrelated to the pathology of interest (101). One solution is to utilise the animal's intact vasculature to allow rapid perfusion of a fixative solution throughout the tissues in the whole body.

A modified version of methods to transcardially perfuse fixatives, as previously described (102, 103), was used in this body of work. Firstly, perfusion pump was prepared by running through heparinised saline and the PLP light fixative in the respective tubing to remove any air bubbles. The animal was sacrificed by terminal anaesthesia, which involved administering an intraperitoneal injection of 2mL of dilute pentobarbitone. Upon confirmation of deep anaesthesia, in the form of loss of pedal reflex and loss of corneal reflex, a transverse incision

was made through the skin and abdominal wall to expose the abdominal cavity. The liver was separated from the diaphragm, diaphragm was incised and the rib cage opened to allow access to the thoracic cavity. An incision was made into the right atrium to create an outlet for drainage of blood and perfusate.

The needle for infusing the heparinised saline was inserted via the apex of the heart into the still beating left cardiac ventricle. Perfusion of the animal occurred at a slow flow rate (*ca.* 40mL/min) until the vasculature was cleared of blood. Then, PLP light was perfused through the animal using the second needle inserted into the same site as previous. Successful fixation was confirmed by initiation of fixation tremors and perfusion continued for 2-3mins after the end of the tremors. Following on, the head was separated from the mouse body and the brain harvested by peeling back the skull.

The harvested brain was post-fixed by immersion in PLP light in a 7mL bijou for 4-6hrs, then immersed in a cryoprotective solution of 30% v/v sucrose in dH_2O for at least 24hrs. The specimens were then removed from the sucrose solution, briefly dried on a paper towel, coated with a thin layer of OCT mountant and snap frozen using pre-chilled isopentane on dry ice. The brain remained immersed in the isopentane for a few minutes to ensure adequate cooling of the centre of the specimen, before removal for long-term storage in a -80°C freezer.

2.2.6 Gene knockdown

2.2.6.1 Ribonucleic acid interference (RNAi)

Small interfering ribonucleic acids (siRNA) were used to transiently induce gene expression knockdown in tumour cells via RNAi, as previously described (104). A pool of siRNAs, pre-

designed and selected for potency and specificity, were used to target human messenger RNA (mRNA) that translate the protein of interest, integrin α_4 (ITGA4). Following confirmation of successful gene expression knockdown, with techniques described in subsequent sections, individual siRNAs within the pool were re-tested for potency of knockdown. Furthermore, a pool of siRNA was used to transiently induce gene expression knockdown of the cyclophilin B (PPIB) protein, as a validated positive knockdown control. A negative control for determination of baseline cellular responses involved a pool of siRNAs that have minimal targeting of human genes. Finally, a fluorescently-labelled negative control siRNA was used to assess transfection efficiency.

Prior to use, the lyophilised siRNAs were reconstituted in RNase-free 1x siRNA Buffer (60mM KCl, 6mM HEPES-pH 7.5, and 0.2mM $MgCl_2$) to achieve a desired concentration of 20μM stock solution. The concentration was verified by measuring absorbance at 260nm (A_{260}) using ultraviolet (UV) spectrophotometry; for siRNA, 1μM = 13.3ng/μL. Calculating the final concentration of the resuspended siRNA used the Beer-Lambert Law, with the following equation:

$$A_{260} = (\mathcal{E})(C)(L)$$

Where $\mathcal{E}$ is the extinction coefficient as supplied by the manufacturer, C is the siRNA concentration and L is the path length of the cuvette. The 20μM was aliquoted into smaller volumes prior to storage at -20°C to minimise freeze-thaw cycles.

2.2.6.2 Liposomal siRNA delivery

Transfection of the various siRNAs into the tumour cells was performed using liposomal vehicle delivery, as previously described (105, 106). This involved the generation of a spherical

vesicle with a lipid bilayer that encases the siRNA and is capable of crossing the cell membrane to introduce the cargo into the cytoplasmic space. A forward transfection method was employed on pre-plated cultured tumour cells following the standardised Lipofectamine RNAiMAX Transfection protocol (2013; Life Technologies), which has previously been shown to allow efficient and reproducible gene silencing (107).

Briefly, tumour cells were plated on a sterile multi-well culture plate to be 60-80% confluent on the day of transfection. At the point of transfection, Lipofectamine RNAiMAX reagent diluted in Opti-MEM medium was mixed in equal parts to siRNA (5-30pmol, dependent on the well size) also diluted in Opti-MEM medium. The mixture was incubated for 5mins at room temperature, before a recommended volume of the siRNA-lipid complex was added to the adherent cells. For each experiment, a mock transfection involving addition of liposomes without siRNA to cells was performed as additional negative controls. The cells were incubated for 48-72hrs at 37°C to allow adequate uptake of the siRNA and then they were either analysed for successful gene silencing or harvested for *in vivo* experiments.

2.2.7 Western blotting

Western blotting is a well-described analytical method used to identify and quantify specific proteins from a complex cellular extract. The three elements underlying this technique are: 1.) separation of proteins by molecular weight through polyacrylamide gel electrophoresis (PAGE), 2.) adsorption of the separated proteins to a supporting membrane made of polyvinylidene fluoride (PVDF) or nitrocellulose, and 3.) immunolabelling the protein of interest using appropriate antibodies (108). Probing of the specified protein was performed using a chemiluminescent detection system, as previously described (109, 110).

2.2.7.1 Protein quantitation

Following 72hrs of incubation in siRNA and transfection agent, the cells were harvested with a cell scraper. The cell mixture was centrifuged (1500rpm, 5mins, 4°C), supernatant aspirated and cell pellet resuspended in ice cold PBS. A further centrifugation step with PBS wash was performed to remove any traces of growth medium. The cell pellet was resuspended in a protein extraction mixture comprising 100µL RIPA buffer, 2µL protease inhibitor cocktail and 2µL EDTA and incubated on ice for 15mins – the volume of the protein extraction mixture can be adjusted according to the desired protein concentration. To ensure maximum protein extraction, the cell suspension was disrupted by sonication (30% amplitude, 5 pulses, 10secs). The homogenised cell mixture was pelleted in a microcentrifuge (13000rpm, 15mins, 4°C). Finally, the protein-enriched supernatant was collected and stored on ice, whilst the remaining cell residue was discarded.

Protein quantitation was conducted using the Pierce™ BCA Protein Assay Kit (Thermo Scientific) and followed the recommended protocol. Briefly, a set of protein standards of varying dilutions of BSA were prepared (0, 25, 125, 250, 500, 750, 1000, 1500 and 2000µg/mL) in PBS and triplicate 5µL of each dilution were loaded in wells of a 96-well microplate. Triplicate 5µL of each test sample were also loaded in the same plate. The BCA working reagent was prepared by mixing Reagent A with Reagent B at a ratio of 50 parts to 1 part volume, respectively. A volume of 200µL of working reagent was added to each well and mixed thoroughly on a plate shaker for 30secs. The plate was covered and incubated at 37°C for 15mins. After a successful reaction was visually confirmed, by colour change from translucent green to purple as shown in Fig 2.4, colorimetric analysis was performed by measuring

absorbance at 562nm on a multiwall spectrophotometer. Using values from the standard protein set, a blank-corrected standard concentration curve was plotted, thus permitting the interpolation of the protein concentration of the test samples.

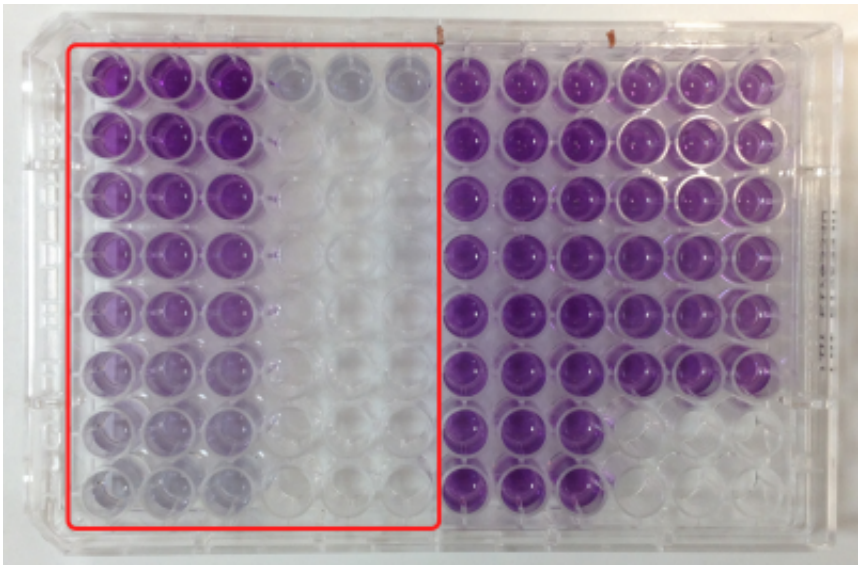


Fig 2.4. Protein quantitation assay. Bicinchoninic acid (BCA) assay demonstrating the colour change, from translucent green to dark purple, associated with increasing protein concentrations. Red box denotes the protein standards of varying dilutions, in triplicates, from highest concentration in the top left to lowest concentration in the bottom left wells and triplicate blank controls in the adjacent wells.

2.2.7.2 SDS-PAGE

An aliquot of each sample was diluted to the desired concentration, *ca.* 20-30µg/mL, in PBS. To facilitate the PAGE, samples were incubated in the anionic detergent SDS and the reducing agent dithiothreitol (DTT) to cause protein denaturation and impart a uniform negative charge (111). This involved mixing the protein sample with Laemmli sample buffer and DTT at a ratio of 6.5 parts to 2.5 parts to 1 part, respectively, ensuring the total volume does not exceed

20µL. The mixture was boiled at 100°C for 5mins in a closed Eppendorf, before rapid cooling in ice and centrifugation to collect any condensate.

A pre-cast polyacrylamide gel cassette (10% Mini Protean TGX 12 well; 20µL per well) was mounted with a balancer in the electrophoresis chamber (BioRad Mini Protean Tetra cell) pre-filled with 1x running buffer diluted in dH_2O. A standard molecular weight marker (Precision Plus Protein Dual Color Standards; 7µL) was loaded in the first well, followed by 20µL of each sample. After sample loading, a 4mA electric current was passed through the electrophoresis chamber at 100V and allowed to run for *ca.* 70-80mins, until there was adequate separation of protein bands on the gel.

Following completion of PAGE, the cassette was disassembled to retrieve the gel. The intact gel was placed in direct contact with a PVDF membrane, prior activated in methanol for 1min, before being sandwiched between 2 pieces of filter paper and 2 sponges soaked in 1x transfer buffer (10x transfer buffer stock solution diluted with 20% v/v methanol and 70% v/v dH_2O). The order of placement in the transfer cassette was vital to ensure correct transference of the proteins from the gel to the membrane, see Fig 2.5 for reference. The cassette was placed into the transfer chamber and a 4mA electric current was passed through the chamber at 100V in an ice cold bath for 1hr. Upon completion, the membrane was retrieved and blocked in 5% w/v dry whole milk powder in PBS, by incubation on a platform shaker for 1hr at room temperature. The membrane was then divided, by cutting transverse to the direction of protein separation, so that sections could be probed for different proteins of interest provided they were sufficiently separate by molecular weight.

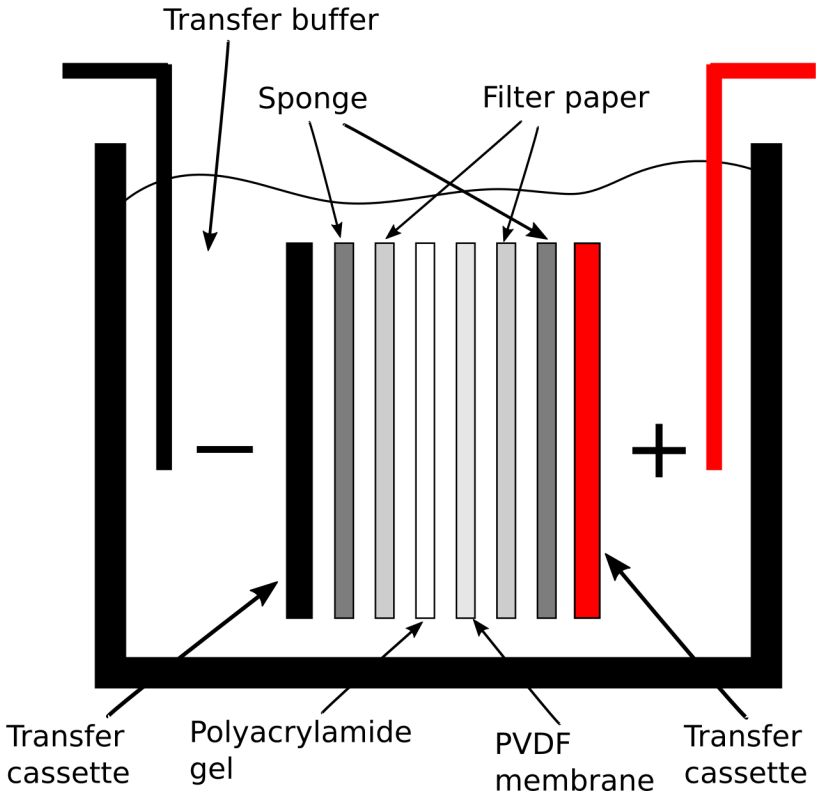


Fig 2.5. Protein transfer from gel to member for western blot. Diagram illustrating the order of components required to transfer the separated proteins from the polyacrylamide gel to the PVDF membrane as an electric current is passed through the transfer buffer solution in the electrophoresis chamber.

The section of the membrane containing proteins between 75 to 250kDa was incubated in the rabbit anti-human ITGA4 antibody (1µg/mL). The section of the membrane containing proteins between 25 to 75kDa was incubated in the rabbit anti-human glyceraldehyde 3-phosphate dehydrogenase (GAPDH) antibody (0.33µg/mL). The final section containing proteins between 10 to 25kDa was incubated in the rabbit anti-human PPIB antibody (1 in 1000). All primary antibodies were diluted in 2.5% w/v whole milk powder in PBS-T. The membranes were incubated overnight at 4°C under constant agitation on a platform shaker.

The next day, the blot membranes were retrieved and washed in 3 changes of PBS-T for 5mins. They were then incubated in a secondary goat anti-rabbit IgG conjugated to HRP (0.33µg/mL), diluted in 2.5% w/v whole milk powder in PBS-T, for 1hr at room temperature on a platform shaker. After, the blot membranes were rinsed in 3 changes of PBS-T for 5mins. Prior to imaging on the Odyssey Fc workstation, the membranes were incubated for 1min in the enhanced chemiluminescence (ECL) substrate. Imaging duration was between 5 to 20mins dependent on chemiluminescent signal intensity.

2.2.8 Cell-based phenotypic assays

2.2.8.1 Cell viability assays

Cell viability assays have been used to assess cytotoxicity of different treatment conditions and can be performed in many formats. The two methods used in this thesis were live/dead cell counting and the colorimetric MTT assay. Manual live/dead cell counting is one of the most basic cell viability assays and relies on vital stains, such as the azo dye trypan blue and the fluorescent intercalating agent propidium iodide. The trypan blue dye exclusion tests function on the principle that live cells with an intact cell membrane are impermeable to this dye, whilst dead cells permit its influx and are stained blue (112). The main advantages of this method are its simplicity and low cost. One disadvantage is that manual counting of live/dead cells is time-consuming, although automated techniques such as flow cytometry can help to overcome this issue at the expense of financial cost (113).

The tetrazolium salt 3-(4,5-dimethylthiazol-2-yl)-2,5-diphenyltetrazolium bromide (MTT) in its soluble form is yellow in colour. When taken intracellularly by viable cells, it is reduced by nicotinamide adenine dinucleotide (NADH) and nicotinamide adenine dinucleotide phosphate

(NADPH)-dependent enzymes in the cytosol to the insoluble formazan, which is purple in colour (114-116). This reaction has been frequently exploited in cell biology to infer the metabolic, and by extension the proliferative, activity of a cell population. A modified version of the quantitative colorimetric MTT assay, as previously described by Mosmann (117), was used in this body of work in accordance to the CellTiter 96® Assay (Promega) standardised protocol.

Briefly, tumour cells were plated in a 96 well microplate and underwent liposomal siRNA transfection to achieve ITGA4 gene expression knockdown, as previously mentioned in subsection 2.2.5. To ensure uniform testing conditions, the transfection procedure was timed so that the endpoints (either 3 days or 7 days post-transfection) occurred on the same day. On the day of testing, the cells were rinsed briefly in PBS and the growth medium was exchanged to provide a uniform volume of 100µL per well. To this, 15µL of the pre-prepared Dye solution was added to each well and mixed into the media by gentle rotational agitation. The microplate was incubated at 37°C in a humidified CO_2 incubator for 3-4hrs, before the reaction was quenched by addition of 100µL of Stop/Solubilisation solution per well, which was thoroughly mixed by repeat pipetting. After a further 1hr incubation at room temperature, to ensure sufficient solubilisation of the coloured formazan crystals, the absorbance was measured for each well at 570nm wavelength on a multiwall spectrophotometer. A reference wavelength at 650nm was also used.

2.2.8.2 Static binding assay

A modified form of an assay used to assess tumour cell adherence to endothelial cells, as previously described (59). Murine endothelial-derived sEnd-1 cells were plated on sterile glass

coverslips and monocultured in a 24 well plate. Once the cells were at 70-80% confluence they were briefly rinsed with PBS and the growth medium was exchanged with fresh medium containing 5ng/mL recombinant murine IL-1β and incubated at 37°C in a humidified CO_2 incubator for 4hrs, to stimulate endothelial VCAM-1 expression.

Following VCAM-1 activation, trypsinised tumour cells treated with various siRNA transfection conditions – untransfected (UNT), scrambled negative control (SCR), ITGA4 kd (at time points: 3 days, 7 days, 10 days and 14 days post-transfection) – were seeded onto the endothelial cell monolayer, with the exception of one sEnd-1-coated coverslip. Specifically, 1 x 10^4 tumour cells suspended in 1mL growth medium were added to the sEnd-1 cells and were incubated at 37°C in a humidified CO_2 incubator for 30mins, to allow sufficient time for the tumour cells to settle and attach to the activated endothelium. Following the test period, the coverslips were gently rinsed in 3 changes of PBS to remove unattached cells and the remaining adherent cells were fixed in 4% w/v PFA in PBS.

To assess tumour cell attachment, immunofluorescence was conducted targeting tumour specific markers, as described in subsection 2.2.3.5. For the coverslip coated with sEnd-1 cells only, immunofluorescence targeting VCAM-1 was used to confirm successful endothelial activation. The cells were counterstained with DAPI, before mounting with Vectashield onto a glass slide and finally imaging on a confocal microscope. Each treatment group was performed in triplicates and the entire experiment was duplicated with the same protocol on a separate occasion.

2.2.8.3 Cell transmigration assay

The Transwell assay was performed with kind assistance from Christina Simoglou Karali. A modified version of migration assays described by Schlesinger (59) was used to assess the effect of ITGA4 kd on transmigration of tumour cells across an endothelial cell layer. Firstly, trypsinised hCMEC/D3 cells in 200μL growth medium were seeded on the top surface of the permeable polyester Transwell filter inserts, pre-coated with collagen type IV and fibronectin (1:100 dilution). The cells remained in culture for 3-4 days until the cells have formed a fully confluent layer covering the membrane surface, confirmed by visual inspection under light microscopy.

At the experimental timepoint, trypsinised tumour cells treated with various siRNA transfection conditions – untransfected (UNT), scrambled negative control (SCR), ITGA4 kd (at time points: 3 days, 7 days, 10 days and 14 days post-transfection) – were seeded onto the endothelial cell layer. Specifically, 1 x 10^4 tumour cells suspended in 180μL growth medium with 10% v/v EndoGRO medium were added to the Transwell inserts and were incubated at 37°C in a humidified CO_2 incubator for 24hrs, to allow sufficient time for tumour cells to transmigrate through the endothelial layer and seed onto the well base. A 200μL layer of tumour cell growth medium was added to the base of the well.

The next day, the Transwell inserts were removed and the corresponding wells were gently washed with 2 changes of PBS. The wells were briefly washed with 1% v/v acetic acid in methanol to fix any cells adhering to the base. The wells were then filled with Coomassie Brilliant Blue dye and incubated at room temperature for 2hrs to stain the cells, before the

wells were washed in dH_2O and air dried overnight before analysis. Stained cells were counted under light microscopy using a 10x objective lens. Each treatment group was performed in triplicates and the entire experiment was duplicated with the same protocol on a separate occasion.

2.2.9 Pre-clinical MRI

2.2.9.1 Mouse brain imaging

Mouse MRI data were acquired using a 7.0T MRI spectrometer. On the day of imaging, tumour-injected mice were anaesthetised with 2-3% v/v vaporised isofluorane in a mixed 70% nitrogen:30% oxygen gas delivery and injected intravenously via a tail vein with 4mg Fe/kg body mass VCAM-MPIO (n = 5-6 per group) or IgG-MPIO (n = 4-5 per group) in 100µL saline. A further cohort of naïve SCID mice were injected intravenously with VCAM-MPIO as above (n = 5). At 30mins after MPIO injection, animals were positioned in a customised cradle inside a quadrature birdcage coil (26mm internal diameter; RAPID Biomedical GmbH, Rimpar Germany). Respiration monitoring was performed and body temperature was maintained at approximately 37°C.

Prior to image acquisition for each animal, inhomogeneities in the main magnetic field (B0) were corrected through active shimming of the coils. A pre-imaging scan was performed for each animal, to warm up the spectrometer to a stable running temperature, as follows: Multi gradient-echo 3D (MGE3D) sequence, flip angle = 15°, repetition time (TR) = 65.1ms, echo time (TE) = 2.5ms, 2nd echo time (TE2) = 4.0ms, number of echoes (NE) = 15, spectral width (SW) = 150kHz, averages (NT) = 1, matrix size = 256 x 192 x 96, field of view (FOV) = 22.5 x 22.5 x 22.5mm; total warming up time ~20min. For VCAM-MPIO detection, a T_2*-weighted 3D

gradient echo dataset (MGE3D) was acquired as above, except matrix size = 256 x 192 x 192 and total acquisition time ~40mins. The mid-point of acquisition was 1 ± 0.2hr after MPIO injection. Data were zero-filled to 256 x 256 x 256, to a final isotropic resolution of 88µm, and the final images were reconstructed offline by adding individual echoes using the square root of a sum-of-squares algorithm. Subsequently, a set of ten axial T_1-weighted images (slice thickness = 1mm) was acquired using a 2D spin-echo sequence (TR = 500ms, TE = 11.5ms, matrix size = 128 × 128, number of slices (NS) = 10, NT = 1, FOV = 25 × 25mm), both pre- and 5mins post-intravenous gadolinium-DTPA injection (30µL), to identify BBB permeability. The combined image of the multiple gradient echoes was constructed by using the square root of the sum of squares of signal intensities taken on a pixel-by-pixel basis from the individual echoes, as previously described (118).

2.2.9.2 Rat brain imaging

Rat MRI data were acquired by Dr Nicholas de Pennington, using a 9.4T MRI spectrometer. On the day of imaging, tumour-injected rats were anaesthetised with 2-3% v/v vaporised isofluorane in a mixed 70% nitrogen:30% oxygen gas delivery and injected intravenously via a tail vein with 4mg Fe/kg body mass VCAM-MPIO (n = 5-6 per group) or IgG-MPIO (n = 6 per group) in 100µL saline. A further cohort of control nude rats, with intrastriatal injection of PBS only, were injected intravenously with VCAM-MPIO or IgG-MPIO as above (n = 3 per group). At 30mins after MPIO injection, animals were positioned in a customised cradle inside a quadrature birdcage coil (72mm internal diameter; RAPID Biomedical GmbH, Rimpar Germany). Respiration monitoring was performed and body temperature was maintained at approximately 37°C.

Prior to image acquisition for each animal, inhomogeneities in the main magnetic field (B0) were corrected through active shimming of the coils. Subsequently, a set of 24 axial T_2-weighted images (slice thickness = 0.5mm) was acquired using a 2D fast spin-echo sequence (TR = 3000ms, TE = 35.65ms, matrix size = 256 × 256, number of slices (NS) = 24, NT = 2, FOV = 32 × 32mm). For VCAM-MPIO detection, a T_2*-weighted 3D gradient echo dataset (GE3D) was acquired pre- and post-MPIO administration with the following parameters: flip angle 27°, TR = 65ms, TE = 7.5ms, FOV = 32mm x 32mm x 16mm, matrix size = 256 x 192 x 96, NT = 2 and total acquisition time ~40mins. The mid-point of acquisition was 1 ± 0.2hr after MPIO injection. Finally, the animal underwent T_1-weighted imaging using a GE3D sequence, pre- and 5mins post-intravenous gadolinium-DTPA injection (30µL), to identify BBB permeability with the following parameters: flip angle 10°, TR = 5.38ms, TE = 2.71ms, FOV = 32mm x 32mm x 16mm, matrix size = 256 x 192 x 96, NT = 8 and total acquisition time ~13mins. Data were zero-filled to 256 x 256 x 256, to a final isotropic resolution of 120µm.

2.2.9.3 MR Image processing

Each dataset of T_2*-weighted images was manually masked and segmented to exclude extracerebral structures using ITK-SNAP (itksnap.org). Automated image processing of segmented images were performed using a custom designed MATLAB code (119). Briefly, hypointense signals were defined as a voxel value 0.65 times less than the mean value. Signals arising from ventricles or sinuses, which appear hypointense naturally, were excluded by imposing an upper threshold size limit of 20 voxels. A lower threshold filter of 1 voxel size was used to exclude noise. The threshold cut-offs and automated analysis were optimised in prior work to enable a detection rate of 98.3 ± 0.49% of total brain hypointensities (119). Segmented images were reconstructed to visualize the spatial distribution of MPIO binding,

with hypointense voxels assigned to the red channel, as shown in Fig 2.6. Voxel volumes were summed and expressed as raw volumes in microlitres.

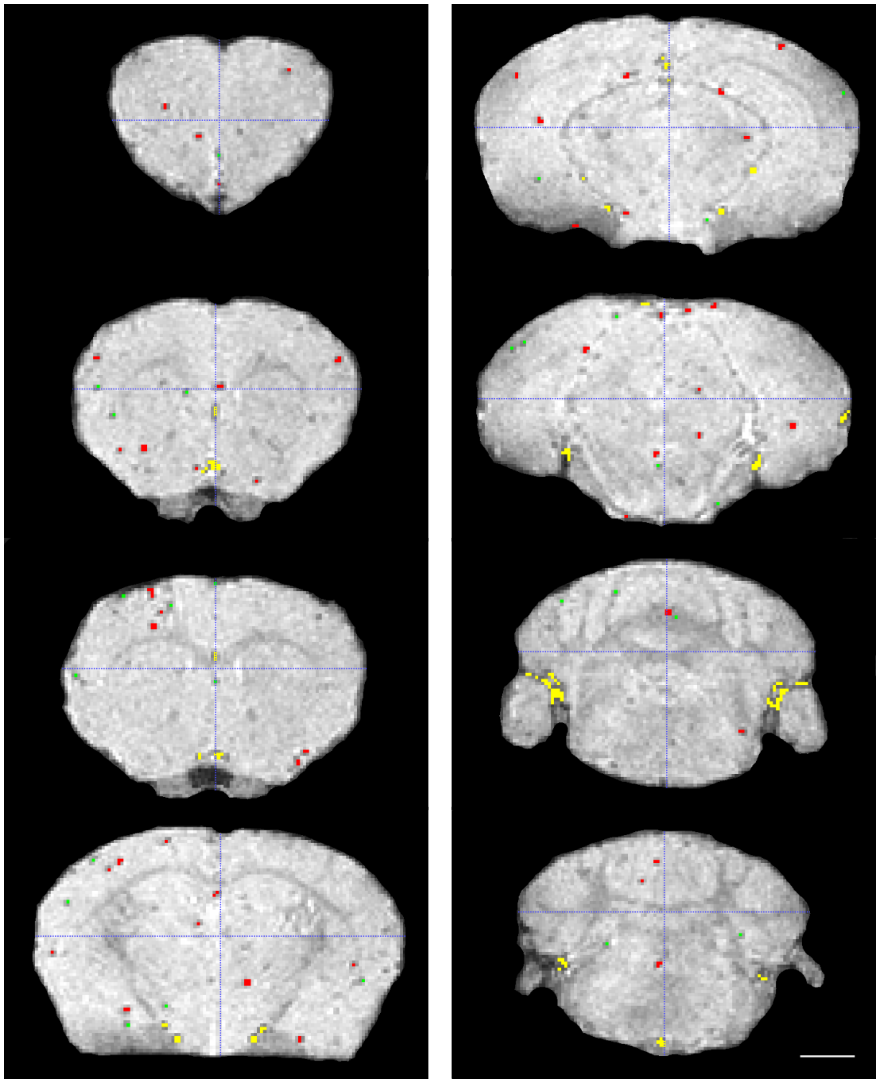


Fig 2.6. Post-processing mask of hypointensities from T_2^*-weighted MRI. Post-processing mask of a mouse brain with MDA231Br-GFP metastases following intravenous injection of VCAM-MPIO showing segmented hypointense regions classified by colour: green (1 voxel), red (between 2 and 19 voxels) and yellow (≥20 voxels). The mask was overlaid on the corresponding T_2^*-weighted images to verify the accuracy of the analysis; scale bar = 1.5mm.

2.2.9.4 Comparison of hypointense signal on T_2^*-weighted MRI with gadolinium enhancement on T_1-weighted MRI

To enable quantitation of hypointense signal, a custom designed MATLAB code was used to align the matrices of the post-MPIO T_2^*-weighted MGE3D and post-gadolinium T_1-weighted GE3D sequences. The contrast enhanced region at the site of the intrastriatal tumour was manually segmented using ITK-SNAP from post-gadolinium administered T_1-weighted images. The hypointensity mask, generated as described in Section 2.2.9.3, was aligned with the corresponding contrast enhancement segmentation mask and, using the same MATLAB code, values were automatically calculated for the volume of hypointensities within and outside the T_1-weighted contrast enhanced region. The volume of hypointensities was normalised to the surface area of the tumour segmentation mask.

2.2.10 Human data collection

2.2.10.1 Stereotactic brain biopsy

Human brain metastasis samples were obtained by the neurosurgical team at The Walton Centre NHS Foundation Trust by image-guided biopsy, as previously described (120). Briefly, consenting patients recruited to participate in the study underwent MRI prior to surgery, with T_1-weighted pre- and post-gadolinium enhancement and diffusion-weighted image (DWI) sequences. The DWI were converted into apparent diffusion coefficient (ADC) maps, which were then overlaid onto the structural post-gadolinium enhanced images, to identify the tumour and specifically its “leading edge” at the tumour-brain interface. Guided by these fused sequences, samples were taken using a Suretrak© probe mounted on biopsy forceps.

Three cases of human brain metastasis, each with three to four biopsy locations per case, were obtained for breast cancer (n = 10 samples), lung adenocarcinoma (n = 11 samples) and melanoma (n = 12 samples) (ethics reference: 11/WNo03/02). The samples were selected to contain tissue at the tumour-brain interface. The corresponding MR images for each patient were anonymised and downloaded as DICOM files for subsequent offline analysis. Moreover, the vectors specifying the location of this sample ("edge"), along with one from the tumour interior ("core") were extracted from the image-guidance software post-operatively (StealthStation S7, Medtronic Inc., MN, USA). These allowed identification of specific regions of interest (ROI) that co-localised to the tissue samples taken intra-operatively.

2.2.10.2 MRI data acquisition

Human MRI data, corresponding to the above mentioned clinical subjects, were provided by a collaborating research team at The Walton Centre NHS Foundation Trust. At a median of 5 days prior to surgery, patients underwent an MRI brain scan, as previously described (120). Sequences were protocoled by a clinical neuro-radiologist; for diagnosis T_2 and unenhanced T_1 sequences were acquired using standard parameters. For diagnosis and neuro-navigation, a volumetric fast spoiled gradient echo sequence was taken after gadolinium injection at a standard dose of 0.1mmol/kg (flip angle = 15°, TR = 9ms, TE = 1.4ms, matrix = 256 × 256, volume = 180 × 1 mm slices at zero angle gantry). DWI with single-shot echo planar imaging at b values of 0 and 1000 second/mm^2 was obtained.

CHAPTER 3: VCAM-1 TARGETED MAGNETIC RESONANCE IMAGING FOR THE DETECTION OF BRAIN MICROMETASTASES

3.1 Introduction

Cerebral metastasis, the spread of malignant tumours from an extracranial primary site of origin to the brain, is a leading cause of cancer mortality and morbidity (121). Patients with brain metastases typically survive for less than 6 months from diagnosis, unless definitive treatment proves possible (122). The poor survival is attributed in large part to the late stage of diagnosis and failure of current diagnostic methods to detect occult micrometastatic disease (37, 123).

Micrometastasis describes the presence of small clusters of cancer cells that have disseminated from the primary tumour and have spread to another part of the body through the lymphatic and/or vascular system. Whilst felt to be biologically distinct from isolated tumour cells, the separation of these two phenomena remains challenging (124, 125). By definition micrometastases are visible only under microscopic examination and have an accepted size criterion of 0.2-2.0mm diameter (124). Our understanding of micrometastases and their impact on patient outcomes is largely derived from studies of breast cancer and probing of sentinel lymph nodes. The Dutch MIRROR study showed that even minimal lymph node involvement in patients with early stage breast cancer results in a significant reduction in disease-free survival for patients not having adjuvant systemic therapy (126, 127). The prognostic significance of micrometastases has also been considered for other tumour types including melanoma (128) and non-small cell lung cancer (NSCLC) (129).

Much less is known about the natural history of micrometastases in the brain. Owing to the relative inaccessibility within the cranium and the risks associated with tissue sampling, histological confirmation of intracerebral micrometastases is difficult. Therefore, any mechanism for detection of brain micrometastases will be heavily dependent on non-invasive imaging. Gadolinium-based contrast enhanced magnetic resonance imaging (MRI) remains the preferred clinical diagnostic method for detecting brain metastases. Previous attempts to detect micrometastases in the brain have relied on escalating doses of gadolinium, and Hanssens *et al.* showed that additional lesions could be diagnosed on MRI following triple dose gadolinium administration in just under half of patients in the study (130). Furthermore, they showed that treating these additional lesions with stereotactic radiosurgery (SRS) from the outset not only reduces the incidence of distant in-brain recurrences, but also defers the need for prophylactic whole brain radiotherapy (WBRT) or salvage WBRT following diagnosis of distant recurrence. However, as gadolinium contrast agent extravasation requires a disrupted blood-brain barrier (BBB), it is likely that there remains a significant underdiagnosis of early stage tumours prior to BBB disruption.

With the availability of targeted agents that have improved BBB penetration, such as Tesevatinib (131) and Osimertinib (132), and new strategies for selective BBB permeabilisation at metastatic sites (133), a wider range of therapeutic options for patients with brain metastases are emerging, particularly for microscopic disease where intervention will be most effective (134). This underscores the value of expanding the potential of current imaging modalities for detecting occult brain micrometastases (<2mm diameter) (135), whilst opening up the diagnostic window will provide further impetus for the development of novel therapies.

Metastatic haematogenous dissemination is a multi-step process, for which extravasation of tumour cells into the distant organ is a key step. Specific cell surface proteins, including those belonging to the family of cell adhesion molecules (CAMs), such as vascular cell adhesion molecule-1 (VCAM-1), have been shown to facilitate the binding between tumour cells and the endothelium. It has previously been demonstrated that, in breast cancer brain metastasis mouse models, vascular cell adhesion molecule-1 (VCAM-1) expression is upregulated early in micrometastasis-associated blood vessels and remains upregulated throughout metastatic seeding to, and colonisation of, the brain (58). Furthermore, Serres *et al* demonstrated that by conjugating anti-VCAM-1 antibodies to microparticles of iron oxide (MPIO), cerebral micrometastases could be detected using T_2^*-weighted MRI before visibility with conventional gadolinium-enhanced MRI (94). However, breast cancer is not the only primary tumour with a propensity to metastasise to the brain, and both lung adenocarcinoma and melanoma contribute substantially to the incidence of brain metastasis. Consequently, with a view to determining the broader potential for clinical translation of this method, I sought to determine whether VCAM-targeted MRI is more broadly applicable for early micrometastasis detection.

The primary aim of this chapter, therefore, was to determine whether VCAM-1 targeted MRI enables detection brain micrometastases across the three different primary tumour types that represent the greatest burden of brain metastases in humans. By developing and characterising pre-clinical xenograft mouse models of brain metastases for breast cancer, melanoma and lung adenocarcinoma, I tested the following hypotheses:

1. Primary cell lines from human breast cancer, melanoma and lung adenocarcinoma produce viable tumours in the brain parenchyma;

2. Intracardial injection of tumour cells from human breast cancer, melanoma or lung adenocarcinoma induces brain metastases that have a defined micrometastatic phase with an intact BBB;
3. VCAM-1 expression is upregulated on endothelial cells near to brain micrometastases across different tumour types; and
4. VCAM-1 conjugated MPIO in combination with MRI enable detection of brain micrometastases across different primary tumour types, before there is evidence of BBB breakdown.

3.2 Methods

3.2.1 Intracerebral injection brain metastasis models

To determine the specific inducibility of endothelial VCAM-1 in the model organism, female severe combined immunodeficiency (SCID) BALB/c variant mice, aged 8 to 9 weeks old, were intracerebrally injected with either 1ng interleukin-1β (IL-1β) in 0.5μL sterile PBS or PBS only into the left striatum (n = 3 per group). Following a 3hr incubation period, animals were sacrificed by transcardial perfusion with 0.9% heparinised saline and fixation with PLP_{light} under terminal anaesthesia. Animal brains were collected and cryopreserved, before tissue sectioning of the striatum and storage at -80°C.

For model development, female SCID BALB/c variant mice, aged 8 to 9 weeks old, were intracerebrally injected with either 5 x 10^3 MDA231Br-GFP (breast cancer), H1_DL2 (melanoma) or SEBTA-001 (lung adenocarcinoma) cells in 0.5μL sterile PBS into the left striatum, see Fig 3.1 for experimental schedule (section 2.2.4.3). Another group of animals were intracerebrally injected with PBS, to serve as a control cohort. To establish the effect of

tumour progression on BBB integrity, tumour bearing and non-tumour bearing animals (n = 3 per group) underwent serial MRI with pre- and post-gadolinium T_1-weighted MRI at weekly intervals. The maximum time point studied was 28 days, with the exception of SEBTA-001 tumour bearing animals who were imaged up to 35 days due to the observed slower growth rate of these tumours. To assess tumour volume, based on histology, at weekly intervals up to 28 days or 35 days (n = 3 per timepoint), tumour bearing animals were sacrificed by transcardial perfusion with 0.9% heparinised saline and fixation with PLP light under terminal anaesthesia. Animal brains were collected and cryopreserved, before tissue sectioning of the striatum and storage at -80°C.

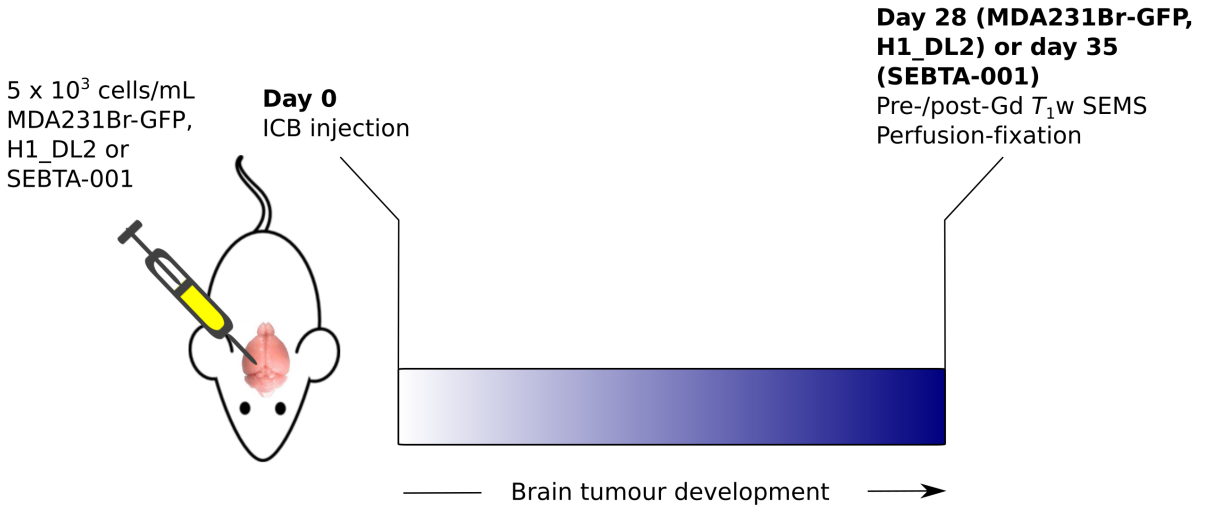


Fig 3.1. Experimental schedule for intrastriatal xenograft induction. Diagram illustrating experimental schedule for intracerebral (ICB) brain tumour development, from tumour cell injection to MR imaging of the brain with gadolinium contrast. Animals were sacrificed by perfusion-fixation following imaging.

3.2.2 Intracardiac injection brain metastasis models

Female SCID BALB/c variant mice, aged 8 to 9 weeks old, were injected in the left cardiac ventricle under ultrasound guidance, with $1x10^5$ MDA231Br-GFP, H1_DL2 cells or SEBTA-001 cells in 100µl PBS, as described in Section 2.2.4.5. To establish tumour progression over time, animals (n = 3 per time point) were sacrificed and brains harvested for histological examination at weekly intervals (up to 28 days) for MDA231Br-GFP and H1_DL2 tumour-bearing mice, or at fortnightly intervals (up to 56 days) for SEBTA-001 tumour-bearing mice, as these tumours are slower-growing. Animals undergoing MRI were imaged at either 21 days (MDA231Br-GFP and H1_DL2) or 42 days (SEBTA-001) after intracardiac injection. Imaging time points were selected based on the growth rates of the different cell lines, such that a time point was chosen for each model at which the metastases were established within the brain, but still expected to be within the micrometastatic phase prior to BBB breakdown. Owing to their relatively slower growth pattern, the SEBTA-001 cells were imaged at a later time point than the MDA231Br-GFP and H1_DL2 cells.

3.2.3 *In vivo* imaging

Antibody conjugated-carboxylic acid MPIO were prepared and synthesised as described in Section 2.2.3.1. VCAM-MPIO or control IgG-MPIO were injected intravenously into each animal prior to MRI, as described in Section 2.2.4.6. See Fig 3.2 for experimental schedule of *in vivo* imaging.

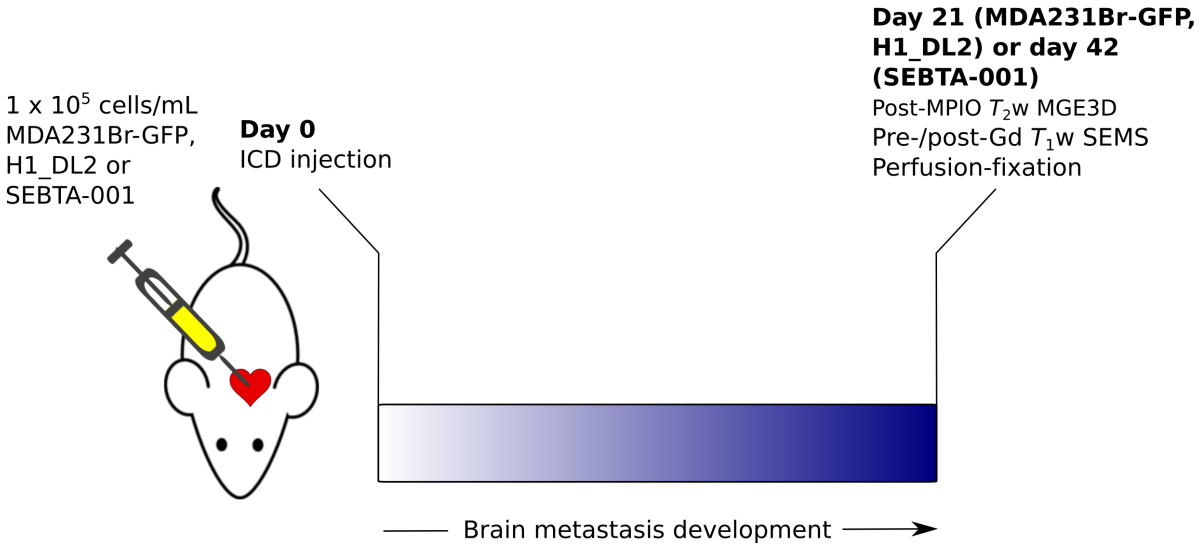


Fig 3.2. Experimental schedule for intracardiac brain metastasis induction. Diagram illustrating experimental schedule for intracardiac (ICD) brain metastasis development, from tumour cell injection to MR imaging of the brain with post-MPIO T_2-weighted and pre-/post-gadolinium T_1-weighted sequences. Animals were sacrificed by perfusion-fixation following imaging.

MRI data were acquired using a 7.0T MRI (Section 2.2.8.1). Prior to imaging, an intravenous cannula was inserted into the lateral tail vein, allowing for administration of either VCAM-MPIO or IgG-MPIO (5-6 animals per tumour group; 4 animals per PBS group) and then gadolinium for sequential imaging sequences. For each animal, post-VCAM-MPIO T_2^*-weighted images, together with pre- and post-gadolinium T_1-weighted images were collected to assess VCAM-MPIO binding and BBB permeability, respectively. Each image dataset was saved offline for further analysis, as outlined in Section 2.2.8.3. A further cohort of naïve SCID mice were injected intravenously with VCAM-MPIO as above (n = 5). At 30mins after MPIO injection, animals were positioned in a customised cradle inside a quadrature birdcage coil. Respiration monitoring was performed to allow anaesthetic depth to be regulated and body temperature was maintained at approximately 37°C.

3.2.4 Immunohistochemistry for VCAM-1 expression

Brain tissue sections from tumour-bearing mice and control cohorts were assessed immunohistochemically for VCAM-1 expression and additionally examined for co-localisation to metastasis-associated vasculature. Selected sections of human brain metastases for breast cancer, lung adenocarcinoma and melanoma, obtained via image-guided biopsy (Walton Research Tissue Bank reference: 11/WNo03/02), were assessed immunohistochemically for VCAM-1 upregulation. See Sections 2.2.9.1 and 2.2.3 for full details of tissue sampling and immunohistochemical analysis, respectively.

3.2.5 Quantitation of tumour volume and VCAM-1 expression

Alternate sections for each brain were stained immunohistochemically with tumour-specific markers. Histological slides were digitally scanned on an Aperio CS2 Brightfield scanner at x20 magnification. The digital images were visualised using Imagescope software and manually annotated to outline individual tumours on each section as a region of interest (ROI). The tumour area was returned for each ROI, in μm^2, and data for the remaining alternate sections were calculated by linear interpolation. The sum of the tumour areas was multiplied by the slice thickness (10µm) to determine the total volume of tumours in each brain, reported in mm^3.

To quantify VCAM-1 expression in each brain, alternate sections were immunohistochemically stained for VCAM-1 and digitally scanned on an Aperio CS2 Brightfield scanner at x20 magnification. The digital images were visualised using Imagescope software and manually annotated to outline the entire section as a region of interest, excluding the choroid plexus

and ventricles as these are known sites of false positive staining. Using the in-built Positive Pixel Count v.9 algorithm, all medium and strong intensity brown pixels (Intensity threshold between 0 to 174, Intensity threshold of negative pixels = -1, Colour saturation threshold = 0.04, Hue width = 0.5) were summed for each section and divided by the total area of the corresponding ROI to determine the VCAM-1 staining, reported as number of positive pixels per mm^2 of brain.

3.2.6 MR image analysis

Gadolinium enhancement in the brains of intracerebral tumour animal models was determined by digitally subtracting the pre-contrast from the post-contrast T_1-weighted MR images. In the resulting images, the slices corresponding to the region of the brain containing the striatum were separated for analysis. As demonstrated in Fig 3.3, on these processed MRI slices, freehand ROIs were annotated to delineate the left and right striatum. The mean grey pixel intensity was measured within each ROI. Hypointensity analysis was performed on post-MPIO T_2^*-weighted MR images, as described in Section 2.2.8.3.

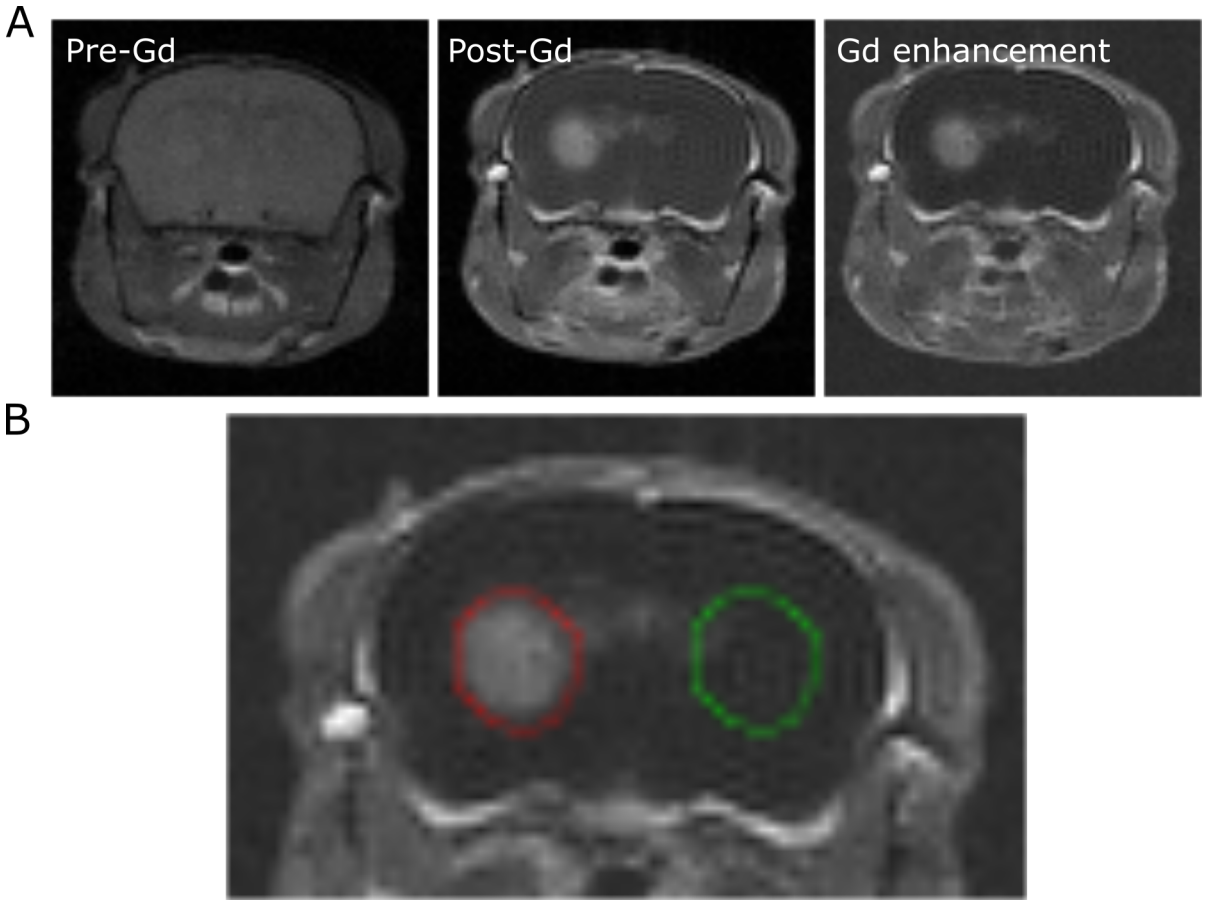


Fig 3.3. Method of analysing gadolinium enhancement on MRI. (A) Digital processing to generate the gadolinium (Gd) enhanced images, by subtracting the pre-Gd T_1-weighted image from the corresponding post-Gd image. (B) Specific ROIs delineating the left (red) and right (green) striatum were annotated for measurement of mean grey pixel intensity values.

3.2.7 Statistical analysis

Differences in VCAM-1 expression in the striatum of mouse brain injected with either IL-1β or PBS were assessed by Student's t-test. To assess gadolinium enhancement over the time course, a repeated measures one-way analysis of variance (ANOVA) was used to measure differences in grey pixel intensity in the ipsilateral striatum at weekly intervals. Post-hoc multiple comparison tests with Bonferroni correction were used to detect individual differences between groups.

For MRI hypointensity and tumour volumes, differences between animal cohorts for all tumour types were identified by one-way ANOVA. Post-hoc Tukey tests were used to identify specific differences between groups. VCAM-1 positive staining was calculated based on number of strong intensity positive pixels in proportion to brain volume. Difference in VCAM-1 expression across multiple time-points was assessed by one-way ANOVA tests for each tumour type, with post-hoc Tukey tests. All statistical analyses were two-sided and performed with a significance level of 0.05.

3.3 Results

3.3.1 Development of *in vivo* pre-clinical models of brain metastasis

Following intracerebral injection of IL-1β, abundant VCAM-1 expression was evident in the ipsilateral striatum, as shown in Fig 3.4. This upregulation ranged from 2.5 to 4 times greater than the VCAM-1 expression observed in the contralateral striatum, thus demonstrating that induction of inflammation causes a localised reaction. Furthermore, the brains of the control cohort with intracerebral PBS injection did not show any upregulation of VCAM-1 in the ipsilateral striatum compared to the contralateral side. A significantly greater ratio of ipsilateral *vs.* contralateral VCAM-1 expression was evident in the IL-1β group compared to the PBS only group ($p = 0.0145$). However, a significant increase in VCAM-1 activation in the brains of the IL-1β cohort was also found in the contralateral striatum compared to the contralateral striatum of the PBS only cohort ($p = 0.0034$; $0.052 \pm 0.01mm^2$ *vs.* $0.016 \pm 0.0006mm^2$), although the absolute expression for both cohorts remained negligible in comparison to the ipsilateral striatum. This finding indicates that focal unilateral IL-1β

injection causes mild upregulation of VCAM-1 contralaterally, albeit with a far greater activation in the ipsilateral side.

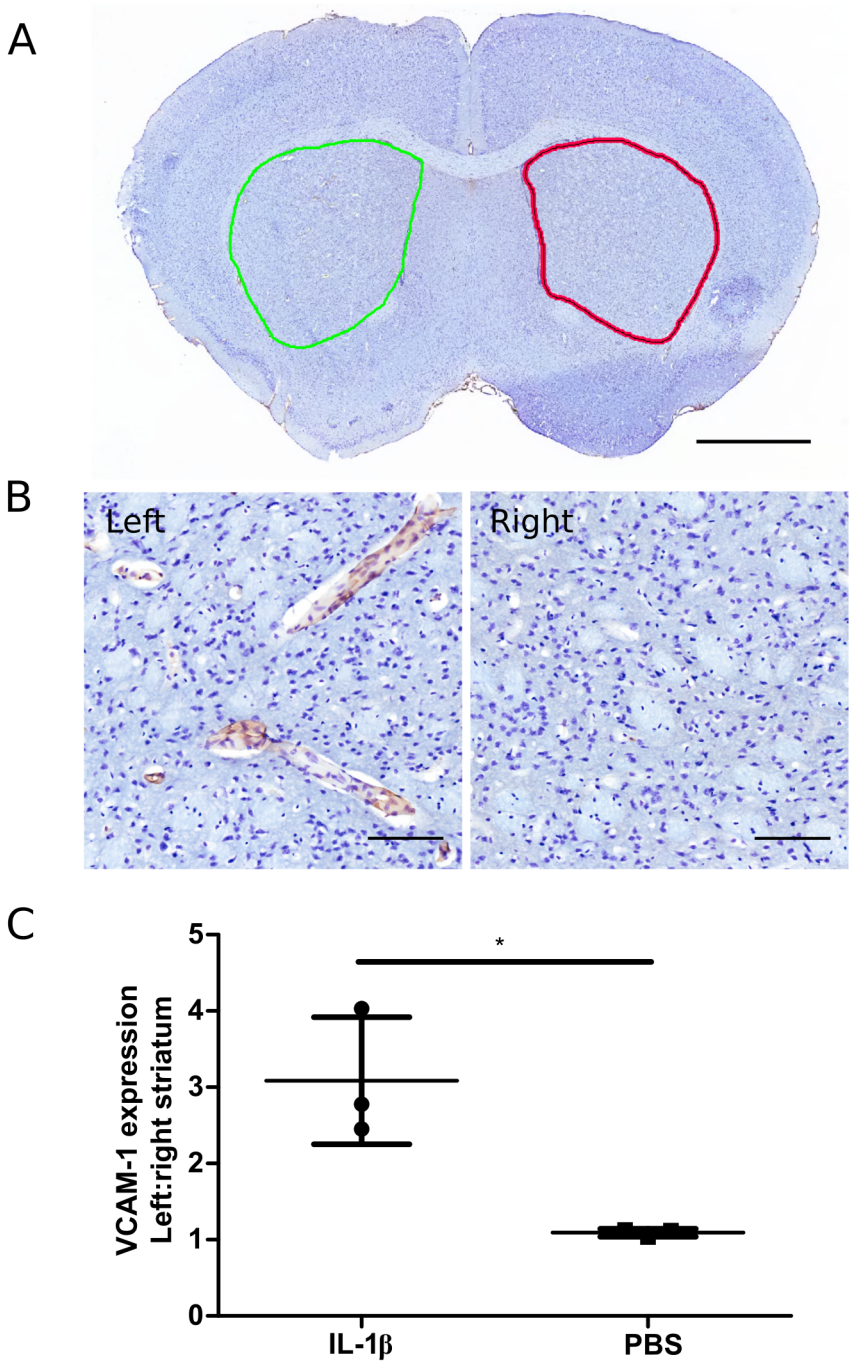


Fig 3.4. Intrastriatally injected interleukin-1β induces local inflammation in SCID mice. (A) Representative histological section of mouse brain stereotactically injected with 1ng IL-1β in the left striatum (green). The contralateral striatum is annotated in red; scale bar = 1.5mm. (B) High

power magnification images confirm upregulation of endothelial VCAM-1 expression (brown colour) present in the ipsilateral striatum compared to the contralateral side; scale bar = 100μm. (C) There was a marked increase in the ratio of VCAM-1 expression between the left:right striatum in animals intrastriatally injected with IL-1β compared to animals with PBS only injections (n = 3 per injection group; *p<0.05).

3.3.2 Time course of tumour growth following intracerebral induction

All three tumour cell lines successfully induced parenchymal tumours following introduction by intrastriatal injection. As shown in Fig 3.5, the growth dynamics varied between the cell lines, with a protracted growth pattern for the SEBTA-001 tumours taking more than 28 days to reach an average volume of > 0.2μL. By comparison, the MDA231Br-GFP tumour reached this volume within 28 days, whilst the H1_DL2 tumours grew even faster and, on average, were more than 0.2μL in volume by 21 days. At 28 days, the H1_DL2 tumours were the largest with a mean volume of 0.81 ± 0.16μL, followed by the MDA231Br-GFP tumours at 0.22 ± 0.03μL. The SEBTA-001 tumours remained negligible in size at this time point, measuring only 0.012 ± 0.005μL in volume. It was only at 35 days following tumour cell inoculation that the SEBTA-001 tumours showed a significantly increased volume compared to any of the earlier timepoints (p = 0.0006; Fig 3.5).

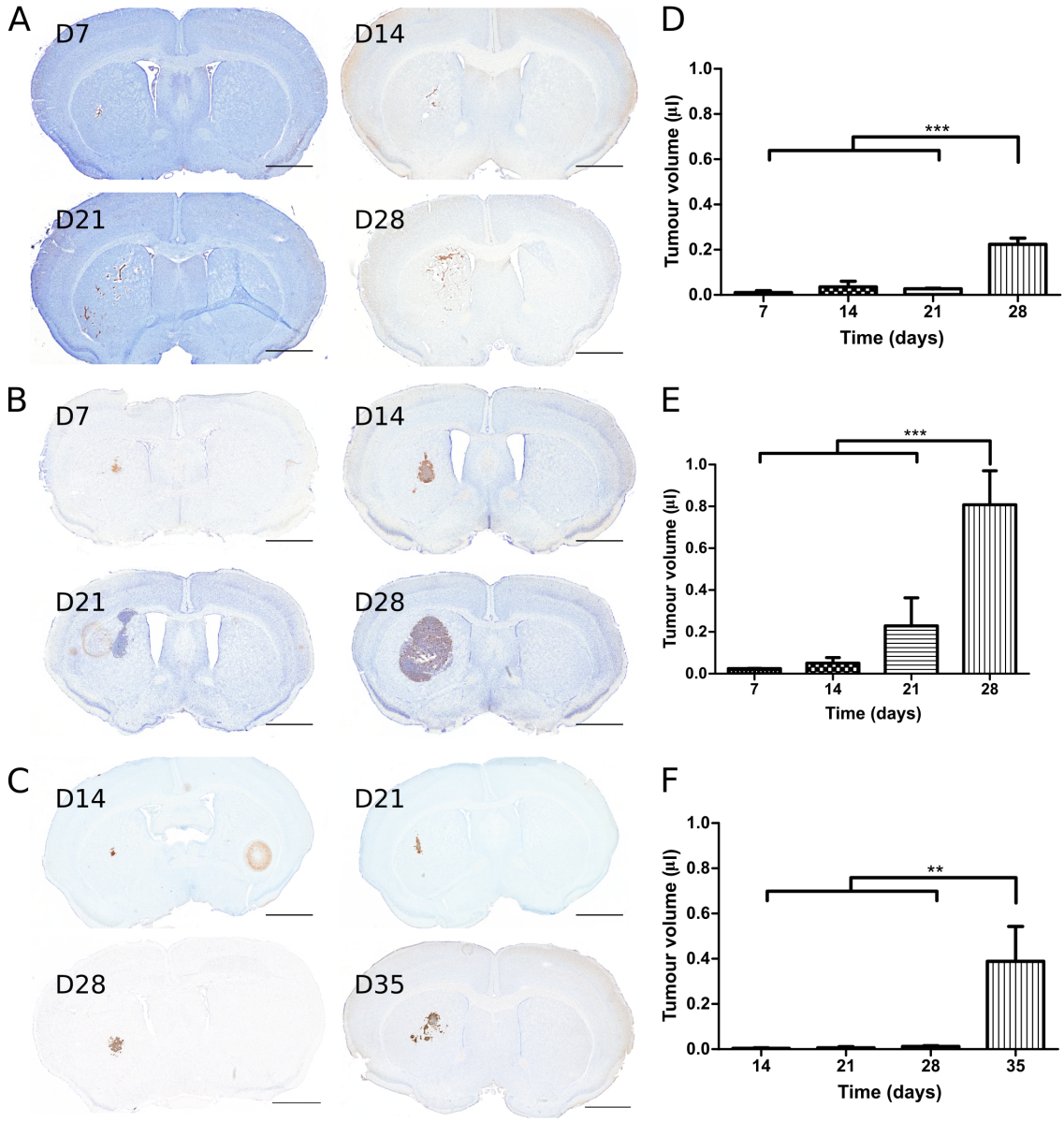


Fig 3.5. Volume of intrastriatal xenografts from different cancer types. Representative histological sections of mouse brains intrastriatally injected with (A) MDA231Br-GFP, (B) H1_DL2 and (C) SEBTA-001 tumour cells (brown colour), taken at various time points according to the experimental schedule; scale bar = 1.5mm. Calculation of tumour volumes over the time course showed varying growth patterns of the (D) MDA231Br-GFP, (E) H1_DL2 and (F) SEBTA-001 tumours (n = 3 per time-point; ***p<0.001, **p<0.01).

For tumour bearing animals that underwent T_1-weighted MRI, digital subtraction of the images prior to gadolinium administration from the post-contrast scan revealed that contrast enhancement was present at the later imaging timepoints. This finding was indicative of BBB breakdown caused by an enlarging tumour in the striatum. Notably, whilst gadolinium enhancement was visibly appreciable at an earlier timepoint, as seen in Fig 3.6, no significant enhancement, measured by grey pixel intensity, was found until 28 days after MDA231Br-GFP ($p = 0.0132$) or H1_DL2 ($p = 0.0064$) tumour cell injection and 35 days after SEBTA-001 ($p = 0.0002$) tumour cell injection. Thus, based on the results presented here, visible contrast enhancement on T_1-weighted MRI could be seen at a tumour volume of $\geq 0.011 \pm 0.004\mu L$, although this was not quantitatively significant until tumours had reached $\geq 0.22 \pm 0.027\mu L$.

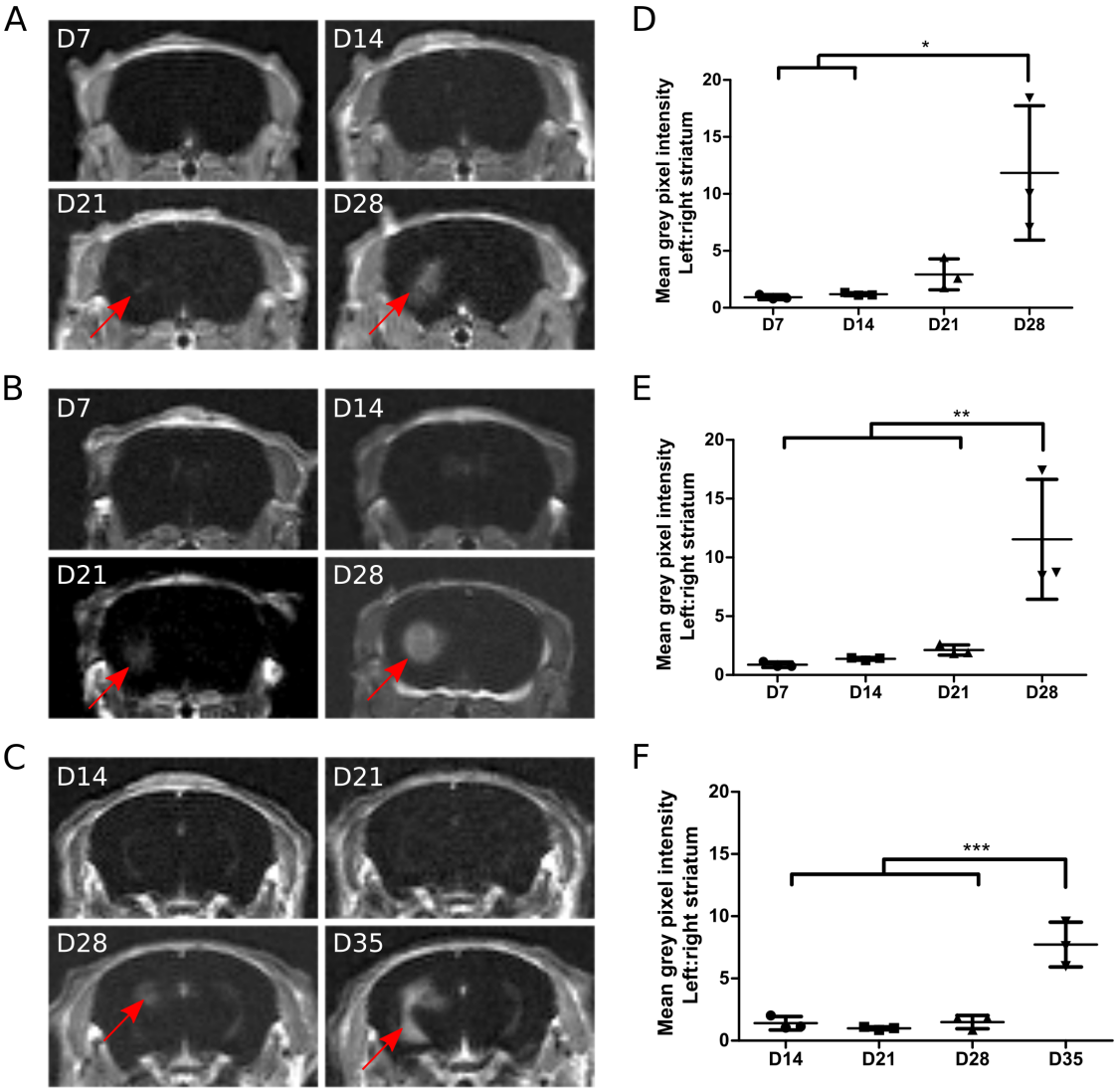


Fig 3.6. Gadolinium contrast enhancement of intrastriatal xenografts on T_1-weighted MRI. Representative T_1-weighted contrast enhancement MR images, with pre-gadolinium contrast images digitally subtracted from post-contrast images, for (A) MDA231Br-GFP, (B) H1_DL2 and (C) SEBTA-001 intrastriatal tumours. Red arrow denotes areas of visible contrast enhancement. (D-F) Grey pixel intensity analysis over the time course showed there was greater enhancement in the ipsilateral striatum compared to the contralateral side at the later time points for the corresponding tumour types (n = 3 per time-point; ***p<0.001, *p<0.05).

3.3.3 Time course of metastatic growth in the brain following intracardial induction

All animals reached their pre-defined endpoint without overt clinical signs. Metastases were present in all mice following intracardiac tumour cell injection and were disseminated throughout the brain parenchyma. Metastatic growth varied according to tumour type over the experimental time course, shown in Fig 3.7A-C. Overall tumour burden in mice injected with SEBTA-001 cells was substantially lower than that of mice injected with either MDA231Br-GFP or H1_DL2 cells over the first 28 days from inoculation (Fig 3.7D-F), indicating a much slower rate of growth in this phase. At the selected imaging time points for each tumour type, the mean ± SD tumour burden for MDA231Br-GFP was 0.033 ± 0.013µl (21 days), 0.0076 ± 0.0008µl for H1_DL2 (21 days) and 0.027 ± 0.019µl for SEBTA-001 (42 days). VCAM-1 expression in proximity to metastatic colonies for all tumour types was upregulated from the earliest time-point (Fig 3.8) and maintained throughout the time course. Co-localisation of VCAM-1 specifically along the endothelial lining was confirmed by immunofluorescence (Fig 3.9).

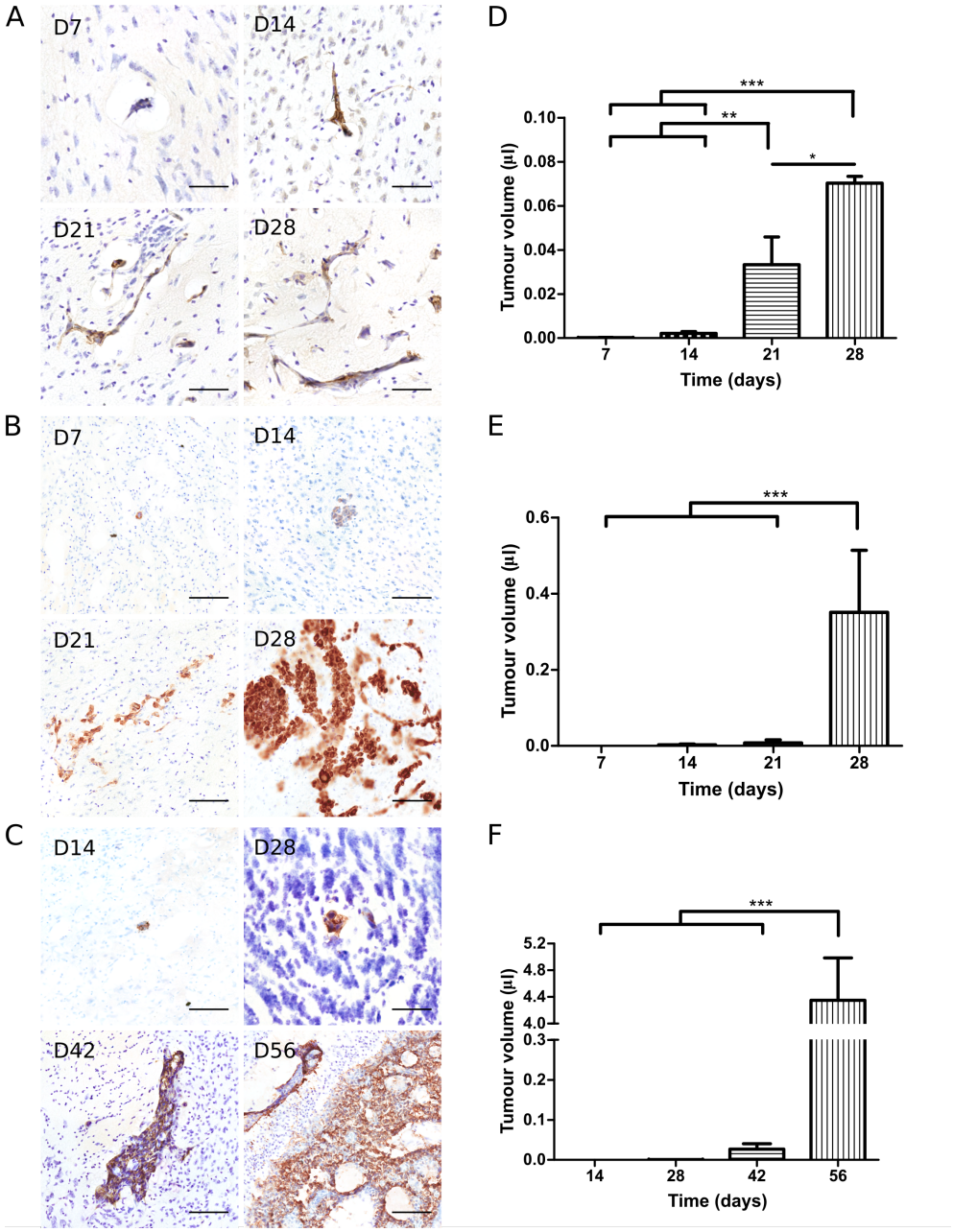
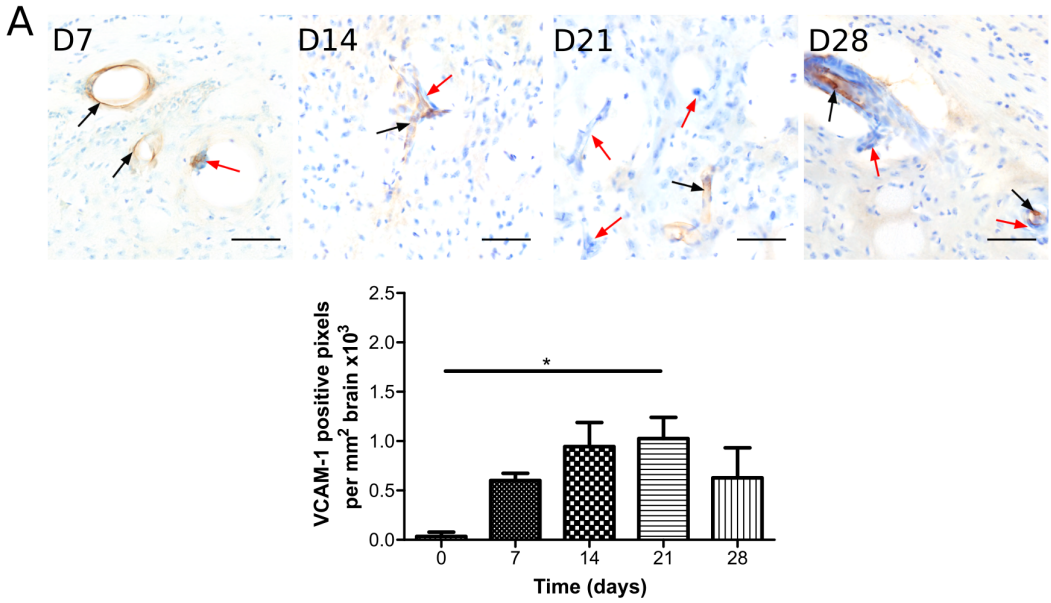
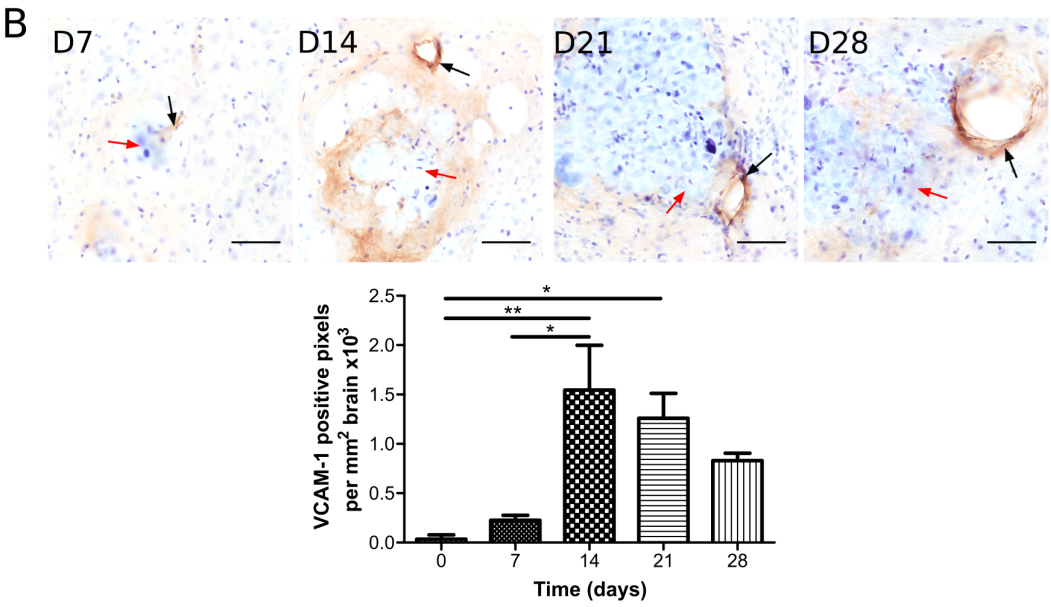


Fig 3.7. Volume of brain metastases in mice at different timepoints. Representative histological images demonstrating presence of metastatic tumours within the brain parenchyma for each model (brown colour denotes stained tumour cells); (A) MDA231Br-GFP, (B) H1_DL2 and (C) SEBTA-001; scale bar = 50µm. Graphs showing increasing metastatic tumour burden in the brain measured over time following intracardiac injection of (D) MDA231Br-GFP (up to 28 days), (E) H1_DL2 (up to 28 days) and (F) SEBTA-001 cells (up to 42 days) (n = 3 per time-point; ***p<0.001, **p<0.01, *p<0.05).


A
D7
D14
D21
D28
VCAM-1 positive pixels per mm² brain x10³
2.5
2.0
1.5
1.0
0.5
0.0
*
0
7
14
21
28
Time (days)


B
D7
D14
D21
D28
VCAM-1 positive pixels per mm² brain x10³
2.5
2.0
1.5
1.0
0.5
0.0
*
**
*
0
7
14
21
28
Time (days)

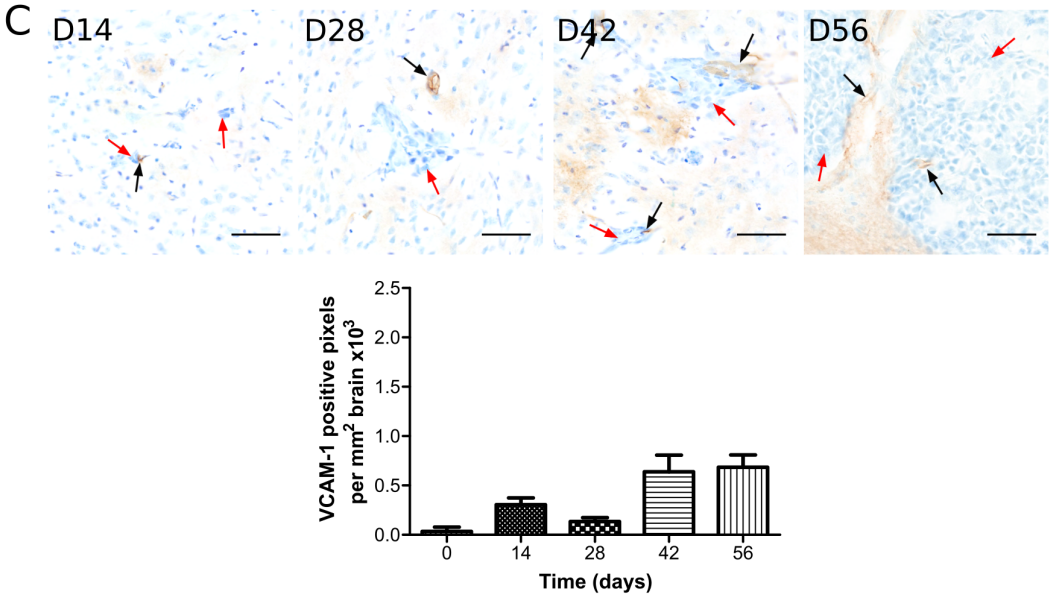

C
D14
D28
D42
D56
VCAM-1 positive pixels per mm² brain x10³
2.5
2.0
1.5
1.0
0.5
0.0
0
14
28
42
56
Time (days)

Fig 3.8. Endothelial VCAM-1 expression in relation to mouse brain metastases over time. Representative images of DAB-stained histological sections for VCAM-1 expression (brown colour) demonstrating upregulation on blood vessels (black arrows) in proximity to (A) MDA231Br-GFP, (B) H1_DL2 and (C) SEBTA-001 metastases (red arrows); scale bar = 50µm. Graphs showing time course of VCAM-1 upregulation for (A) MDA231Br-GFP, (B) H1_DL2 and (C) SEBTA-001 metastases (n = 3 animals per time-point; *p<0.05, **p<0.01). Time point at 0 days denotes mean baseline VCAM-1 expression in brains of naïve animals (n = 3 animals).

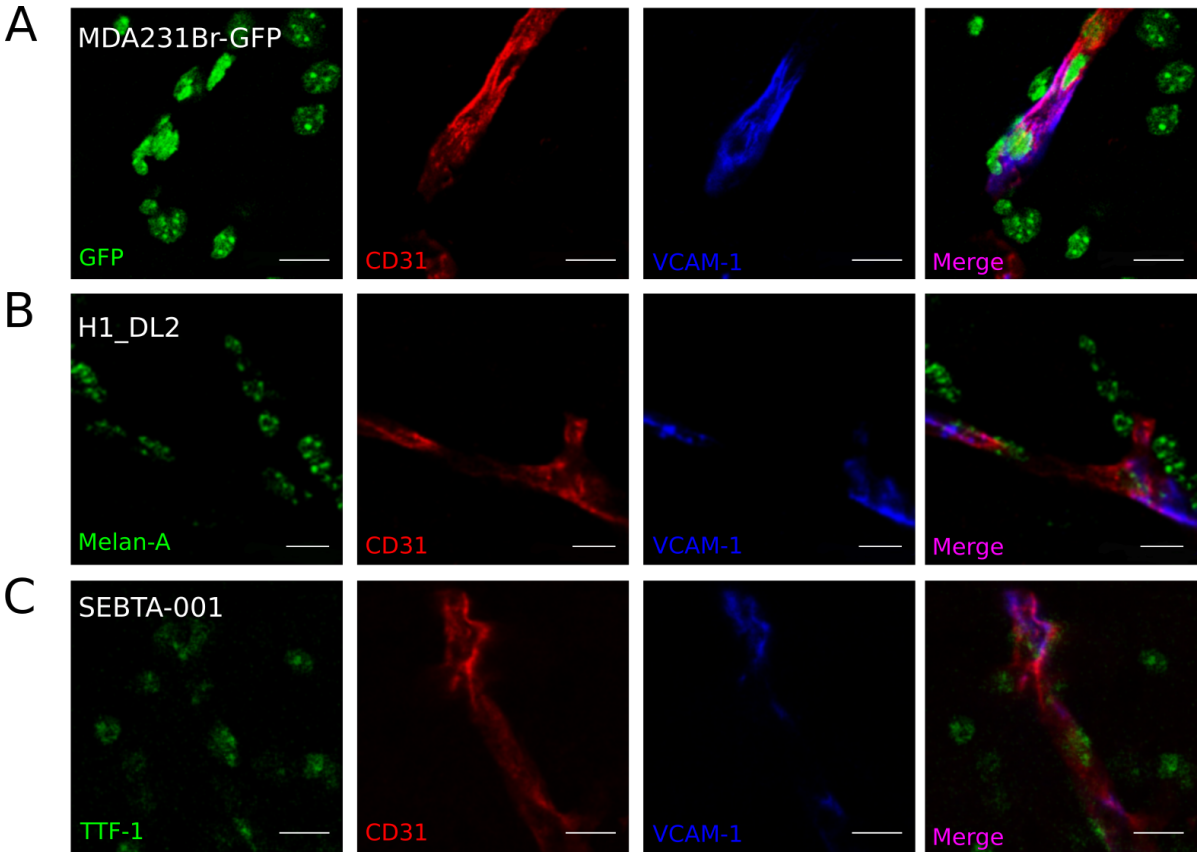


Fig 3.9. Co-localisation of VCAM-1 to vasculature in proximity to tumour. Representative immunofluorescence images from mouse brain sections showing co-localisation of VCAM-1 expression (blue) with vascular endothelium (red) in close proximity to metastatic tumours (green) for all three models; (D) MDA231Br-GFP (day 21), (E) H1_DL2 (day 21) and (F) SEBTA-001 (day 42). Co-localisation is evident in merged images (purple); scale bar = 20µm.

In some cases, VCAM-1 expression appeared not to co-localise with the endothelium, likely reflecting expression on the surface of an out-of-plane tumour or glial cell; VCAM-1 is known to be expressed on some tumour cells (136), as well as microglia and astrocytes (58). It should be noted that VCAM-1 upregulation on other cells is not relevant to the methodology presented here, since the VCAM-MPIO remain intravascular and, thus, only have access to luminal VCAM-1 on endothelial cells.

3.3.4 In vivo detection of VCAM-1 upregulation by MRI

Marked hypointensities were evident on T_2^*-weighted images for all tumour-bearing mice injected with VCAM-MPIO, as can be seen in Fig 3.10. Histological examination confirmed the presence of widespread micrometastases for all tumour types. Spatial correlation between MRI detectable hypointensities and the presence of metastases was assessed. Owing to differences in spatial resolution between MRI and histology (MGE3D isotropic resolution of 88µm^3 *vs.* maximum histological slice thickness of 10µm), it was necessary to stack alternate histological sections within each image slice space, to generate a composite image containing all metastases within that imaging slice (Fig 3.11D-F). Immunohistochemical analysis demonstrated VCAM-1 positive vessels in close proximity to micrometastases (Fig 3.11G-I) and the presence of VCAM-MPIO within VCAM-1 positive vessels (Fig 3.11J-L).

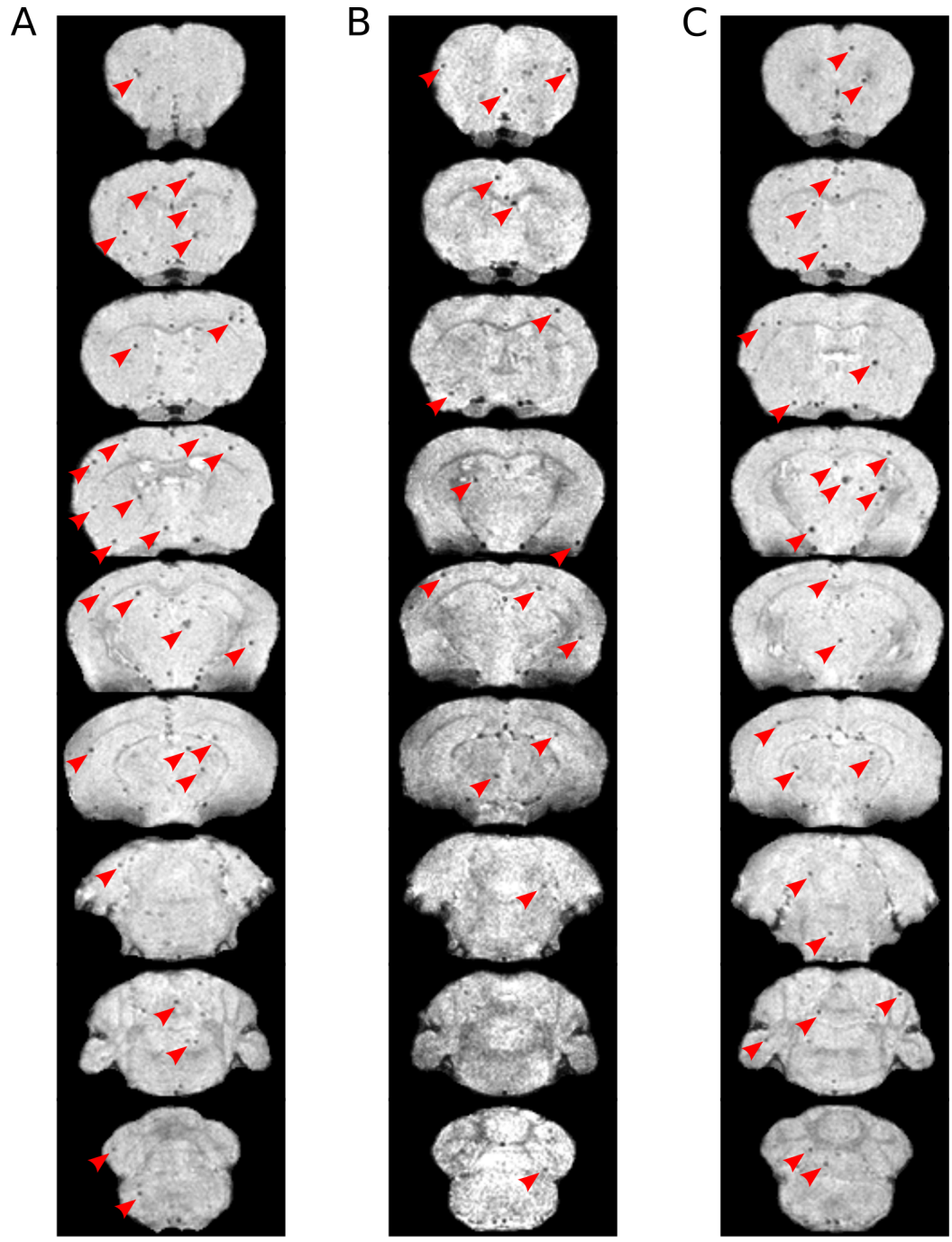


Fig 3.10. Example T_2^*-weighted images in tumour-bearing mouse brains following VCAM-MPIO administration. Representative T_2^*-weighted axial images of mouse brains bearing (A) MDA231Br-GFP, (B) H1_DL2 or (C) SEBTA-001 intracardially disseminated brain metastases, following i.v. administration of VCAM-MPIO contrast agent. Red arrows indicate visible hypointensities, corresponding to sites of VCAM-MPIO binding.

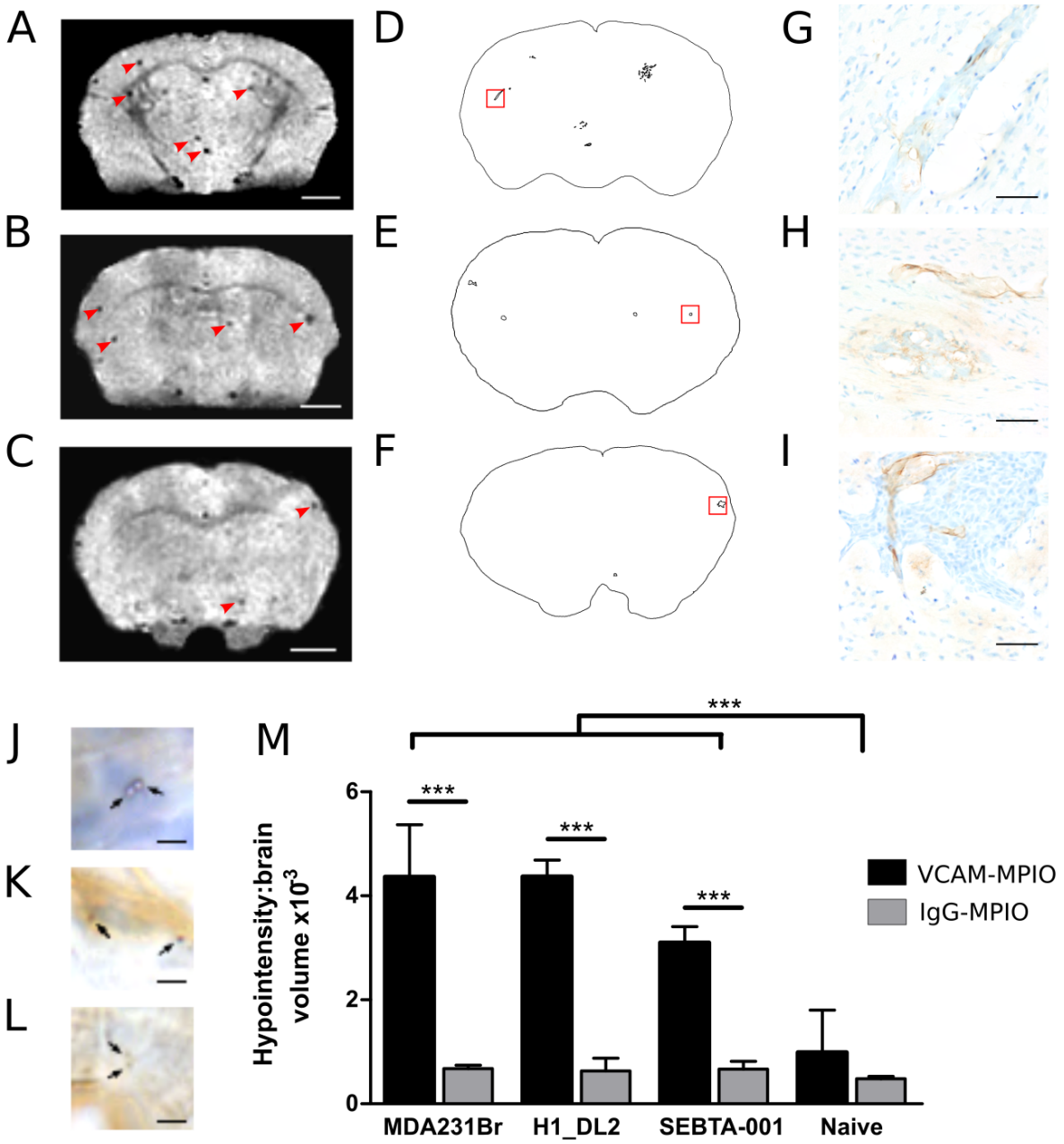


Fig 3.11. Hypointensity analysis on T_2^*-weighted MRI and histology following VCAM-MPIO administration. Representative T_2^*-weighted images from mouse brain bearing (A) MDA231Br-GFP, (B) H1_DL2 and (C) SEBTA-001 metastases, following i.v. injection of VCAM-MPIO; scale bar = 1.5mm. Red arrows highlight focal hypointensities, which are congruous with metastatic deposits evident on composite images of corresponding sequential histological sections (D-F). (G-I) Immunohistochemical detection of VCAM-1 positive vessels (brown) in close proximity to micrometastases highlighted in red boxes in D-F. Sections counterstained with cresyl violet; scale

bar = 50µm. Images from (J) MDA231Br-GFP, (K) H1_DL2 and (L) SEBTA-001 micrometastases showing VCAM-MPIO (black arrow) bound to VCAM-1 positive vessels (brown); scale bar = 2.5µm. (M) Graph showing volumes of hypointensities on T_2^*-weighted images for all groups. Volumes of hypointensities were significantly greater for all three tumour groups injected with VCAM-MPIO than either tumour-bearing mice injected with non-specific IgG-MPIO or tumour-bearing naive mice injected with VCAM-MPIO (***p<0.001).

Quantitatively, significantly greater volumes of hypointensities were found in VCAM-MPIO injected tumour bearing animals than the IgG-MPIO control cohorts (Figure 3.11M). In contrast, no significant differences were evident between naïve animals injected with VCAM-MPIO or IgG-MPIO. Moreover, few hypointensities were observed on T_2^*-weighted images from tumour-bearing mice injected with non-targeting IgG-MPIO or naïve animals injected with VCAM-MPIO, see Fig 3.12.

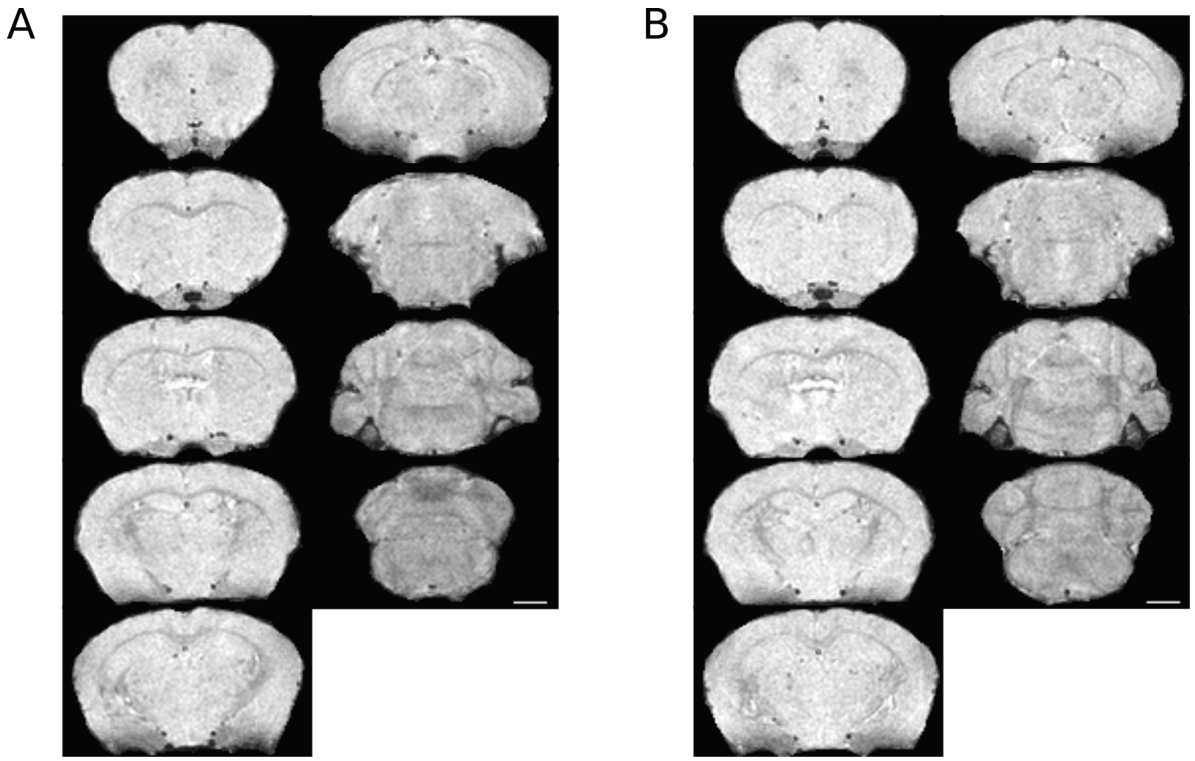


Fig 3.12. VCAM-MPIO imaging in control cohorts. Selected T_2^*-weighted images from (A) a naïve mouse following intravenous injection of VCAM-MPIO and (B) a mouse bearing MDA231Br-GFP metastases following intravenous injection of IgG-MPIO; scale bar = 1.5mm. Minimal background (non-specific) hypointensities are evident.

For all mice injected with either MDA231Br-GFP or H1_DL2 cells, no contrast enhancement was evident on post-gadolinium T_1-weighted images at the time point of VCAM MRI (Fig 3.13 and Fig 3.14). One mouse injected with SEBTA-001 cells did show one discrete area of gadolinium enhancement, in the left cerebral cortex, on post-contrast T_1-weighted imaging, demonstrated in Fig 3.15. This region correlated with a large cerebral metastasis (volume = 0.12µl) confirmed histologically. This metastasis was also visible on T_2^*-weighted MRI following VCAM-MPIO administration, alongside additional focal hypointensities where gadolinium enhancement was not evident. This non-conforming metastasis was excluded from the subsequent hypointensity analysis to avoid detracting from my objective of detecting micrometastatic disease (i.e. prior to the size threshold required to produce contrast enhancement).

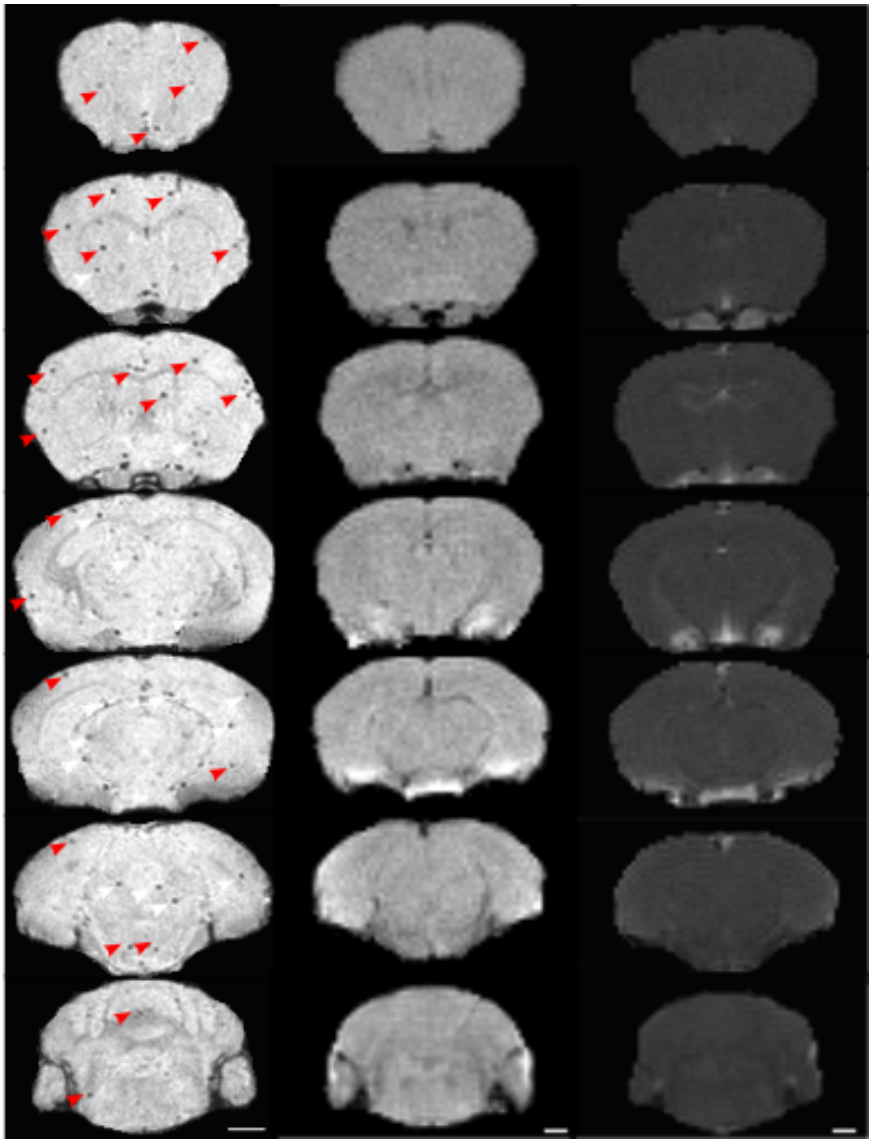


Fig 3.13. Example MRI sequences for a MDA231Br-GFP metastasis bearing mouse brain. Corresponding images from a mouse brain bearing MDA231Br-GFP metastases for post-VCAM-MPIO T_2^*-weighted MRI (left column), pre-gadolinium T_1-weighted MRI (middle column) and post-gadolinium T_1-weighted MRI (right column); scale bar = 1.5mm. Multiple focal hypointensities are visible (red arrows), despite lack of contrast enhancement on T_1-weighted MRI following i.v. gadolinium administration.

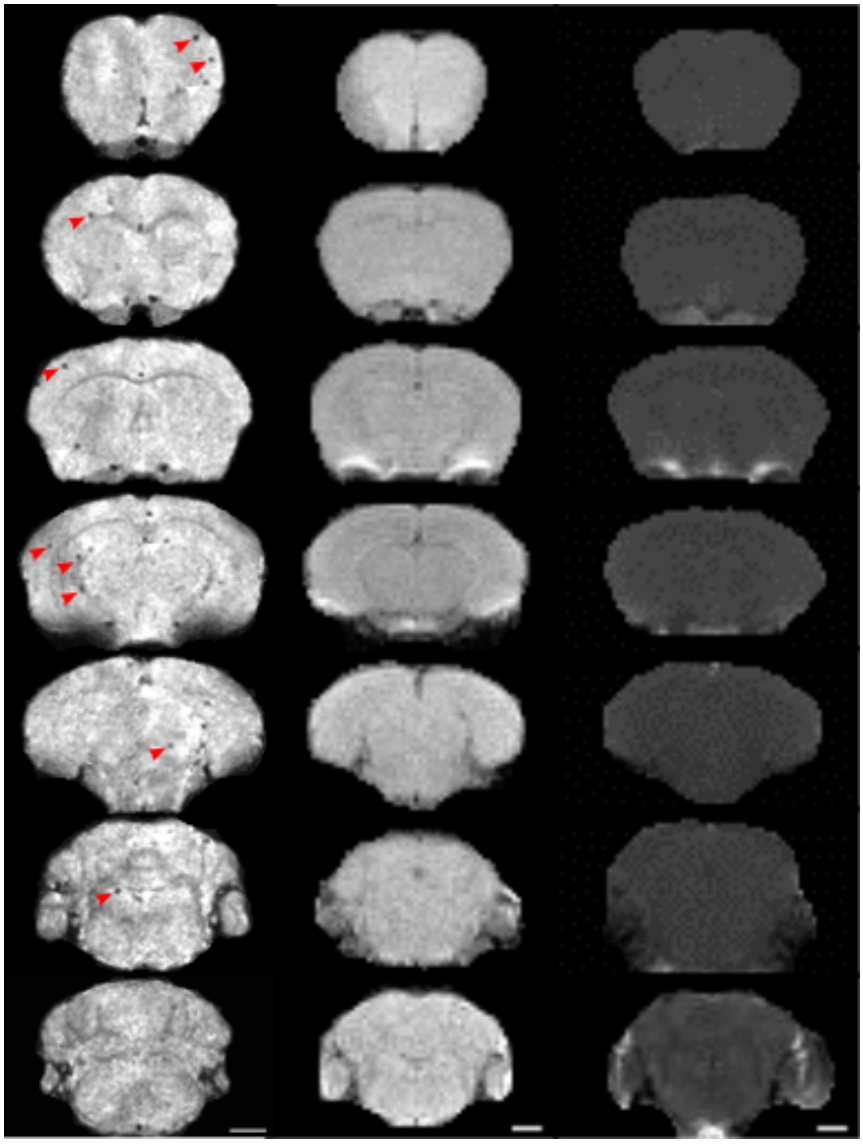


Fig 3.14. Example MRI sequences for a H1_DL2 metastasis bearing mouse brain. Corresponding images from a mouse brain bearing H1_DL2 metastases for post-VCAM-MPIO T_2^*-weighted MRI (left column), pre-gadolinium T_1-weighted MRI (middle column) and post-gadolinium T_1-weighted MRI (right column); scale bar = 1.5mm. Multiple focal hypointensities are visible (red arrows), despite lack of contrast enhancement on T_1-weighted MRI following i.v. gadolinium administration.

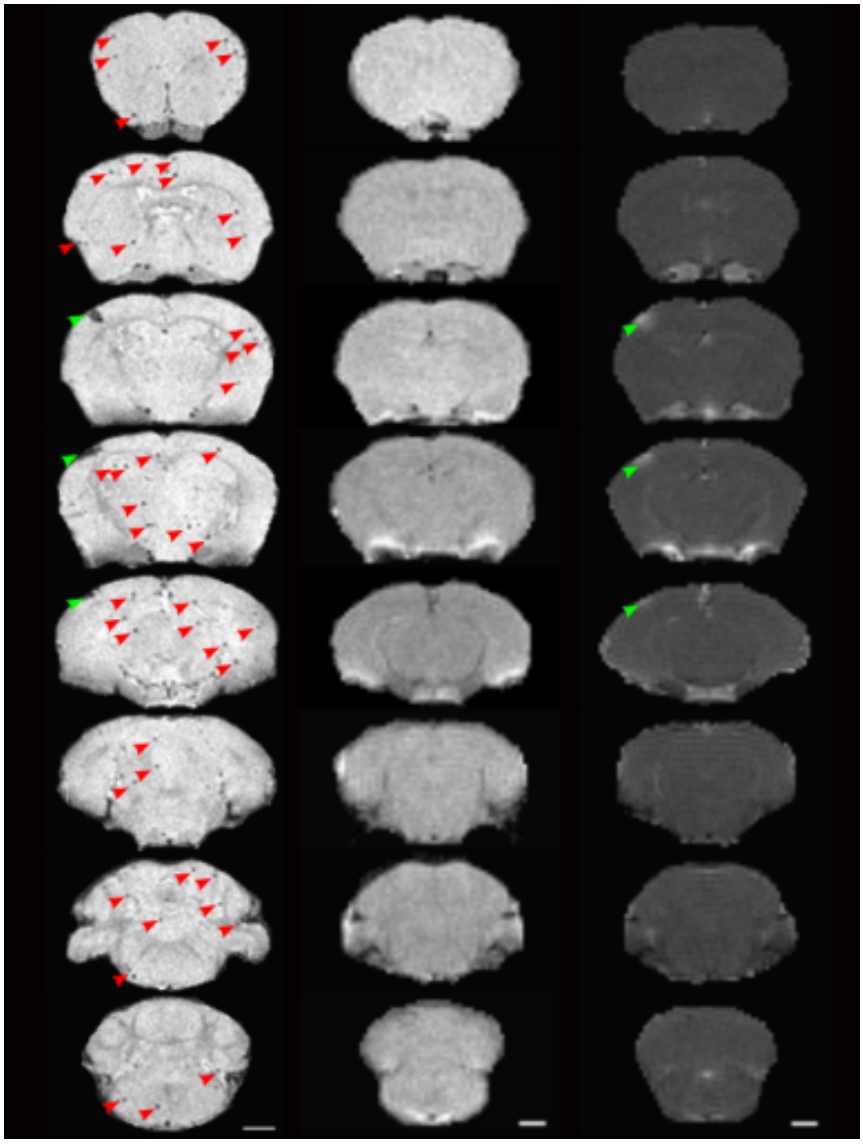


Fig 3.15. Example MRI sequences for a SEBTA-001 metastasis bearing mouse brain. Corresponding images from a mouse brain bearing SEBTA-001 metastases for post-VCAM-MPIO T_2^*-weighted MRI (left column), pre-gadolinium T_1-weighted MRI (middle column) and post-gadolinium T_1-weighted MRI (right column); scale bar = 1.5mm. Gadolinium enhancement confirmed presence of a single large metastasis (green arrow) exhibiting blood-brain barrier breakdown in a mouse brain bearing SEBTA-001 tumours. The presence of additional micrometastases is indicated on the T_2^*-weighted images as multiple focal hypointensities (red arrows), which are not detected on the post-contrast T_1-weighted images.

3.3.5 Assessment of VCAM-1 expression and VCAM-MPIO MRI positivity

Individual brain metastases across all mice were classified according to immunohistochemical detection of VCAM-1 on vessels in proximity to each metastasis. The mean ± S.D. for the number of brain metastases found for each tumour type were as follows: 102 ± 30, 22 ± 6 and 12 ± 5 tumours per animal for MDA231Br-GFP, H1_DL2 and SEBTA-001, respectively. Despite the lower number of SEBTA-001 tumours (Fig 3.16C & 3.16F), some of the individual tumours were considerably larger than either the MDA231Br-GFP or H1_DL2 metastases. In some cases, VCAM-1 expression was observed up to 150 μm from the nearest metastasis.

As shown in Fig 3.16A-C, the majority of tumours were associated with upregulated VCAM-1. For MDA231Br-GFP metastases, overall 89% were VCAM-1 positive, and for tumours above the median volume ($6.5x10^{-4}$μl) 98% were VCAM-1 positive. Similarly, overall 72% of H1_DL2 metastases were VCAM-1 positive, with 84% of tumours greater than the median volume ($1.4x10^{-4}$μl) associated with VCAM-1 expression. For the SEBTA-001 tumours, 93% elicited VCAM-1 upregulation on immunohistochemistry and in the cohort of tumours above the median volume ($2x10^{-4}$μl) 96% were VCAM-1 positive. Even below the median volume, the majority of MDA231Br-GFP and SEBTA-001 metastases were VCAM-1 positive rather than negative (80% *vs.* 20% and 89% *vs.* 11%, respectively). In contrast, below the median volume the percentage of tumours that were VCAM-1 positive *vs.* negative was closer to equal for the H1_DL2 group (60% *vs.* 40%).

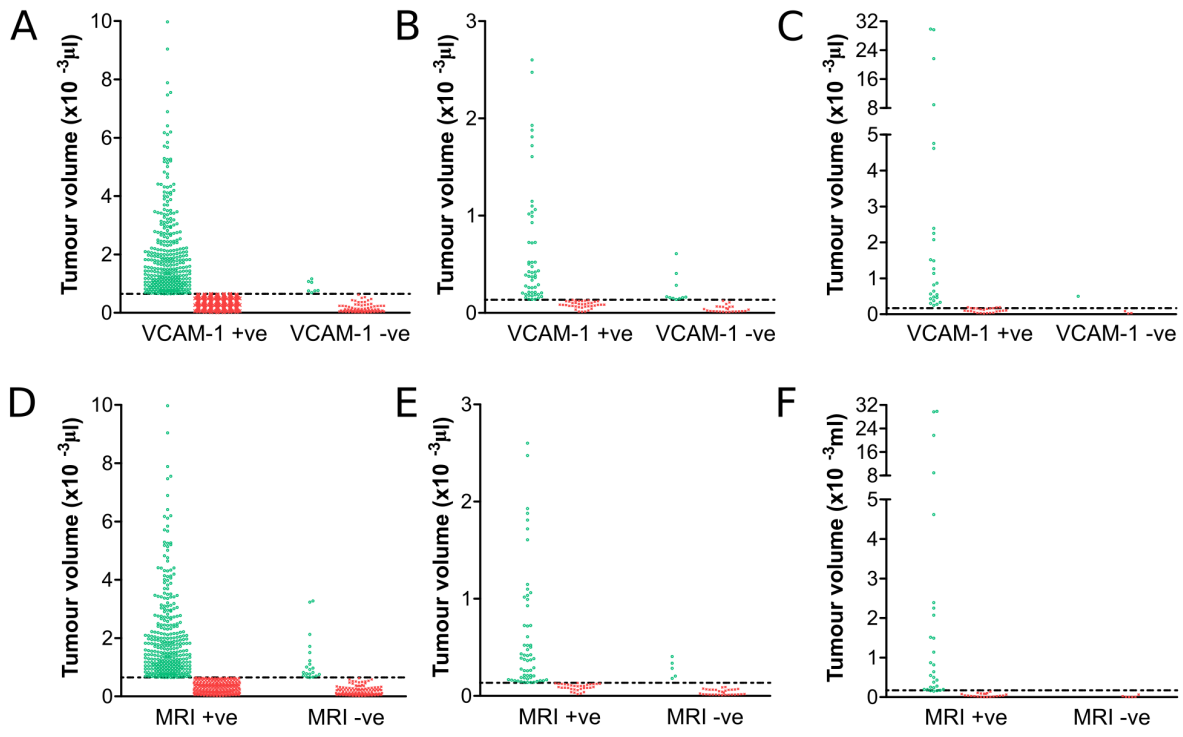


Fig 3.16. VCAM-1 and MRI positivity in relation to tumour volume. (A-C) Scatter plots showing individual VCAM-1 positive and negative tumours above (green ○) and below (red x) the median volume for (A) MDA231Br-GFP, (B) H1_DL2 and (C) SEBTA-001 metastases. (D-F) Corresponding plots indicating metastatic tumours that are hypointensity positive and negative, above (green ○) and below (red x) the median volume, on T2*-weighted MRI following intravenous VCAM-MPIO injection. Dashed horizontal line denotes the median volume for each tumour type.

Individual metastases were also correlated with the T_2^*-weighted MRI to determine the presence of corresponding hypointensities. As shown in Fig 3.16D-F, the majority of metastases corresponded to a hypointense signal on MRI, with 82%, 72% and 89% positivity for the MDA231Br-GFP, H1_DL2 and SEBTA-001 tumours, respectively. Notably, since numerous vessels can be activated to be VCAM-1 positive around a tumour, this can give rise to more than one hypointense foci corresponding to a single metastasis (Fig 3.17). As for VCAM-1 expression, the majority of tumours above the median volume were MRI positive;

94%, 92% and 100% for the MDA231Br-GFP, H1_DL2 and SEBTA-001 tumours, respectively. Again, as for VCAM-1 expression, below the median volume a greater percentage of MDA231BR-GFP and SEBTA-001 metastases were MRI positive (69% *vs.* 31% and 78% *vs.* 22%, respectively), whilst numbers were approximately equal for the H1_DL2 group (52% *vs.* 48%).

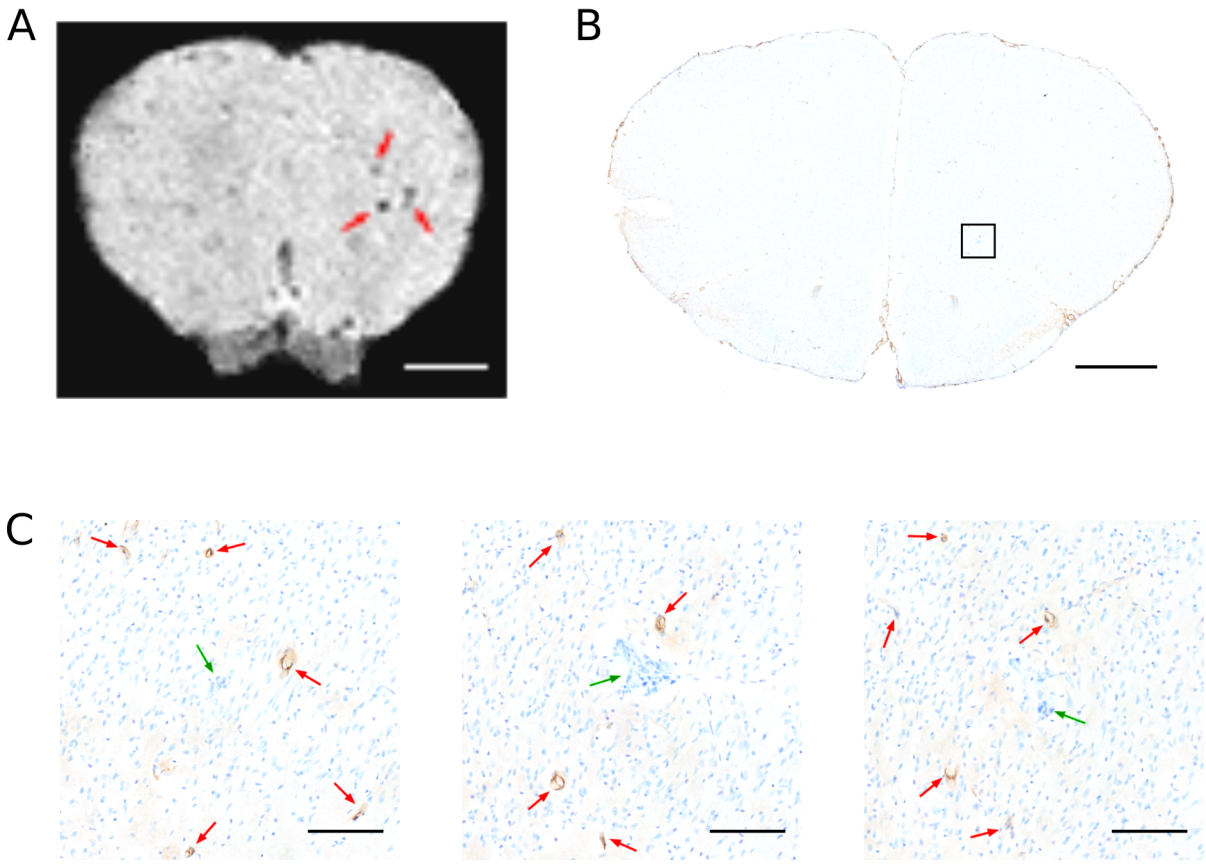


Fig 3.17. VCAM-1 positive vessels around a SEBTA-001 tumour. (A) Axial T_2^*-weighted image slice of a mouse brain following intracardiac injection of SEBTA-001 cells with several hypointensities (red arrows); scale bar = 1.5mm. (B) One corresponding histological section of the same mouse demonstrating a single SEBTA-001 metastasis in this location (black box); scale bar = 1.5mm. (C) Magnified images from alternate sections of the highlighted metastasis showing multiple VCAM-1 activated vessels (red arrows) around the periphery of the tumour (green arrow); scale bar = 100µm.

3.3.6 VCAM-1 expression in human brain metastasis

Immunohistochemistry of image-guided brain metastasis biopsies from human brain showed prominent VCAM-1 expression in the brain parenchyma adjacent to brain metastases from breast carcinoma, lung adenocarcinoma and melanoma in all cases studied. The location of the biopsy specifically targeted the brain-tumour interface and along this edge, small metastatic foci were present corresponding to early stages of invasion. VCAM-1 expression was upregulated along the tumour border and in close association with micrometastatic foci (Fig 3.18A-C). VCAM-1 upregulation was evident predominantly on the endothelium in proximity to the tumour tissue (Fig 3.18D-F).

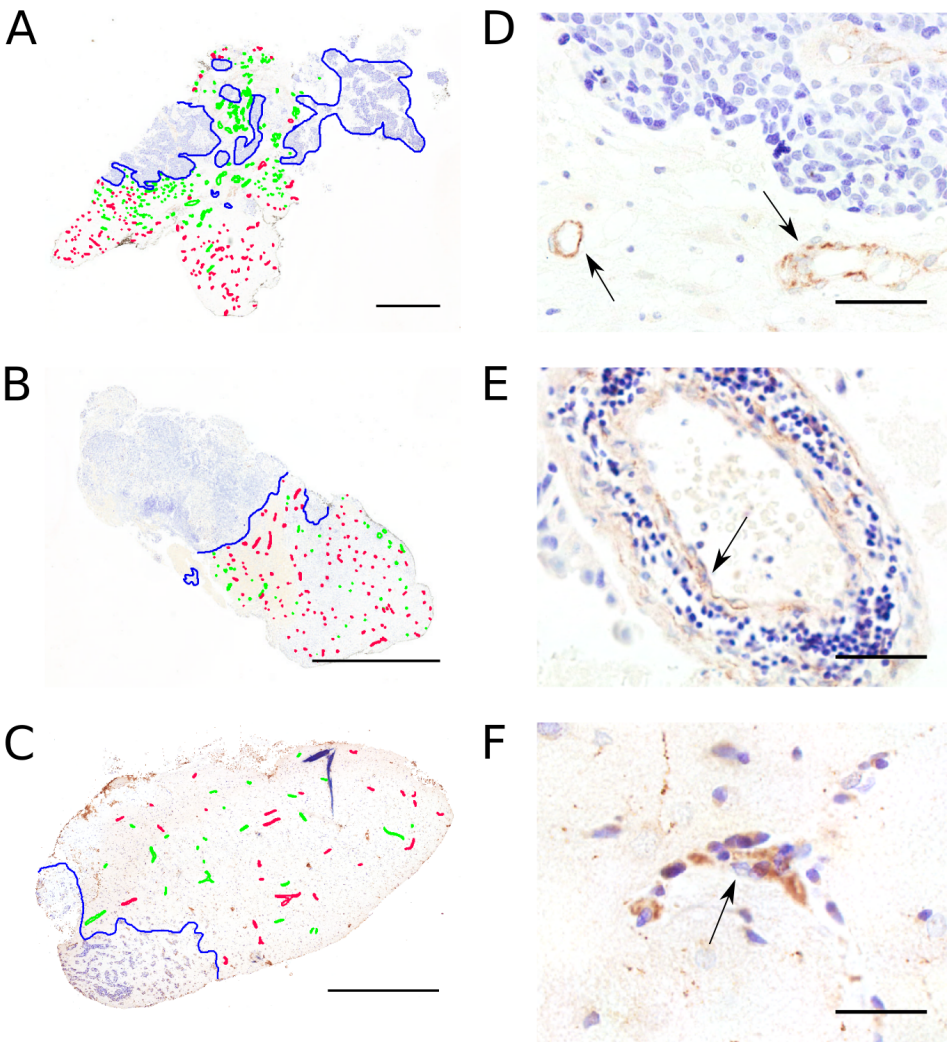


Fig 3.18. Expression of endothelial VCAM-1 in human brain metastasis biopsies. Representative immunohistochemical images from human brain metastasis biopsies of (A) breast carcinoma, (B) lung adenocarcinoma and (C) melanoma stained for VCAM-1 (brown). Blue denotes tumour border, green indicates VCAM-1 positive vessels and red indicates VCAM-1 negative vessels; scale bar = 1mm. (D-F) Higher magnification images demonstrating upregulation of VCAM-1 on vessels (brown) near to the tumour border of the corresponding tumours. Arrows indicate VCAM-1 positive vessels; scale bar = 50μm.

3.4 Discussion

Brain metastasis is an increasing clinical burden, as cancer patients survive extracranial disease owing to improved systemic anti-cancer treatment (137, 138), and earlier diagnosis is critical. In this study, we have shown that a targeted contrast agent with specific binding to VCAM-1 enables detection of brain micrometastases below the limits that conventional clinical methods (passive gadolinium enhancement) allow. Importantly, using *in vivo* models of brain metastases for breast cancer, melanoma and lung adenocarcinoma, we have demonstrated that VCAM-1 targeted MRI is applicable for the detection of micrometastases in the brain in multiple primary tumour types. Breast cancer, melanoma and non-small cell lung cancer, including lung adenocarcinoma, currently comprise almost 80% of brain metastasis diagnoses.

3.4.1 Pre-clinical models of brain metastases from different primary tumour types

The MDA231Br-GFP (subclone of metastatic human breast carcinoma) cell line and the H1_DL2 (human brain metastasis-derived melanoma) cell line have previously been shown to have specific tropism to the brain when injected intracardially *in vivo* (58, 139). The SEBTA-

001 cell line is derived from a human brain metastasis of lung adenocarcinoma origin and has only been maintained in *in vitro* cell culture previously (140). As previously discussed in Section 1.4.1, selection of an appropriate animal model is a vital step in the experimental process. The advantage of xenograft models is the ready abundance of human cancer cells that can be used to generate tumours derived from different primary cancers, when engrafted into an animal host. However, successful tumour engraftment through avoidance of immune rejection requires the use of an immunocompromised host. Since, VCAM-1 in its physiological role is known to mediate immune surveillance through facilitation of leucocyte trafficking, it was important to establish whether an immunocompromised model organism would display defective VCAM-1 expression. The localised activation of VCAM-1 following direct introduction of the pro-inflammatory cytokine, IL-1β, into the brain of immunocompromised mice confirmed the suitability of the SCID animal model for these experiments. Furthermore, previous studies have reported similar levels of VCAM-1 expression between immunocompromised and immunocompetent mice (58, 141).

To test the viability of the tumours in the environment of the brain parenchyma, I used intracerebral models of brain tumour development by direct injection of tumour cells into the striatum. This method provided a means to reliably deliver a consistent quantity of tumour cells into the brain and, alongside the lack of extracranial metastases, ensured that an assessment of intracerebral tumour growth dynamics and its impact on the host was feasible. Graft survival in the brain is one of the determinants of the ability of tumour cells disseminated via the circulation to colonise this organ. Furthermore, the rate of tumour growth provides an indication as to the timepoints required for the intracardiac model. Thus, the intracerebral tumour model development served to provide vital information about the tumour

characteristics that permitted rapid optimisation of the intracardiac tumour models, in keeping with the principles of the 3Rs (73). The observation that the SEBTA-001 tumour cells had a slower growth rate *in vivo* compared to the MDA231Br-GFP and H1_DL2 cells was in keeping with the lack of prior conditioning of this cell line in the brain microenvironment. The observation of gadolinium contrast enhancement on T_1-weighted MRI provided an assessment of the likely tumour burden required to cause BBB disruption.

Injection of tumour cells into the left cardiac ventricle under ultrasound guidance is a well-characterised method of inducing brain metastases in animal models (18). This approach successfully recapitulates the conditions under which tumour cells are haematogenously transported to a distant organ and results in widely disseminated synchronous brain metastases. Significantly, the brain metastasis growth dynamics suggested a period of time following tumour cell inoculation where there was low tumour burden for all three tumour types. This provided a suitable window for testing the VCAM-1 targeted MRI, as in this period micrometastatic disease was present but the low tumour burden was unlikely to induce BBB breakdown.

Since mouse brain is not equivalent to human brain, the pattern of dissemination observed throughout the brain following intracardiac injection may not be fully representative of human brain metastasis. However, it is known that metastases can present both cortically and sub-cortically in the human brain, and to this extent the model reflects the human condition. Moreover, the presented data demonstrate that micrometastases can be detected anywhere within the brain using the VCAM-targeted approach. This work has recapitulated previous studies with the MDA231Br-GFP and H1_DL2 cell lines, and has further demonstrated the

ability of the SEBTA-001 cell line to induce brain metastases when injected intracardially in the mouse. In all cases, an increase in tumour burden was evident over time, together with marked VCAM-1 upregulation from the earliest time-points.

3.4.2 Endothelial VCAM-1 upregulation in association with micrometastases

More than 70% of metastases showed upregulated VCAM-1 expression selectively on nearby vasculature, supporting the concept that targeting VCAM-1 is a good strategy for detecting brain micrometastases. Moreover, VCAM-1 expression in the micrometastatic stages was shown to be independent of primary tumour type, thus supporting the broad clinical applicability of this diagnostic approach. Importantly, as a protein present on the endothelial lining, VCAM-1 provides an attractive surrogate marker for early micrometastatic disease that exploits changes in the metastatic microenvironment, in spite of an undisrupted blood-brain barrier.

The observation that VCAM-1 activated vessels are present outside the immediate confines of the tumour periphery (up to *ca.* 150µm from a nearby metastasis) means that a hypointensity focus does not give a precise location for the metastasis with which it is associated. This apparently distant activation may represent a loco-regional inflammatory reaction stimulated by the tumour metastasis, for example through an immune-mediated cytokine release or indeed the presence of another metastasis out of plane. Consequently, local and focussed therapy may not be possible on the basis of the VCAM-targeted approach. Nevertheless, this method has a major strength in assessing the overall metastatic burden within the brain and for informing on the application of systemic therapies that can target disseminated disease.

In one recent study, it was shown that adjuvant systemic treatment, with either targeted therapy or immunotherapy, improves the median overall survival by over 8 months for patients with melanoma brain metastases treated upfront with SRS for definitive local control (142). Thus, evidence is emerging that intervention with systemic therapies in microscopic disease will be most effective in the pre-symptomatic stage. With the arrival of new generation targeted drug therapies and immunotherapies, detection of micrometastatic disease may expand the therapeutic options for patients, leading to reduced morbidity and mortality.

The current imaging gold standard for detecting brain metastases is MRI with gadolinium contrast enhancement. The effectiveness of gadolinium-based contrast is limited to detecting metastases of sufficient size for the BBB to have become compromised; in experimental models, this typically occurs in tumours more than 500μm in diameter (35), whilst human metastases must be 2 to 5mm in diameter before they become visible by MRI (135). In this study, with the exception of one experimental subject with a large SEBTA-001 metastasis, no animals demonstrated contrast enhancement on T_1-weighted MRI following intravenous gadolinium-DTPA injection.

3.4.3 Pre-clinical application of VCAM-1 targeted MRI to detect brain micrometastases

Superparamagnetic iron oxide particles produce a contrast effect through distortion of the magnetic field, resulting in local field inhomogeneities that are detectable via T_2^*-weighted MRI (143). By targeting VCAM-1 with MPIO, I have shown that it is possible to detect brain micrometastases before they are visible on conventional gadolinium-enhanced MRI across *in*

vivo models of breast cancer, melanoma and lung adenocarcinoma. A significant proportion of tumours found histologically could be co-localised to a corresponding hypointense signal on MRI, and the percentages of MRI-positive metastases (82%, 72% and 89% for breast, melanoma and lung, respectively) and VCAM-1-positive metastases (89%, 72% and 93%, respectively) were in close accord. The smallest detectable micrometastasis was approximately 50μm in diameter. Improvements in the T_2^*-weighted MRI used in this study, from a gradient echo 3D (GE3D) sequence to a multi-gradient echo 3D (MGE3D) sequence (144), has significantly increased contrast-to-noise ratios compared to earlier studies (94), thus increasing the sensitivity to signal hypointensities caused by MPIO.

In the larger metastases (greater than median volume) the majority of tumours were both VCAM-1 and MRI positive in all models, supporting the sensitivity of this marker for early detection; it should be noted that these tumours are still considerably smaller (median tumour size *ca.* 1×10^3 cells) than the current level of detection that is possible clinically (*ca.* 1×10^7 cells) (94). Moreover, even below the median volume, the majority of metastases in the MDA231Br-GFP and SEBTA-001 models were both VCAM-1 and MRI positive, whilst *ca.* 50% of the H1_DL2 tumours were associated with endothelial VCAM-1 expression and corresponding MRI detection. Thus, although there is likely to be a size limit below which a VCAM-1 targeted approach is less reliable, these tumours will still become detectable using VCAM-1-targeted MRI much earlier than through conventional gadolinium-enhanced imaging.

Minimal contrast effects were evident in any of the control cohorts, indicating the high specificity of the VCAM-1 targeted approach. Variation in the hypointensity volume for naïve animals injected with VCAM-MPIO may be accounted for by low levels of non-specific VCAM-

1 upregulation. However, no significant signal disruption compared to the other control cohorts was evident in these mice, indicating that any constitutive expression will not markedly reduce the sensitivity of VCAM-MPIO MRI for tumour detection.

Immunohistochemistry of co-registered image-guided biopsies of human brain metastasis confirmed the upregulation of VCAM-1 in tumour-associated blood vessels for all three main primary tumour types in all samples assessed. In particular, small metastatic foci present at the tumour edge, representing the invasive edge of the tumour, were closely associated with VCAM-1 positive vessels. These invasive edge metastatic foci can be considered to be analogous to early micrometastatic disease (145), which is not readily accessible in human post-mortem tissue. Although the spatial resolution achievable in mice is considerably higher than is currently possible clinically it has been extrapolated, based on detection limits observed in non-clinical field strengths for mice and measurements from normal human brain using common clinical resolutions at 3T, that metastases of greater than or equal to 300µm in diameter should be detectable clinically with this approach (94).

3.4.4 Clinical potential of VCAM-1 targeted MRI for the detection of brain micrometastases

Ideally, the chosen biomarker, VCAM-1, would only be present on vessels that are stimulated by proximity to malignancy. However, it is known that CAMs, including VCAM-1, may be upregulated on the cerebral vasculature by a host of inflammatory diseases, for example multiple sclerosis (146), infection (147) and stroke (148). Nevertheless, where “at risk” primary cancer patients are being assessed with this approach, the probability that intracranial VCAM-1 expression reflects metastatic involvement rather than an alternative pathology is greatly increased. At the same time, it is expected that the spatial presentation

of VCAM-1 upregulation would be substantially different depending on the underlying cause and, therefore, the 3-dimensional information afforded by MRI would substantially offset the potential confounds of alternative diseases. Moreover, gadolinium contrast enhancement, the current clinical gold standard, is also not specific to malignancy; diagnostic uncertainty between a cerebral abscess, metastatic tumour or primary malignancy is not uncommon for a solitary enhancing lesion on T_1-weighted MRI (149).

The transition from bench-to-bedside is anticipated to lead to three key clinical improvements: (i) identification of discrete clinical problems where VCAM-targeted MRI will aid clinical decision making between the use of local *vs* systemic therapies; (ii) screening of high risk populations to identify micrometastatic disease, which will inform intervention based upon existing systemic paradigms; and (iii) building sufficient lead time to allow testing of new therapeutic approaches specific to brain micrometastatic disease.

Targeted brain metastasis screening, for a defined 'at risk' population of asymptomatic patients to identify subclinical disease, would represent a major paradigm shift in the management of cancer patients. As an example, for patients with limited stage small cell lung cancer (SCLC), prophylactic cranial irradiation (PCI) has been shown to not only reduce the risk of brain metastasis forming, but it also improves both overall survival and disease-free survival (150). However, there is a growing body of concern that some patients may experience unnecessary harm from adverse effects of PCI exposure, where there is minimal risk of future intracranial relapse (151). Detection of micrometastatic disease using VCAM-MPIO MRI would allow stratification of patients into a susceptible group likely to derive benefit from prophylactic treatment strategies and those who should remain under observation.

Moreover, emerging strategies for drug delivery that overcome the BBB, for example through its permeabilisation with tumour necrosis factor-α (133), vasoactive substances such as bradykinin (152) or ultrasound-generated microbubbles (153), will expand the role of systemic agents for managing brain metastases. Coupling such approaches with a diagnostic method that widens the therapeutic window by detecting micrometastatic disease, which is more likely to respond to systemic agents, may significantly improve survival in lung cancer, breast cancer and melanoma patients with subclinical brain metastases.

Perez-Balderas *et al* have recently developed a biodegradable multimeric MPIO (mMPIO) (154) to enhance the safety profile of the targeted contrast agent for human use. The mMPIO have the additional advantage of exhibiting approximately three times greater T_2 relaxivities compared to commercially available polystyrene-coated MPIO; thus, potentiating the contrast effect in human application (154). As a widely accessible technology in modern medicine with broad patient acceptability, MRI remains an ideal diagnostic tool for neuro-oncological imaging. Therefore, the minimal adaptations required for application of VCAM-1 targeted imaging to existing infrastructure will prove advantageous for its onwards clinical translation.

CHAPTER 4: VCAM-1 TARGETED MAGNETIC RESONANCE IMAGING TO CHARACTERISE THE INVASIVE BORDER OF BRAIN METASTASIS

4.1 Introduction

Tumour cell invasion into the surrounding tissue parenchyma is the single biggest reason why local therapies, such as surgery and targeted radiotherapy, fail to stop cancer from returning. As previously discussed in section 1.1.2, invasion is one of the hallmarks of cancer and is thought to be related to genetic changes that alter the phenotype of the malignant cell towards a dedifferentiated state that more closely resembles a stem cell-like state, through epithelial-mesenchymal transition (EMT). Notably, as these changes result from the acquisition of somatic mutations, the cells that have the greatest invasive potential form a subset population within a heterogeneous tumour.

As tumour cells invade normal tissue stroma, through the release of proteolytic enzymes and pro-inflammatory soluble factors, they initiate changes in the local milieu and adapt it into a distinct tumour microenvironment (TME). A prime example of this is vascular remodelling, as cytokines and growth factors released by infiltrating immune cells and directly by tumour cells, incite angiogenesis and increased vascular permeability (155-157). These changes, besides facilitating the survival and dissemination of the tumour, also cause negative sequelae for the host tissue with loss of function due to disruption of the normal tissue architecture. One direct manifestation of this abnormal vasculature is the presence of peritumoural vasogenic oedema. Within the brain, vasogenic oedema can have particularly devastating consequences owing to the fixed space of the encasing cranium and the associated raised intracranial pressure means

that affected patients present with debilitating symptoms of headache, visual disturbance, vomiting and altered consciousness (158).

Due to the challenge of penetrating the blood-brain barrier (BBB), systemic anti-cancer agents such as chemotherapies, which are the current mainstay treatment option for disseminated cancers, are largely ineffective against brain metastases. Therefore, in amenable tumours, local therapies such as surgery and focal radiotherapy remain the preferred options, particularly as they minimise the risk of adverse effects to the normal brain tissue. Surgical debulking is usually indicated in patients with a single brain metastasis in an accessible region, particularly for large tumours that are causing significant mass effect or are compressing eloquent areas of the brain. Moreover, this treatment modality is preferred for patients with good pre-morbid functional status and where the extracranial disease is limited or controlled (37, 159). One advantage of tumour resection is the immediate alleviation of neurological deficits caused by a compressive mass.

Focal radiotherapy may be delivered as either single dose stereotactic radiosurgery (SRS), such as Gamma Knife or Cyberknife, or fractionated stereotactic radiotherapy (FSRT), given as conformal radiotherapy. Both forms of radiotherapy result in a high dose of radiation being precisely directed to the tumour, to concentrate the treatment dose to the malignant cells, whilst sparing normal tissue. SRS has been shown to provide improved local control of tumours over the previous standard of whole brain radiotherapy (WBRT). Despite this improvement, it is important to consider potential serious complications such as radionecrosis, tissue death caused by radiation, the risk of which rises as the total brain volume treated is increased (160). Based on this evidence, the UK NHS Commissioning Board, in its policy of SRS

for brain metastases, has set an upper limit of 20cm^3 for total brain volume that may be treated in this way, which is equivalent to a single metastasis with a diameter of 3.2cm (41). For tumours ≥3cm in diameter or those in proximity to critical brain structures, where single fraction high dose SRS is not suitable due to associated toxicity, FSRT offers an equivalent degree of local control compared to SRS (40, 161-163). Previous studies have failed to establish a superior clinical benefit between surgical excision and SRS in the local control of brain metastases, however focal radiotherapy is particularly indicated for smaller multifocal tumours, not causing overt symptoms and that are located deeply within the brain.

Despite the availability of local therapies, their success is predicated on the ability to capture all the tumour cells, since any residual disease will lead to a future relapse. Indeed, whilst surgical resection and focal radiotherapy are known to be effective in controlling localised disease, there remains a significant proportion of patients who subsequently develop local in-brain progression. In the landmark EORTC 22952-26001 study, it was found that even after adjuvant WBRT was delivered to patients treated with local therapies approximately 27% and 19% of patients relapsed at the initial site within two years following either surgery or SRS, respectively (164). This finding suggests that undetected residual disease is a major problem that contributes to disease recurrence in the brain following local treatments. Therefore, the decision to treat with local therapies and the choice of modality is dependent on having a clear understanding of the location of the tumour and the extent of the disease.

In clinical practice, there have been attempts to overcome this issue, for example neurosurgeons build in a margin of resection. For brain metastasis, whilst surgical resection represents the best opportunity for clearing a single lesion or a single cluster of metastases, if

a tumour lies close to an eloquent area of the brain or near a critical structure such as the brainstem then this is not possible. For focal radiotherapy, including stereotactic radiosurgery such as Gamma Knife, the oncologist defines the tumour bulk in the gross tumour volume (GTV) based on visible tumour on imaging, usually guided by MRI that is subsequently co-registered with the CT planning scan. Furthermore, a planning target volume (PTV) is built in as a margin for uncertainties in planning and delivery of the radiotherapy (165, 166).

At present, the application of the surgical resection margin and the focal radiotherapy field remains the greatest unknown quantity in treatment planning for patients. As this region represents tissue that may contain microscopic disease, it is usually poorly defined with existing imaging techniques. Attempts to account for the invasive margin have typically relied on historical post-mortem series, which means that it is not individualised to the patient. Therefore, the clinician must make a judgement on the size of the margin that balances the effective control of subclinical disease to prevent recurrence against potential harm to the patient through damage to, or removal of, normal tissue. Consequently, the size of this margin is applied inconsistently in practice. Moreover, it has previously been shown that there is a significant degree of inter-observer and inter-institutional variation when contouring the gross tumour bulk of brain metastases for stereotactic radiosurgery (167, 168).

The prevailing view of brain metastases is that they exist as well-circumscribed lesions embedded within the brain parenchyma, with little invasion into the surrounding parenchyma (169). Historical studies have demonstrated that some intracerebral metastases are surrounded by a dense desmoplastic reaction, termed the glial pseudo-capsule, which is caused by activation of astrocytes and microglial. This stromal response has been used by

surgeons as a demarcating border for macroscopic removal of the tumour bulk, also known as gross total resection (GTR). The desmoplastic reaction may also account for the sharp delineation of the tumour border on neuroimaging, commonly seen with brain metastases. However, more recent autopsy studies have shown that the interaction between the tumour and the adjacent brain parenchyma is less distinct than was previously thought, as the majority of tumours display an infiltrative pattern of growth (170-172).

The ability to differentiate between malignancy and uninvolved brain tissue in treatment planning is heavily dependent on non-invasive imaging. As previously discussed, MRI offers superior anatomic characterisation and soft tissue contrast compared to CT or PET imaging. Nevertheless, there are still major limitations in the ability of standard gadolinium-enhanced MRI to delineate the tumour border and attempts to improve the resolution of MRI to detect the invasive margin is an ongoing area of research. Much of existing research in the hunt for appropriate imaging biomarkers of the tumour invasive margin has focused on intrinsic brain tumours, in particular glioblastoma due to its highly infiltrative nature. Previous imaging studies have attempted to use techniques such as diffusion tensor imaging (DTI) to detect disruption of the white matter tracts by infiltrating tumour cells (173, 174), MR spectroscopy for cellular metabolism (175, 176) and perfusion changes with relative cerebral blood volume (rCBV) measurements (177, 178). Nevertheless, despite promising results from these newer imaging parameters, the challenge in detecting mild tumour infiltration remains. Moreover, the dearth of evidence available for metastatic brain disease highlights the need for better imaging markers of the tumour margin for brain metastases.

In this chapter, I will seek to identify ways of using MRI to detect the invasive margin of brain metastases. Using human MRI data, human brain metastasis biopsies and orthotopic xenograft rat models, I will test the following hypotheses:

1. Multi-parametric MRI enables the detection of the tumour margin using human MRI data;
2. Human brain metastases induce increased VCAM-1 expression in the endothelial cells by the invasive margin;
3. The tumour invasive front is biologically distinct from the tumour core and the uninvolved brain in xenograft models of primary and secondary brain cancer; and
4. VCAM-1 targeted MRI enables the detection of the tumour margin in intrastriatal rat models of glioma and breast cancer.

4.2 Methods

4.2.1 Human brain MRI image analysis

MR images of human brain with metastatic disease from either breast cancer (n = 3), lung adenocarcinoma (n = 5) or melanoma (n = 4) were acquired as previously described (Section 2.2.9) by colleagues at The Walton Centre NHS Foundation Trust. Where available, Digital Imaging and Communications in Medicine (DICOM) images relating to post-gadolinium T_1-weighted and diffusion weighted sequences were selected for analysis.

Post-gadolinium T_1-weighted DICOM images were analysed using ImageJ and four specific ROIs were marked at the location of the tumour biopsy based on the tumour core, tumour rim, adjacent brain parenchyma and contralateral striatum (Fig 4.1). The mean grey pixel intensity was measured. Diffusion weighted DICOM images were accessed using DTIstudio. As

illustrated in Fig 4.2, the DWI data were converted into an apparent diffusion coefficient (ADC) map using a pre-defined low angular gradient table. Based on the map, ADC values were measured using the same four specific ROIs, as previously mentioned.

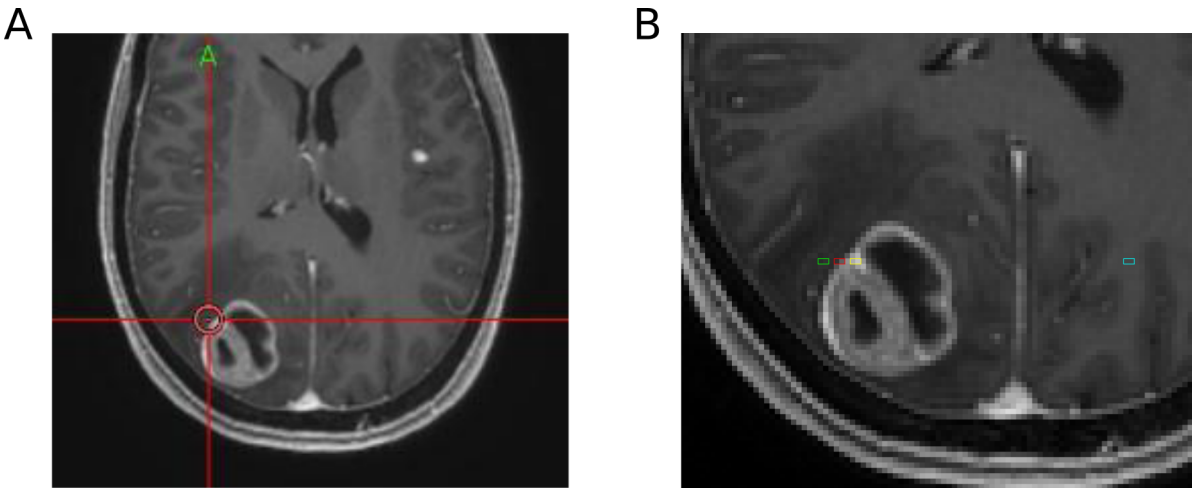


Fig 4.1. Method for analysing post-gadolinium T_1-weighted human MR images. (A) An example post-gadolinium T_1-weighted axial MR image of a human subject demonstrating a right occipital enhancing lesion, in keeping with a melanoma brain metastasis. The red marker indicates the site of the stereotactic biopsy, which was collected under image guidance, as described by Zakaria (120). (B) Specific regions of interest, marking the tumour core (yellow rectangle), tumour border (red rectangle), adjacent parenchyma (green rectangle) and contralateral brain (cyan rectangle), were used to measure the mean grey pixel intensity corresponding to the biopsy location.

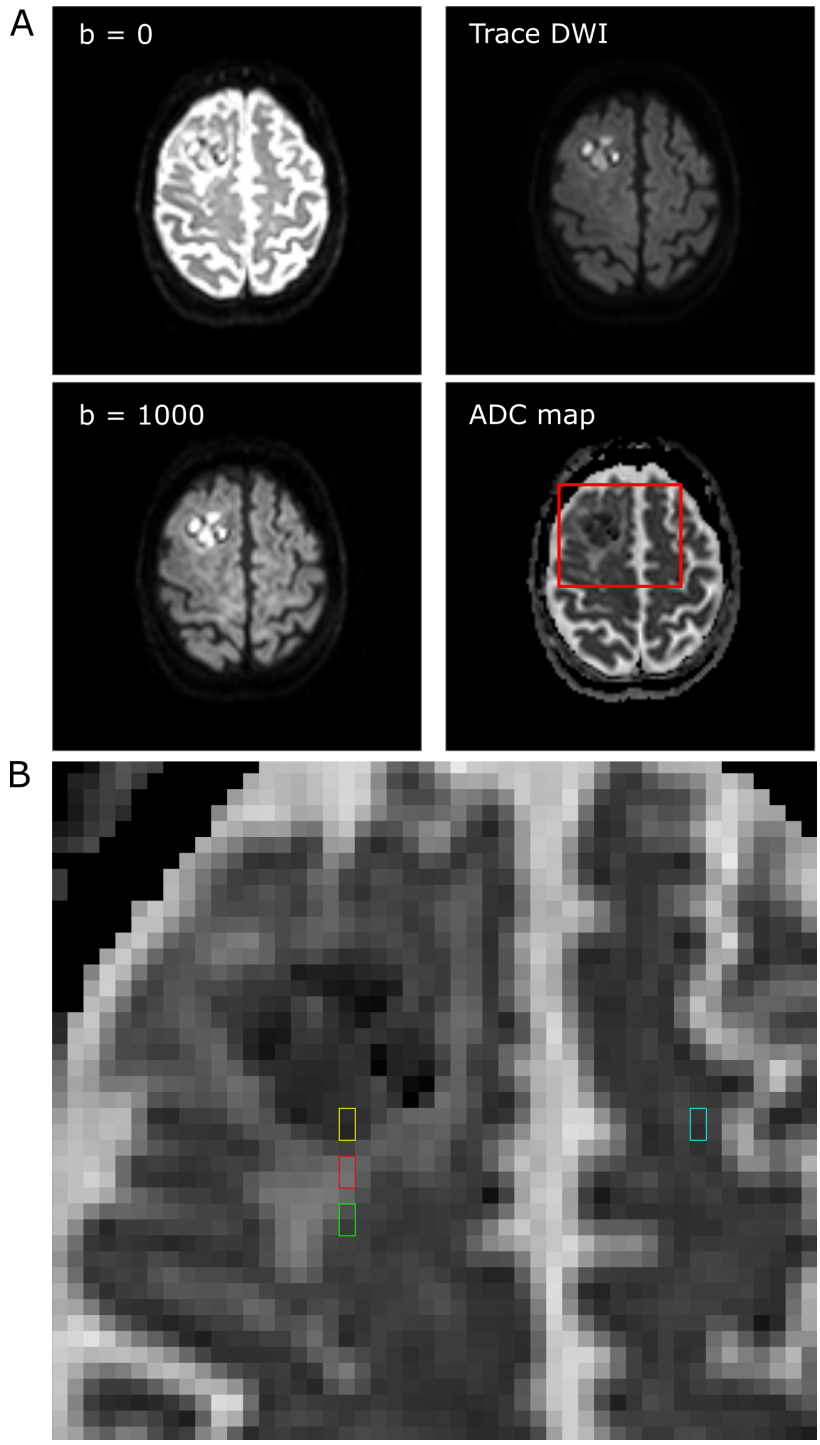


Fig 4.2. Method for analysing diffusion-weighted human MR images. (A) Example diffusion-weighted axial MR images of a human subject demonstrating a right frontal enhancing lesion, in keeping with a lung adenocarcinoma brain metastasis. Images were taken at b = 0 and 1000s/mm^2. A trace diffusion-weighted image (DWI) was calculated as the mean of the various gradients and from this an apparent diffusion coefficient (ADC) map was derived. (B) At the site of the tumour

(red box), specific regions of interest, marking the tumour core (yellow rectangle), tumour border (red rectangle), adjacent parenchyma (green rectangle) and contralateral brain (cyan rectangle), were used to measure the ADC values corresponding to the biopsy location.

4.2.2 Immunohistochemistry: Human tissue

Formalin-fixed paraffin embedded (FFPE) samples, from biopsies of human breast cancer, lung adenocarcinoma and melanoma brain metastasis, were sectioned and prepared as previously described (Section 2.2.3). Deparaffinised 6μm-thick sections were immunohistochemically stained for markers to define the tumour cells (CAM5.2 for breast cancer and lung adenocarcinoma; melan-A for melanoma), endothelium (CD31) and endothelial VCAM-1 expression. Stained tissue sections were digitally scanned on the Aperio CS2 machine, at x40 magnification, with the images stored offline for analysis.

The digital images were visualised using Imagescope software and manually annotated to highlight the following regions of interest (ROIs): tumour and VCAM-1 positive vessels. To determine the relationship between endothelial VCAM-1 activation and proximity to tumour, standard 100μm x 100μm square ROIs were randomly dispersed across the expanse of the brain parenchyma and the number of VCAM-1 positive vessels within each ROI was quantified, expressed as positive vessels per mm^2. Fig 4.3 demonstrates the methodology for quantification of endothelial VCAM-1 expression. Microvessel density was quantified based on number of CD31 stained vessels within three specified ROI of peri-tumoural brain: within 500μm, between 500μm to 1mm, or more than 1mm distance from the tumour border.

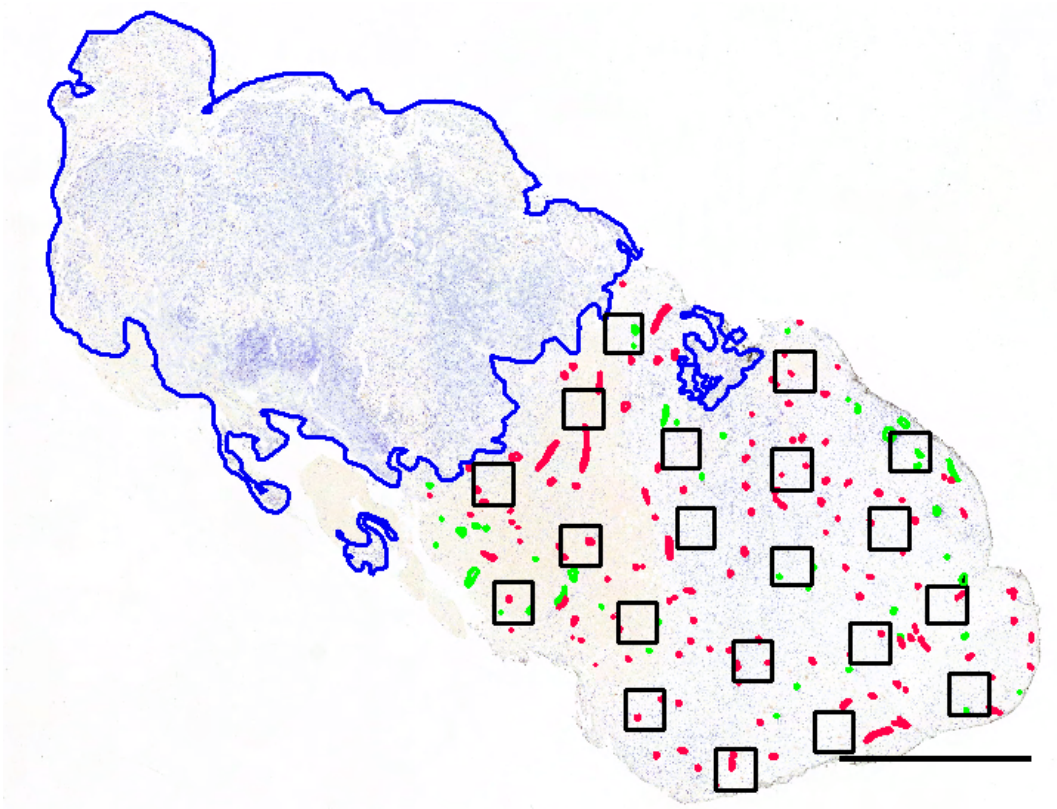


Fig 4.3. Method for quantification of peri-tumoural VCAM-1 positive vessel **distribution.** Example histological section of a human brain metastasis biopsy that has been immunohistochemically stained for VCAM-1 expression. Annotations denote the following regions of interest (ROI): tumour (blue), VCAM-1 positive vessels (green) and VCAM-1 negative vessels (red). 200µm by 200µm square ROIs (black square) were randomly dispersed on the peri-tumoural brain. Proportion of VCAM-1 stained blood vessels within each square ROI was quantified and measured from the tumour border. Scale bar = 1mm.

4.2.3 Intrastriatal tumour models

Male RNU rats, aged 10 to 12 weeks old, were intracerebrally injected with either 5 x 10^3 MDA231Br-GFP or U87 cells in 0.5µL sterile PBS into the left striatum, see Fig 4.4 for experimental schedule (Section 2.2.4.5). Another group of animals were intracerebrally injected with PBS, to serve as a control cohort. At 28 days after tumour cell or PBS inoculation

the animals underwent MRI, as detailed in Section 5.2.2. The animals were sacrificed following imaging, by transcardial perfusion with 0.9% heparinised saline and fixation with PLP light under terminal anaesthesia. Animal brains were collected and cryopreserved, before tissue sectioning of the striatum and storage at -80°C.

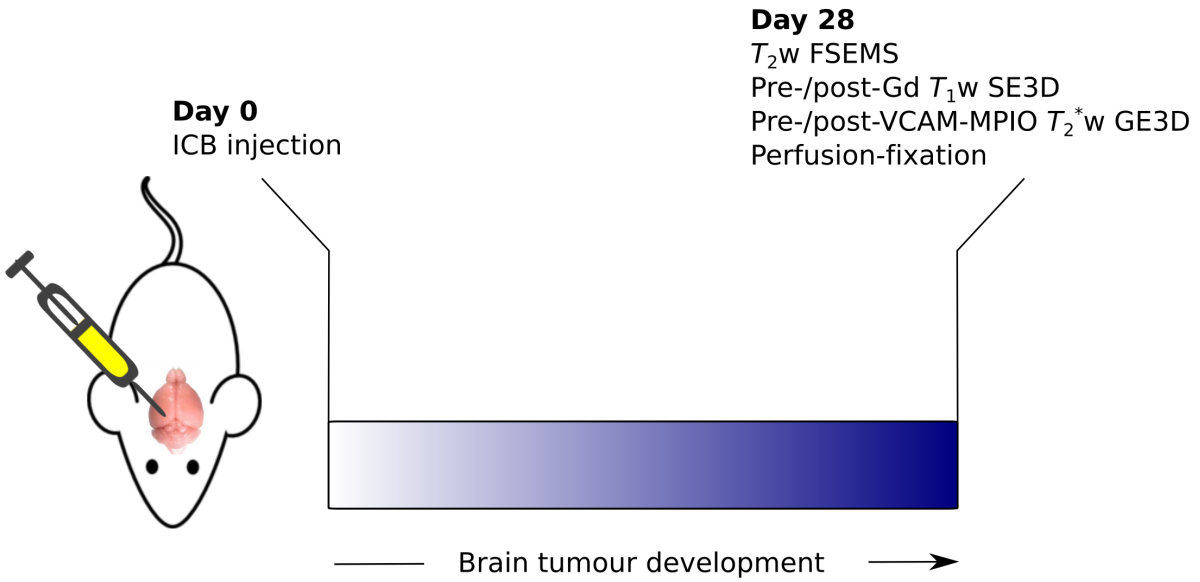


Fig 4.4. Experimental schedule for rat brain imaging of intrastriatal tumours. Schedule of animal experiments, starting with injection of tumour cells or sterile PBS vehicle into the left striatum of RNU rat brains. At 28 days after tumour induction, animals underwent multi-parametric MRI – 2D T_2-weighted fast spin echo multi-slice (FSEMS), pre-VCAM-MPIO T_2^*-weighted 3D gradient echo (GE3D), pre-gadolinium (Gd) T_1-weighted 3D spin echo (SE3D), followed by administration of VCAM-MPIO/IgG-MPIO then repeat T_2^*-weighted GE3D, and finally Gd administration before T_1-weighted SE3D. Animals were sacrificed after imaging by perfusion-fixation and their brains were harvested for histological examination.

4.2.4 *In vivo* MRI

Animals that had received intrastriatal injections were imaged at 28 days after the procedure on a 9.4T MRI spectrometer (section 2.2.8.2). Prior to imaging, an intravenous cannula was inserted into the lateral tail vein, allowing for administration of MPIO, conjugated with either anti-VCAM-1 or mouse isotype control IgG antibodies (4-7 animals per tumour group; 3 animals per PBS group) and then gadolinium for sequential imaging sequences. For each animal, T_2, T_2^* and T_1-weighted images were collected to assess anatomical structure, VCAM-MPIO binding and BBB permeability, respectively (Section 2.2.8.2). Each image dataset was saved offline for further analysis, as outlined in Section 2.2.8.3.

4.2.5 Immunohistochemistry: Rat tissue

Rat brain sections (*ca*. 8 per animal) were immunohistochemically stained for markers to define the tumour cells (Vimentin), endothelium (CD31), endothelial VCAM-1 expression, tumour cell stemness (nestin, SOX2) and cellular proliferation (Ki67); see Section 2.2.3.4. Stained tissue sections were digitally scanned on the Aperio CS2 machine, at x20 magnification, with the images stored offline for analysis.

The digital images were visualised using Imagescope software and manually annotated to highlight the following regions of interest (ROIs): tumour core, defined as 90% of the tumour bulk, excluding any brain parenchyma; tumour rim, defined as the remaining tumour periphery, including a margin of adjacent brain parenchyma within 200μm from the edge of the tumour core; and the contralateral striatum. Fig 4.5 shows an example of how these three ROIs were delineated. Using the in-built Positive Pixel Count v.9 algorithm, all medium and strong intensity brown pixels (Intensity threshold between 0 to 174, intensity threshold of

negative pixels = -1, colour saturation threshold = 0.04, Hue width = 0.5) were summed for each section and divided by the total area of the corresponding ROI to determine the relative staining of each marker, reported as number of positive pixels per mm^2.

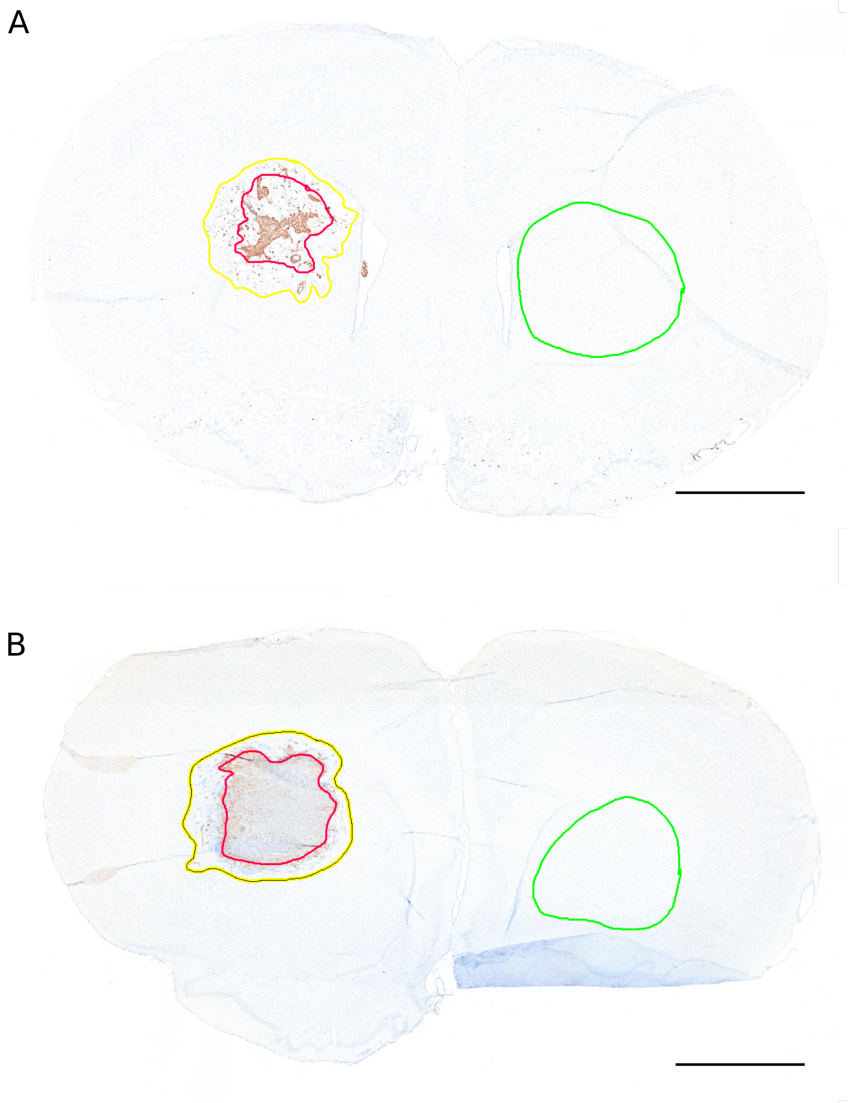


Fig 4.5. Annotation of specific regions of interest in rat brain slices with intrastriatal tumours. Example histological sections from RNU rats intrastriatally injected with (A) MDA231Br-GFP or (B) U87 tumour cells. Tumour cells have been immunohistochemically stained to highlight human vimentin expression (brown colour). Specific regions of interest were annotated by free hand to delineate the tumour core (red), the tumour rim (yellow) and the contralateral striatum (green). Scale bar = 2mm.

4.2.6 Statistical analysis

A repeated measures one-way analysis of variance (ANOVA) test was used to test differences in either grey pixel intensity or ADC value between the tumour core, tumour border, adjacent brain parenchyma and contralateral brain. A multiple comparisons test with Bonferroni correction was used post-hoc to detect individual differences between groups, if overall significance was detected. The same test was applied on analysis of microvessel density according to distance from tumour edge in human brain metastases and immunohistochemical marker expression in rat brain tumours.

For rat brain immunohistochemistry corrected by tumour cell density, Student t-tests were used to measure differences in Ki67, nestin or SOX2 expression between the tumour core and rim. The relationship between distance from tumour edge and endothelial VCAM-1 positivity was assessed by linear regression. A two-way ANOVA test was used to measure differences in hypointensity volume between the left and right striatum and between the VCAM-MPIO and the control cohorts (IgG-MPIO and PBS only) assessment of VCAM-MPIO MRI. Bonferroni post-hoc tests were performed to compare replicate means by row. Finally, a Bland-Altman analysis was performed to determine consistency of tumour dimensions measured on VCAM-MPIO MRI compared to either gadolinium contrast enhanced MRI or T_2-weighted MRI.

All statistical tests were performed two-sided with a significance level of 0.05. Measures of central tendency and dispersion are reported as mean $\pm$ standard deviation, unless otherwise stated.

4.3 Results

4.3.1 Defining the brain metastasis-brain interface on human MRI

Each of the human subjects included in this study had a single lesion in the supratentorial region of the brain, arising from either a breast cancer, lung adenocarcinoma or melanoma primary. Based on T_1-weighted imaging, the mean gross tumour volume was measured as 12.77 ± 9.5mL, 4.71 ± 4.3mL and 14.34 ± 3.8mL for the breast cancer, lung adenocarcinoma and melanoma brain metastases, respectively (n = 3 per group). The low tumour volume of the lung adenocarcinoma brain metastases is largely accounted for by the significant cystic component of each lesion.

An overall significant difference was evident in the grey pixel intensity, measured between the tumour core, tumour border, adjacent brain parenchyma and contralateral brain, in post-gadolinium T_1-weighted images for subjects with breast cancer ($p = 0.0008$) and melanoma ($p = 0.0057$) brain metastasis (Fig 4.6). However, post-hoc analysis revealed that whilst differences were apparent between the tumour core and unaffected brain for both tumour types and between the tumour core and the adjacent brain parenchyma for breast cancer alone, there was no detectable difference at the border of the tumour compared to the adjoining brain tissue in either tumour type. For lung adenocarcinoma brain metastases, no significant difference was detected across the brain metastasis-brain parenchyma (BM-BP) interface and the unaffected brain. The general trend, particularly for breast cancer and melanoma brain metastases, is a reduction in grey pixel intensity from the tumour core to the periphery. However, the reverse trend is present for lung adenocarcinoma brain metastases, with a gradual increase in grey pixel intensity moving towards the peri-tumoural region, which may reflect the cystic nature of these tumours.

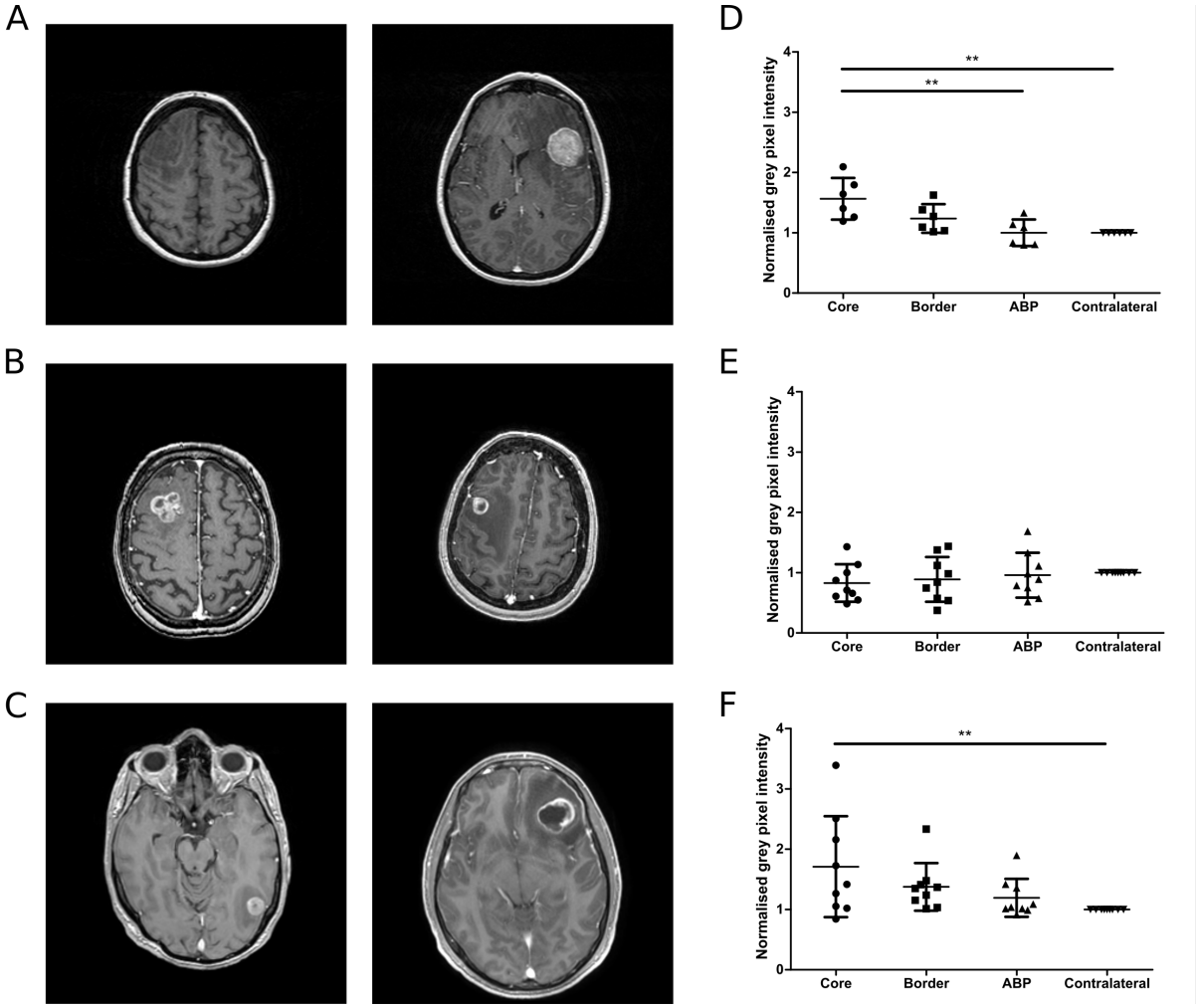


Fig 4.6. Contrast enhancement across the brain metastasis-brain parenchyma interface in human MRI. Representative images of post-gadolinium T_1-weighted axial slices of human subjects with brain metastasis from (A) breast cancer, (B) lung adenocarcinoma and (C) melanoma. Graphs showing the grey pixel intensity at the tumour core, border and adjacent brain parenchyma (ABP) with values normalised to the contralateral brain for (D) breast cancer, (E) lung adenocarcinoma and (F) melanoma brain metastases (n = 4 subjects per group). Each data point represents a single biopsy; mid-line and whiskers represent mean and standard deviation, respectively (**p<0.01).

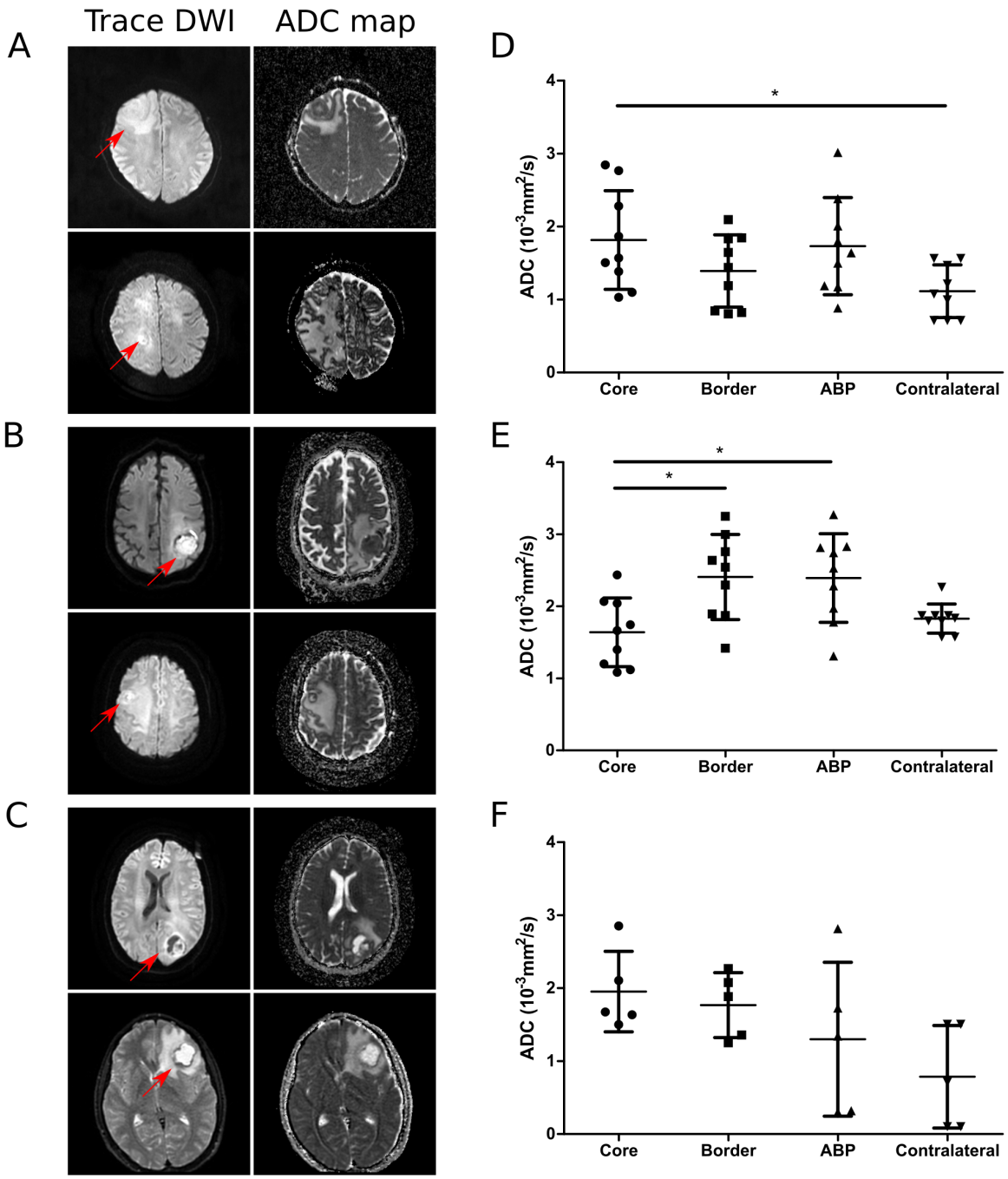


Fig 4.7. ADC values across the brain metastasis-brain parenchyma interface in human MRI. Representative images of trace DWI axial slices and corresponding ADC maps of human subjects with brain metastases (red arrow) from (A) breast cancer, (B) lung adenocarcinoma and (C) melanoma. Graphs showing the ADC value at the tumour core, border, adjacent brain parenchyma (ABP) and contralateral brain for (D) breast cancer, (E) lung adenocarcinoma and (F) melanoma brain metastases (n = 4 subjects per group). Each data point represents a single biopsy; mid-line and whiskers represent mean and standard deviation, respectively (*$p<0.05$).

Conversely, with the diffusion-weighted imaging, a significant difference was noted in the ADC values between the tumour core and the peri-tumoural regions of the tumour border and the adjacent brain parenchyma, for lung adenocarcinoma brain metastases ($p = 0.008$), see Fig 4.7. Breast cancer brain metastases also showed an overall significant difference in ADC values ($p = 0.0227$), although post-hoc analysis showed that individual differences between groups were only apparent when the tumour core ADC was compared to the contralateral brain ADC. Meanwhile, in the melanoma brain metastasis cohort no significant difference was evident between the various locations along the BM-BP interface. There was no consistent pattern in distribution of ADC values, across the four regions of interest, between the different tumour types. For breast cancer and melanoma, the general trend appeared to be a reduction in ADC values from the tumour core to the adjacent brain parenchyma. However, the lung adenocarcinoma metastases seemed to show a rise in ADC between the tumour core and the tumour border, which along with the adjacent brain parenchyma had a high ADC value compared to the contralateral brain.

4.3.2 Endothelial VCAM-1 distribution in the peri-tumoural region of human brain metastasis

Microvessel density in the peri-tumoural brain was heterogeneous across the different primary tumour types (Fig 4.8). The mean number of vessels per mm^2 was quantified as 92.8 $\pm$ 53.9 for breast cancer, 70.3 $\pm$ 35.5 for lung adenocarcinoma and 42.2 $\pm$ 23.1 for melanoma. Moreover, assessment of the vascular distribution showed that there was no statistical difference in the microvessel density within the peri-tumoural brain according to distance from the tumour border, for any of the tumour types.

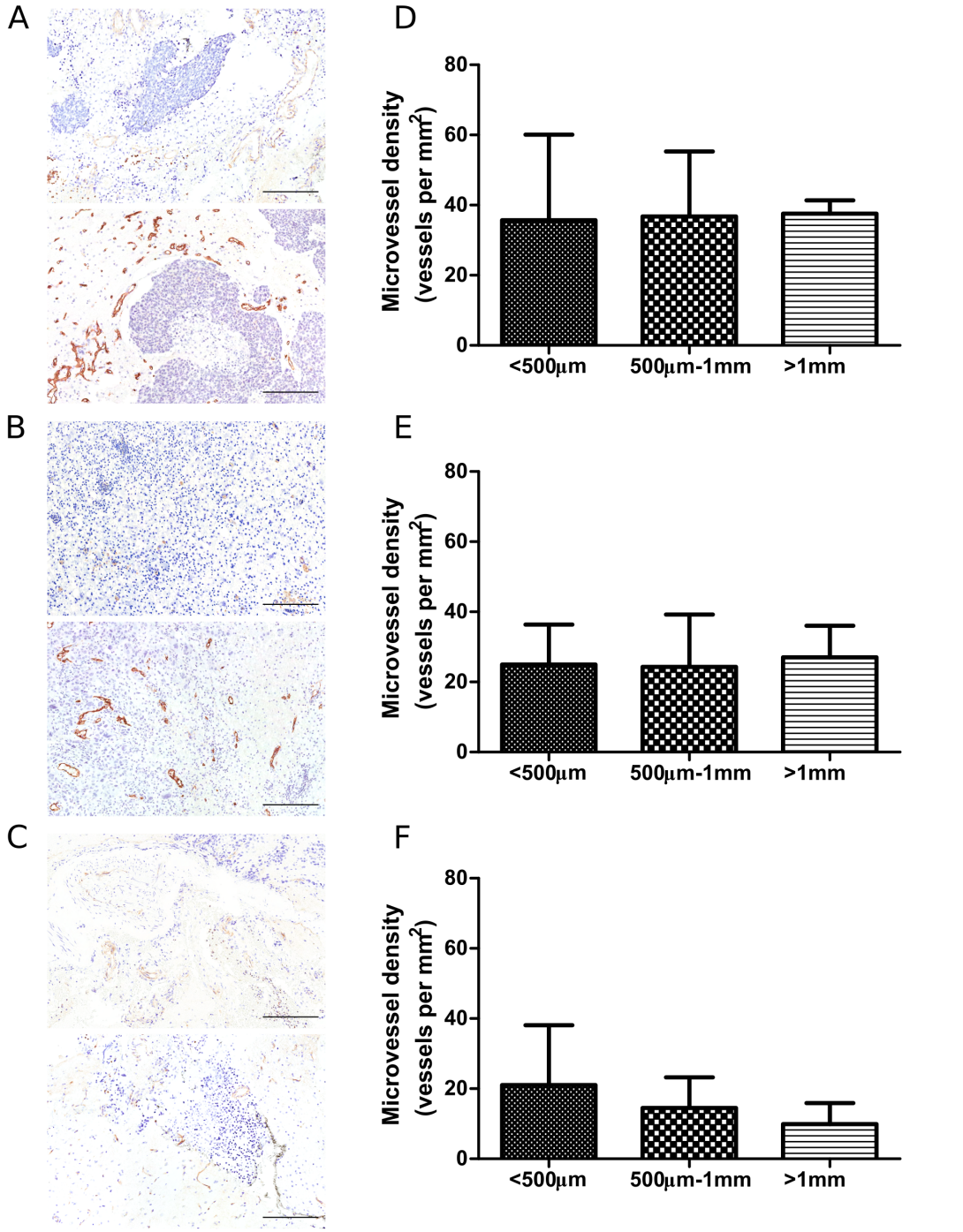


Fig 4.8. Peri-tumoural microvessel density in human brain metastases. Representative histological images of human brain metastasis samples for (A) breast cancer (n = 10 biopsies), (B) lung adenocarcinoma (n = 9 biopsies) and (C) melanoma (n = 12 biopsies), which have been stained for the cell surface antigen, CD34 (brown colour), a marker for endothelial progenitor and endothelial cells. Scale bar = 200µm. Graphs showing the density of microvessels at different

regions of the peri-tumoural brain, according to distance from tumour border, for (D) breast cancer, (E) lung adenocarcinoma and (F) melanoma brain metastases.

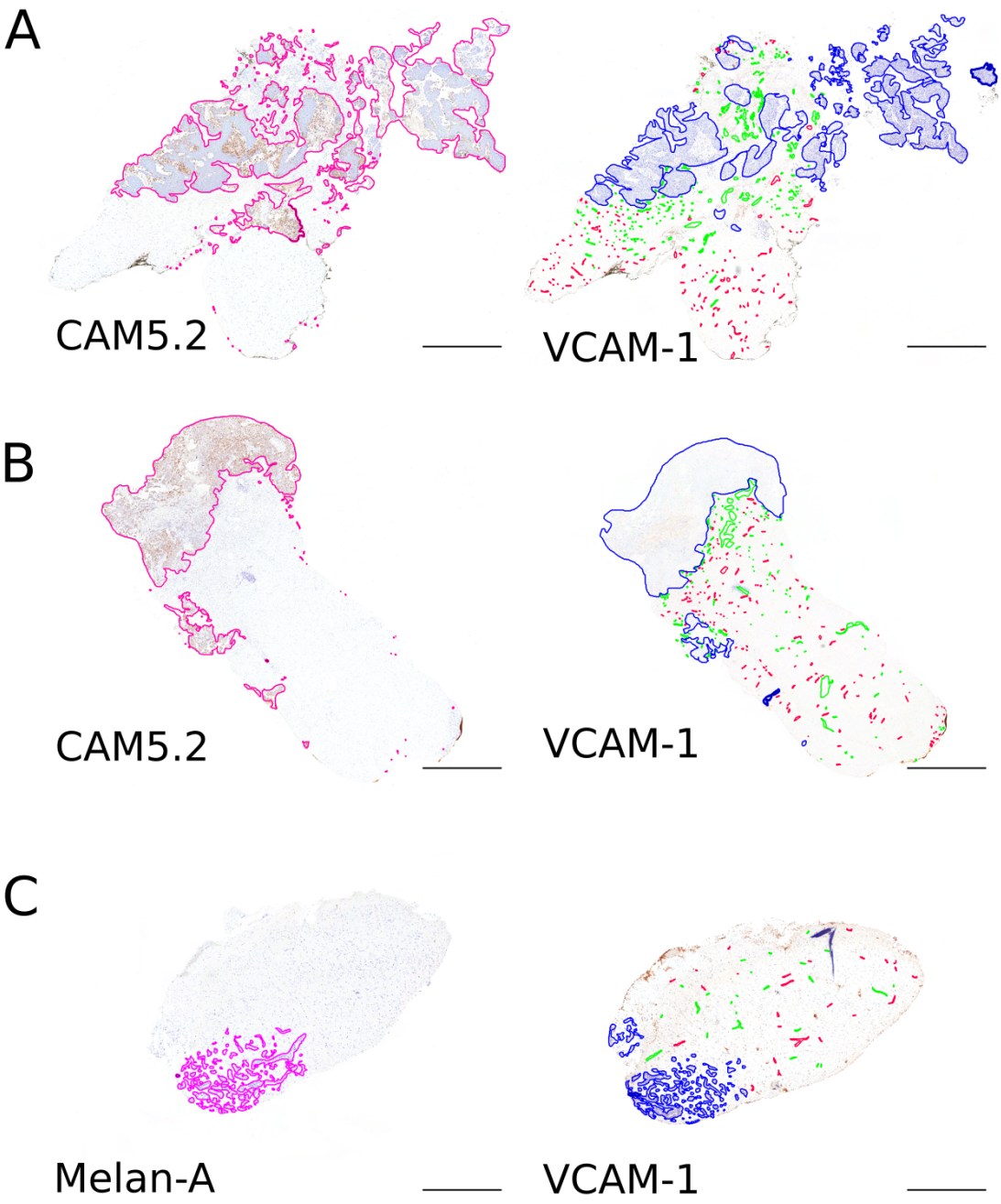


Fig 4.9. Assessment of vessel distribution in relation to human brain metastasis tumour. Representative histologic sections that have been stained for tumour-specific stains: CAM5.2 for (A) breast cancer and (B) lung adenocarcinoma brain metastases, and melan-A for (C) melanoma brain

metastasis. Cells expressing the corresponding tumour-specific marker (brown colour) have been outlined (pink) in the middle column; scale bar = 1mm. Adjacent tissue sections were examined for VCAM-1 expression (brown colour), with tumour (blue), VCAM-1 positive vessels (green) and VCAM-1 negative vessels (red) annotated; scale bar = 1mm.

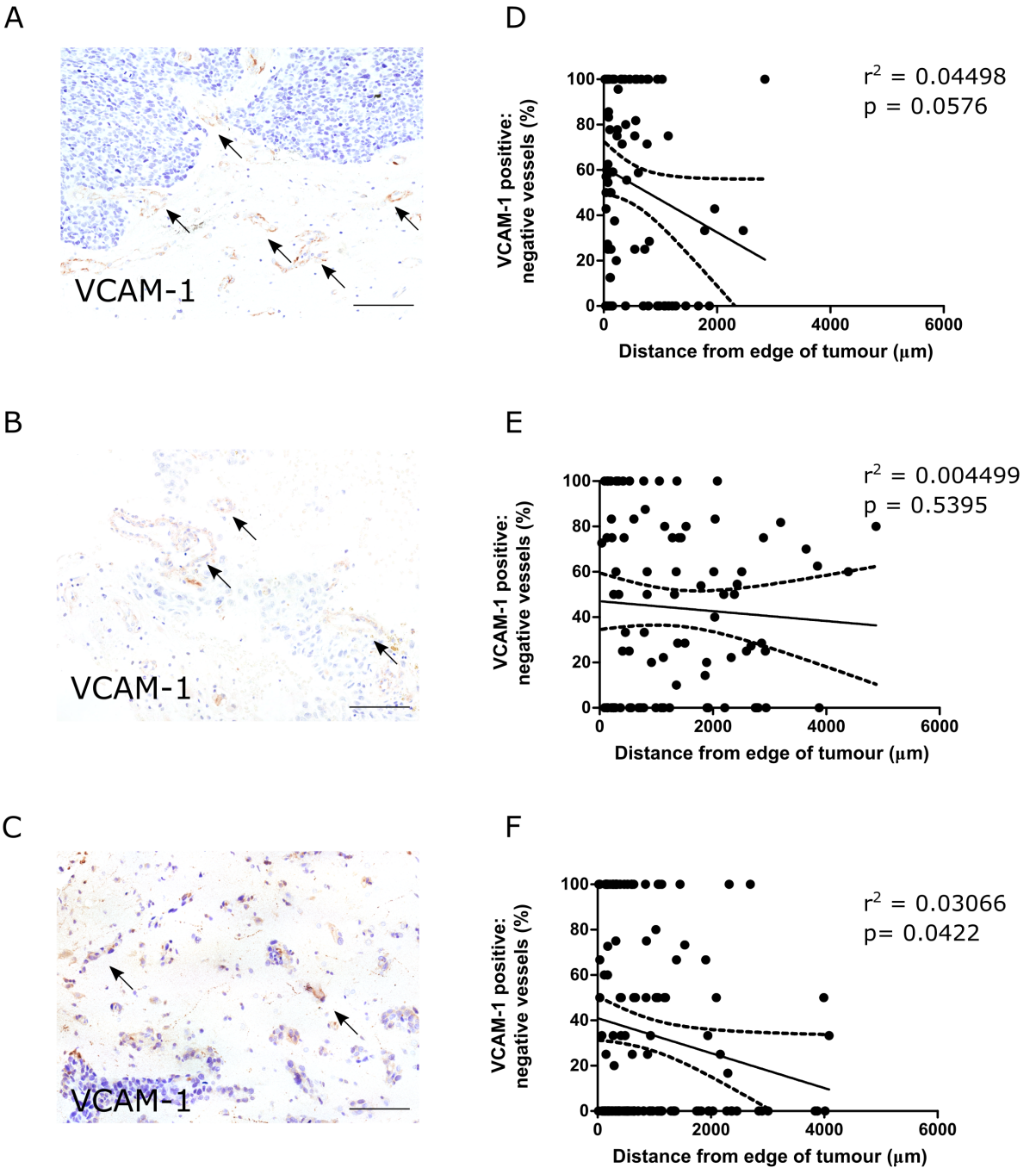


Fig 4.10. Peri-tumoural VCAM-1 positive vessel distribution in human brain metastases. Representative histologic sections that have been stained for VCAM-1 for (A) breast cancer and (B) lung adenocarcinoma brain metastases, and melan-A for (C) melanoma brain metastasis. VCAM-1 positive vessels (black arrow) are shown in proximity to the leading edge of the tumour; scale bar = 100μm. Scatter plots show the relationship of VCAM-1 positive vessel density to distance from the tumour border for (D) breast cancer (n = 10 biopsies), (E) lung adenocarcinoma (n = 9 biopsies) and (F) melanoma (n = 12 biopsies); linear regression line shown with 95% confidence intervals. Each data point represents a single 200μm x 200μm ROI in the peri-tumoural brain.

Analysis of the endothelial VCAM-1 distribution showed that generally a greater concentration of VCAM-1 positive vessels was located within 2mm of the tumour border compared to beyond 2mm. Where VCAM-1 expression was visible further than 2mm from the tumour border, adjacent sections stained for tumour specific markers revealed isolated tumour cells or tumour clusters nearby (Fig 4.9). In the melanoma brain metastasis samples, there was a statistically significant inverse relationship between the concentration of VCAM-1 positive vessels and the distance from the tumour border ($p = 0.0422$). Whilst the breast cancer and lung adenocarcinoma brain metastasis samples did show a similar correlation they did not reach statistical significance, although for breast cancer brain metastasis there was a trend towards significance ($p = 0.0576$). These findings are illustrated in Fig 4.10. Of note, the maximum length of the peri-tumoural region of the biopsy varied between the tumour types, measured at 3.29mm for breast cancer, 5.88mm for lung adenocarcinoma and 4.37mm for melanoma biopsy samples.

4.3.3 Tumour biology at the invasion front in pre-clinical models

Based on intracerebral xenograft models of breast cancer, MDA231Br-GFP, brain metastasis and primary glioblastoma, U87, tumour, the marker expression profile of tumour cells and the adjoining brain parenchyma was interrogated by immunohistochemistry. In terms of vascular characteristics, a significant difference in median microvessel density was evident between the tumour core, tumour rim and contralateral brain regions for both tumour types ($28.85 \pm 7.8 \times 10^{-2}$ pixels/mm^2 *vs.* $70.64 \pm 31.7 \times 10^{-2}$ pixels/mm^2 for MDA231Br-GFP and U87 tumours, respectively), see Figs 4.11H and 4.12H. Moreover, there was a highly significant difference in the microvessel density at the tumour rim compared to either the tumour core or the contralateral brain. In contrast, whilst VCAM-1 expression was qualitatively greater at this location, owing to wide variation between samples, this only achieved statistical significance in the MDA231Br-GFP tumours when measured between the tumour rim and the contralateral brain.

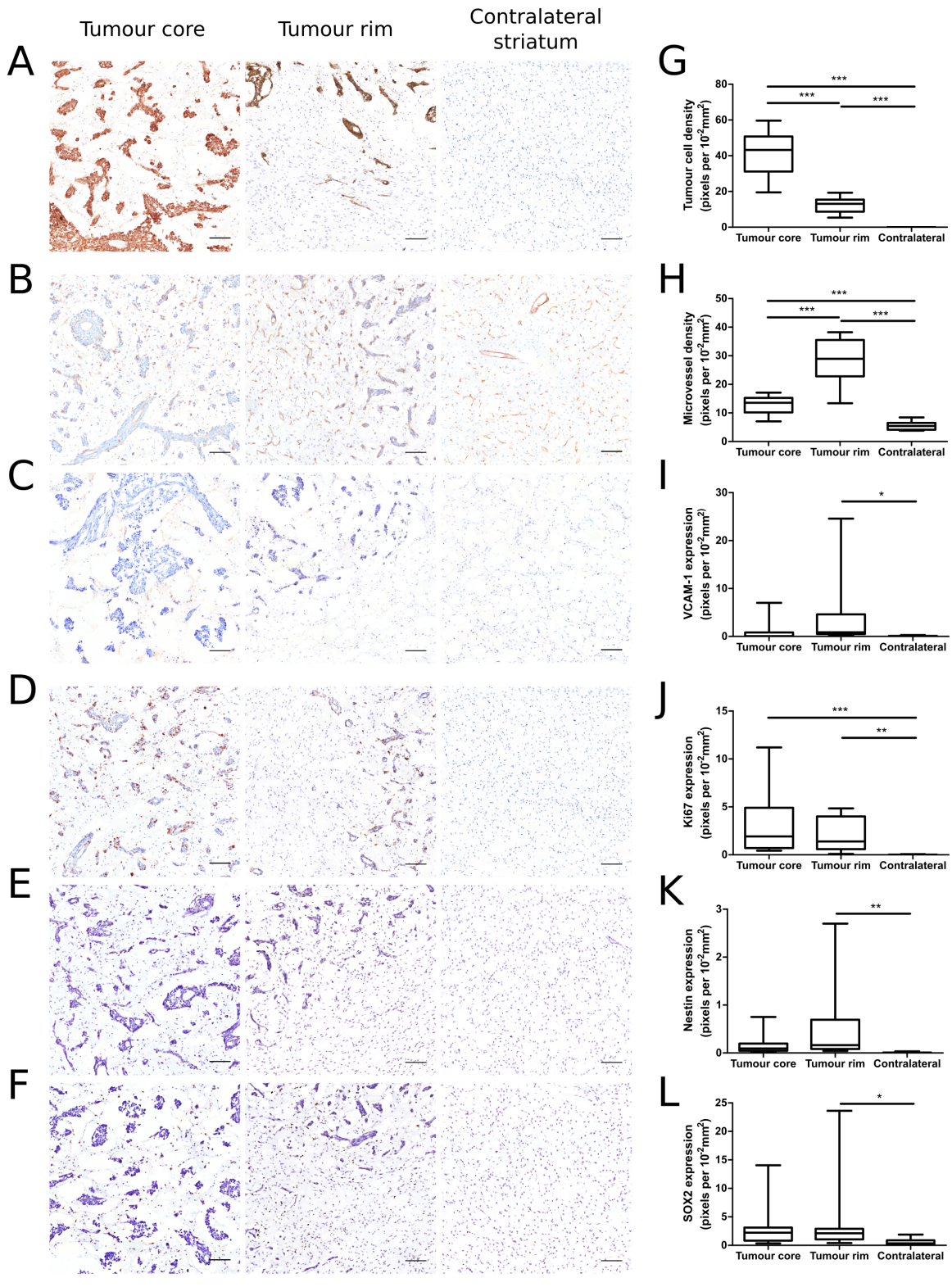


Fig 4.11. Histological examination of intrastriatal MDA231Br-GFP tumours. Representative histologic sections of rat brains with intrastriatal MDA231Br-GFP tumours, examined for (A) vimentin, (B) CD31, (C) VCAM-1, (D) Ki67, (E) nestin and (F) SOX2 expression. Expression of the forementioned

markers were partitioned according to location at the tumour core, the tumour rim or the contralateral striatum. Scale bar = 20µm. (G-L) Box and whisker plots illustrating marker expression relative to the area of each region of interest (*p<0.05; **p<0.01; ***p<0.001). Whiskers indicates min and max values; box denotes median ± interquartile range.

Minimal Ki67 expression in the contralateral brain suggests a low basal proliferative rate within the normal brain parenchyma. Assessment of tumour cell proliferation revealed that median absolute expression of Ki67 was similar between the tumour core and the tumour rim for MDA231Br-GFP (1.55×10^{-2} pixels/mm^2 *vs.* 1.26×10^{-2} pixels/mm^2) and U87 (10.23×10^{-2} pixels/mm^2 *vs*. 9.22×10^{-2} pixels/mm^2) tumours. However, when corrected for tumour cell density, there was a relative increase in the median Ki67 expression of 60.2% and 32.35%, from the tumour core to the rim, for MDA231Br-GFP and U87 tumours, respectively; although this rise was only significant for MDA231Br-GFP tumours ($p = 0.0476$), as illustrated in Fig 4.13A.

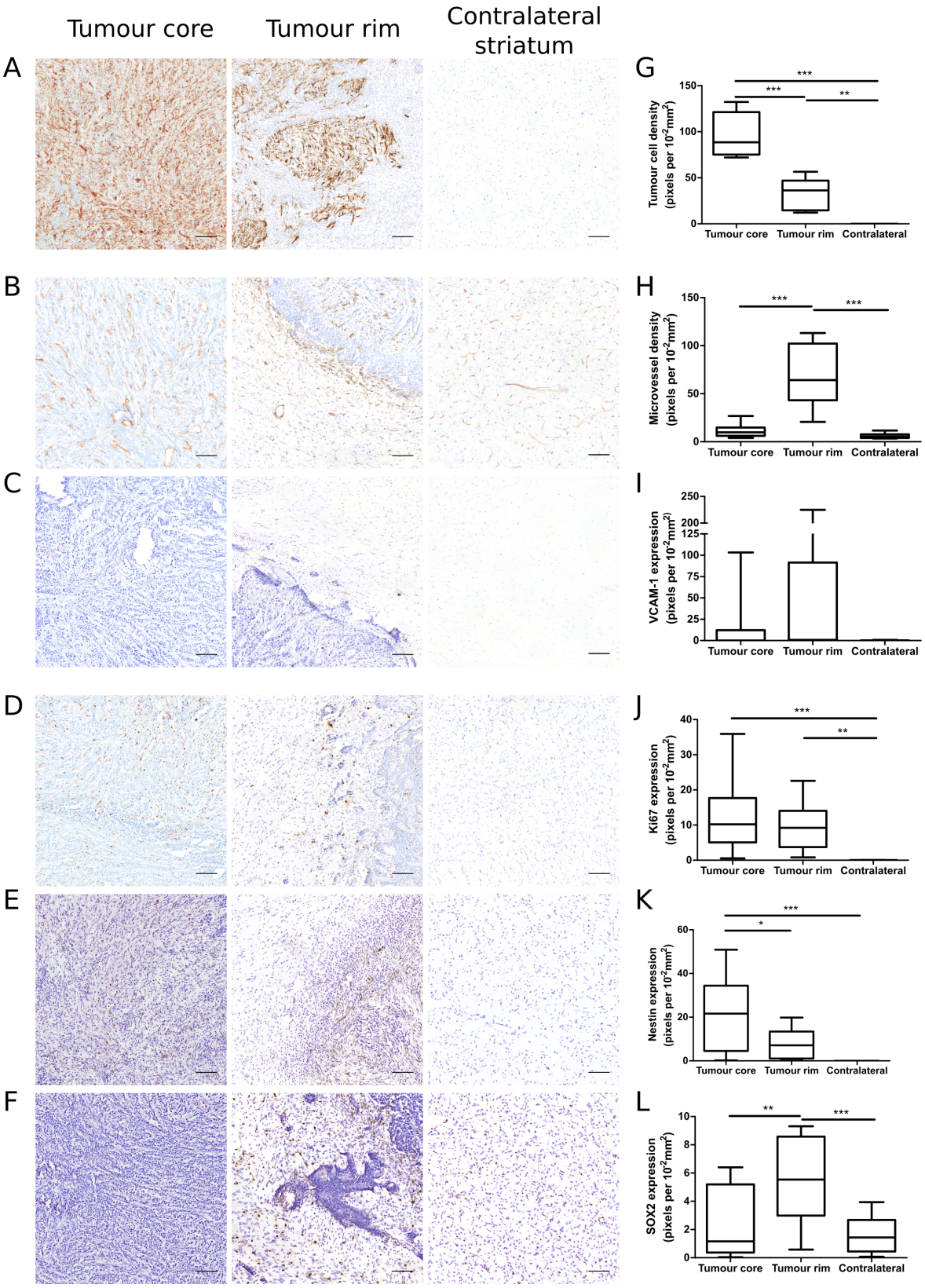


Fig 4.12. Histological examination of intrastriatal U87 tumours. Representative histologic sections of rat brains with intrastriatal U87 tumours, examined for (A) vimentin, (B) CD31, (C) VCAM-1, (D) Ki67, (E) nestin and (F) SOX2 expression. Expression of the forementioned markers were partitioned

according to location at the tumour core, the tumour rim or the contralateral striatum. Scale bar = 20µm. (G-L) Box and whisker plots illustrating marker expression relative to the area of each region of interest (*p<0.05; **p<0.01; ***p<0.001). Whiskers indicates min and max values; box denotes median ± interquartile range.

A similar finding was established with two markers of cell stemness, namely nestin and SOX2. Both antigens are expressed on the cell nuclei, as shown on Figs 4.11E-F and 4.12E-F. and analysis of the contralateral brain suggests a low basal expression of nestin and SOX2 in normal brain parenchyma. Between the two tumour models, there was a differential expression of the stemness markers, with a relatively higher SOX2 expression compared to nestin for MDA231Br-GFP tumours and *vice versa* for U87 tumours, demonstrated in Figs 4.11K-L and 4.12K-L. For MDA231Br-GFP tumours there was no difference, in either nestin or SOX2 expression, between the core and rim. In contrast, for U87 tumours, there was significantly greater expression of nestin in the tumour core compared to the rim and *vice versa* for SOX2 expression. However, accounting for tumour cell density revealed significantly higher tumour cell SOX2 expression at the tumour rim compared to the core for both tumour models, although this was not replicated with nestin expression (Fig 4.13B-C).

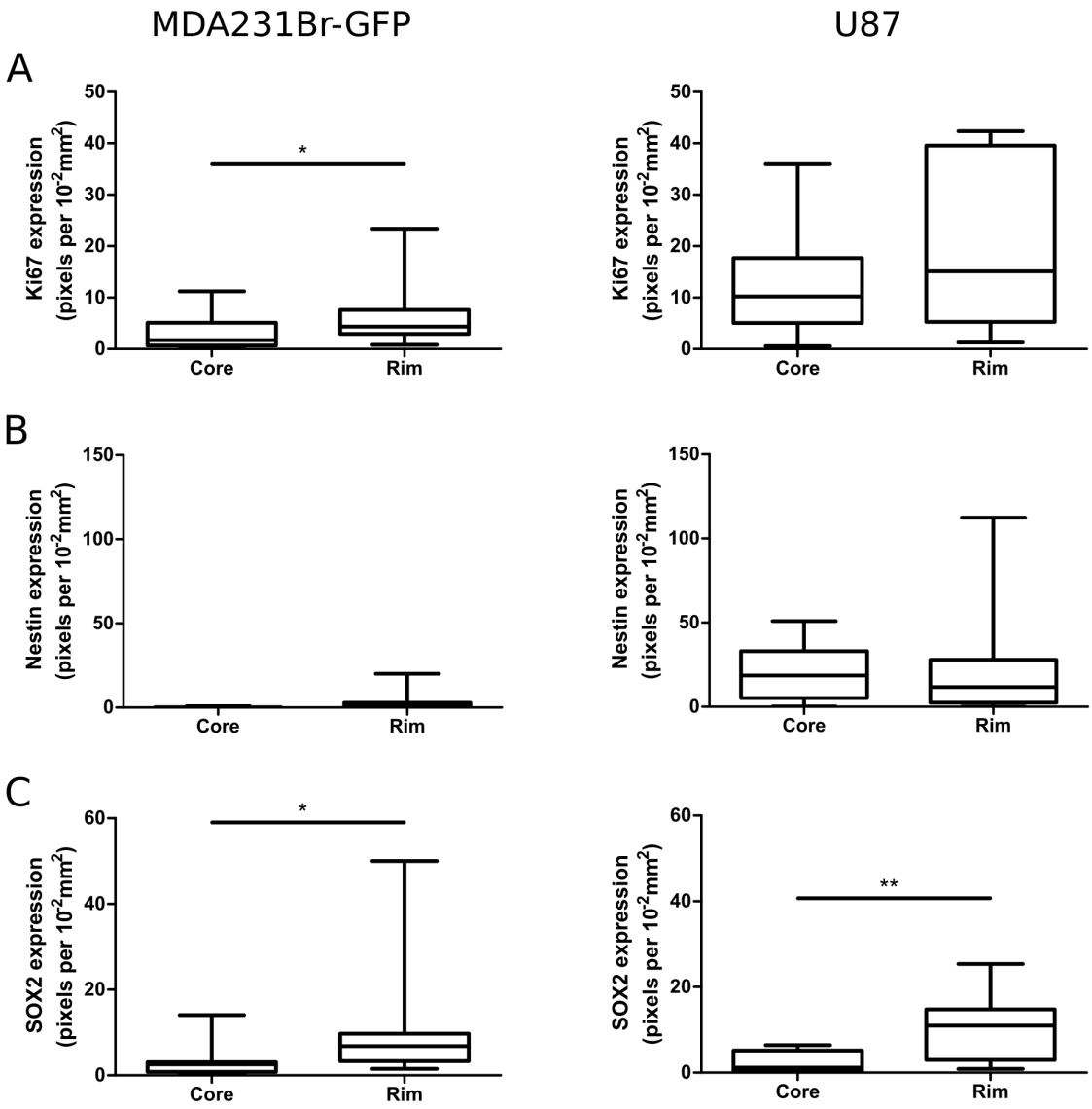


Fig 4.13. Tumour marker expression corrected by tumour cell density. Box and whisker plots showing expression of (A) Ki67, (B) nestin and (C) SOX2, corrected by tumour cell density, at the core or rim of MDA231Br-GFP and U87 intrastriatal tumours. (*p<0.05; **p<0.01). Whiskers indicates min and max values; box denotes median ± interquartile range.

4.3.4 VCAM-MPIO MRI in intrastriatal tumour rat brain models

All tumour-bearing animals had visible tumours present on T_2-weighted imaging and the tumours were appropriately located in the left striatum. Interestingly, the MDA231Br-GFP tumours were not visible on post-gadolinium T_1-weighted imaging (Fig 4.14A-C), suggesting

that there was no BBB breakdown associated with these tumours at 28 days post-tumour cell injection. In contrast, post-gadolinium enhancement was present on T_1-weighted imaging with the U87 intrastriatal tumours (Fig 4.15A-C). In rats intrastriatally injected with PBS only no MRI detectable changes were evident.

Prior to injection of MPIO contrast agents, hypointensities were visible in the ipsilateral striatum, corresponding to the location of the tumour, on T_2^*-weighted images. After intravenous injection of VCAM-MPIO, MDA231Br-GFP tumour bearing mice showed significantly increased volumes of hypointensities in the left striatum, consistent with binding of the MPIO to upregulated endothelial VCAM-1; whereas, minimal hypointensities were seen in the contralateral striatum (Fig 4.14E). Furthermore, neither control cohorts, comprising tumour-bearing animals injected with the non-specific anti-rat IgG-MPIO and PBS-injected animals imaged with VCAM-MPIO, displayed significantly elevated volumes of hypointensity in either the ipsilateral or contralateral striatum. Subsequent, histological analysis of the tumour demonstrated specific binding of VCAM-MPIO beads in the luminal surface of vessels in proximity to the edge of the tumour, concurrently expressing VCAM-1 (Fig 4.14F).

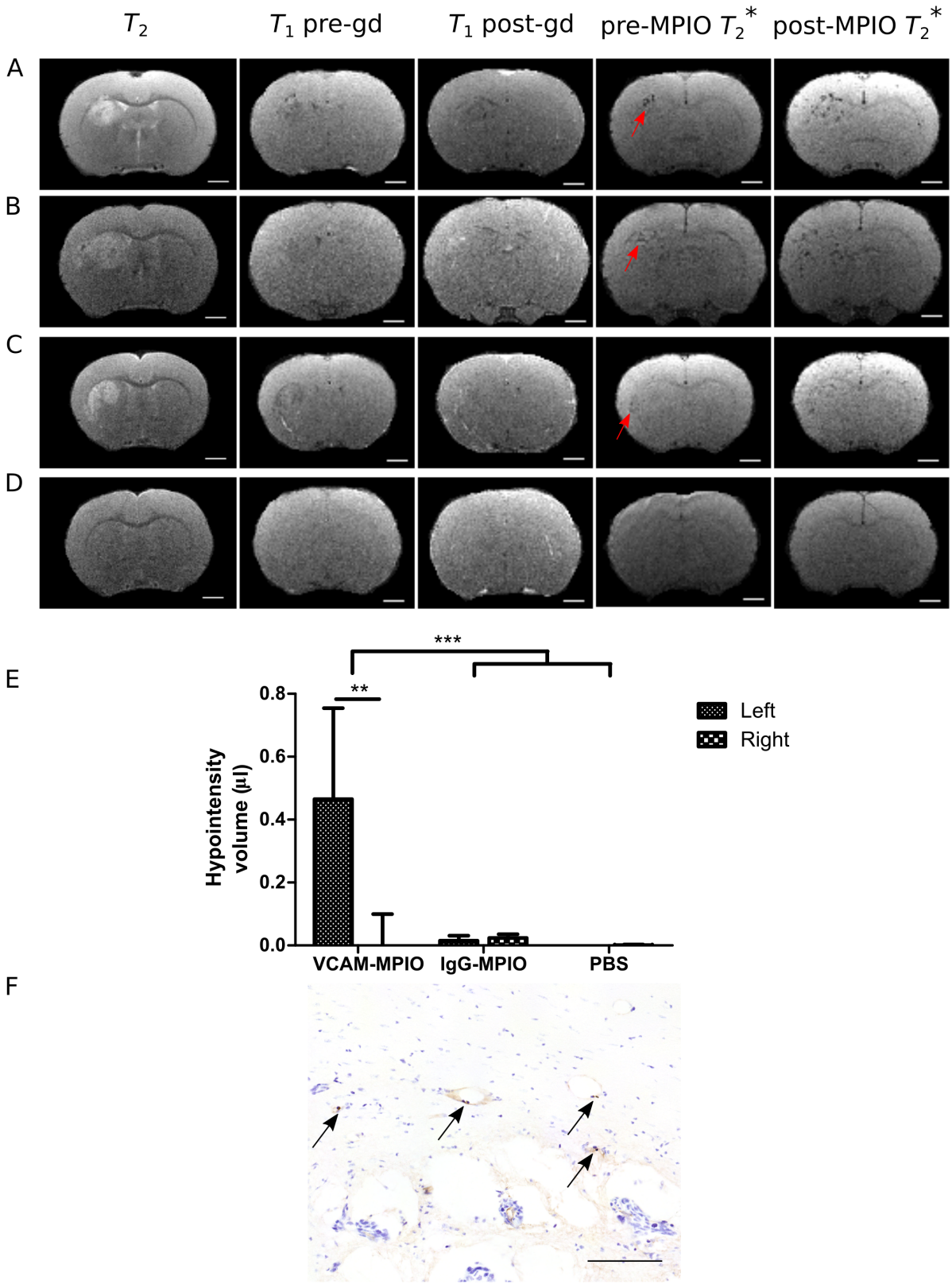


Fig 4.14. Hypointensity analysis for VCAM-MPIO imaging with MDA231Br-GFP tumours. Representative axial MR slices of rat brains, involving T_2-weighted, pre- and post-gadolinium T_1-weighted, and pre- and post-MPIO T_2^*-weighted imaging sequences for three different rat brains with left-sided

intrastriatal MDA231Br-GFP tumours following intravenous injection with (A-B) VCAM-MPIO or (C) IgG-MPIO. (D) An additional control group with animals injected intracerebrally with PBS only and then i.v. VCAM-MPIO prior to imaging was used; scale bar = 2mm. Hypointensities were visible in the pre-MPIO T_2^*-weighted imaging (red arrow). (E) Hypointensities in the ipsilateral striatum of MDA231Br-GFP tumour-bearing rats were significantly greater in volume compared to the contralateral striatum (**p<0.01; ***p<0.001). (F) Representative histological section of a mouse brain containing a MDA231Br-GFP intrastriatal tumour demonstrating VCAM-1 positive vessels (brown colour) at the periphery of the tumour and intraluminally bound VCAM-MPIOs (black arrow); scale bar = 100µm.

Similarly, U87 tumour bearing mice showed significantly increased volumes of hypointensity in the left striatum after VCAM-MPIO MRI, compared to the baseline T_2^*-weighted images, with minimal hypointensities in the contralateral striatum (Fig 4.15E). The distribution of hypointensities appeared to conform to the circumference of the tumour. Furthermore, neither control cohorts, comprising tumour-bearing animals injected with the non-specific anti-rat IgG-MPIO and PBS-injected animals imaged with VCAM-MPIO, displayed significantly elevated volumes of hypointensity in either the ipsilateral or contralateral striatum. Subsequent, histological analysis of the tumour demonstrated specific binding of VCAM-MPIO beads in the luminal surface of vessels in proximity to the edge of the tumour, concurrently expressing VCAM-1 (Fig 4.15F).

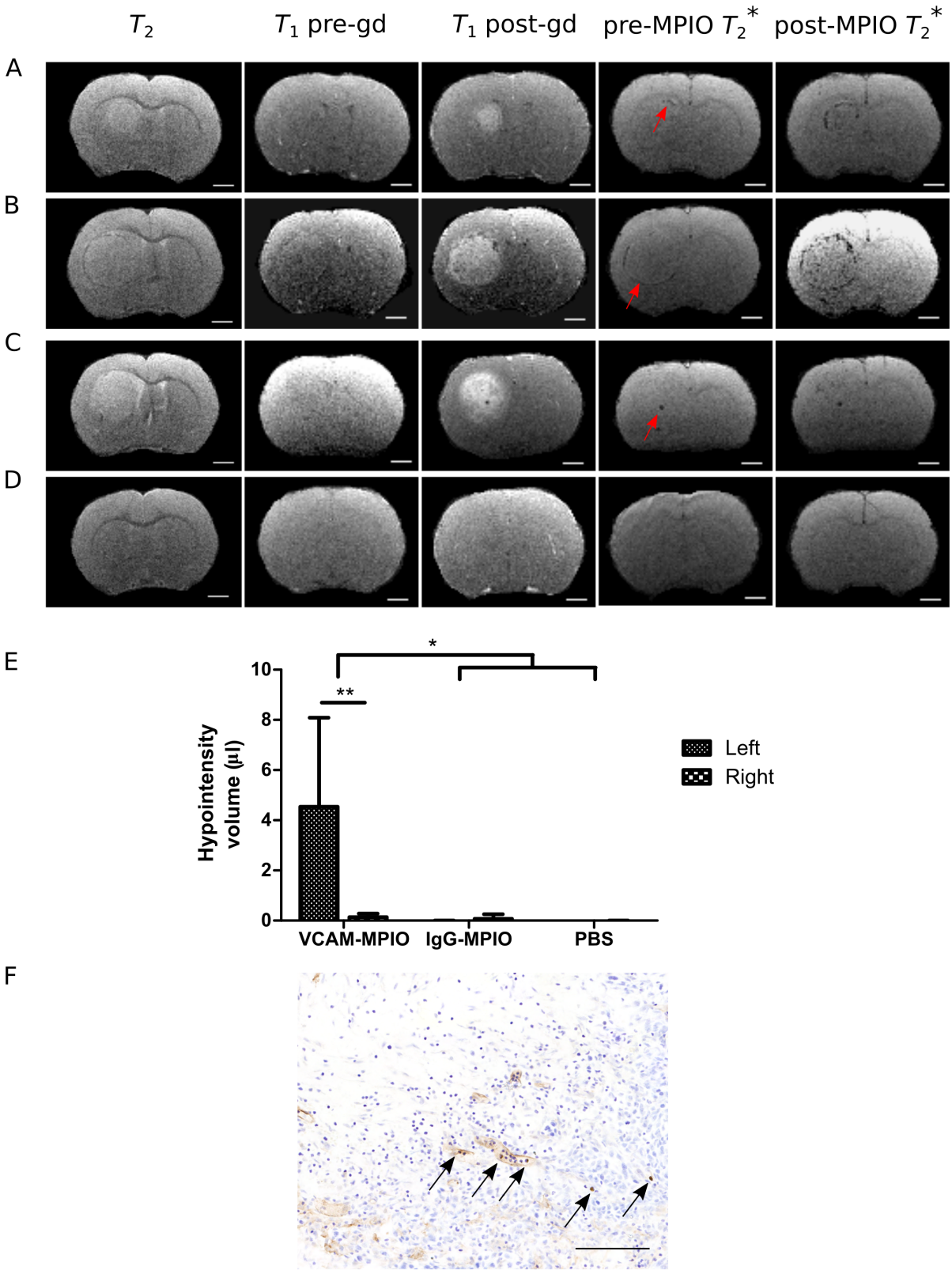


Fig 4.15. Hypointensity analysis for VCAM-MPIO imaging with U87 tumours. Representative axial MR slices of rat brains, involving T_2-weighted, pre- and post-gadolinium T_1-weighted, and pre- and post-MPIO T_2^*-weighted imaging sequences for three different rat brains with left-sided

intrastriatal U87 tumours following intravenous injection with (A-B) VCAM-MPIO or (C) IgG-MPIO. (D) An additional control group with animals injected intracerebrally with PBS only and then i.v. VCAM-MPIO prior to imaging was used; scale bar = 2mm. Hypointensities were visible in the pre-MPIO T_2^*-weighted imaging (red arrow). (E) Hypointensities in the ipsilateral striatum of U87 tumour-bearing rats were significantly greater in volume compared to the contralateral striatum (*p<0.05; **p<0.001). (F) Representative histological section of a mouse brain containing a U87 intrastriatal tumour demonstrating VCAM-1 positive vessels (brown colour) at the periphery of the tumour and intraluminally bound VCAM-MPIOs (black arrow); scale bar = 100µm.

Assessment of the tumour dimensions visualised using the different scan sequences appeared to show some difference in the definition of the tumour. Owing to the lack of apparent BBB disruption caused by the MDA231Br-GFP tumours, there was no visibly enhanced tissue in the left striatum following i.v. gadolinium (Fig 4.16A). However, as previously noted, there were focal hypointensities present in the expected distribution for the tumour and this appeared to correlate well with the distribution seen on T_2-weighted imaging. A comparison of the tumour dimensions between VCAM-MPIO imaging and conventional MRI sequences showed concordance in the measurements between the standard and the new techniques, as shown in (Fig 4.16F).

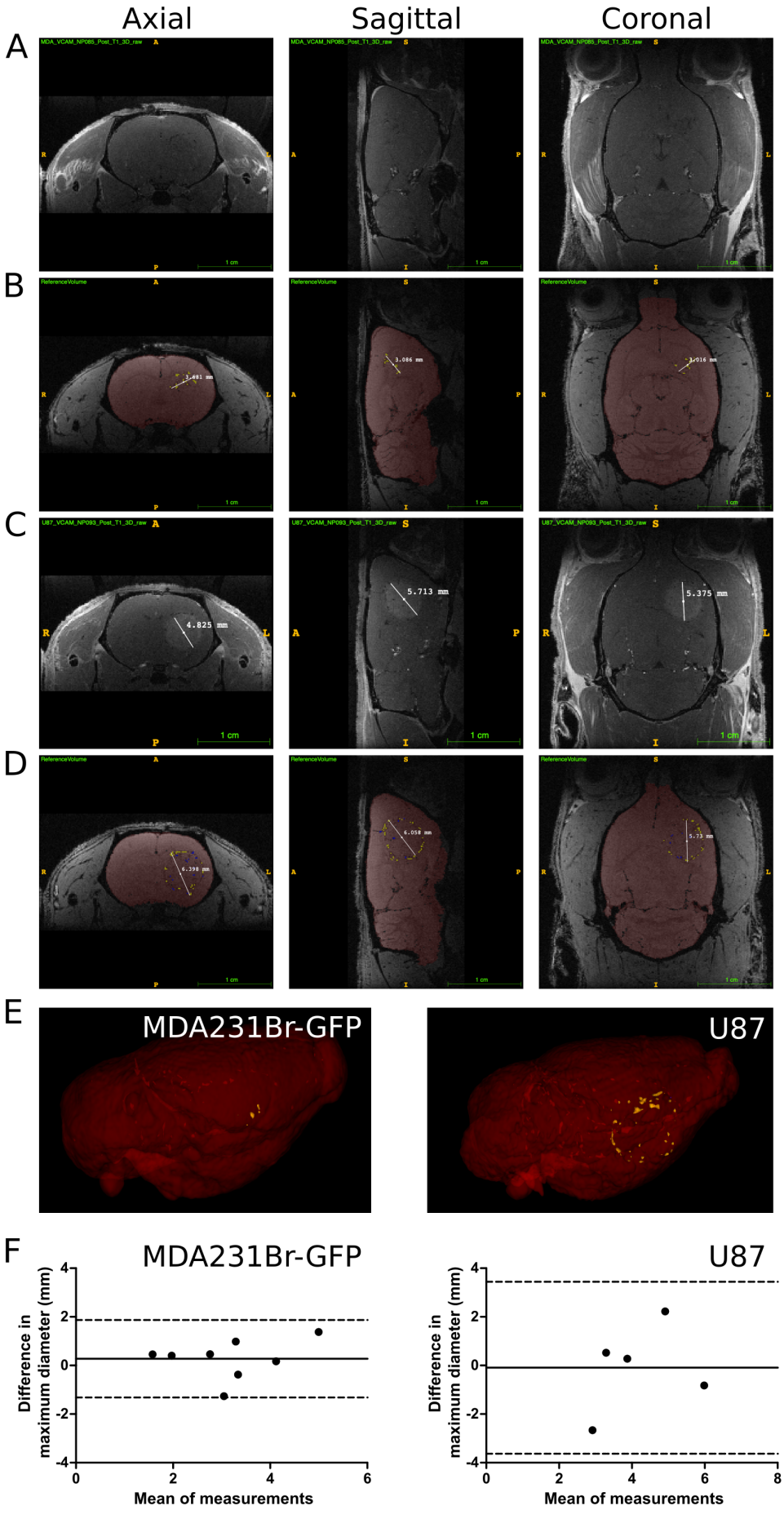

Axial
Sagittal
Coronal
A
B
C
D
E
F
4.825 mm
5.713 mm
5.375 mm
MDA231Br-GFP
U87
MDA231Br-GFP
U87
Difference in maximum diameter (mm)
Mean of measurements

Fig 4.16. Comparison of VCAM-MPIO imaging vs. standard MRI sequences. Representative images in three orthogonal planes of (A) post-gadolinium T_1-weighted and (B) post-VCAM-MPIO T_2^*-weighted sequences for a rat with an intrastriatal MDA231Br-GFP tumour. (C) and (D) are the equivalent sequences for a rat with an intrastriatal U87 tumour. The red semi-opaque mask denotes the brain tissue, whilst the yellow indicates the detected hypointensities that delineate the tumour. Maximum diameter was measured, where the tumour is visible on either the post-gadolinium T_1-weighted and/or the post-VCAM-MPIO T_2^*-weighted images. (E) A post-processing reconstruction for each corresponding rat brain illustrates the 3D distribution of the hypointensities that conform to the circumference of the tumour. (F) Bland-Altman plots demonstrate agreement in diametric measurements between two different imaging parameters; T_2 *vs.* post-VCAM-MPIO T_2^* and post-gadolinium T_1 *vs.* post-VCAM-MPIO T_2^* for MDA231Br and U87 tumours, respectively. Solid line indicates mean difference and dashed lines indicate 95% confidence limits.

Qualitative assessment of the VCAM-MPIO MR images revealed that the hypointensities conformed closely to the perimeter of the tumour seen on conventional imaging. Although tumour-induced gadolinium enhancement did not occur with the MDA231Br-GFP tumours, comparison with the T_2-weighted images enabled localisation of the hypointense pixels to the tumour (Fig 4.17). Hypointensities were visible at sites beyond the edge seen on conventional MRI. Furthermore, quantitative assessment of the hypointensities from T_2^*-weighted imaging demonstrated that a significantly greater volume of hypointensities extended beyond the segmentation of gadolinium enhancement, evident on T_1-weighted MRI, for both MDA231Br-GFP ($p = 0.0019$) and U87 ($p = 0.0232$) tumours, when compared to the corresponding IgG-MPIO cohorts (Figs 4.17 and 4.18).

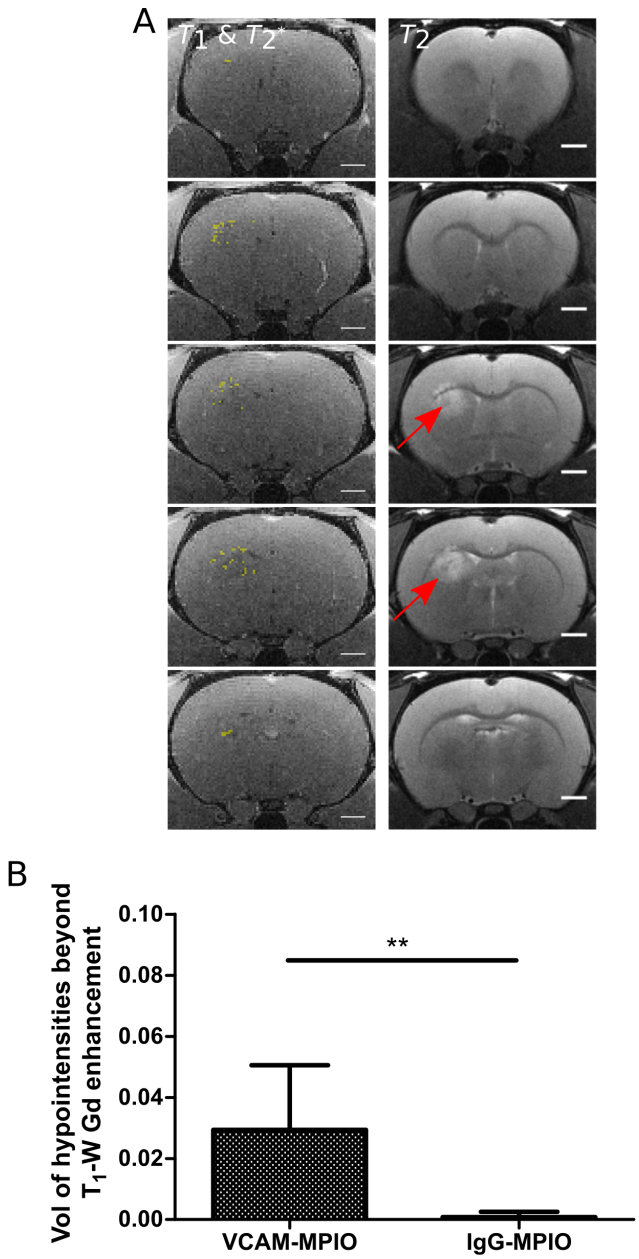


Fig 4.17. Hypointensities beyond gadolinium enhancement in MDA231Br-GFP rat brain xenografts. (A) Representative axial image slices of rat brain with MDA231Br-GFP intrastriatal tumour. Overlay of T_2^*-weighted segmented mask following i.v. VCAM-MPIO administration on T_1-weighted sequence post-i.v. gadolinium (Gd) administration demonstrated hypointensities (yellow) extending beyond the edge of contrast enhancement. Corresponding T_2-weighted images illustrate location of the tumour (red arrow); scale bar = 2mm. (B) Volume of hypointensities extending beyond T_1-weighted Gd enhancement was significantly greater in the VCAM-MPIO group compared to IgG-MPIO ($p < 0.01$).

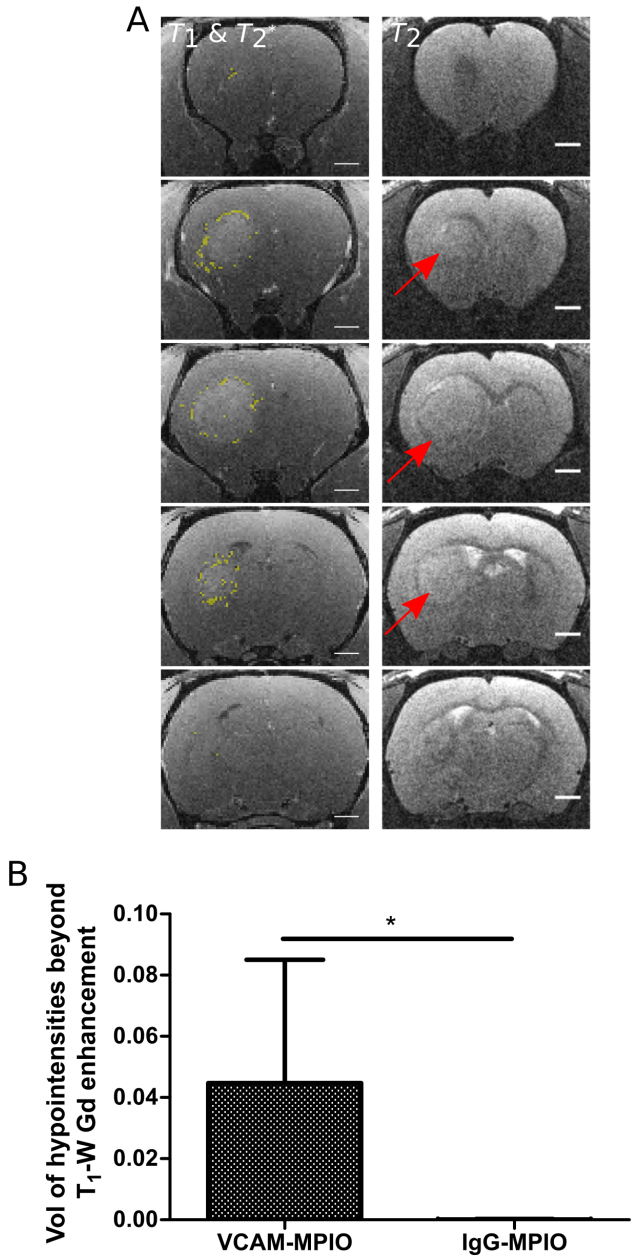


Fig 4.18. Hypointensities beyond gadolinium enhancement in U87 rat brain xenografts. (A) Representative axial image slices of rat brain with U87 intrastriatal tumour. Overlay of T_2^*-weighted segmented mask following i.v. VCAM-MPIO administration on T_1-weighted sequence post-i.v. gadolinium (Gd) administration demonstrated hypointensities (yellow) extending beyond the edge of contrast enhancement. Corresponding T_2-weighted images illustrate location of the tumour (red arrow); scale bar = 2mm. (B) Volume of hypointensities extending beyond T_1-weighted Gd enhancement was significantly greater in the VCAM-MPIO group compared to IgG-MPIO ($p < 0.01$).

4.4 Discussion

A reverse translation approach was taken to examine the ability of standard human MRI techniques to characterise the edge of brain metastases and, subsequently, the application of VCAM-1 targeted MRI in pre-clinical xenograft brain tumour models for the same function. By histological examination, I have demonstrated that endothelial VCAM-1 is a suitable surrogate biomarker for the tumour border in human brain metastases, as well as for sites of brain parenchyma infiltrated by isolated malignant cells. Using intrastriatally injected models of breast cancer brain metastasis and glioblastoma, I showed that the tumour margin is biologically distinct from the core mass and that endothelial VCAM-1 is upregulated in proximity to the tumour edge. Finally, the utility of the imaging contrast agent, VCAM-MPIO, in discriminating the tumour border with T_2^*-weighted MRI as an adjunct to standard MRI sequences has been demonstrated.

4.4.1 Limitations of human MRI in accurately delineating brain metastasis

Despite providing superior soft tissue resolution of the brain compared to other imaging modalities, MRI is limited in its ability to detect microscopic changes in the brain matter. Nonetheless, MRI remains the gold standard non-invasive imaging technique for intracranial tumour characterisation. It is critical, therefore, that accurate information about the tumour can be obtained from this imaging modality. This work focuses on assessing the current capabilities of two standard MR sequences to detect the edge of human brain metastases, investigating the suitability of endothelial VCAM-1 as a biomarker for the invasive margin of brain metastases and exploring the potential of the targeted imaging contrast agent, VCAM-MPIO, for enhancing the resolution of MRI at the BM-BP border.

The availability of image-guided biopsies of the BM-BP border, from patients who had breast cancer, lung adenocarcinoma or melanoma brain metastases, coupled with the corresponding MR sequences, enabled the specific examination of how this border is defined on MRI. Based on two MR sequences commonly used in the detection of brain metastases, namely gadolinium contrast enhanced T_1-weighted imaging and diffusion weighted imaging, it was shown that there was no measurable change in signal intensity that reliably separates the tumour border from both the tumour core and the adjacent parenchyma. This finding is important as it confirms the reliance on subjective assessment of the cerebral metastasis to brain boundary. It is also consistent with prior work examining the use of ADC values to distinguish glioma tissue from peritumoural brain tissue, which found that there was a considerable overlap in values between these regions suggesting it was not a useful parameter in this respect (179). A study investigating the correlation between image-guided stereotactic biopsies and abnormalities defined on conventional MRI found that isolated infiltrative tumour cells were present even at sites without T_1- and T_2-weighted prolongation (180, 181). Moreover, where there was T_1- and T_2-weighted prolongation, negative biopsies were also obtained from these regions, which corresponded instead to oedematous tissue without tumour infiltration (182). Thus, it is apparent that standard MRI has inadequate sensitivity and specificity to accurately differentiate the invasive margin from surrounding brain parenchyma.

Immunohistochemical assessment of image-guided stereotactic biopsies from human brain metastases revealed that there was no difference in microvessel density according to distance from the edge of the tumour. However, with the exception of the lung adenocarcinoma samples, there was an appreciably higher proportion of VCAM-1 positive vessels in closer

proximity to the tumour margin than a further distance away. Although no relationship was seen between endothelial VCAM-1 positivity and distance from the tumour edge for the lung adenocarcinoma samples, one explanation is the presence of isolated tumour cells far from the border of the lesion that was observed in this tumour type. The results show that isolated individual tumour cells or small clusters of tumour cells are associated with VCAM-1 activation in adjacent vessels. This finding indicates that endothelial activation is associated with nearby microscopic disease, currently undetectable with standard gadolinium enhanced MRI, and thus VCAM-1 expression appears to delineate even diffusely infiltrative tumours.

One must exercise caution when interpreting measurements based on a two dimensional space such as a tissue section. Measuring distance from the tumour edge assumes that the biopsy was collected directly orthogonal to the tumour margin, which is not always feasible. It was not possible to make a correction for this in the analysis, as the precise orientation of the biopsy was not known and, therefore, the length of the peritumoural brain tissue may have been overestimated. Nevertheless, the evidence of VCAM-1 upregulation on blood vessels adjacent or near to the brain metastasis margin adds weight to its use as a surrogate biomarker for the invasive tumour margin. Moreover, endothelial VCAM-1 activation may have been stimulated by infiltrating cells distant from the tumour edge at a different plane to the tissue section. This concept is demonstrated by the presence of stained tumour cells at the far edge of the biopsy, which was not observed in the adjacent section stained for VCAM-1 (Fig 4.9). Thus, upregulated endothelial VCAM-1 expression beyond the immediate confines of the tumour border could indicate additional sites of local spread.

As previously reported by Berghoff *et al*, contrary to conventional wisdom, the histopathology of brain metastases demonstrates heterogeneity in the invasion pattern of these tumours (170). Those authors identified three distinct invasion patterns: a well-demarcated border of the tumour mass to the surrounding parenchyma; multicellular tumour cell outgrowths from the tumour mass protruding into the brain parenchyma through vascular co-option; and diffuse infiltration of single tumour cells into the surrounding brain parenchyma. Moreover, infiltration of metastatic tumour cells has been shown to correlate with an unfavourable prognosis compared to tumours with a non-infiltrating growth pattern (171). The results of the histological staining of the image-guided stereotactic biopsies support the notion that human brain metastases are not wholly encapsulated tumours and, instead, form an invasive margin. The interaction between the infiltrative tumour cells and the brain parenchyma generates a tumour microenvironment characterised by local inflammation, which is evident by increased VCAM-1 expression.

4.4.2 Pre-clinical xenograft models of brain tumours for VCAM-MPIO imaging

To examine the application of molecular MRI targeting VCAM-1 in detecting the edge of brain metastases, pre-clinical *in vivo* models were established by intrastriatal injection of human-derived tumour cells into rat brains. The specific tumour cell lines used in the xenograft models were from human breast cancer, MDA231Br-GFP, and a human glioblastoma, U87. A glioblastoma cell line was selected as this is a well-characterised model for studying tumour cell invasion (183, 184). Furthermore, the intracerebral method of tumour implantation has been extensively used in the study of brain tumours, both primary and secondary, and has the benefit of greater control over quantity of tumour cells delivered and elimination of systemic dissemination (185). Although the intracerebral model bypasses the early steps of the

metastatic cascade this was considered inconsequential in the current study, as I was predominantly interested in established tumours and their surrounding microenvironment. Importantly, the control cohort of rats, intrastriatally injected with PBS vehicle only, demonstrated no detectable abnormalities in the ipsilateral striatum on either MRI or histology. Whereas, in both the MDA231Br-GFP and U87 models, animals exhibited intrastriatal tumours of relatively consistent size that demonstrated an irregular border, in keeping with invasion at the tumour margin. Therefore, reproducible and relevant *in vivo* models were available to test VCAM-MPIO imaging.

Immunohistochemistry of the MDA231Br-GFP and U87 brain tumours revealed a spatial heterogeneity of antigenic distribution across the axis of the tumour. Smith *et al* have previously shown that the molecular profile of the invasive margin of glioblastoma tumours is distinct from the tumour core and the enhancing rim of T_1-weighted MRI. Specifically, they showed that there was a significant difference in cell density, cell proliferation and vascularity across the aforementioned regions. Interestingly, however, they also found that there was decreased expression of the stemness marker, nestin, in the malignant cells at the invasive margin (186). These results are broadly consistent with the findings from the animal model for U87 intrastriatal tumours used here, although I have also shown that SOX2 expression is elevated at the tumour rim, a transcription factor that is thought to play a role in tumorigenesis through its association with the cancer stem cell phenotype and regulation of cell invasiveness (187, 188).

Whilst, there is increasing evidence that invasive primary brain tumours have distinct cellular subpopulations at the tumour margin, whether this translates similarly to brain metastasis

biology is less clear. Here, it has been shown that the region of the tumour rim contains a relatively sparse population of tumour cells compared to the tumour core, however it is associated with significantly increased microvessel density and VCAM-1 expression. Furthermore, there was a higher tumour proliferation, negligible nestin expression and greater SOX2 expression at the rim than at the core of the MDA231Br tumours. These findings were consistent with the observed phenotype of the U87 tumours, although absolute marker expression was lower for the MDA231Br tumours. These results point to an altered cellular phenotype at the edge of the tumour and also vascular changes in the adjacent brain parenchyma, thus highlighting the complex and interdependent interaction between cancer cells and the TME. It is postulated that metastatic tumour cells develop mechanisms to physically adapt their immediate surroundings, a process coined niche construction, that facilitates the survival of the tumour (189). These changes include secretion of pro-angiogenic factors, like vascular endothelial growth factor (VEGF), and creation of a pro-inflammatory environment through direct release of cytokines or indirectly by interaction with the host immune cells. Of particular interest, the increased vascularity and endothelial VCAM-1 expression at the tumour border for both the brain metastasis and primary brain tumour models provide a unified biomarker in the TME for the invasive margin, independent of tumour type.

The choice of animal model for imaging was to specifically exploit the larger cranium of a rat compared to that of a mouse's head. The increased number of voxels that can be used to image the rat brain permits a higher spatial resolution and greater signal-to-noise ratio (SNR) than can be afforded with a mouse brain (190). Moreover, the high field strengths used in pre-clinical scanners, in this case 9.4T, enables increased SNR; however, high field strength

scanning is also more prone to imaging artefacts, particularly due to susceptibility variation and chemical shift (191). T_2^*-weighted imaging relies on differences in the intrinsic magnetic susceptibility of tissue compartments to an externally applied, static, homogeneous magnetic field and the resulting image contrast (192). As previously described, spin dephasing is enhanced by these field perturbations, known as the T_2^* effect, which leads to changes in the corresponding transverse relaxation rate (R_2^*). It has been shown that at ultra high magnetic field strengths, R_2^* for blood rises exponentially (193), whereas the R_2^* of tissue parenchyma increases approximately linearly (194). Indeed, in the presence of lower oxygen tensions this phenomenon is further intensified (195), leading to visualisation of intravascular venous blood. Coupled with the observation of increased vascularity around the tumour border in the pre-clinical models, this effect may explain the presence of hypointensities in the T_1- and T_2^*-weighted images prior to the administration of the paramagnetic VCAM-MPIO contrast agent. Regardless, the demonstrable increase in hypointensities following VCAM-MPIO injection, alongside the specific binding of the targeted MPIO observed on histology, confirmed that VCAM-MPIO MRI does enhance visualisation of the tumour border.

4.4.3 Clinical potential of VCAM-MPIO MRI for detection of the brain metastasis border

Effective application of local therapies such as surgical resection, SRS or FSRT is heavily dependent on the correct delineation of the brain metastasis border. As a single cancer cell carries the potential to proliferate and form a malignant tumour, even minimal residual disease will likely have deleterious consequences for the patient's survival. Therefore, the clinician must have accurate knowledge of the tumour localisation and the extent of its spread to plan the treatment, which relies on pre-operative non-invasive imaging such as MRI (196, 197). As an example, in considering tumour resection, a surgeon must be confident in their

ability to remove the gross tumour bulk with an adequate margin to capture invasive microscopic disease that is currently undetectable on conventional imaging. Owing to the eloquent nature of specific regions of the brain, the surgeon must also determine the potential morbidity associated with iatrogenic injury to critical structures, especially if it may lead to permanent neurological deficit.

Advances in the surgical management of brain metastases includes the use of multimodality techniques such as DTI (173), functional MRI (fMRI) and cortical mapping (198); intraoperative neuronavigation with co-registered pre-operative stereotactic MRI (199); and intraoperative fluorescence imaging. A prime example of fluorescence-guided surgery is the oral administration of 5-aminolevulinic acid (5-ALA) pre-operatively, which accumulates in some brain metastatic tumours and is converted to protoporphyrin IX (PpIX) that fluoresces under blue-light illumination. However, whilst the utility of 5-ALA in improving resection of primary malignant brain tumours has been proven, this evidence is lacking for brain metastases and such studies will likely be hampered by 5-ALA's low sensitivity in detecting this disease (200). Another approach that is gaining interest is the wide margin (>5mm) surgical excision of brain metastases, a concept known as supramarginal resection or microscopic total resection. Here, retrospective studies have shown that brain metastasis resection in non-eloquent regions of the brain extending beyond the visible glial pseudo-capsule to achieve a tumour cell-free margin, determined through intraoperative histological analysis, resulted in lower local recurrence rates compared to GTR alone (36, 201, 202).

On a similar note, radiotherapy planning is largely dependent on non-invasive imaging, in particular MRI for brain tumour contouring. The clinician relies on the ability to define the

brain metastasis border to accurately contour the radiotherapy field; thus, ensuring that the maximum dose of radiation can be delivered to the tumour, whilst sparing the uninvolved brain parenchyma. Escalating the dose of radiation to the tumour volume has been shown to increase local control, with a dose of 21 gray (Gy) or more providing a greater than 80% rate compared to less than half if <15Gy is administered (203). However, this increase in dose may be achieved only if the target area can be more clearly defined to separate infiltrating tumour from surrounding healthy tissue.

For the forestated reasons, an imaging technique that enhances the ability of MRI to delineate the tumour border is of major clinical importance in the management of patients with brain metastases. With the increasing sophistication of MRI and as more powerful image analysis tools are developed, there has been a move towards multi-parametric imaging to interrogate different biological characteristics of a tumour, beyond simple anatomical characterisation offered by conventional gadolinium-enhanced MRI. Some examples of how such techniques have been used in clinical diagnosis and assessment of brain tumours include the differentiation between high grade primary brain tumours and secondary brain tumours (204) and distinguishing pseudoprogression from true disease progression of brain metastases following SRS (205). Moreover, the application of a radiomics approach to conventional MRI has allowed an in-depth analysis of a wide multitude of discriminatory image features to generate diagnostic biomarker signatures for different brain metastasis tumour types (206). Here, VCAM-1 targeted MRI has been shown to provide additional information relating to the extent of metastatic tumour invasion into the adjacent brain parenchyma. Specifically, using endothelial VCAM-1 as a surrogate marker, nearby invading tumour cells at the tumour rim could be detected. It is this phenomenon, which currently poses the greatest diagnostic

challenge to conventional gadolinium-enhanced MRI. These findings suggest that the VCAM-MPIO approach could be a powerful tool to successfully interrogate the tumour border and, consequently, will augment existing MRI techniques.

The high local recurrence rate of brain metastases following local therapies, including surgery and SRS, challenges the widely accepted belief that these tumours are sharply delimited. Emerging evidence, and the data presented here, support the notion that, similar to extracranial disease, some metastatic tumours in the brain do demonstrate local invasion and more diffuse infiltration into the brain parenchyma. The ability to differentiate infiltrative from non-infiltrative tumours and more accurate definition of the tumour border through MRI, will ensure that unnecessary and/or ineffective treatments are not given, thus avoiding potential harm to the patient. As already discussed, more accurate pre-operative imaging will also enhance the planning of local treatments, leading to improved efficacy and better outcomes for patients receiving these therapies.

CHAPTER 5: DISRUPTING VLA-4 FUNCTION TO PREVENT BRAIN METASTASES

5.1 Introduction

Haematogenous spread of malignant cells from a primary tumour to a secondary site involves a complex cascading pathway, as previously discussed in Section 1.1.2. One of the critical steps for tumour seeding requires the cells to attach to the luminal surface of the endothelium before transendothelial migration into the tissue parenchyma. The process of extravasation is, at least partly, mediated by tumour-expressed cell adhesion molecules (CAMs). This extends beyond the direct attachment to the endothelial cells and includes the recruitment of immune cells and homotypic aggregation of the tumour cells.

Moreover, the predisposition of the distant organ to metastatic seeding requires specific changes in the local microenvironment, coined the premetastatic niche. Such changes include vascular inflammation, which promotes the attachment of tumour cells at the end organ through upregulation of corresponding endothelial CAMs. It is thought that the primary tumour is capable of modulating the distant organ's microenvironment before metastatic spread has even occurred. Although this process remains poorly understood, one mechanism may be through the combined systemic effect of circulating tumour-secreted factors and extracellular vesicles.

There has been recent interest in blocking the function of specific CAMs as a method of preventing tumour seeding at a target organ. For example, it has been shown that the

inhibition of the CAM, E-selectin, using a high-affinity antagonistic aptamer targeted against this molecule, reduced the number of lung metastases in preclinical *in vivo* breast cancer models. Importantly, the study also showed that restricting the formation of lung metastases did not result in relocation of the tumour cells to an alternative metastatic site, such as the brain (207). Furthermore, Schlesinger *et al*. linked VLA-4 to metastasis development by blocking its function with siRNA knockdown, targeted antibody inhibition or heparin derivatives in experimental models of melanoma lung metastasis (208).

Specifically with brain metastasis, Soto *et al*. demonstrated that functional inhibition of activated leucocyte cell adhesion molecule (ALCAM) and VLA-4 using neutralising antibodies significantly reduced by the number of metastases in the brain in pre-clinical models of breast cancer, although total tumour burden was only significantly decreased with ALCAM blockade (58). Moreover, inhibition of VLA-4 function appeared to influence the phenotypic characteristics of the tumours, with significantly increased vessel co-option compared to the control groups and altered metastasis morphology. The implication of this study is that functional inhibition of VLA-4 prevents the successful attachment of tumour cells at the distant organ through the VLA-4/VCAM-1 interaction. However, the Soto *et* al. study involved treating the human breast cancer tumour cells in culture with a mouse monoclonal antibody targeting the α_4 integrin subunit prior to *in vivo* introduction. Thus, blockade of VLA-4 would be transient and reduced as tumour cells proliferate. A more effective approach to VLA-4 inhibition would be through gene silencing.

In this chapter, I will seek to elucidate the relevance of VLA-4 function on brain metastasis formation, by testing the following hypotheses:

1. Tumour cell expression of VLA-4 is reduced by ribonucleic acid interference (RNAi);
2. Tumour cell adhesion and transendothelial migration is reduced by disrupting VLA-4 expression; and
3. Metastatic formation in the brain is inhibited by disruption of VLA-4 expression.

5.2 Methods

5.2.1 Knockdown of ITGA4 expression

Human metastatic breast carcinoma, MDA231Br-GFP, cells and human brain metastasis melanoma, H1_DL2, cells were transfected with a liposomal delivery vehicle containing siRNA against ITGA4 (Section 2.2.5). Four siRNA target sequences were used: ITGA4-06 (GACAAGACCUGUAGUAAUU), ITGA4-07 (GCAUAUAUAUUCAGCAUUG), ITGA4-08 (CAGAGUGACUGUAGCAAUA) and ITGA4-09 (AGAGACAGUUGGAGUUAUA). A non-targeting siRNA pool was used as a scrambled control (SCR) and an siRNA targeting cyclophilin B (PPIB) was selected as a positive knockdown control. Gene expression knockdown was confirmed by Western blotting and immunofluorescence (Sections 2.2.6 and 2.2.3.5, respectively). An MTT assay was used to assess cellular proliferation and metabolism (Section 2.2.7.1). Phenotypic profiling for both cell lines involved a static binding assay (Section 2.2.7.2) and Transwell cell migration assay (Section 2.2.7.3).

5.2.2 Quantitation of static binding assay

The number of bound tumour cells in the static binding assay was objectively measured using a standardised sequence in ImageJ (Fig 5.1). Briefly, the composite immunofluorescence image was split into the green and blue channels, corresponding to the tumour cells and the counterstained cell nuclei respectively. The green channel was converted into an 8-bit

grayscale channel, which was inverted and subsequently thresholded to yield a black and white image. With the in-built processing tools, the image underwent one round of dilation, followed by 2 rounds of erosion to isolate individual cells. Using the "Analyze Particles" function, the number of cells was automatically counted (size = 2mm^2-Infinity; circularity = 0-1; edge exclusion) and calculated according to area of sampling.

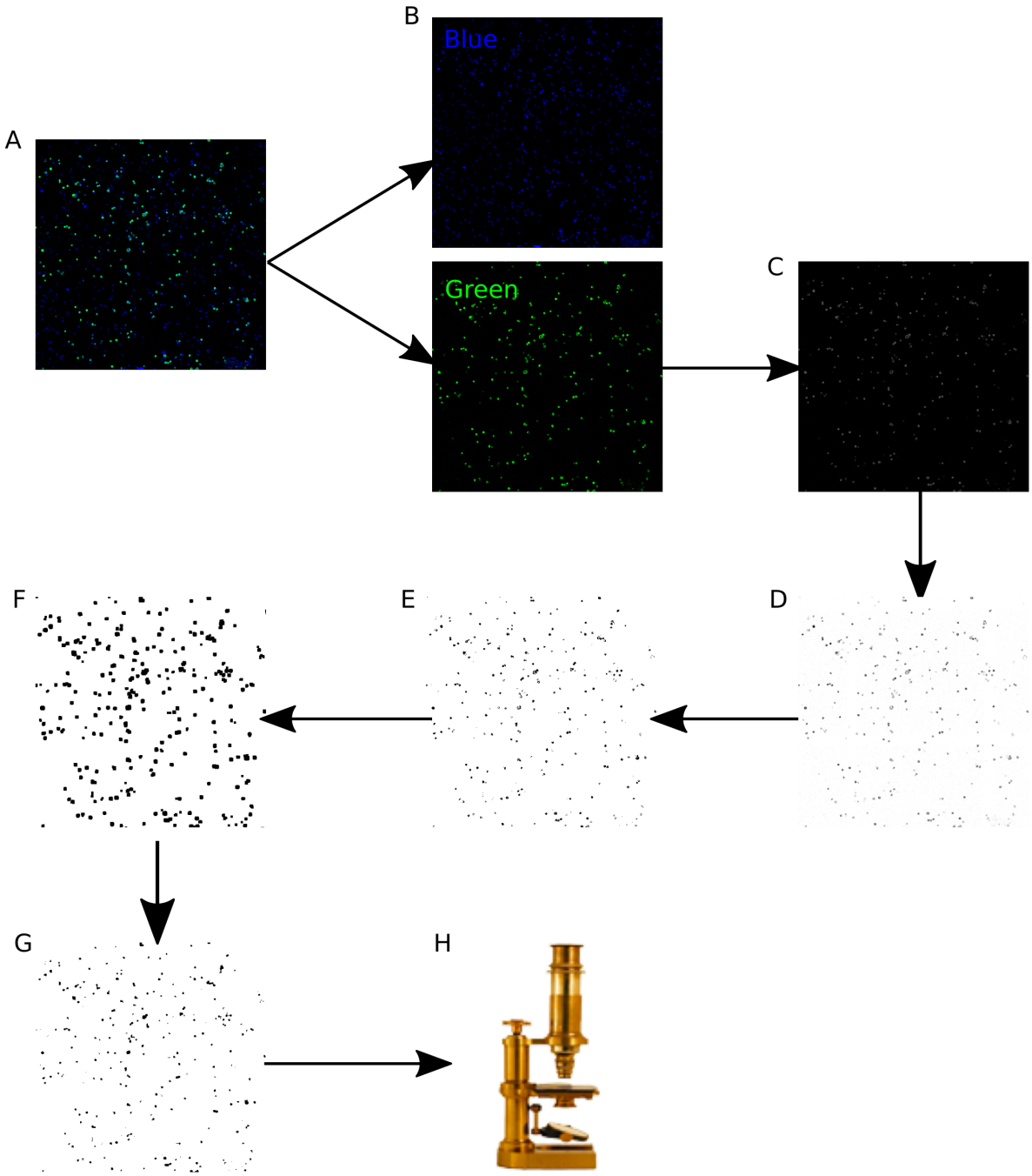


Fig 5.1. Method for analysing static binding assay confocal images. (A) Original composite image is (B) split into corresponding blue and green channels. Taking the green channel, containing the tumour cells, this is converted to an (C) 8-bit grayscale image, which is (D) inverted and then (D) thresholded before undergoing 2 rounds of (F) dilation and (G) erosion sequentially. (H) The processed images were analysed in ImageJ.

5.2.3 Animal studies

Female BALB/c variant SCID mice, aged 8 to 10 weeks old, were intracardially injected with either MDA231Br-GFP or H1_DL2 cells (Section 2.2.4.5), see Fig 5.2 for experimental schedule; three groups per cell line (UNT, SCR and ITGA4 kd). Animals were terminally anaesthetised, at 21 days after intracardiac injection, transcardially perfusion-fixed with 0.9% heparinised saline followed by 50mL PLP_{light}. Brains were collected and cryopreserved, before sectioning of the whole brain and storage at -80°C.

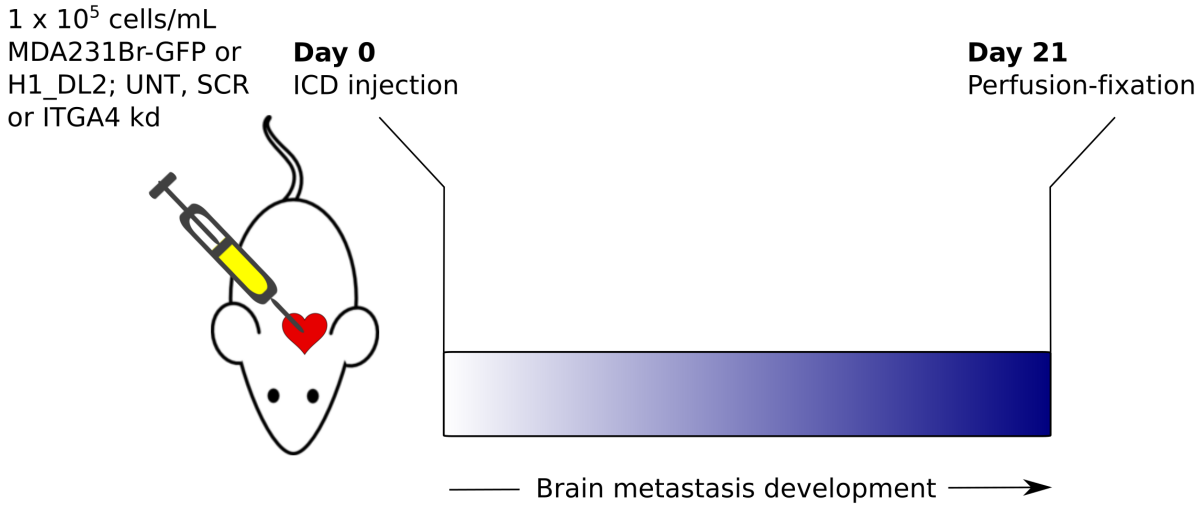


Fig 5.2. Experimental schedule for brain metastasis induction by intracardiac injection. Schedule of *in vivo* experiments involving intracardiac (ICD) injection of tumour cells, under various treatment conditions of siRNA transfection. Brain metastases were allowed to develop over 21 days before

the animals were sacrificed by perfusion-fixation under terminal anaesthesia. UNT = untreated; SCR = scrambled control siRNA; ITGA4 kd = VLA-4 α_4 subunit knockdown.

5.2.4 Immunohistochemistry

In each brain, every other tissue section was immunohistochemically stained for tumour-specific antigens CAM5.2 and melan-A to quantify the MDA231Br-GFP and H1_DL2 tumour volumes, respectively (Section 2.2.3.4). Stained tissue sections were digitally scanned on the Aperio CS2 machine with the images stored offline for analysis. Tumours were annotated, with quantification of tumour cross-sectional area and number of tumours. Data for the remaining alternate sections were determined by linear interpolation, which permitted calculation of the tumour volume (Section 3.2.5).

5.2.5 Statistical analysis

All raw data were collated and processed in Microsoft Excel spreadsheets to obtain mean and standard deviation (SD) values as measures of central tendency and dispersion, respectively. Processed values were statistically analysed in GraphPad Prism v5, using one-way analysis of variance (ANOVA) and post-hoc Tukey tests for multiple comparisons between groups. The threshold for defining statistical significance was set at $p<0.05$.

5.3 Results

5.3.1 Selection of siRNA for optimum VLA-4 expression knockdown

The set of 4 individual targeted siRNAs were tested for their efficiency in silencing the ITGA4 gene in the MDA231Br-GFP cell line initially. As shown in Fig 5.3, at 7 days following transfection the most potent knockdown was achieved by the ITGA4-06 siRNA sequence, with

a mean reduction in VLA-4 expression in MDA231Br cells by 84.8 ± 3%, compared to 73.4 ± 6.1% for the ITGA4-07 sequence and <60% reduction with the other 2 sequences (p<0.001).

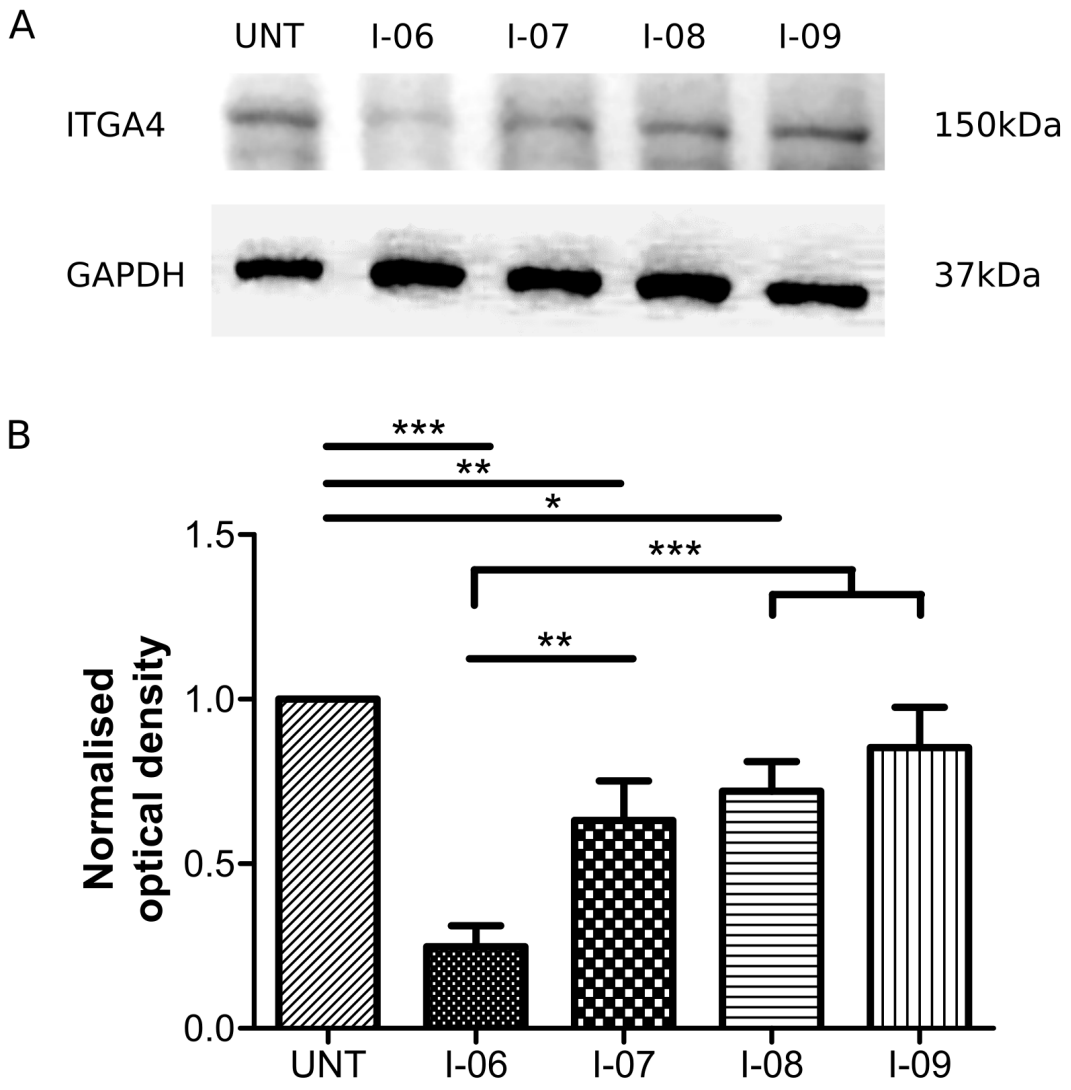


Fig 5.3. Selection of siRNA for maximum ITGA4 knockdown. (A) Representative Western blot image of integrin α_4 (ITGA4) and GAPDH protein expression for untreated MDA231Br-GFP tumour cells (UNT) compared against MDA231Br-GFP cells treated with 4 different siRNA target sequences against ITGA4: ITGA4-06 (I-06), ITGA4-07 (I-07), ITGA4-08 (I-08) and ITGA4-09 (I-09). (B) Graph showing mean optical density of Western blots for each siRNA treatment group normalised to the UNT group, across 3 experimental repeats (*p<0.05, **p<0.01, ***p<0.001); error bars denote SD.

5.3.2 Quantitation of VLA-4 expression knockdown

Subsequently, efficacy of VLA-4 knockdown was assessed in both MDA231Br-GFP and H1_DL2 cell lines over a more complete time course for the optimal siRNA sequence, ITGA4-06. Following delivery of targeted siRNA against the ITGA4 gene by liposomal transfection, a significant downregulation in ITGA4 protein production was evident compared to the untransfected (UNT) group as elicited by Western blotting (Fig 5.4C-D). For both the MDA231-GFP and H1_DL2 cells this was most evident at 7 days following siRNA transfection, with a mean reduction of 87.4 ± 12.2% ($p<0.05$) and 84.2 ± 15.0% ($p<0.01$) respectively, compared to the UNT cells. No differences in ITGA4 production were evident between the UNT cells and the control groups. Moreover, the H1_DL2 cells showed a significant reduction in ITGA4 at 14 days post-siRNA transfection compared to the UNT group, although to a lesser degree than observed with the MDA231Br cells, at 57.6 ± 31.2% ($p<0.05$).

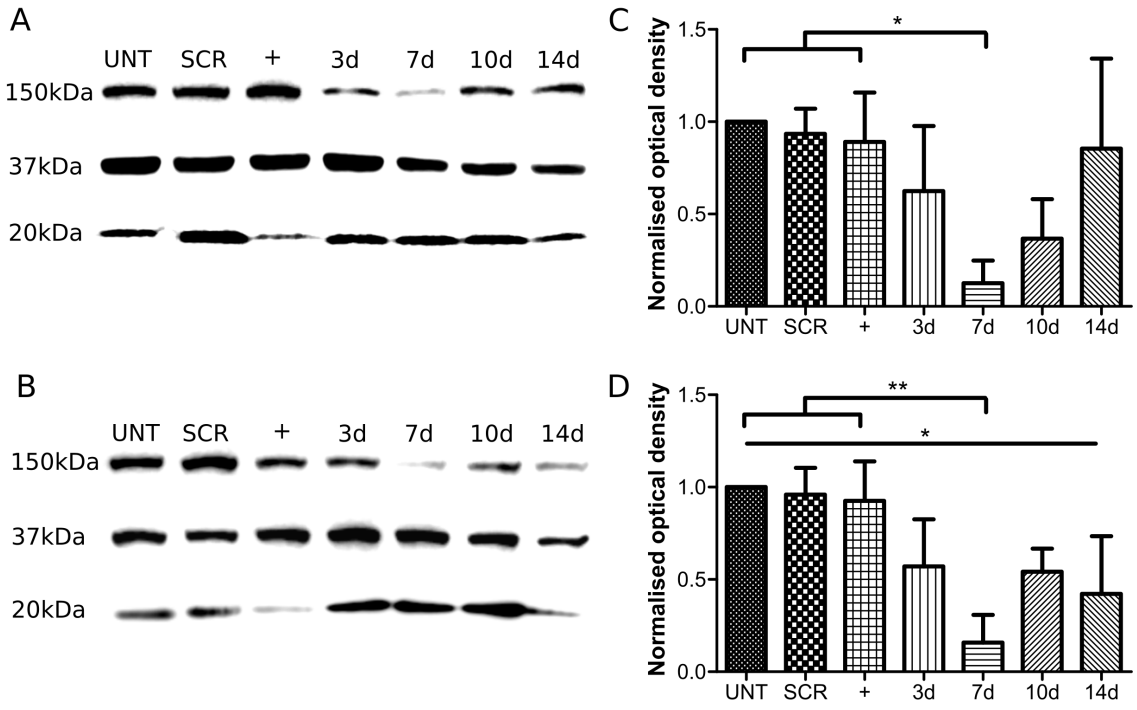


Fig 5.4. Tumour cell ITGA4 protein quantitation following siRNA transfection. Representative Western blot images of ITGA4, GAPDH and cyclophilin B (PPIB) protein expression for (A) MDA231Br-GFP and (B) H1_DL2 cells treated with ITGA4-06 siRNA against at 4 different time points: 3d, 7d, 10d and 14d. Control groups with UNT, non-targeting scrambled (SCR) and PPIB positive knockdown (+) cells were used as comparison. Corresponding normalised mean optical densities, from 3 experimental repeats, were calculated showing relative knockdown of ITGA4 expression compared to control cohorts for (C) MDA231Br-GFP and (D) H1_DL2 cells (*$p<0.05$, **$p<0.01$); error bars denote SD.

The cellular expression of ITGA4 was confirmed by immunofluorescence, which demonstrated a predominantly cytoplasmic distribution of staining with some membranous component for both cell lines (Fig 5.5A-B). ITGA4 expression was significantly reduced following 7 days post-siRNA transfection with a reduction in mean fluorescent intensity, indicating cellular ITGA4 expression, by 74.4 ± 15.0% ($p<0.05$) and 74.5 ± 21% ($p<0.05$) for MDA231Br-GFP and H1_DL2 cells, respectively.

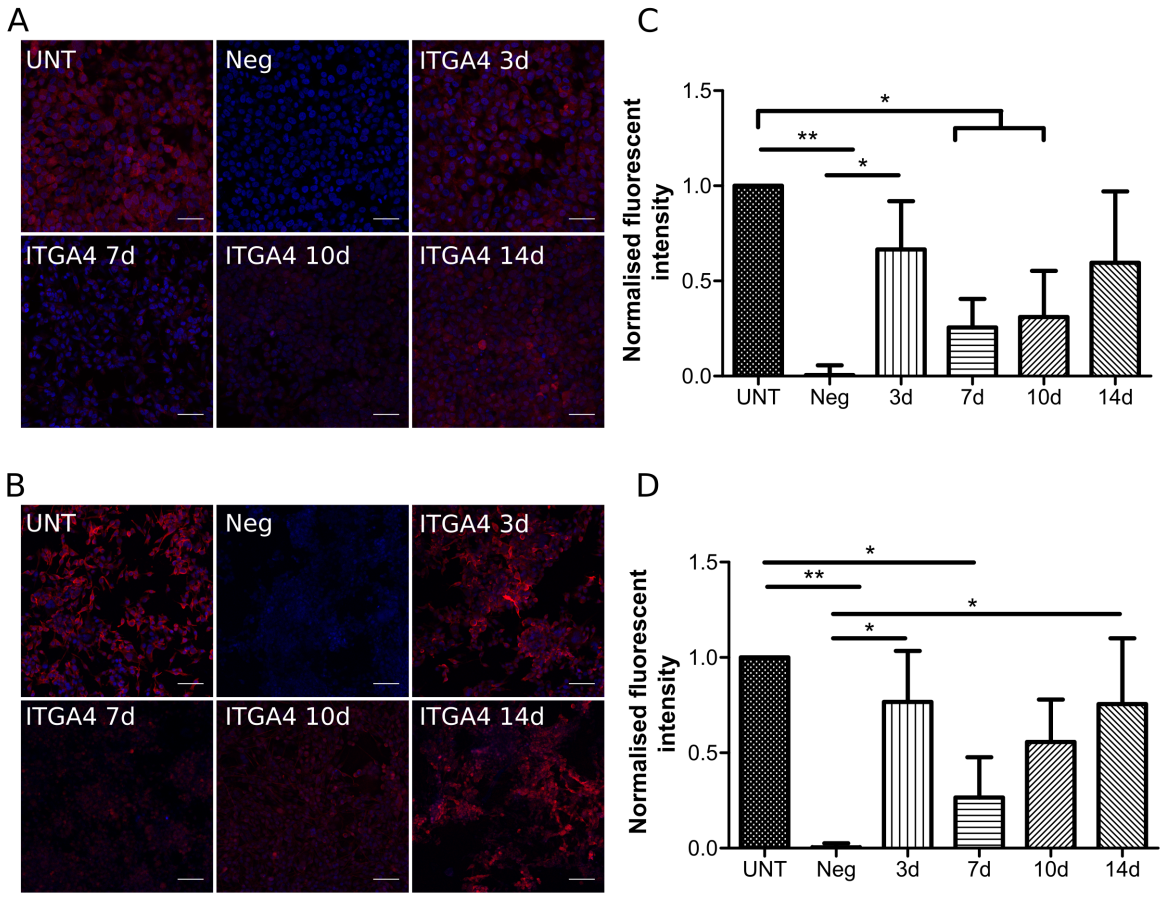


Fig 5.5. Cellular ITGA4 expression following siRNA transfection. Representative immunofluorescence images of (A) MDA231Br-GFP and (B) H1_DL2 cells demonstrating integrin α_4 expression (red), at different time points following ITGA4-06 siRNA transfection, with a DAPI counterstain (blue); scale bar = 50µm. Corresponding normalised mean fluorescent intensities, from 3 experimental repeats, were calculated showing relative knockdown of ITGA4 expression compared to control cohorts for (C) MDA231Br-GFP and (D) H1_DL2 cells (*p<0.05, **p<0.01); error bars denote SD.

5.3.3 Phenotypic profiling of reduced cellular ITGA4 expression

Viability and proliferation of the MDA231Br-GFP and H1_DL2 cells at 3 days and 7 days after treatment with targeted siRNA against ITGA4, as determined by MTT assay, did not show significant differences compared to the UNT cells and control groups (Fig 5.6).

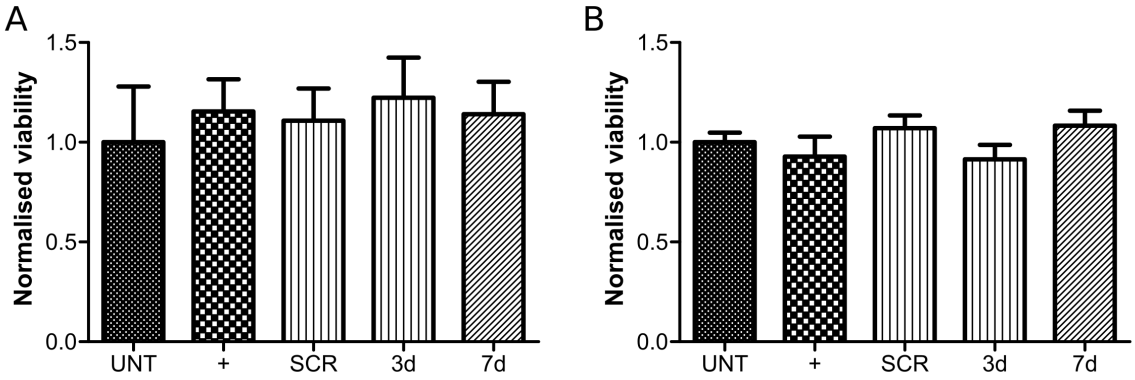


Fig 5.6. MTT assay of ITGA4 siRNA transfected cells. Viability of (A) MDA231Br-GFP and (B) H1_DL2 cells, normalised to the UNT population, at two different time points (3d and 7d) following ITGA4 siRNA transfection was compared against the PPIB kd (+) and SCR control groups. Mean values calculated across 3 experimental repeats and error bars denote SD.

The static binding assay showed that, for both the MDA231Br-GFP and H1_DL2 cells, loss of ITGA4 expression resulted in significant reduction in the number of cells adhering to activated mouse endothelial cells (Fig 5.7). The most marked difference was seen at 7 days following siRNA transfection, with a reduction from 4.2 ± 0.6 bound UNT tumour cells per mm^2 to 0.1 ± 0.3 bound transfected tumour cells per mm^2 for MDA231Br-GFP ($p<0.001$). Meanwhile, the effect on H1_DL2 cells was similar, though less dramatic, with a reduction from 3.1 ± 0.8 bound UNT tumour cells per mm^2 to 0.2 ± 0.3 bound transfected tumour cells per mm^2 ($p<0.05$). At the later time points, the ability of the transfected tumour cells to adhere to the endothelial monolayer remained suppressed up to 10 days, however this was only significant for the MDA231Br cells with a reduction to 1.6 ± 0.7 bound transfected tumour cells per mm^2 compared to the UNT group ($p<0.05$). No difference in the quantities of bound tumour cells was evident between the UNT group and the tumour cells with the shortest treatment period of 3 days for both cell lines.

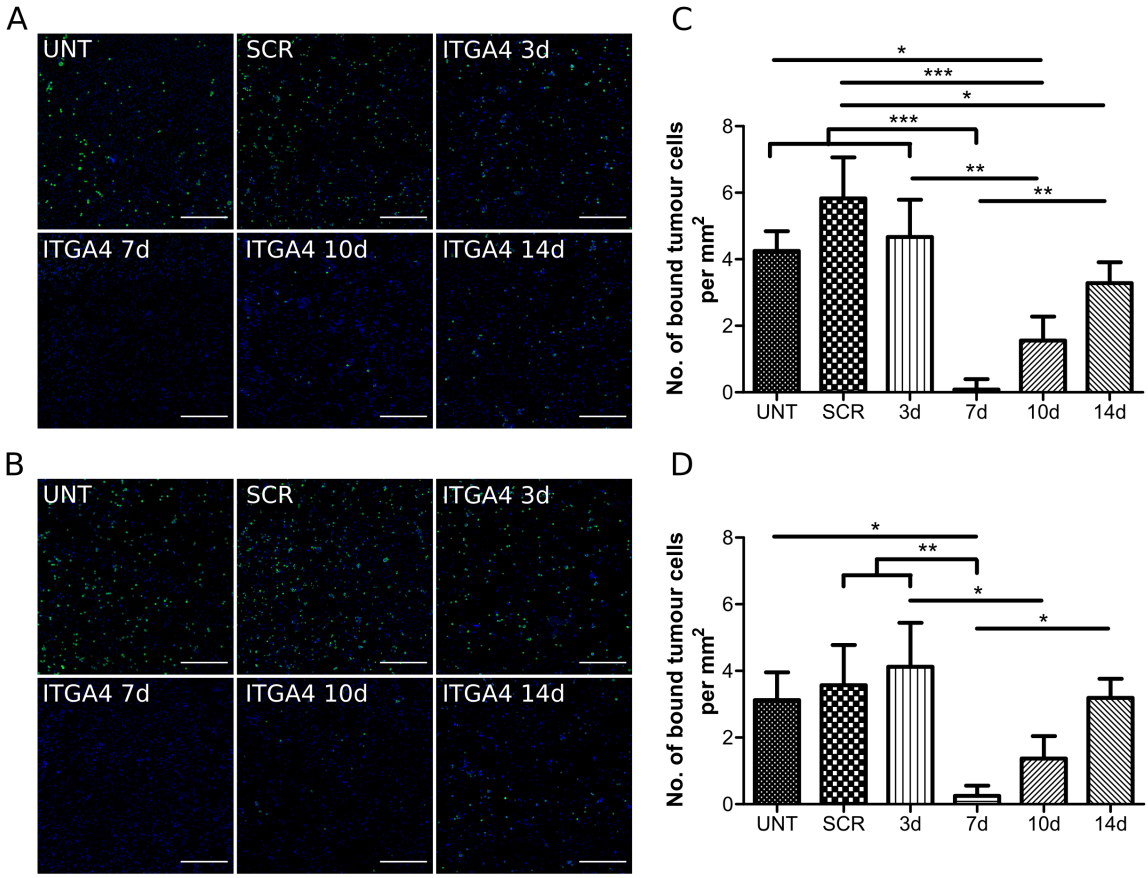


Fig 5.7. Static binding assay of ITGA4 knockdown tumour cells. Representative immunofluorescence images of (A) MDA231Br-GFP and (B) H1_DL2 cells (green) bound to a monolayer of activated sEND-1 cells counterstained with DAPI (blue), for different time points following ITGA4 siRNA transfection; scale bar = 1.5mm. The mean number of bound (C) MDA231Br-GFP and (D) H1_DL2 cells were quantified across 3 experiments, for 4 time points following ITGA4 siRNA transfection (*p<0.05, **p<0.01, ***p<0.001).

Transendothelial migration, as measured by the number of tumour cells migrating through a brain endothelial barrier in a Transwell assay, was significantly different across the different treatment groups for both MDA231Br-GFP ($p < 0.005$) and H1_DL2 ($p < 0.005$) cells. As shown in Fig 5.8A-B, the migration of tumour cells was significantly disrupted for both MDA231Br-GFP and H1_DL2 cells at the 7 day time point, with a reduction in number of migrating cells of 65.6 ± 14.5% and 74.5 ± 14.5% compared to the UNT cells (both $p<0.05$), respectively. All other

time points for the treated cells showed no significant differences to the UNT group. Moreover, inspection of the tumour cells that had migrated through the endothelial barrier by light microscopy revealed altered morphological characteristics of cells transfected with anti-ITGA4 siRNA. Specifically, in the UNT form, the tumour cells tended to hold a more elongated shape, particularly evident in the MDA231Br-GFP cells (Fig 5.8C). Following siRNA disruption of ITGA4 expression, the MDA231Br-GFP cells carried a more rounded morphology with the greatest number occurring in the 7 day time point. Similar changes were observed with the H1_DL2, although the elongated morphology in UNT was generally less pronounced (Fig 5.8D).

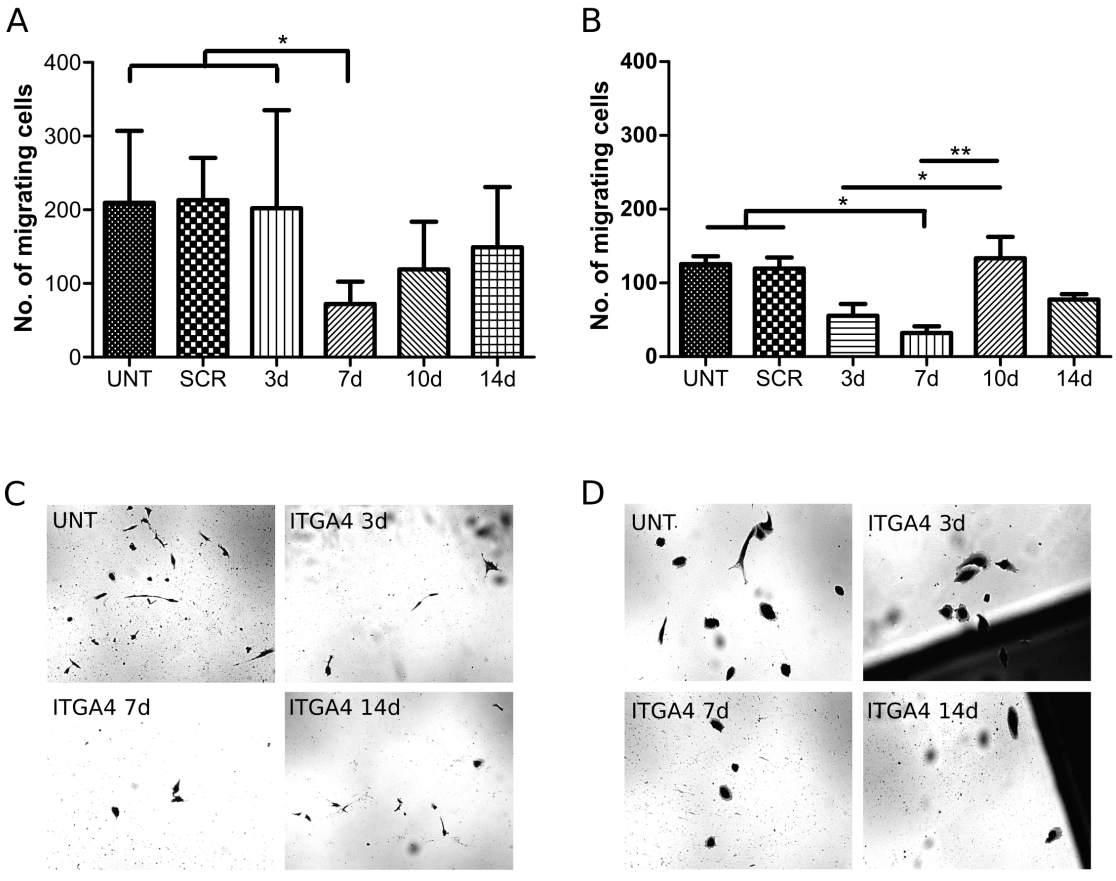


Fig 5.8. Transwell assay of ITGA4 knockdown tumour cells. (A) MDA231Br-GFP and (B) H1_DL2 cells were seeded onto a fully confluent monolayer of hCMEC/D3 human microvascular endothelial cells on Transwell semi-permeable inserts. 24hrs later, cells that had migrated through the barrier

were counted. Various time points were selected following ITGA4 siRNA transfection and four technical repeats were performed for each group. The columns represent mean values of 3 experimental repeats and error bars denote SD (*p<0.05, **p<0.01). Both (C) MDA231Br-GFP and (D) H1_DL2 cells demonstrated changes in morphological characteristics following ITGA4 siRNA transfection.

5.3.4 Effect on *in vivo* brain metastasis development

Based on the *in vitro* findings, the time point for optimum ITGA4 knockdown was chosen to be 7 days after siRNA liposomal transfection. Brains of mice intracardially injected with transfected tumour cells were examined for metastatic burden (Fig 5.9). A trend towards a reduction in metastatic burden was apparent for MDA231Br-GFP tumours, with a mean total volume of 0.041 ± 0.01µL in the UNT group compared to 0.033 ± 0.03µL in the ITGA4 siRNA transfected group; however, owing to the large variability the difference was not significant. Comparing the metastasis volume across the UNT, the scrambled negative control and the ITGA4 transfected groups showed a significant difference in metastatic burden for H1_DL2 metastases (ANOVA; $p < 0.05$). Post-hoc analysis showed a significant difference between the SCR and ITGA4 kd groups ($p < 0.05$). However, significance between the UNT and the ITGA4 siRNA transfected groups was not reached, despite a reduction in the mean total volume from 0.059 ± 0.019µL to 0.038 ± 0.0096µL.

The number of metastatic deposits in the brain was not significantly reduced by ITGA4 knockdown for either tumour models; although, again, there was a trend towards a reduction. The average number of MDA231Br-GFP metastases fell from 69.5 ± 30.4 tumours or 37.5 ± 0.71 tumours, for the SCR and UNT groups respectively, to 17.8 ± 21 tumours in the ITGA4

siRNA transfected group (p = 0.072). Similarly, the average number of H1_DL2 metastases fell from 73.5 ± 30.8 tumours or 57.6 ± 15.6 tumours, for the SCR and UNT groups respectively, to 41.3 ± 15.4 tumours in the ITGA4 siRNA transfected group (p = 0.052).

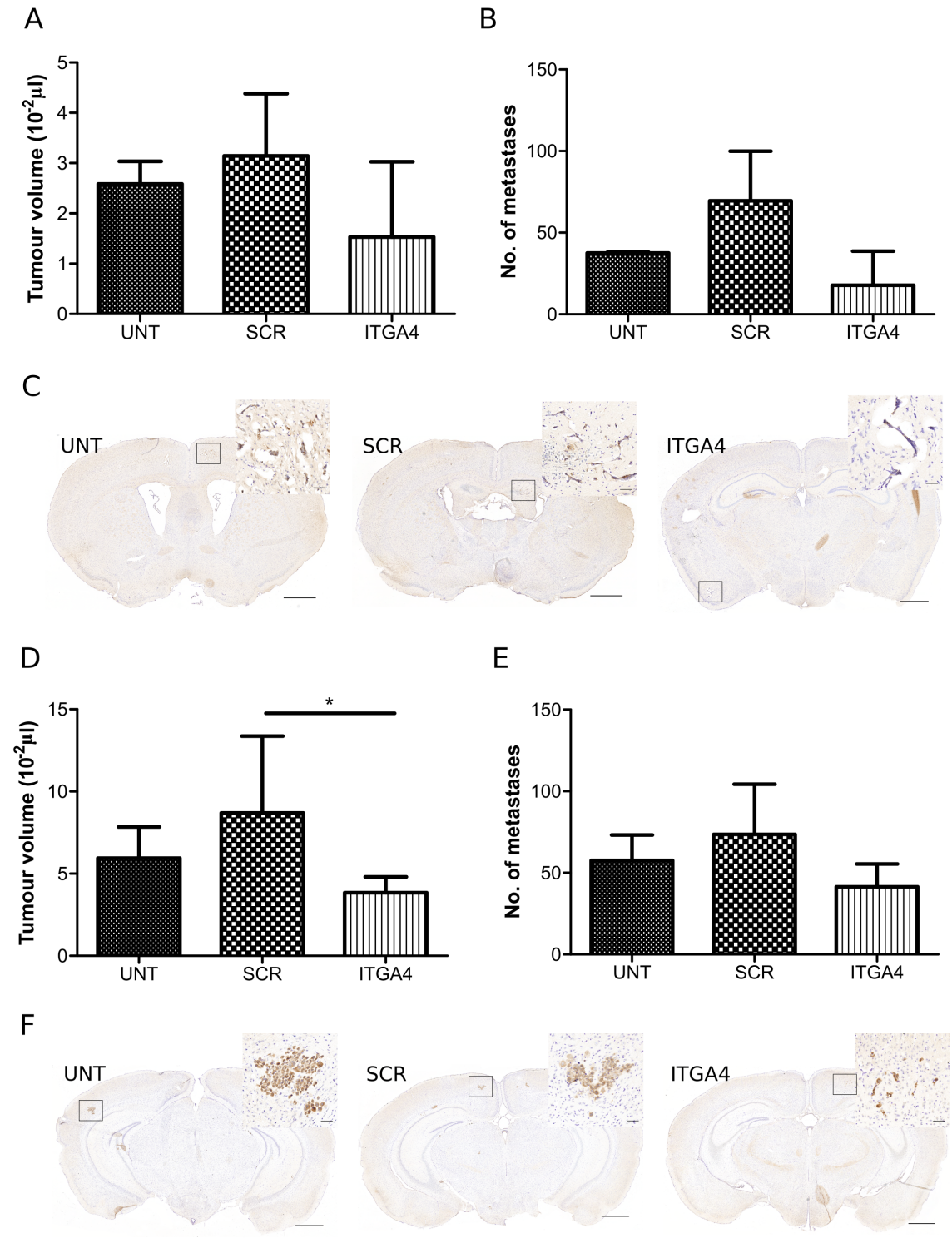


Fig 5.9. *In vivo* brain metastases from ITGA4 knockdown tumour cells. Metastatic burden in the brain from MDA231Br-GFP tumours, measured by (A) total tumour volume and (B) number of metastases, after 21 days was compared between UNT, SCR and ITGA4 siRNA-treated cohorts; error bars denote SD. (C) Representative images of brain tissue sections from each group; scale bar = 1mm. Inset images highlight a typical section of MDA231Br-GFP brain metastasis (black box) for each group; scale bar = 50μm. (D-F) Similar results were seen with H1_DL2 tumours (*p<0.05).

5.4 Discussion

5.4.1 Disruption of VLA-4 expression interferes with tumour cell adhesion and migration

Here, I have shown that VLA-4, a heterodimeric integrin composed of an α_4 and a β_1 subunit, is present on human tumour cells of 2 different cancer types that commonly metastasise to the brain: breast cancer and melanoma. Its presence was successfully disrupted by targeting the function of the ITGA4 gene through RNAi, using siRNA delivered intracellularly in a liposomal vehicle, as evidenced by reduced protein synthesis and cellular expression. Furthermore, the downregulation was shown to be delayed, with maximum knockdown occurring after 3 days for both cell lines and expression levels starting to recover from 7 days onwards. This delay in downregulation would be consistent with previous findings suggestive of a low cellular turnover of the α_4 molecule (209). Moreover, the recovery pattern is in keeping with disruption at the transcriptional level.

Examination of the impact of ITGA4 knockdown on tumour cell phenotype revealed that treated cells had a reduced capacity to bind to activated endothelial cells. The ability to adhere appeared to positively correlate with the expression of VLA-4, as the greatest reduction in cell adhesion occurred at 7 days post-siRNA transfection compared to either the control groups or

the other time points. Similarly, at the 7 day time point, tumour cells were least able to transmigrate through a brain microvascular endothelial barrier compared to either the UNT or SCR control groups or the other time points. Consequently, the *in vitro* results clearly highlight the importance of VLA-4 for the attachment of tumour cells and their subsequent transmigration across the endothelium, as previously reported (208, 210, 211).

The altered cell morphology and function following VLA-4 disruption points to an inability to adhere to the substratum. There is existing evidence that VLA-4 is intimately associated with the cytoskeletal scaffold via adaptor proteins, with α_4-integrin adhesiveness being predominantly regulated by paxillin (212, 213). Besides the importance of this cytoskeletal integration for intracellular mechanotransductive signalling, paxillin has been shown to enable resistance to mechanical shear stress by the VLA-4/VCAM-1 bond, as well as modulating focal adhesion turnover (213-215). Moreover, it has been shown that activated VLA-4 is localised at the leading edge of lamellipodia in migrating cells (216, 217); thus further implicating its role in cell motility. Given the diverse role of VLA-4 in cell function and survival, the demonstration that ITGA4 knockdown was not associated with loss of cell viability or reduced metabolic function was particularly vital.

5.4.2 Brain metastasis seeding is attenuated by VLA-4 disruption

Interestingly, despite the apparent effect of disrupted VLA-4 function on cell motility and transendothelial migration *in vitro*, the impact on *in vivo* brain metastasis formation was less apparent. Although there was a trend towards a reduction in total brain metastasis volume with the MDA231Br-GFP ITGA4 kd cohort, no significant decrease in total brain metastases burden was found. Similarly, a stronger trend towards a reduction in the number of brain

metastases for the MDA231Br-GFP ITGA4 kd cohorts was evident, but did not quite reach significance. For the H1_DL2 ITGA4 kd groups similar results were found, although in this case a significant reduction in tumour volume was observed between the SCR and ITGA4 kd groups. Based on the current results, with a false negative error (β-error) of 0.2 and a false positive error (α-error) of 0.05, sample size calculations suggest that a significant difference in total brain metastasis volume between untreated and VLA-4 knockdown cohorts would have been detected with a sample of either 111 or 7 animals, for MDA231Br-GFP and H1_DL2 models respectively. The same calculations for detecting a significant difference in the number of brain metastases between untreated and VLA-4 knockdown cohorts would have been possible with sample sizes of either 9 or 8 animals, for MDA231Br-GFP and H1_DL2 models respectively.

The current findings are broadly comparable to data previously reported by Soto *et al*., in which no significant difference was found in metastatic tumour volume in the brain between MDA231Br cells treated with an anti-integrin α_4 blocking antibody and untreated MDA231Br cells (58). However, this same study did show a significant reduction in the number of MDA231Br brain metastases following treatment of the cells with the anti- integrin α_4 blocking antibody. For lung metastases, it has been shown that the number of tumours is greatly attenuated by disruption of VLA-4, either by treatment with a neutralising antibody or by RNAi; although statistical significance is not achieved when comparing the untreated and the VLA-4 knockdown cohorts directly (59, 208).

5.4.3 RNAi to achieve VLA-4 knockdown

The degree of knockdown of VLA-4 protein expression by transfected siRNA in the current work exceeded the amount reported in studies using either similar or alternative techniques.

Indeed, here a reduction of around 85% was achieved, whereas an effect on *in vitro* function and *in vivo* metastatic seeding was previously seen with a reported reduction in VLA-4 expression of 40 to 60% (58, 59, 208, 211). To explain this observation despite the incomplete knockdown, Schlesinger *et al.* inferred that cell binding was not dependent on complete involvement of all VLA-4 molecules and/or that this process requires a certain threshold of functional molecules (208). The question of functionality is important, as the VLA-4 molecule is known to have multiple conformational states that correspond to differing functional activity (218, 219). Consequently, the measured total integrin α_4 subunit by Western blot and immunofluorescence in the resting state may not be a true reflection of the quantity of functional VLA-4, leading to an overestimation of the knockdown effect.

ITGA4 knockdown was achieved using antisense siRNA that was delivered intracellularly in a liposomal carrier vehicle. This is a widely used method for post-transcriptional gene silencing by RNAi and is known to provide an efficient and relevant means of interrogating gene function. In addition, synthetic siRNAs are the main form of RNAi-therapies currently under investigation and, therefore, they represent a clinically relevant method of disrupting gene function (220). Previous studies investigating the metastatic potential of tumour cells have shown that VLA-4 expression can be successfully disrupted using siRNA targeted against ITGA4 (208, 211). However, as demonstrated in this study, the disruption is only temporary and gene silencing is usually lost at approximately 7 days in rapidly dividing cells, consequent to a dilution effect (221). As tumour cells typically extravasate within 1 to 3 days of entering the host circulation, even a transient knockdown of protein expression should be adequate for assessment of impact on tumour seeding, provided an appropriate time point is selected.

The *in vivo* experiments were performed with cells that had been transfected 7 days previously, as the tumour cells were shown to have the least VLA-4 expression at this time point. A gradual recovery in VLA-4 expression at subsequent time points, with associated improvement in cell adhesion and transendothelial migration, both vital in the extravasation process. This raises the possibility that following injection of the tumour cells there is functional recovery of VLA-4 expression leading to reacquisition of binding and invasion properties; thus, reducing the effect of knocking down VLA-4 expression.

An alternative approach to RNAi is to use short hairpin RNA (shRNA), which is commonly introduced into the mammalian cell genome via lentiviral or plasmid vectors. The integrated shRNA sequence becomes transcribed into siRNA duplexes, which bind to the target mRNA and lead to their degradation via the RNA-induced silencing complex (RISC); thus preventing translation of the protein of interest (222). This approach has the benefit of generating a stable knockdown of the target protein and can have a higher chance of successful knockdown compared to exogenous siRNA in some cells (223). Previous studies have shown that shRNA introduction can selectively inhibit the expression of VLA-4 in malignant cells (59, 224). Furthermore, more recently developed gene editing techniques, such as the clustered regularly interspaced palindromic repeats (CRISPR)/CRISPR-associated 9 (Cas9) protein and transcription activator-like effector nucleases (TALENs), have opened the opportunity for highly precise gene modification to elucidate its function (225, 226) and has been previously demonstrated in VLA-4 knockdown (227).

5.4.4 Beyond the VLA-4/VCAM-1 interaction

Here, tumour-expressed VLA-4 has been presented as an important molecule in the development of brain metastasis through the initiation of tumour cell attachment at the endothelium, as part of the stepwise cascade leading to colonisation of the brain. This interaction is largely mediated by docking with its natural ligand, endothelium-expressed VCAM-1, and to a lesser extent with the extracellular matrix glycoprotein, fibronectin. However, as previously discussed, the role of VLA-4 in malignancy is far more diverse and complex. Unusual amongst the β_1 integrins, VLA-4 is involved in cell-cell interactions and previous studies have implicated it in both heterotypic and homotypic aggregation of natural killer (NK) cells, B- and T-lymphocytes (228-230). Therefore, VLA-4 may have immunomodulatory effects that are exploited by tumour cells to survive in the face of a hostile host immune system. VLA-4 has also been shown to permit the specific distribution of circulating bone marrow-derived progenitor cells to sites of active neovascularisation, which is thought to play a role in priming a distant organ for future tumour seeding through establishment of a premetastatic niche (231-233). This homing mechanism may also be directly used by tumour cells, as tumour-expressed VLA-4 preferentially binds to VCAM-1 on actively remodelling vessels.

Accordingly, given the multitude of favourable effects VLA-4 confers on tumourigenicity, it was perhaps more surprising that a stronger inhibition was not seen on brain metastasis development *in vivo* following VLA-4 disruption. An acknowledgement needs to be made on the limitations of the *in vivo* xenograft model used, as the lack of a fully competent immune system may have negated some of the effects of VLA-4; thus, underplaying its significance in

metastatic seeding in the brain. Moreover, the question as to why tumour cells that do not express VLA-4 may still be highly metastatic is explained by the presence of accessory mechanisms mediating the critical steps of extravasation from the circulation (234). Indeed, a wide range of ligands and receptors including integrins, cadherins, selectins and Ig superfamily have been shown to modulate the heterotypic adhesion between tumour cells and the endothelium. Therefore, even with the significant degree of VLA-4 knockdown achieved in this work, the effect on tumour seeding may have been counteracted by these other mechanisms.

Integrins provide a direct link between the extracellular and the intracellular environments, through ligand binding and triggering of cytoskeletal components. Thus, integrin-mediated adhesion, such the VLA-4/VCAM-1 interaction, may be regulated through a process called inside-out signalling or priming, whereby external factors including cytokines and foreign antigens act on the cell to induce conformational changes in the VLA-4 molecule from a resting phase to activation and *vice versa*; thus impacting on its adhesiveness to the VCAM-1 ligand (235). Furthermore, the adhesion of VLA-4 to VCAM-1 causes redistribution or clustering of additional VLA-4 molecules, as well as sequential activation of VLA-5 through outside-in signalling (236-238). This dynamic equilibrium between the inside-out and outside-in signalling pathways is important in successfully modulating the adhesion cascade between the circulating cell and endothelium, as it progresses from initial capture, to cell arrest and finally transmigration. Consequently, whilst a reduction in VLA-4 expression may reduce the efficiency of cell adhesion, the tendency of cells to redistribute residual VLA-4 and recruit other integrins on the cell surface may explain why, in spite of a significant knockdown of VLA-4 expression, the associated decrease in brain metastases was less than expected.

5.4.5 Choice of ITGA4 knockdown

As VLA-4 is a heterodimer, disrupting its function may be achieved through knockdown of either the α_4 or β_1 subunits. In this present work, I had chosen to target the α_4 molecule. This subunit is known to pair *in vivo* with either the β_1 or the β_7 subunits, to form VLA-4 and lymphocyte Peyer's patch adhesion molecule-1 (LPAM-1), respectively. LPAM-1 binds to mucosal addressin cell adhesion molecule-1 (MAdCAM-1) and, like VLA-4, has also been shown to bind to the connecting segment-1 (CS-1) of fibronectin (239). Moreover, the α_4 subunit may interact directly with another α_4-subunit, permitting binding in a homotypic fashion (240).

It has previously been shown that the pre-β_1 subunit is produced in excess at the endoplasmic reticulum, meaning the quantity of pre-α subunit represents the limiting factor in the expression of β_1 integrins (241); thus, highlighting the α_4 subunit as the preferred target for disruption of VLA-4 expression over the β_1 subunit. Furthermore, the β_1 subunit is known to combine with 6 different α subunits (242), to form the VLA subfamily, which are all involved in cellular adhesion. Therefore, targeting the β_1 molecule would have been more likely to induce unintended knock-on effects and would compromise the interpretation of the effect of VLA-4 disruption. Moreover, previous attempts to disrupt the β_1 subunit has yielded conflicting results, which is thought to reflect the dynamic regulation of cell behaviour by β_1 that is influenced by the tissue microenvironment (243, 244). It should be noted that, since the integrin expression profile was not fully characterised for the 2 tumour cell lines used in this work, it is not possible to comment on specific downstream effects. However, it is conceivable that variation in this expression profile may account for the differences in the observed brain metastasis formation following VLA-4 knockdown.

5.4.6 Translational potential of disrupting the VLA-4/VCAM-1 interaction in cancer

As part of the interface between the primary tumour and the distant organ, the vascular endothelium represents a crucial gatekeeper and the binding of tumour cells to this intermediary may be therapeutically targeted to prevent the entry of disseminated tumour cells into the target organ. The VLA-4/VCAM-1 interaction provides an attractive target that has been extensively investigated for its role in cancer metastasis. Here, I have shown that the VLA-4/VCAM-1 interaction is an important step in the cell adhesion and transmigration cascade and is functionally relevant in two different tumour types. However, in terms of the impact on *in vivo* development of brain metastases based on xenograft mouse models following intracardiac injection of tumour cells, for reasons previously discussed, this effect is much less pronounced. Nevertheless, the tentative reduction in number of brain metastases seen in both tumour types tested and the significant reduction in metastatic tumour volume in the H1_DL2 cohort suggests that the disruption of tumour cell attachment to the secondary organ vasculature via the VLA-4/VCAM-1 interaction is, at least in part, an important contributor towards successful tumour colonisation.

An additional reason for exploring VLA-4 as a target is the availability of a clinically approved humanised monoclonal antibody, natalizumab, against the human integrin α_4 chain. This antibody is able to fully blockade α_4 molecules and their interaction with ligands, such as VCAM-1. By doing so, natalizumab has been proven to be of therapeutic benefit to people with serious inflammatory disorders, like relapsing-remitting multiple sclerosis (245, 246) and inflammatory bowel disease (247). To date, according to the ClinicalTrials.gov database of clinical studies conducted worldwide, there has only been one clinical trial in cancer

specifically multiple myeloma, although the study was terminated early due to poor recruitment (248). Even so, therapies targeting integrins and their receptors continue to be a source of investigation for tackling cancer (249). Furthermore, developments of newer small molecule agents that block the action of VLA-4 through various mechanisms means that more options may become available in the future that may be tested to prevent brain metastasis (250-253).

In a clinical context, consideration of the impact of reduced VLA-4 expression on the primary tumour is vital, as it is not considered in the *in vivo* models presented here. As previously stated, CAMs play an important role in cell adhesion and can suppress tumourigenesis by controlling cell proliferation through contact inhibition, as well as preventing cellular dissociation (254, 255). This was reinforced by Qian *et al*., who observed that when VLA-4 expression was inhibited, melanoma cells in the primary tumour lost homotypic cell adhesion and were more likely to invade and disseminate to form pulmonary metastasis (71).

5.4.7 Future work

Although a link between the VLA-4/VCAM-1 interaction and brain metastasis development has been established, using murine xenograft models of breast cancer and melanoma brain metastases, it is apparent that the role of CAMs in the adhesion cascade leading to the extravasation of circulating tumour cells is a complex process that warrants further investigation. Specifically, to address the limitations in the study, it would be appropriate to expand the number of timepoints examined for ITGA4 knockdown, particularly to determine if there is a more optimum window for *in vivo* testing. By selecting the most prolonged period where VLA-4 expression remains at trough levels, the risk of contamination due to recovery

of ITGA4 production following siRNA knockdown would be minimised. Furthermore, based on the promising results presented here, future work with alternative gene-silencing techniques, such as shRNA or CRISPR is recommended.

Future studies characterising the CAM profile of metastatic tumour cells are warranted. Moreover, disrupting a combination of CAMs rather than a single CAM may prove more effective at reducing brain metastasis seeding. Finally, the use of systemically delivered agents to block cellular adhesion, including the VLA-4/VCAM-1 interaction, and prevent tumour cell seeding on the brain endothelium should be studied and, importantly, their potential impact on the primary tumour. Further beyond the scope of this current work, rather than focusing solely on Paget's "seed", i.e. the tumour cell expression of CAMs, an interesting future area of focus will be to determine if the "soil", i.e. the pre-metastatic niche, may be successfully manipulated to prevent seeding of disseminated tumour cells.

CHAPTER 6: DISCUSSION

6.1 The translational gap in brain metastasis research

Invasion and metastasis are two of the most devastating consequences of cancer and, collectively, are the prime cause of patient morbidity and mortality (8). Cancer that spreads to the brain typically represents the terminal phase in the course of a patient's illness (256, 257). The widening availability of both effective local and systemic treatment options for brain metastases provides reason for optimism regarding its management in the future. However, there remain a number of clinical challenges that hamper our goal of effectively controlling this disease, specifically in the diagnosis and prevention of brain metastases.

The process by which malignant cells develop metastatic potential and detach from the primary tumour, leading to colonisation of a distant organ, is complex. This invasion-metastasis cascade is usually presented as a linear sequence of biological events (258); however, this theory fails to resolve the organ specific tropism observed in certain tumour types (12). Indeed, it is well-documented that lung cancer, breast cancer and melanoma have a higher risk of metastasising to the brain compared to other primary tumour types (23), although there remains an overall much greater tendency to metastasise to organs other than the brain. Our understanding of cancer biology has shifted dramatically in recent decades, with the recognition that cancer is a heterogeneous disease. The clonal evolution of cancer cells, both within a tumour and following metastatic spread between tumours, highlights the challenge of developing a single targeted approach against cancer (19, 259, 260), be that diagnostic or therapeutic.

An alternative solution is to utilise the interaction between the cancer cells and the normal tissue. Cell adhesion molecules are a group of cell surface glycoproteins that play a significant role in cancer invasion and metastasis, through facilitation of cell attachment and migration. Very late antigen-4 (VLA-4) and vascular cell adhesion molecule-1 (VCAM-1) are complementary adhesion molecules expressed on some tumour cells and on activated endothelial cells, respectively. The VLA-4/VCAM-1 interaction has been shown to contribute to metastasis formation, although its role in the development of brain metastasis is less well understood (58). Furthermore, cancer is also known to stimulate changes in its microenvironment that make it more conducive for tumour survival, which is partly mediated through pro-inflammatory cytokines. Brain endothelial cells have low constitutive expression of VCAM-1 when unstimulated (261), so its upregulation on vessels in proximity to breast cancer brain metastases, demonstrated in rodent models and post-mortem human tissue (94), suggests that endothelial VCAM-1 is a sensitive surrogate biomarker for metastatic disease.

In this thesis, I investigated the role of VLA-4 and VCAM-1 in brain metastases with a focus on three different themes:

1. The natural course of brain metastasis development for three different human tumour cell lines – MDA231Br-GFP, H1_DL2 and SEBTA-001 – engrafted into immunocompromised mice. The presence of endothelial VCAM-1 upregulation according to tumour type and the application of VCAM-1 targeted magnetic resonance imaging (MRI) to detect micrometastases from different primary tumours (Chapter 3);
2. Correlation of VCAM-1 expression at the human brain metastasis invasive margin and its potential for enhancing delineation of the tumour border. Intrastriatal xenograft rat

models, for MDA231Br-GFP and U87 cells, were used to interrogate tumour biology at the invasive margin and the application of VCAM-1 targeted MRI to detect the tumour border (Chapter 4); and

3. The VLA-4 expression of the MDA231Br-GFP and H1_DL2 tumour cell lines and the impact of gene silencing with small interfering ribonucleic acid (siRNA) targeted against the integrin α_4 subunit. *In vitro* and *in vivo* data are presented demonstrating the impact of VLA-4 knockdown on tumour cell metastatic potential (Chapter 5)

6.2 VCAM-1 targeted MRI enables detection of brain micrometastases from different primary tumours

Diagnosis of brain metastases is reliant on non-invasive imaging, with MRI being the preferred imaging modality owing to its superior tissue characterisation of the brain. However, the gold standard of gadolinium contrast-enhanced MRI is limited by the need for passive extravasation of contrast, which only occurs if the BBB is disrupted. Therefore, conventional MRI techniques are currently unable to detect brain micrometastases, as these do not cause BBB breakdown. An intravascular MRI contrast agent using MPIO conjugated with anti-VCAM-1 antibodies (VCAM-MPIO) has been shown *in vivo* to specifically bind to upregulated VCAM-1 associated with acute neuroinflammation (262). Serres *et al* demonstrated the feasibility of detecting breast cancer micrometastases in the brain using intracardiac syngeneic and xenograft mouse models (94). However, to maximise clinical potential, ideally the contrast agent would also be applicable to other tumour types.

In Chapter 3, I characterised xenograft mouse models of breast cancer, melanoma and lung adenocarcinoma brain metastases. Using the intrastriatal method of introducing tumour cells, I established that each of the tumour models had a different growth pattern in the brain and, after the tumour cells were disseminated via injection into the left cardiac ventricle, were capable of establishing metastatic colonies in the brain with a distinct micrometastatic phase. Furthermore, through histological examination, I demonstrated that VCAM-1 is upregulated in the micrometastatic phase and that activation of VCAM-1 was co-localised to blood vessels in close proximity to micrometastases.

With the relevant tumour models and timepoints, I applied VCAM-1 targeted MRI to test the hypothesis that this MRI technique could detect brain micrometastases. The findings support the concept that the VCAM-MPIO contrast agent binds specifically to upregulated VCAM-1 on the luminal surface of blood vessels associated with brain metastases and causes signal distortion on T_2^*-weighted MRI that is visualised as focal hypointensities. Moreover, detection at the micrometastastatic stage was confirmed through lack of BBB breakdown seen on gadolinium contrast enhanced T_1-weighted MRI. Finally, the clinical relevance of VCAM-1 as a surrogate biomarker of brain metastases was confirmed through histological examination of stereotactic image-guided biopsies of human brain metastasis, which showed that abundant VCAM-1 expression was present on the endothelium of blood vessels adjacent to the tumour border and nearby invading micrometastatic foci.

Therapeutic intervention for brain micrometastases is not a new concept and has been successfully applied in the management of small cell lung cancer (SCLC) through prophylactic cranial irradiation (PCI), which has been shown to provide a significant survival advantage even

for patients with limited stage disease (150). The term prophylaxis is a misnomer, as it suggests that PCI is effective in preventing metastatic disease in the brain. In reality, PCI is only beneficial to patients where metastatic seeding in the brain has already occurred, but is undetectable with existing imaging techniques. A similar strategy for PCI has not been shown to lead to a survival advantage in non-small cell lung cancer (NSCLC). However, the RTOG 0214 study showed a clear reduction in risk of developing brain metastases, from 18% in patients under observation alone to 7.7% in those receiving PCI (263), implicating the presence of micrometastatic disease in locally advanced NSCLC. Given the concerns around the neurocognitive sequelae arising from PCI (264, 265), the opportunity to separate patients with brain micrometastatic disease likely to derive the greatest benefit from adjuvant therapies will further enhance the personalisation of care. This paradigm represents just one facet in which detection of brain micrometastases may improve outcomes for patients in the future.

6.3 VCAM-1 targeted MRI enhances detection of the invasive margin in brain metastases

To attempt to detect the invasive margin of brain metastases may appear counter-intuitive, since prevailing clinical practice assumes that brain metastases are well-encapsulated tumours that do not infiltrate into the surrounding brain parenchyma. This viewpoint is evident in the application of local therapies, such as the lack of clinical target volume (CTV) and planning target volume (PTV) beyond the contrast-enhancing tumour in stereotactic radiosurgery (SRS) (266, 267) and the continued surgical recommendation for gross total resection (GTR) (37). However, with a growing body of evidence for the invasive potential of brain metastases (170-172), there is increasing advocacy for the inclusion of a safety margin through a widened CTV (268) or supramarginal resection (202) to achieve greater local in-brain control.

In Chapter 4, based on MRI of brain metastasis patients obtained by colleagues at The Walton Centre NHS Foundation Trust, I showed that the brain metastasis border is not reliably defined by either gadolinium enhanced T_1-weighted or diffusion weighted MR sequences. Furthermore, using stereotactic image-guided biopsies of human brain metastases from our collaborators, I found that VCAM-1 was upregulated on blood vessels adjacent to the tumour border, with more distant VCAM-1 positive vessels likely activated by neighbouring isolated or small clusters of infiltrative tumour cells in adjacent sections.

With xenograft rat models of intrastriatal MDA231Br-GFP or U87 (primary brain) tumours, I found that the interface between the brain tumour invasive edge and the adjacent brain parenchyma was biologically distinct from either the tumour core or the uninvolved brain parenchyma, based on microvessel density, VCAM-1 expression and markers of cellular proliferation and stemness. Importantly, endothelial VCAM-1 expression was greater at the margin indicating its potential utility as a surrogate biomarker of tumour invasion. Application of VCAM-1 targeted MRI revealed that tumour bearing animals had higher levels of hypointensities compared to the control cohorts on T_2^*-weighted sequences, consistent with specific binding of VCAM-MPIO to activated vessels, which was confirmed on histological examination. Although the pattern of hypointensities broadly conformed to the tumour border seen on either T_1- or T_2-weighted sequences, there was also apparent extension of the hypointensities beyond the border observed with those modalities, suggesting sites of microscopic tumour infiltration. Statistical analysis revealed close agreement in the tumour dimensions measured with either VCAM-MPIO imaging or conventional MRI, indicating comparability of the different modalities in defining the tumour. However, qualitative

assessment suggested additional information could be gleaned based on the location of the hypotensities. The lack of tumour visualisation on gadolinium enhanced T_1-weighted imaging for the MDA231Br-GFP, considered the gold standard in MR imaging, highlights the fallibility of using a single parameter approach to characterise tumours and lends weight to the concept that augmenting conventional imaging with VCAM-1 targeted MRI could improve the detection of the invasive margin in brain tumours (primary and secondary).

Use of local therapies to treat brain metastases is reliant on non-invasive imaging to define the tumour geometry in relation to the brain anatomy. Accuracy in delineating the tumour underpins the ability to offer more radical treatment, whilst avoiding damage to healthy tissue. By developing an imaging technique that provides additional information about the edge of the tumour, which is independent of the tumour type, the existing management of brain metastases could be enhanced by removing some of the uncertainty around clinical decision-making. Consequently, more intelligent patient stratification or better treatment planning would be possible, leading to improved patient outcomes.

6.4 Disrupting tumour-expressed VLA-4 to prevent metastatic seeding in the brain

VLA-4 is the natural counterligand for endothelial expressed VCAM-1 and, in its physiological role, contributes to the ability of circulating leucocytes to adhere to and transmigrate through the endothelial layer into the tissue parenchyma at sites of inflammation (269, 270). When tumour cells aberrantly express VLA-4 they can hijack this mechanism for cell-endothelium adhesion to facilitate metastatic seeding (59, 208). However, whether VLA-4 plays a dominant role in metastatic seeding in the brain is unclear. Soto *et al*. previously showed that VLA-4 was abundantly expressed on human and murine breast cancer brain metastases following

intracardiac injection. Furthermore, by inhibiting the action of VLA-4 with neutralising antibodies, the number of metastatic deposits was reduced compared to untreated controls, although no significant difference was found in the overall tumour volume in the brain (58).

In Chapter 5, I showed that VLA-4 expression was present on MDA231Br-GFP and H1_DL2 tumour cells constitutively; indicating that VLA-4 is not tumour type specific. Moreover, utilising a gene silencing approach, with liposomally encapsulated siRNA targeted against the integrin α_4 subunit, I induced a significant, albeit transient, global knockdown of VLA-4 (ITGA4 kd) expression. This knockdown caused phenotypic changes in the tumour cells' morphology, binding capacity and ability to transmigrate across an endothelial barrier, when tested *in vitro*; thus, implicating VLA-4's function in enabling arrest of circulating tumour cells and endothelial transmigration in the presence of VCAM-1. Interestingly, these findings failed to translate into a significant reduction in tumour burden, measured either by total tumour volume or number of metastases, when comparing the ITGA4 kd cells against the untreated cells injected *in vivo*. However, considering the impact of RNAi *per se*, when the ITGA4 kd cells were compared against the cells transfected with a scrambled non-targeting siRNA the effects were more pronounced, with a significant reduction in tumour volume. This finding raises the possibility that the siRNA transfection process may be producing off-target effects that are masking the true impact of VLA-4 knockdown.

Metastasis prevention is a novel strategy for targeting one of the more serious effects of cancer (271, 272). At present, the only approach available in this respect is with adjuvant or neoadjuvant therapies. However, these treatments are only effective where micrometastatic deposition in distant organs has already occurred and are not targeted against circulating

metastatic tumour cells, which have the potential to re-colonise a secondary site. The interface between the circulation and the distant organ is a key gateway through which disseminating tumour cells must pass to enter the tissue parenchyma. By interpreting VCAM-1 and VLA-4 as the lock and key, respectively, to this gateway one can see the attraction of targeting CAMs to counteract the ability of circulating tumour cells to extravasate and seed metastatic deposits. The findings in Chapter 5 do not support the hypothesis that anti-VLA-4 treatment prevents brain metastases formation when targeted in isolation. However, other CAMs are known to be implicated in the process of adhesion and extravasation. Therefore, the observed trend to benefit suggests that further investigation of blocking the VLA-4/VCAM-1 interaction in combination with other CAMs is warranted.

6.5 A new paradigm for managing brain metastases

In this thesis, I have tackled three discrete clinical problems, relating to different phases in the development of brain metastases: disrupting tumour cell extravasation into the brain, detecting early brain colonisation with micrometastases, and delineating the invasive margin of brain macrometastases. As discussed here, and in previous chapters, each scenario contributes to the lethality of brain metastases. By targeting the VLA-4/VCAM-1 axis, I have shown that the diagnosis of brain micrometastases and macrometastases can be improved, and tentatively demonstrated the potential for metastasis prevention through disruption of VLA-4/VCAM-1 binding. As illustrated in Fig 6.1, a combined strategy that incorporates these developments may be adopted and it is vital that their clinical translation should go hand-in-hand with ongoing innovation in new therapies for brain metastases.

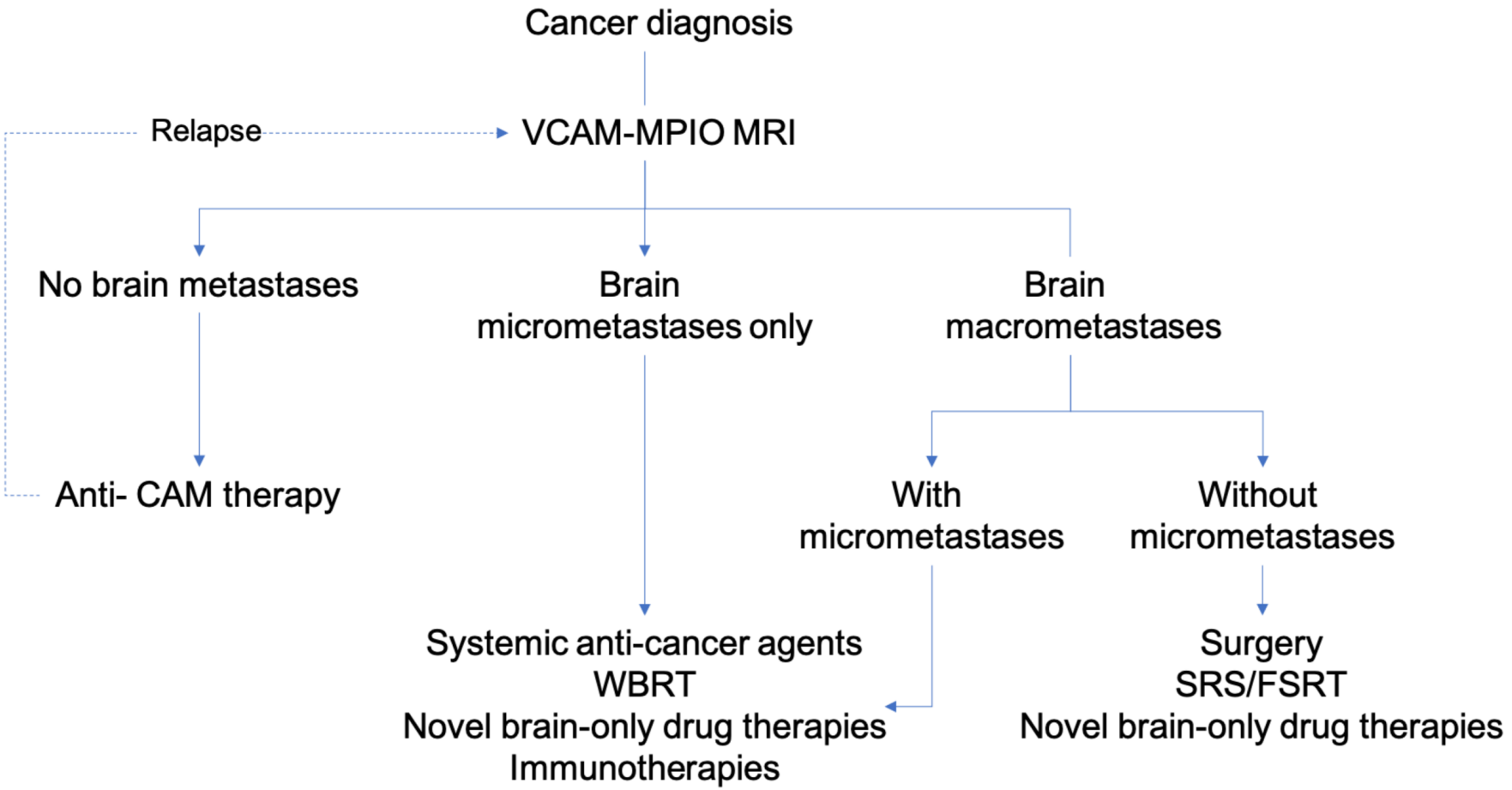


Fig 6.1. Diagnostic and therapeutic strategy against brain metastases using anti-CAM therapy and VCAM-MPIO imaging. Schematic flow diagram illustrating the potential management flow of patients investigated with VCAM-MPIO magnetic resonance imaging (MRI) with different treatment options dependent on diagnosis. WBRT = whole brain radiotherapy; SRS = stereotactic radiosurgery; FSRT = fractionated stereotactic radiotherapy; CAM = cellular adhesion molecule.

REFERENCES

1. Hall JM, Lee MK, Newman B, Morrow JE, Anderson LA, Huey B, et al. Linkage of early-onset familial breast cancer to chromosome 17q21. Science. 1990;250(4988):1684-9.
2. Lynch HT, Casey MJ, Snyder CL, Bewtra C, Lynch JF, Butts M, et al. Hereditary ovarian carcinoma: heterogeneity, molecular genetics, pathology, and management. Mol Oncol. 2009;3(2):97-137.
3. Knudson AG, Jr. Mutation and cancer: statistical study of retinoblastoma. Proc Natl Acad Sci U S A. 1971;68(4):820-3.
4. Loeb KR, Loeb LA. Genetic instability and the mutator phenotype. Studies in ulcerative colitis. Am J Pathol. 1999;154(6):1621-6.
5. Sharma S, Kelly TK, Jones PA. Epigenetics in cancer. Carcinogenesis. 2010;31(1):27-36.
6. Hanahan D, Weinberg RA. The hallmarks of cancer. Cell. 2000;100(1):57-70.
7. Hanahan D, Weinberg RA. Hallmarks of cancer: the next generation. Cell. 2011;144(5):646-74.
8. Chaffer CL, Weinberg RA. A perspective on cancer cell metastasis. Science. 2011;331(6024):1559-64.
9. Baccelli I, Trumpp A. The evolving concept of cancer and metastasis stem cells. J Cell Biol. 2012;198(3):281-93.
10. Brabletz T, Kalluri R, Nieto MA, Weinberg RA. EMT in cancer. Nat Rev Cancer. 2018;18(2):128-34.
11. Agarwal PP, Seely JM, Matzinger FR, MacRae RM, Peterson RA, Maziak DE, et al. Pleural mesothelioma: sensitivity and incidence of needle track seeding after image-guided biopsy versus surgical biopsy. Radiology. 2006;241(2):589-94.
12. Valastyan S, Weinberg RA. Tumor metastasis: molecular insights and evolving paradigms. Cell. 2011;147(2):275-92.
13. Li H, Fan X, Houghton J. Tumor microenvironment: the role of the tumor stroma in cancer. J Cell Biochem. 2007;101(4):805-15.
14. Ewing J. Neoplastic Diseases: A Treatise on Tumours. British Journal of Surgery. 1928;16(61):174-5.
15. Wirtz D, Konstantopoulos K, Searson PC. The physics of cancer: the role of physical interactions and mechanical forces in metastasis. Nat Rev Cancer. 2011;11(7):512-22.
16. Weiss L. Patterns of Metastasis. Cancer and Metastasis Reviews. 2000;19(3):281-301.
17. Chen W, Hoffmann AD, Liu H, Liu X. Organotropism: new insights into molecular mechanisms of breast cancer metastasis. NPJ Precis Oncol. 2018;2(1):4.
18. Paget S. The distribution of secondary growths in cancer of the breast. 1889. Cancer Metastasis Rev. 1989;8(2):98-101.
19. Gerlinger M, Rowan AJ, Horswell S, Math M, Larkin J, Endesfelder D, et al. Intratumor heterogeneity and branched evolution revealed by multiregion sequencing. N Engl J Med. 2012;366(10):883-92.
20. Allison KH, Sledge GW. Heterogeneity and cancer. Oncology (Williston Park). 2014;28(9):772-8.
21. Coffelt SB, de Visser KE. Systemic inflammation: Cancer's long-distance reach to maximize metastasis. Oncoimmunology. 2016;5(2):e1075694.
22. Wu Y, Zhou BP. Inflammation: a driving force speeds cancer metastasis. Cell Cycle. 2009;8(20):3267-73.

23. Nayak L, Lee EQ, Wen PY. Epidemiology of brain metastases. Curr Oncol Rep. 2012;14(1):48-54.
24. van Meerbeeck JP, Fennell DA, De Ruysscher DK. Small-cell lung cancer. Lancet. 2011;378(9804):1741-55.
25. CRUK. Statistics by cancer type 2018 [Available from: https://www.cancerresearchuk.org/health-professional/cancer-statistics/statistics-by-cancer-type].
26. Andreucci M, Solomon R, Tasanarong A. Side effects of radiographic contrast media: pathogenesis, risk factors, and prevention. Biomed Res Int. 2014;2014:741018.
27. Basu S, Alavi A. Molecular imaging (PET) of brain tumors. Neuroimaging Clin N Am. 2009;19(4):625-46.
28. Xie D, Xie K. Pancreatic cancer stromal biology and therapy. Genes Dis. 2015;2(2):133-43.
29. Tong X, Srivatsan A, Jacobson O, Wang Y, Wang Z, Yang X, et al. Monitoring Tumor Hypoxia Using (18)F-FMISO PET and Pharmacokinetics Modeling after Photodynamic Therapy. Sci Rep. 2016;6:31551.
30. Hirata K, Terasaka S, Shiga T, Hattori N, Magota K, Kobayashi H, et al. (1)(8)F-Fluoromisonidazole positron emission tomography may differentiate glioblastoma multiforme from less malignant gliomas. Eur J Nucl Med Mol Imaging. 2012;39(5):760-70.
31. Harada H. Hypoxia-inducible factor 1-mediated characteristic features of cancer cells for tumor radioresistance. J Radiat Res. 2016;57 Suppl 1:i99-i105.
32. Korchinski DJ, Taha M, Yang R, Nathoo N, Dunn JF. Iron Oxide as an MRI Contrast Agent for Cell Tracking. Magnetic resonance insights. 2015;8(Suppl 1):15-29.
33. Abbott NJ, Ronnback L, Hansson E. Astrocyte-endothelial interactions at the blood-brain barrier. Nat Rev Neurosci. 2006;7(1):41-53.
34. Patching SG. Glucose Transporters at the Blood-Brain Barrier: Function, Regulation and Gateways for Drug Delivery. Mol Neurobiol. 2017;54(2):1046-77.
35. Zhang RD, Price JE, Fujimaki T, Bucana CD, Fidler IJ. Differential permeability of the blood-brain barrier in experimental brain metastases produced by human neoplasms implanted into nude mice. Am J Pathol. 1992;141(5):1115-24.
36. Pessina F, Navarria P, Cozzi L, Ascolese AM, Maggi G, Rossi M, et al. Role of Surgical Resection in Patients with Single Large Brain Metastases: Feasibility, Morbidity, and Local Control Evaluation. World Neurosurg. 2016;94:6-12.
37. Hatiboglu MA, Wildrick DM, Sawaya R. The role of surgical resection in patients with brain metastases. Ecancermedicalscience. 2013;7:308.
38. Mulvenna P, Nankivell M, Barton R, Faivre-Finn C, Wilson P, McColl E, et al. Dexamethasone and supportive care with or without whole brain radiotherapy in treating patients with non-small cell lung cancer with brain metastases unsuitable for resection or stereotactic radiotherapy (QUARTZ): results from a phase 3, non-inferiority, randomised trial. Lancet. 2016;388(10055):2004-14.
39. Nieder C, Grosu AL, Gaspar LE. Stereotactic radiosurgery (SRS) for brain metastases: a systematic review. Radiat Oncol. 2014;9:155.
40. Ernst-Stecken A, Ganslandt O, Lambrecht U, Sauer R, Grabenbauer G. Phase II trial of hypofractionated stereotactic radiotherapy for brain metastases: results and toxicity. Radiother Oncol. 2006;81(1):18-24.
41. NHS. Clinical Commissioning Policy: Stereotactic Radiosurgery/Radiotherapy for Cerebral Metastases. In: Health Do, editor. 2013.

42. Prakasam AK, Maruthamuthu V, Leckband DE. Similarities between heterophilic and homophilic cadherin adhesion. Proc Natl Acad Sci U S A. 2006;103(42):15434-9.
43. Wai Wong C, Dye DE, Coombe DR. The role of immunoglobulin superfamily cell adhesion molecules in cancer metastasis. International journal of cell biology. 2012;2012:340296.
44. Goodman SR. Medical cell biology. 3rd ed. ed. Amsterdam ; London: Elsevier/Academic Press; 2008.
45. Lodish HF. Molecular cell biology. 4th ed. New York, NY ; Basingstoke: Freeman; 2000. xxxix, 1084, 17, 36 p. p.
46. Hosoi H, Ikeda H, Imai N, Amaike C, Wang L, Orito Y, et al. Stimulation through very late antigen-4 and -5 improves the multifunctionality and memory formation of CD8(+) T cells. Eur J Immunol. 2014;44(6):1747-58.
47. Elices MJ, Osborn L, Takada Y, Crouse C, Luhowskyj S, Hemler ME, et al. VCAM-1 on activated endothelium interacts with the leukocyte integrin VLA-4 at a site distinct from the VLA-4/fibronectin binding site. Cell. 1990;60(4):577-84.
48. Munoz M, Serrador J, Sanchez-Madrid F, Teixido J. A region of the integrin VLA alpha 4 subunit involved in homotypic cell aggregation and in fibronectin but not vascular cell adhesion molecule-1 binding. J Biol Chem. 1996;271(5):2696-702.
49. Chan PY, Aruffo A. VLA-4 integrin mediates lymphocyte migration on the inducible endothelial cell ligand VCAM-1 and the extracellular matrix ligand fibronectin. J Biol Chem. 1993;268(33):24655-64.
50. Smith CW. 3. Adhesion molecules and receptors. The Journal of allergy and clinical immunology. 2008;121(2 Suppl):S375-9; quiz S414.
51. Ley K, Huo Y. VCAM-1 is critical in atherosclerosis. J Clin Invest. 2001;107(10):1209-10.
52. Cannella B, Raine CS. The adhesion molecule and cytokine profile of multiple sclerosis lesions. Ann Neurol. 1995;37(4):424-35.
53. Ockenhouse CF, Tegoshi T, Maeno Y, Benjamin C, Ho M, Kan KE, et al. Human vascular endothelial cell adhesion receptors for Plasmodium falciparum-infected erythrocytes: roles for endothelial leukocyte adhesion molecule 1 and vascular cell adhesion molecule 1. J Exp Med. 1992;176(4):1183-9.
54. Ley K, Laudanna C, Cybulsky MI, Nourshargh S. Getting to the site of inflammation: the leukocyte adhesion cascade updated. Nat Rev Immunol. 2007;7(9):678-89.
55. Greenwood J, Etienne-Manneville S, Adamson P, Couraud PO. Lymphocyte migration into the central nervous system: implication of ICAM-1 signalling at the blood-brain barrier. Vascul Pharmacol. 2002;38(6):315-22.
56. Scholz D, Devaux B, Hirche A, Potzsch B, Kropp B, Schaper W, et al. Expression of adhesion molecules is specific and time-dependent in cytokine-stimulated endothelial cells in culture. Cell Tissue Res. 1996;284(3):415-23.
57. McCarron RM, Wang L, Stanimirovic DB, Spatz M. Differential Regulation of Adhesion Molecule Expression by Human Cerebrovascular and Umbilical Vein Endothelial Cells. Endothelium. 1995;2(4):339-46.
58. Soto MS, Serres S, Anthony DC, Sibson NR. Functional role of endothelial adhesion molecules in the early stages of brain metastasis. Neuro Oncol. 2014;16(4):540-51.
59. Schlesinger M, Roblek M, Ortmann K, Naggi A, Torri G, Borsig L, et al. The role of VLA-4 binding for experimental melanoma metastasis and its inhibition by heparin. Thromb Res. 2014;133(5):855-62.

60. Yan M, Jurasz P. The role of platelets in the tumor microenvironment: From solid tumors to leukemia. Biochim Biophys Acta. 2016;1863(3):392-400.
61. Menter DG, Tucker SC, Kopetz S, Sood AK, Crissman JD, Honn KV. Platelets and cancer: a casual or causal relationship: revisited. Cancer Metastasis Rev. 2014;33(1):231-69.
62. Hsieh HJ, Liu CA, Huang B, Tseng AH, Wang DL. Shear-induced endothelial mechanotransduction: the interplay between reactive oxygen species (ROS) and nitric oxide (NO) and the pathophysiological implications. J Biomed Sci. 2014;21:3.
63. Cook-Mills JM, Marchese ME, Abdala-Valencia H. Vascular cell adhesion molecule-1 expression and signaling during disease: regulation by reactive oxygen species and antioxidants. Antioxid Redox Signal. 2011;15(6):1607-38.
64. DeVerse JS, Sandhu AS, Mendoza N, Edwards CM, Sun C, Simon SI, et al. Shear stress modulates VCAM-1 expression in response to TNF-alpha and dietary lipids via interferon regulatory factor-1 in cultured endothelium. Am J Physiol Heart Circ Physiol. 2013;305(8):H1149-57.
65. Simiantonaki N, Jayasinghe C, Kirkpatrick CJ. Effect of pro-inflammatory stimuli on tumor cell-mediated induction of endothelial cell adhesion molecules in vitro. Exp Mol Pathol. 2002;73(1):46-53.
66. Gil-Bernabe AM, Ferjancic S, Tlalka M, Zhao L, Allen PD, Im JH, et al. Recruitment of monocytes/macrophages by tissue factor-mediated coagulation is essential for metastatic cell survival and premetastatic niche establishment in mice. Blood. 2012;119(13):3164-75.
67. Chen Q, Zhang XH, Massague J. Macrophage binding to receptor VCAM-1 transmits survival signals in breast cancer cells that invade the lungs. Cancer Cell. 2011;20(4):538-49.
68. Lin KY, Lu D, Hung CF, Peng S, Huang L, Jie C, et al. Ectopic expression of vascular cell adhesion molecule-1 as a new mechanism for tumor immune evasion. Cancer Res. 2007;67(4):1832-41.
69. Kawaguchi S, Kikuchi K, Ishii S, Takada Y, Kobayashi S, Uede T. VLA-4 molecules on tumor cells initiate an adhesive interaction with VCAM-1 molecules on endothelial cell surface. Jpn J Cancer Res. 1992;83(12):1304-16.
70. Martin-Padura I, Mortarini R, Lauri D, Bernasconi S, Sanchez-Madrid F, Parmiani G, et al. Heterogeneity in human melanoma cell adhesion to cytokine activated endothelial cells correlates with VLA-4 expression. Cancer Res. 1991;51(8):2239-41.
71. Qian F, Vaux DL, Weissman IL. Expression of the integrin alpha 4 beta 1 on melanoma cells can inhibit the invasive stage of metastasis formation. Cell. 1994;77(3):335-47.
72. Chen Q, Massague J. Molecular pathways: VCAM-1 as a potential therapeutic target in metastasis. Clin Cancer Res. 2012;18(20):5520-5.
73. Russell WMS, Burch RL. The principles of humane experimental technique. 1959.
74. Gengenbacher N, Singhal M, Augustin HG. Preclinical mouse solid tumour models: status quo, challenges and perspectives. Nat Rev Cancer. 2017;17(12):751-65.
75. Vandamme TF. Use of rodents as models of human diseases. Journal of pharmacy & bioallied sciences. 2014;6(1):2-9.
76. Huszthy PC, Daphu I, Niclou SP, Stieber D, Nigro JM, Sakariassen PO, et al. In vivo models of primary brain tumors: pitfalls and perspectives. Neuro Oncol. 2012;14(8):979-93.
77. Peterson JK, Houghton PJ. Integrating pharmacology and in vivo cancer models in preclinical and clinical drug development. Eur J Cancer. 2004;40(6):837-44.
78. Pulaski BA, Ostrand-Rosenberg S. Mouse 4T1 breast tumor model. Curr Protoc Immunol. 2001;Chapter 20:Unit 20 2.

79. Dun MD, Chalkley RJ, Faulkner S, Keene S, Avery-Kiejda KA, Scott RJ, et al. Proteotranscriptomic Profiling of 231-BR Breast Cancer Cells: Identification of Potential Biomarkers and Therapeutic Targets for Brain Metastasis. Mol Cell Proteomics. 2015;14(9):2316-30.
80. Yoneda T, Williams PJ, Hiraga T, Niewolna M, Nishimura R. A bone-seeking clone exhibits different biological properties from the MDA-MB-231 parental human breast cancer cells and a brain-seeking clone in vivo and in vitro. J Bone Miner Res. 2001;16(8):1486-95.
81. Rangarajan A, Weinberg RA. Opinion: Comparative biology of mouse versus human cells: modelling human cancer in mice. Nat Rev Cancer. 2003;3(12):952-9.
82. Walsh NC, Kenney LL, Jangalwe S, Aryee KE, Greiner DL, Brehm MA, et al. Humanized Mouse Models of Clinical Disease. Annu Rev Pathol. 2017;12:187-215.
83. Gillet JP, Calcagno AM, Varma S, Marino M, Green LJ, Vora MI, et al. Redefining the relevance of established cancer cell lines to the study of mechanisms of clinical anti-cancer drug resistance. Proc Natl Acad Sci U S A. 2011;108(46):18708-13.
84. Hidalgo M, Amant F, Biankin AV, Budinska E, Byrne AT, Caldas C, et al. Patient-derived xenograft models: an emerging platform for translational cancer research. Cancer Discov. 2014;4(9):998-1013.
85. Heyer J, Kwong LN, Lowe SW, Chin L. Non-germline genetically engineered mouse models for translational cancer research. Nat Rev Cancer. 2010;10(7):470-80.
86. Day CP, Merlino G, Van Dyke T. Preclinical mouse cancer models: a maze of opportunities and challenges. Cell. 2015;163(1):39-53.
87. Richmond A, Su Y. Mouse xenograft models vs GEM models for human cancer therapeutics. Dis Model Mech. 2008;1(2-3):78-82.
88. Sakamoto S, Inoue H, Ohba S, Kohda Y, Usami I, Masuda T, et al. New metastatic model of human small-cell lung cancer by orthotopic transplantation in mice. Cancer Sci. 2015;106(4):367-74.
89. Zhang C, Lowery FJ, Yu D. Intracarotid Cancer Cell Injection to Produce Mouse Models of Brain Metastasis. J Vis Exp. 2017(120).
90. Schackert G, Fidler IJ. Development of in vivo models for studies of brain metastasis. Int J Cancer. 1988;41(4):589-94.
91. Daphu I, Sundstrom T, Horn S, Huszthy PC, Niclou SP, Sakariassen PO, et al. In vivo animal models for studying brain metastasis: value and limitations. Clin Exp Metastasis. 2013;30(5):695-710.
92. Balathasan L, Beech JS, Muschel RJ. Ultrasonography-guided intracardiac injection: an improvement for quantitative brain colonization assays. Am J Pathol. 2013;183(1):26-34.
93. Zhou H, Zhao D. Ultrasound imaging-guided intracardiac injection to develop a mouse model of breast cancer brain metastases followed by longitudinal MRI. J Vis Exp. 2014(85).
94. Serres S, Soto MS, Hamilton A, McAteer MA, Carbonell WS, Robson MD, et al. Molecular MRI enables early and sensitive detection of brain metastases. Proc Natl Acad Sci U S A. 2012;109(17):6674-9.
95. Hoffman EA, Frey BL, Smith LM, Auble DT. Formaldehyde crosslinking: a tool for the study of chromatin complexes. J Biol Chem. 2015;290(44):26404-11.
96. Lunn G, Sansone EB. Safe disposal of diaminobenzidine. Trends Genet. 1992;8(1):7.
97. Seligman AM, Karnovsky MJ, Wasserkrug HL, Hanker JS. Nondroplet ultrastructural demonstration of cytochrome oxidase activity with a polymerizing osmiophilic reagent, diaminobenzidine (DAB). J Cell Biol. 1968;38(1):1-14.

98. Bratthauer GL. The avidin-biotin complex (ABC) method and other avidin-biotin binding methods. Methods Mol Biol. 2010;588:257-70.
99. Bussolati G, Radulescu RT. Blocking endogenous peroxidases in immunohistochemistry: a mandatory, yet also subtle measure. Applied immunohistochemistry & molecular morphology : AIMM. 2011;19(5):484.
100. O'Brien ER, Kersemans V, Tredwell M, Checa B, Serres S, Soto MS, et al. Glial activation in the early stages of brain metastasis: TSPO as a diagnostic biomarker. J Nucl Med. 2014;55(2):275-80.
101. Tao-Cheng JH, Gallant PE, Brightman MW, Dosemeci A, Reese TS. Structural changes at synapses after delayed perfusion fixation in different regions of the mouse brain. J Comp Neurol. 2007;501(5):731-40.
102. Gage GJ, Kipke DR, Shain W. Whole animal perfusion fixation for rodents. J Vis Exp. 2012(65).
103. Jonkers BW, Sterk JC, Wouterlood FG. Transcardial perfusion fixation of the CNS by means of a compressed-air-driven device. J Neurosci Methods. 1984;12(2):141-9.
104. Paddison PJ, Hannon GJ. RNA interference: the new somatic cell genetics? Cancer Cell. 2002;2(1):17-23.
105. Bochicchio S, Dalmoro A, Barba AA, Grassi G, Lamberti G. Liposomes as siRNA delivery vectors. Curr Drug Metab. 2014;15(9):882-92.
106. Hughes J, Yadava P, Mesaros R. Liposomal siRNA delivery. Methods Mol Biol. 2010;605:445-59.
107. Rosner M, Siegel N, Fuchs C, Slabina N, Dolznig H, Hengstschlager M. Efficient siRNA-mediated prolonged gene silencing in human amniotic fluid stem cells. Nat Protoc. 2010;5(6):1081-95.
108. Mahmood T, Yang PC. Western blot: technique, theory, and trouble shooting. N Am J Med Sci. 2012;4(9):429-34.
109. Crisp SJ, Dunn MJ. Detection of proteins on protein blots using chemiluminescent systems. Methods Mol Biol. 1994;32:233-7.
110. Alegria-Schaffer A, Lodge A, Vattem K. Performing and optimizing Western blots with an emphasis on chemiluminescent detection. Methods Enzymol. 2009;463:573-99.
111. Al-Tubuly AA. SDS-PAGE and Western Blotting. Methods Mol Med. 2000;40:391-405.
112. Strober W. Trypan Blue Exclusion Test of Cell Viability. Curr Protoc Immunol. 2015;111:A3 B 1-3.
113. Avelar-Freitas BA, Almeida VG, Pinto MC, Mourao FA, Massensini AR, Martins-Filho OA, et al. Trypan blue exclusion assay by flow cytometry. Braz J Med Biol Res. 2014;47(4):307-15.
114. Liu Y, Peterson DA, Kimura H, Schubert D. Mechanism of cellular 3-(4,5-dimethylthiazol-2-yl)-2,5-diphenyltetrazolium bromide (MTT) reduction. J Neurochem. 1997;69(2):581-93.
115. Berridge MV, Herst PM, Tan AS. Tetrazolium dyes as tools in cell biology: new insights into their cellular reduction. Biotechnol Annu Rev. 2005;11:127-52.
116. Berridge MV, Tan AS. Characterization of the cellular reduction of 3-(4,5-dimethylthiazol-2-yl)-2,5-diphenyltetrazolium bromide (MTT): subcellular localization, substrate dependence, and involvement of mitochondrial electron transport in MTT reduction. Arch Biochem Biophys. 1993;303(2):474-82.
117. Mosmann T. Rapid colorimetric assay for cellular growth and survival: application to proliferation and cytotoxicity assays. J Immunol Methods. 1983;65(1-2):55-63.

118. Schieda N, Avruch L, Shabana WM, Malone SC. Multi-echo gradient recalled echo imaging of the pelvis for improved depiction of brachytherapy seeds and fiducial markers facilitating radiotherapy planning and treatment of prostatic carcinoma. J Magn Reson Imaging. 2015;41(3):715-20.
119. Hamilton A. The effect of the systemic inflammatory response on the development of brain metastasis. University of Oxford: University of Oxford; 2013.
120. Zakaria R. Investigation of local brain invasion by cerebral metastases and implications for clinical management. University of Liverpool Repository: University of Liverpool; 2016.
121. Hayat MA. Brain Metastases from Primary Tumors, Volume 3: Epidemiology, Biology, and Therapy of Melanoma and Other Cancers: Elsevier Science; 2016.
122. Stelzer KJ. Epidemiology and prognosis of brain metastases. Surg Neurol Int. 2013;4(Suppl 4):S192-202.
123. Khan M, Lin J, Liao G, Li R, Wang B, Xie G, et al. Comparison of WBRT alone, SRS alone, and their combination in the treatment of one or more brain metastases: Review and meta-analysis. Tumour Biol. 2017;39(7):1010428317702903.
124. de Mascarel I, MacGrogan G, Debled M, Brouste V, Mauriac L. Distinction between isolated tumor cells and micrometastases in breast cancer: is it reliable and useful? Cancer. 2008;112(8):1672-8.
125. Cserni G, Amendoeira I, Bianchi S, Chmielik E, Degaetano J, Faverly D, et al. Distinction of isolated tumour cells and micrometastasis in lymph nodes of breast cancer patients according to the new Tumour Node Metastasis (TNM) definitions. Eur J Cancer. 2011;47(6):887-94.
126. de Boer M, van Deurzen CH, van Dijck JA, Borm GF, van Diest PJ, Adang EM, et al. Micrometastases or isolated tumor cells and the outcome of breast cancer. N Engl J Med. 2009;361(7):653-63.
127. Tjan-Heijnen VC, de Boer M. Minimal lymph node involvement and outcome of breast cancer. The results of the Dutch MIRROR study. Discovery medicine. 2009;8(42):137-9.
128. Pasquali S, Mocellin S, Campana LG, Bonandini E, Montesco MC, Tregnaghi A, et al. Early (sentinel lymph node biopsy-guided) versus delayed lymphadenectomy in melanoma patients with lymph node metastases : personal experience and literature meta-analysis. Cancer. 2010;116(5):1201-9.
129. Rusch VW, Hawes D, Decker PA, Martin SE, Abati A, Landreneau RJ, et al. Occult metastases in lymph nodes predict survival in resectable non-small-cell lung cancer: report of the ACOSOG Z0040 trial. J Clin Oncol. 2011;29(32):4313-9.
130. Hanssens P, Karlsson B, Yeo TT, Chou N, Beute G. Detection of brain micrometastases by high-resolution stereotactic magnetic resonance imaging and its impact on the timing of and risk for distant recurrences. J Neurosurg. 2011;115(3):499-504.
131. Tonra JR, Poyurovsky M, Liu KG, Patel J, Rao N, Tilton R, et al. Abstract 2590: KD019: Blood brain barrier penetrant HER2/neu, Src, and EGFR inhibitor. Cancer Research. 2015;75:2590-.
132. Ballard P, Yates JW, Yang Z, Kim DW, Yang JC, Cantarini M, et al. Preclinical Comparison of Osimertinib with Other EGFR-TKIs in EGFR-Mutant NSCLC Brain Metastases Models, and Early Evidence of Clinical Brain Metastases Activity. Clin Cancer Res. 2016;22(20):5130-40.
133. Connell JJ, Chatain G, Cornelissen B, Vallis KA, Hamilton A, Seymour L, et al. Selective permeabilization of the blood-brain barrier at sites of metastasis. J Natl Cancer Inst. 2013;105(21):1634-43.

134. Eguchi T, Kodera Y, Nakanishi H, Yokoyama H, Ohashi N, Ito Y, et al. The effect of chemotherapy against micrometastases and isolated tumor cells in lymph nodes: an in vivo study. In vivo (Athens, Greece). 2008;22(6):707-12.
135. Nomoto Y, Miyamoto T, Yamaguchi Y. Brain metastasis of small cell lung carcinoma: comparison of Gd-DTPA enhanced magnetic resonance imaging and enhanced computerized tomography. Jpn J Clin Oncol. 1994;24(5):258-62.
136. Schlesinger M, Bendas G. Vascular cell adhesion molecule-1 (VCAM-1)--an increasing insight into its role in tumorigenicity and metastasis. Int J Cancer. 2015;136(11):2504-14.
137. Samlowski WE, Moon J, Witter M, Atkins MB, Kirkwood JM, Othus M, et al. High frequency of brain metastases after adjuvant therapy for high-risk melanoma. Cancer Med. 2017;6(11):2576-85.
138. Smedby KE, Brandt L, Backlund ML, Blomqvist P. Brain metastases admissions in Sweden between 1987 and 2006. Br J Cancer. 2009;101(11):1919-24.
139. Sundstrom T, Daphu I, Wendelbo I, Hodneland E, Lundervold A, Immervoll H, et al. Automated tracking of nanoparticle-labeled melanoma cells improves the predictive power of a brain metastasis model. Cancer Res. 2013;73(8):2445-56.
140. Jassam SA, Maherally Z, Smith JR, Ashkan K, Roncaroli F, Fillmore HL, et al. CD15s/CD62E Interaction Mediates the Adhesion of Non-Small Cell Lung Cancer Cells on Brain Endothelial Cells: Implications for Cerebral Metastasis. Int J Mol Sci. 2017;18(7).
141. Sa Q, Ochiai E, Sengoku T, Wilson ME, Brogli M, Crutcher S, et al. VCAM-1/alpha4beta1 integrin interaction is crucial for prompt recruitment of immune T cells into the brain during the early stage of reactivation of chronic infection with Toxoplasma gondii to prevent toxoplasmic encephalitis. Infection and immunity. 2014;82(7):2826-39.
142. Gaudy-Marqueste C, Dussouil AS, Carron R, Troin L, Malissen N, Loundou A, et al. Survival of melanoma patients treated with targeted therapy and immunotherapy after systematic upfront control of brain metastases by radiosurgery. Eur J Cancer. 2017;84:44-54.
143. Weinstein JS, Varallyay CG, Dosa E, Gahramanov S, Hamilton B, Rooney WD, et al. Superparamagnetic iron oxide nanoparticles: diagnostic magnetic resonance imaging and potential therapeutic applications in neurooncology and central nervous system inflammatory pathologies, a review. J Cereb Blood Flow Metab. 2010;30(1):15-35.
144. Zarghami N KA, Perez-Balderas F, Sarmiento-Soto M, Sibson, NR. Optimization of molecularly targeted MRI in brain: empirical comparison of sequences and particles. Int J Nanomed. 2018.
145. Lambert AW, Pattabiraman DR, Weinberg RA. Emerging Biological Principles of Metastasis. Cell. 2017;168(4):670-91.
146. Elovaara I, Ukkonen M, Leppakynnas M, Lehtimaki T, Luomala M, Peltola J, et al. Adhesion molecules in multiple sclerosis: relation to subtypes of disease and methylprednisolone therapy. Arch Neurol. 2000;57(4):546-51.
147. Li F, Wang Y, Yu L, Cao S, Wang K, Yuan J, et al. Viral Infection of the Central Nervous System and Neuroinflammation Precede Blood-Brain Barrier Disruption during Japanese Encephalitis Virus Infection. J Virol. 2015;89(10):5602-14.
148. Frijns CJ, Kappelle LJ. Inflammatory cell adhesion molecules in ischemic cerebrovascular disease. Stroke. 2002;33(8):2115-22.
149. Fink KR, Fink JR. Imaging of brain metastases. Surg Neurol Int. 2013;4(Suppl 4):S209-19.
150. Auperin A, Arriagada R, Pignon JP, Le Pechoux C, Gregor A, Stephens RJ, et al. Prophylactic cranial irradiation for patients with small-cell lung cancer in complete remission.

Prophylactic Cranial Irradiation Overview Collaborative Group. N Engl J Med. 1999;341(7):476-84.
151. Halthore A, Goenka A, Sharma R, Knisely JPS. Prophylactic Cranial Irradiation for Resectable Small-Cell Lung Cancer. Clin Lung Cancer. 2017.
152. Matsukado K, Inamura T, Nakano S, Fukui M, Bartus RT, Black KL. Enhanced tumor uptake of carboplatin and survival in glioma-bearing rats by intracarotid infusion of bradykinin analog, RMP-7. Neurosurgery. 1996;39(1):125-33; discussion 33-4.
153. Choi JJ, Selert K, Vlachos F, Wong A, Konofagou EE. Noninvasive and localized neuronal delivery using short ultrasonic pulses and microbubbles. Proc Natl Acad Sci U S A. 2011;108(40):16539-44.
154. Perez-Balderas F, van Kasteren SI, Aljabali AA, Wals K, Serres S, Jefferson A, et al. Covalent assembly of nanoparticles as a peptidase-degradable platform for molecular MRI. Nat Commun. 2017;8:14254.
155. Whiteside TL. The tumor microenvironment and its role in promoting tumor growth. Oncogene. 2008;27(45):5904-12.
156. Man YG, Stojadinovic A, Mason J, Avital I, Bilchik A, Bruecher B, et al. Tumor-infiltrating immune cells promoting tumor invasion and metastasis: existing theories. Journal of Cancer. 2013;4(1):84-95.
157. McDonald DM, Baluk P. Significance of blood vessel leakiness in cancer. Cancer Res. 2002;62(18):5381-5.
158. Dunn LT. Raised intracranial pressure. Journal of neurology, neurosurgery, and psychiatry. 2002;73 Suppl 1:i23-7.
159. Yaeger KA, Nair MN. Surgery for brain metastases. Surg Neurol Int. 2013;4(Suppl 4):S203-8.
160. Minniti G, Clarke E, Lanzetta G, Osti MF, Trasimeni G, Bozzao A, et al. Stereotactic radiosurgery for brain metastases: analysis of outcome and risk of brain radionecrosis. Radiat Oncol. 2011;6:48.
161. Aoyama H, Shirato H, Onimaru R, Kagei K, Ikeda J, Ishii N, et al. Hypofractionated stereotactic radiotherapy alone without whole-brain irradiation for patients with solitary and oligo brain metastasis using noninvasive fixation of the skull. Int J Radiat Oncol Biol Phys. 2003;56(3):793-800.
162. Manning MA, Cardinale RM, Benedict SH, Kavanagh BD, Zwicker RD, Amir C, et al. Hypofractionated stereotactic radiotherapy as an alternative to radiosurgery for the treatment of patients with brain metastases. Int J Radiat Oncol Biol Phys. 2000;47(3):603-8.
163. Fahrig A, Ganslandt O, Lambrecht U, Grabenbauer G, Kleinert G, Sauer R, et al. Hypofractionated stereotactic radiotherapy for brain metastases--results from three different dose concepts. Strahlentherapie und Onkologie : Organ der Deutschen Rontgengesellschaft [et al]. 2007;183(11):625-30.
164. Kocher M, Soffietti R, Abacioglu U, Villa S, Fauchon F, Baumert BG, et al. Adjuvant whole-brain radiotherapy versus observation after radiosurgery or surgical resection of one to three cerebral metastases: results of the EORTC 22952-26001 study. J Clin Oncol. 2011;29(2):134-41.
165. Burnet NG, Thomas SJ, Burton KE, Jefferies SJ. Defining the tumour and target volumes for radiotherapy. Cancer Imaging. 2004;4(2):153-61.
166. Berthelsen AK, Dobbs J, Kjellén E, Landberg T, Möller TR, Nilsson P, et al. What's new in target volume definition for radiologists in ICRU Report 71? How can the ICRU volume definitions be integrated in clinical practice? Cancer Imaging. 72007. p. 104-16.

167. Stanley J, Dunscombe P, Lau H, Burns P, Lim G, Liu HW, et al. The effect of contouring variability on dosimetric parameters for brain metastases treated with stereotactic radiosurgery. Int J Radiat Oncol Biol Phys. 2013;87(5):924-31.
168. Sandstrom H, Jokura H, Chung C, Toma-Dasu I. Multi-institutional study of the variability in target delineation for six targets commonly treated with radiosurgery. Acta oncologica (Stockholm, Sweden). 2018:1-6.
169. Piotrowski W, Brock M, Klinger M. CNS Metastases Neurosurgery in the Aged: Proceedings of the 34th Annual Meeting of the Deutsche Gesellschaft für Neurochirurgie, Mannheim, April 27-30, 1983: Springer Berlin Heidelberg; 2012.
170. Berghoff AS, Rajky O, Winkler F, Bartsch R, Furtner J, Hainfellner JA, et al. Invasion patterns in brain metastases of solid cancers. Neuro Oncol. 2013;15(12):1664-72.
171. Siam L, Bleckmann A, Chaung HN, Mohr A, Klemm F, Barrantes-Freer A, et al. The metastatic infiltration at the metastasis/brain parenchyma-interface is very heterogeneous and has a significant impact on survival in a prospective study. Oncotarget. 2015;6(30):29254-67.
172. Kamp MA, Slotty PJ, Cornelius JF, Steiger HJ, Rapp M, Sabel M. The impact of cerebral metastases growth pattern on neurosurgical treatment. Neurosurgical review. 2018;41(1):77-86.
173. Witwer BP, Moftakhar R, Hasan KM, Deshmukh P, Haughton V, Field A, et al. Diffusion-tensor imaging of white matter tracts in patients with cerebral neoplasm. J Neurosurg. 2002;97(3):568-75.
174. Mori S, Frederiksen K, van Zijl PC, Stieltjes B, Kraut MA, Solaiyappan M, et al. Brain white matter anatomy of tumor patients evaluated with diffusion tensor imaging. Ann Neurol. 2002;51(3):377-80.
175. Croteau D, Scarpace L, Hearshen D, Gutierrez J, Fisher JL, Rock JP, et al. Correlation between magnetic resonance spectroscopy imaging and image-guided biopsies: semiquantitative and qualitative histopathological analyses of patients with untreated glioma. Neurosurgery. 2001;49(4):823-9.
176. McKnight TR, von dem Bussche MH, Vigneron DB, Lu Y, Berger MS, McDermott MW, et al. Histopathological validation of a three-dimensional magnetic resonance spectroscopy index as a predictor of tumor presence. J Neurosurg. 2002;97(4):794-802.
177. Price SJ, Green HA, Dean AF, Joseph J, Hutchinson PJ, Gillard JH. Correlation of MR relative cerebral blood volume measurements with cellular density and proliferation in high-grade gliomas: an image-guided biopsy study. AJNR Am J Neuroradiol. 2011;32(3):501-6.
178. Henry RG, Vigneron DB, Fischbein NJ, Grant PE, Day MR, Noworolski SM, et al. Comparison of relative cerebral blood volume and proton spectroscopy in patients with treated gliomas. AJNR Am J Neuroradiol. 2000;21(2):357-66.
179. Pauleit D, Langen KJ, Floeth F, Hautzel H, Riemenschneider MJ, Reifenberger G, et al. Can the apparent diffusion coefficient be used as a noninvasive parameter to distinguish tumor tissue from peritumoral tissue in cerebral gliomas? J Magn Reson Imaging. 2004;20(5):758-64.
180. Watanabe M, Tanaka R, Takeda N. Magnetic resonance imaging and histopathology of cerebral gliomas. Neuroradiology. 1992;34(6):463-9.
181. Lunsford LD, Martinez AJ, Latchaw RE. Magnetic resonance imaging does not define tumor boundaries. Acta radiologica Supplementum. 1986;369:154-6.

182. Kelly PJ, Daumas-Duport C, Kispert DB, Kall BA, Scheithauer BW, Illig JJ. Imaging-based stereotaxic serial biopsies in untreated intracranial glial neoplasms. J Neurosurg. 1987;66(6):865-74.
183. Shen J, Li G, Liu Q, He Q, Gu J, Shi Y, et al. Marchantin C: a potential anti-invasion agent in glioma cells. Cancer biology & therapy. 2010;9(1):33-9.
184. Cheng V, Esteves F, Chakrabarty A, Cockle J, Short S, Bruning-Richardson A. High-content analysis of tumour cell invasion in three-dimensional spheroid assays. Oncoscience. 2015;2(6):596-606.
185. Soto MS, Sibson NR. Mouse Models of Brain Metastasis for Unravelling Tumour Progression. Adv Exp Med Biol. 2016;899:231-44.
186. Smith SJ, Diksin M, Chhaya S, Sairam S, Estevez-Cebrero MA, Rahman R. The Invasive Region of Glioblastoma Defined by 5ALA Guided Surgery Has an Altered Cancer Stem Cell Marker Profile Compared to Central Tumour. Int J Mol Sci. 2017;18(11).
187. Wuebben EL, Rizzino A. The dark side of SOX2: cancer - a comprehensive overview. Oncotarget. 2017;8(27):44917-43.
188. Schaefer T, Ramadoss A, Leu S, Tintignac L, Tostado C, Bink A, et al. Regulation of glioma cell invasion by 3q26 gene products PIK3CA, SOX2 and OPA1. Brain pathology (Zurich, Switzerland). 2018.
189. Bergman A, Gligorijevic B. Niche construction game cancer cells play. Eur Phys J Plus. 2015;130(10).
190. Hoyer C, Gass N, Weber-Fahr W, Sartorius A. Advantages and challenges of small animal magnetic resonance imaging as a translational tool. Neuropsychobiology. 2014;69(4):187-201.
191. Denic A, Macura SI, Mishra P, Gamez JD, Rodriguez M, Pirko I. MRI in Rodent Models of Brain Disorders. Neurotherapeutics. 82011. p. 3-18.
192. Schweser F, Preda M, Zivadinov R. Susceptibility Weighted MRI in Rodents at 9.4 T. Methods Mol Biol. 2018;1718:205-34.
193. Deistung A, Rauscher A, Sedlacik J, Stadler J, Witoszynskyj S, Reichenbach JR. Susceptibility weighted imaging at ultra high magnetic field strengths: theoretical considerations and experimental results. Magn Reson Med. 2008;60(5):1155-68.
194. Peters AM, Brookes MJ, Hoogenraad FG, Gowland PA, Francis ST, Morris PG, et al. T2* measurements in human brain at 1.5, 3 and 7 T. Magnetic resonance imaging. 2007;25(6):748-53.
195. Ogawa S, Lee TM. Magnetic resonance imaging of blood vessels at high fields: in vivo and in vitro measurements and image simulation. Magn Reson Med. 1990;16(1):9-18.
196. Solomon SB, Silverman SG. Imaging in interventional oncology. Radiology. 2010;257(3):624-40.
197. Miner RC. Image-Guided Neurosurgery. Journal of Medical Imaging and Radiation Sciences. 2017;48(4):328-35.
198. Celix JM, Silbergeld DL. Intraoperative Cortical Mapping Techniques and Limitations. In: Byrne RW, editor. Functional Mapping of the Cerebral Cortex: Safe Surgery in Eloquent Brain. Cham: Springer International Publishing; 2016. p. 63-76.
199. Garber ST, Jensen RL. Image guidance for brain metastases resection. Surg Neurol Int. 2012;3(Suppl 2):S111-7.
200. Ferraro N, Barbarite E, Albert TR, Berchmans E, Shah AH, Bregy A, et al. The role of 5-aminolevulinic acid in brain tumor surgery: a systematic review. Neurosurgical review. 2016;39(4):545-55.

201. Yoo H, Kim YZ, Nam BH, Shin SH, Yang HS, Lee JS, et al. Reduced local recurrence of a single brain metastasis through microscopic total resection. J Neurosurg. 2009;110(4):730-6.
202. Kamp MA, Rapp M, Slotty PJ, Turowski B, Sadat H, Smuga M, et al. Incidence of local in-brain progression after supramarginal resection of cerebral metastases. Acta neurochirurgica. 2015;157(6):905-10; discussion 10-1.
203. Wiggenraad R, Verbeek-de Kanter A, Kal HB, Taphoorn M, Vissers T, Struikmans H. Dose-effect relation in stereotactic radiotherapy for brain metastases. A systematic review. Radiother Oncol. 2011;98(3):292-7.
204. Mouthuy N, Cosnard G, Abarca-Quinones J, Michoux N. Multiparametric magnetic resonance imaging to differentiate high-grade gliomas and brain metastases. Journal of neuroradiology Journal de neuroradiologie. 2012;39(5):301-7.
205. Knitter JR, Erly WK, Stea BD, Lemole GM, Germano IM, Doshi AH, et al. Interval Change in Diffusion and Perfusion MRI Parameters for the Assessment of Pseudoprogression in Cerebral Metastases Treated With Stereotactic Radiation. AJR American journal of roentgenology. 2018;211(1):168-75.
206. Kniep HC, Madesta F, Schneider T, Hanning U, Schonfeld MH, Schon G, et al. Radiomics of Brain MRI: Utility in Prediction of Metastatic Tumor Type. Radiology. 2018:180946.
207. Kang SA, Hasan N, Mann AP, Zheng W, Zhao L, Morris L, et al. Blocking the adhesion cascade at the premetastatic niche for prevention of breast cancer metastasis. Mol Ther. 2015;23(6):1044-54.
208. Schlesinger M, Schmitz P, Zeisig R, Naggi A, Torri G, Casu B, et al. The inhibition of the integrin VLA-4 in MV3 melanoma cell binding by non-anticoagulant heparin derivatives. Thromb Res. 2012;129(5):603-10.
209. Hernandez-Caselles T, Martinez-Esparza M, Lazarovits AI, Aparicio P. Specific regulation of VLA-4 and alpha 4 beta 7 integrin expression on human activated T lymphocytes. J Immunol. 1996;156(10):3668-77.
210. Taichman DB, Cybulsky MI, Djaffar I, Longenecker BM, Teixido J, Rice GE, et al. Tumor cell surface alpha 4 beta 1 integrin mediates adhesion to vascular endothelium: demonstration of an interaction with the N-terminal domains of INCAM-110/VCAM-1. Cell Regul. 1991;2(5):347-55.
211. Klemke M, Weschenfelder T, Konstandin MH, Samstag Y. High affinity interaction of integrin alpha4beta1 (VLA-4) and vascular cell adhesion molecule 1 (VCAM-1) enhances migration of human melanoma cells across activated endothelial cell layers. J Cell Physiol. 2007;212(2):368-74.
212. Manevich E, Grabovsky V, Feigelson SW, Alon R. Talin 1 and paxillin facilitate distinct steps in rapid VLA-4-mediated adhesion strengthening to vascular cell adhesion molecule 1. J Biol Chem. 2007;282(35):25338-48.
213. Alon R, Feigelson SW, Manevich E, Rose DM, Schmitz J, Overby DR, et al. Alpha4beta1-dependent adhesion strengthening under mechanical strain is regulated by paxillin association with the alpha4-cytoplasmic domain. J Cell Biol. 2005;171(6):1073-84.
214. Brown MC, Turner CE. Paxillin: adapting to change. Physiol Rev. 2004;84(4):1315-39.
215. Kassner PD, Alon R, Springer TA, Hemler ME. Specialized functional properties of the integrin alpha 4 cytoplasmic domain. Mol Biol Cell. 1995;6(6):661-74.
216. Hyun YM, Chung HL, McGrath JL, Waugh RE, Kim M. Activated integrin VLA-4 localizes to the lamellipodia and mediates T cell migration on VCAM-1. J Immunol. 2009;183(1):359-69.

217. Goldfinger LE, Han J, Kiosses WB, Howe AK, Ginsberg MH. Spatial restriction of alpha4 integrin phosphorylation regulates lamellipodial stability and alpha4beta1-dependent cell migration. J Cell Biol. 2003;162(4):731-41.
218. Chigaev A, Sklar LA. Aspects of VLA-4 and LFA-1 regulation that may contribute to rolling and firm adhesion. Front Immunol. 2012;3:242.
219. Masumoto A, Hemler ME. Multiple activation states of VLA-4. Mechanistic differences between adhesion to CS1/fibronectin and to vascular cell adhesion molecule-1. J Biol Chem. 1993;268(1):228-34.
220. Tiemann K, Rossi JJ. RNAi-based therapeutics-current status, challenges and prospects. EMBO Mol Med. 2009;1(3):142-51.
221. Bartlett DW, Davis ME. Insights into the kinetics of siRNA-mediated gene silencing from live-cell and live-animal bioluminescent imaging. Nucleic Acids Res. 2006;34(1):322-33.
222. Moore CB, Guthrie EH, Huang MT, Taxman DJ. Short hairpin RNA (shRNA): design, delivery, and assessment of gene knockdown. Methods Mol Biol. 2010;629:141-58.
223. Lambeth LS, Smith CA. Short hairpin RNA-mediated gene silencing. Methods Mol Biol. 2013;942:205-32.
224. Noborio-Hatano K, Kikuchi J, Takatoku M, Shimizu R, Wada T, Ueda M, et al. Bortezomib overcomes cell-adhesion-mediated drug resistance through downregulation of VLA-4 expression in multiple myeloma. Oncogene. 2009;28(2):231-42.
225. Hsu PD, Lander ES, Zhang F. Development and applications of CRISPR-Cas9 for genome engineering. Cell. 2014;157(6):1262-78.
226. Joung JK, Sander JD. TALENs: a widely applicable technology for targeted genome editing. Nat Rev Mol Cell Biol. 2013;14(1):49-55.
227. Hathi DK, Chanswangphuwana C, Rettig MP, Achilefu S, DiPersio JF, Shokeen M. Abstract 2525: Identification of differentially expressed myeloma-specific pathways in the absence of VLA-4. 2018.
228. Campanero MR, Pulido R, Ursa MA, Rodriguez-Moya M, de Landazuri MO, Sanchez-Madrid F. An alternative leukocyte homotypic adhesion mechanism, LFA-1/ICAM-1-independent, triggered through the human VLA-4 integrin. J Cell Biol. 1990;110(6):2157-65.
229. Groux H, Huet S, Valentin H, Pham D, Bernard A. Suppressor effects and cyclic AMP accumulation by the CD29 molecule of CD4+ lymphocytes. Nature. 1989;339(6220):152-4.
230. Macias C, Ballester JM, Hernandez P. Expression and functional activity of the very late activation antigen-4 molecule on human natural killer cells in different states of activation. Immunology. 2000;100(1):77-83.
231. Shokeen M, Zheleznyak A, Wilson JM, Jiang M, Liu R, Ferdani R, et al. Molecular imaging of very late antigen-4 (alpha4beta1 integrin) in the premetastatic niche. J Nucl Med. 2012;53(5):779-86.
232. Kaplan RN, Psaila B, Lyden D. Bone marrow cells in the 'pre-metastatic niche': within bone and beyond. Cancer Metastasis Rev. 2006;25(4):521-9.
233. Jin H, Aiyer A, Su J, Borgstrom P, Stupack D, Friedlander M, et al. A homing mechanism for bone marrow-derived progenitor cell recruitment to the neovasculature. J Clin Invest. 2006;116(3):652-62.
234. Schlesinger M, Bendas G. Contribution of very late antigen-4 (VLA-4) integrin to cancer progression and metastasis. Cancer Metastasis Rev. 2015;34(4):575-91.
235. Luo BH, Carman CV, Springer TA. Structural Basis of Integrin Regulation and Signaling. Annu Rev Immunol. 2007;25:619-47.

236. Hart R, Greaves DR. Chemerin contributes to inflammation by promoting macrophage adhesion to VCAM-1 and fibronectin through clustering of VLA-4 and VLA-5. J Immunol. 2010;185(6):3728-39.
237. Sanz-Rodriguez F, Hidalgo A, Teixido J. Chemokine stromal cell-derived factor-1alpha modulates VLA-4 integrin-mediated multiple myeloma cell adhesion to CS-1/fibronectin and VCAM-1. Blood. 2001;97(2):346-51.
238. Weber C, Alon R, Moser B, Springer TA. Sequential regulation of alpha 4 beta 1 and alpha 5 beta 1 integrin avidity by CC chemokines in monocytes: implications for transendothelial chemotaxis. J Cell Biol. 1996;134(4):1063-73.
239. Yang Y, Cardarelli PM, Lehnert K, Rowland S, Krissansen GW. LPAM-1 (integrin alpha 4 beta 7)-ligand binding: overlapping binding sites recognizing VCAM-1, MAdCAM-1 and CS-1 are blocked by fibrinogen, a fibronectin-like polymer and RGD-like cyclic peptides. Eur J Immunol. 1998;28(3):995-1004.
240. Altevogt P, Hubbe M, Ruppert M, Lohr J, von Hoegen P, Sammar M, et al. The alpha 4 integrin chain is a ligand for alpha 4 beta 7 and alpha 4 beta 1. J Exp Med. 1821995. p. 345-55.
241. Santala P, Heino J. Regulation of integrin-type cell adhesion receptors by cytokines. J Biol Chem. 1991;266(34):23505-9.
242. Hemler ME. VLA proteins in the integrin family: structures, functions, and their role on leukocytes. Annu Rev Immunol. 1990;8:365-400.
243. Hou S, Isaji T, Hang Q, Im S, Fukuda T, Gu J. Distinct effects of β1 integrin on cell proliferation and cellular signaling in MDA-MB-231 breast cancer cells. Scientific Reports. 2016;6:18430.
244. Arroyo AG, Sanchez-Mateos P, Campanero MR, Martin-Padura I, Dejana E, Sanchez-Madrid F. Regulation of the VLA integrin-ligand interactions through the beta 1 subunit. J Cell Biol. 1992;117(3):659-70.
245. Pucci E, Giuliani G, Solari A, Simi S, Minozzi S, Di Pietrantonj C, et al. Natalizumab for relapsing remitting multiple sclerosis. Cochrane Database Syst Rev. 2011(10):Cd007621.
246. Hutchinson M. Natalizumab: A new treatment for relapsing remitting multiple sclerosis. Ther Clin Risk Manag. 2007;3(2):259-68.
247. Ford AC, Sandborn WJ, Khan KJ, Hanauer SB, Talley NJ, Moayyedi P. Efficacy of biological therapies in inflammatory bowel disease: systematic review and meta-analysis. The American journal of gastroenterology. 2011;106(4):644-59, quiz 60.
248. ClinicalTrials.gov. Study of Natalizumab in Relapsed/Refractory Multiple Myeloma 2008 [Available from: https://ClinicalTrials.gov/show/NCT00675428.
249. Raab-Westphal S, Marshall JF, Goodman SL. Integrins as Therapeutic Targets: Successes and Cancers. Cancers. 2017;9(9).
250. Yoshimura N, Watanabe M, Motoya S, Tominaga K, Matsuoka K, Iwakiri R, et al. Safety and Efficacy of AJM300, an Oral Antagonist of α4 Integrin, in Induction Therapy for Patients With Active Ulcerative Colitis. Gastroenterology. 2015;149(7):1775-83.e2.
251. Koo GC, Shah K, Ding GJ, Xiao J, Wnek R, Doherty G, et al. A small molecule very late antigen-4 antagonist can inhibit ovalbumin-induced lung inflammation. American journal of respiratory and critical care medicine. 2003;167(10):1400-9.
252. Theien BE, Vanderlugt CL, Nickerson-Nutter C, Cornebise M, Scott DM, Perper SJ, et al. Differential effects of treatment with a small-molecule VLA-4 antagonist before and after onset of relapsing EAE. Blood. 2003;102(13):4464-71.

253. Kummer C, Petrich BG, Rose DM, Ginsberg MH. A small molecule that inhibits the interaction of paxillin and alpha 4 integrin inhibits accumulation of mononuclear leukocytes at a site of inflammation. J Biol Chem. 2010;285(13):9462-9.
254. Hedrick L, Cho KR, Vogelstein B. Cell adhesion molecules as tumour suppressors. Trends in Cell Biology. 1993;3(2):36-9.
255. Farahani E, Department of Clinical and Experimental Medicine DoCBaIRMCIa, Patra HK, Department of Physics CaBI, Linköping University, 581 83 Linköping, Sweden,, Jangamreddy JR, Department of Clinical and Experimental Medicine DoCBaIRMCIa, et al. Cell adhesion molecules and their relation to (cancer) cell stemness. Carcinogenesis. 2018;35(4):747-59.
256. Spencer K, Hall A, Jain P. Brain metastases. Clinical medicine (London, England). 2014;14(5):535-7.
257. Norden AD, Wen PY, Kesari S. Brain metastases. Current opinion in neurology. 2005;18(6):654-61.
258. Fidler IJ. The pathogenesis of cancer metastasis: the 'seed and soil' hypothesis revisited. Nat Rev Cancer. 2003;3(6):453-8.
259. Burrell RA, Swanton C. Re-Evaluating Clonal Dominance in Cancer Evolution. Trends Cancer. 2016;2(5):263-76.
260. Turajlic S, Swanton C. Metastasis as an evolutionary process. Science. 2016;352(6282):169-75.
261. Wong D, Dorovini-Zis K. Expression of vascular cell adhesion molecule-1 (VCAM-1) by human brain microvessel endothelial cells in primary culture. Microvascular research. 1995;49(3):325-39.
262. McAteer MA, Sibson NR, von Zur Muhlen C, Schneider JE, Lowe AS, Warrick N, et al. In vivo magnetic resonance imaging of acute brain inflammation using microparticles of iron oxide. Nature medicine. 2007;13(10):1253-8.
263. Gore EM, Bae K, Wong SJ, Sun A, Bonner JA, Schild SE, et al. Phase III comparison of prophylactic cranial irradiation versus observation in patients with locally advanced non-small-cell lung cancer: primary analysis of radiation therapy oncology group study RTOG 0214. J Clin Oncol. 2011;29(3):272-8.
264. Frytak S, Shaw JN, O'Neill BP, Lee RE, Eagan RT, Shaw EG, et al. Leukoencephalopathy in small cell lung cancer patients receiving prophylactic cranial irradiation. American journal of clinical oncology. 1989;12(1):27-33.
265. Crossen JR, Garwood D, Glatstein E, Neuwelt EA. Neurobehavioral sequelae of cranial irradiation in adults: a review of radiation-induced encephalopathy. J Clin Oncol. 1994;12(3):627-42.
266. Shiau CY, Sneed PK, Shu HK, Lamborn KR, McDermott MW, Chang S, et al. Radiosurgery for brain metastases: relationship of dose and pattern of enhancement to local control. Int J Radiat Oncol Biol Phys. 1997;37(2):375-83.
267. Breneman JC, Warnick RE, Albright RE, Jr., Kukiatinant N, Shaw J, Armin D, et al. Stereotactic radiosurgery for the treatment of brain metastases. Results of a single institution series. Cancer. 1997;79(3):551-7.
268. Noel G, Simon JM, Valery CA, Cornu P, Boisserie G, Hasboun D, et al. Radiosurgery for brain metastasis: impact of CTV on local control. Radiother Oncol. 2003;68(1):15-21.
269. Oppenheimer-Marks N, Davis LS, Bogue DT, Ramberg J, Lipsky PE. Differential utilization of ICAM-1 and VCAM-1 during the adhesion and transendothelial migration of human T lymphocytes. J Immunol. 1991;147(9):2913-21.

270. Alon R, Kassner PD, Carr MW, Finger EB, Hemler ME, Springer TA. The integrin VLA-4 supports tethering and rolling in flow on VCAM-1. J Cell Biol. 1995;128(6):1243-53.
271. Taketo MM. Reflections on the spread of metastasis to cancer prevention. Cancer prevention research (Philadelphia, Pa). 2011;4(3):324-8.
272. Ghajar CM. Metastasis prevention by targeting the dormant niche. Nat Rev Cancer. 15. England2015. p. 238-47.